Nanoporous filtration membranes based on columnar liquid crystals

Document status and date:
Published: 25/02/2022

Document Version:
Publisher's PDF, also known as Version of Record (includes final page, issue and volume numbers)

Please check the document version of this publication:

Link to publication

Nanoporous filtration membranes based on columnar liquid crystals

PROEFSCHRIFT

ter verkrijging van de graad van doctor aan de Technische Universiteit Eindhoven, op gezag van de rector magnificus prof.dr.ir.F.P.T. Baaijens, voor een commissie aangewezen door het College voor Promoties, in het openbaar te verdedigen op vrijdag 25 february 2022 om 13:30 uur

door

Patricia P. Marín San Román

Geboren te Zaragoza, Spanje

Dit proefschrift is goedgekeurd door de promotoren en de samenstelling van de promotiecommissie is als volgt:

Voorzitter:	prof.dr. F. Galluci
1^e promotor	prof.dr.R.P. Sijbesma
Copromotor(en)	D.C. Nijmeijer
Leden	prof.dr.ir. W.M. de Vos (Universiteit Twente)
	prof.dr. T. Kato (University of Tokyo)
	prof.dr. APHJ Schenning
	dr.ir. JPA Heuts
Adviseur	dr.ir. JAM Lugger (Sabic)

Het onderzoek of ontwerp dat in dit proefschrift wordt beschreven is uitgevoerd in overeenstemming met de TU/e Gedragscode Weenschapsbeoefening

A todos los que creyeron en mí

Nanoporous filtration membranes based on columnar liquid crystals

Patricia P. Marín San Román

Table of Contents

Chapter 7

Optimization of molecular design and performance of LC-based membranes **147**

Chapter 1

Columnar liquid crystal-based membranes for water filtration

Abstract | The most promising materials for the development of improved nanofiltration membranes are reviewed. Selective, high-flux membranes for the efficient removal of emerging organic pollutants from water require the use of well-defined and versatile molecular components as building blocks. Liquid crystals have the ability to self-assemble into highly organized structures with nm scale pores after fixation in a network. Columnar liquid crystals are presented as promising materials for water filtration membranes. With these membranes as state of the art, we establish the efforts required to improve the performance of membranes. These improvements include control over structural order and pore functionalities by molecular design and optimization of the membrane fabrication for the specific recovery and removal of organics from water.

1.1 Introduction

Population growth and rapid industrialization have led to global issues such as climate disruption and industrial pollution with resulting shortages of clean water and other resources. Indeed, the demand for global fresh water, our most precious resource, is predicted to increase by 30% in the coming 10 years due to overuse in food production with the increase of the human population.[1] Current water supplies will not be enough to satisfy the increasing demand creating the challenge to provide the whole world population with clean water. In addition to this, human activities are responsible for the contamination of water with new emerging so-called micropollutants (MPs),[2] which comprise of a complex mixture of organic molecules such as pharmaceuticals, hormones, personal care products and cosmetics, surfactants, chemicals like pesticides and plasticizers from agriculture and other industries. Trace contaminants that are released into the environment endanger many aquatic life forms and are often toxic for humans.[3] Therefore, water and wastewater treatment is becoming increasingly important. Recently developed methods to clean water focus on the removal of these undesired pollutants and/or the selective recovery of valuable compounds for reuse.[4] Cleaning water with the use of conventional techniques such as coagulation or sedimentation is insufficient because only limited levels of removal for micropollutants can be achieved. Adsorption is considered one of the best suitable water treatment methods due to its easy operation and the availability of a wide range of adsorbents for the removal of a large variety of soluble and insoluble organic, inorganic, and biological pollutants.[5] Activated carbon is widely used as an adsorbent for cleaning water due to its high and dense porosity and large surface area. However, it shows several deficiencies like slow adsorption and poor removal of very hydrophilic compounds and high cost in large-scale water treatment.

Thus, to maintain a balance between demand and supply of clean water, new technologies are developed that address water purification in most efficient and environmentally friendly ways.[6] In view of factors such as reducing the use of chemicals in water treatment and effective purification to obtain high-quality water at low cost and with low energy consumption, membrane filtration technology is increasingly being adopted as the separation technique of choice for treatment and purification of waste water.[7] Membrane filtration is capable of removing ions, colloidal pollutants, bacteria, microorganisms, and organic compounds,[8,9] and the integration into other separation processes is relatively easy and scalable.

A membrane can be defined as a solid barrier with mechanical stability that acts as a semipermeable layer between, in this case, two liquid phases, that achieves separation of different species by allowing preferential permeation of one or more components of the mixture. The separation process is driven by a difference in chemical potential, practically done using a concentration or pressure difference over

the membrane (pressurization is commonly the main energy input). Aside from water purification, membrane technology is used in a wide variety of industrial applications in e.g. (waste)water treatment, manure processing, the dairy, food and beverage industry and medical and chemical processes.[10–13]

Molecular separations involve the production of clean water but also can include e.g. removal of microparticles, recovery of valuable solutes like proteins, dyes, minerals, water softening or processing of organic solutes. For a high-quality filtration process, membranes with high water permeability are needed that reach high fluxes at low driving force (e.g. pressure). Pressure-driven membrane processes are classified on the basis of the size of the solutes that are retained, having filtration ranges from suspended solids visible with the human eye to dissolved ions in the Angstrom scale (**Figure 1.1**). Current practice in water purification makes use of anisotropic membranes that are divided mainly into two types: porous membranes, further classified as ultrafiltration (UF) or microfiltration (MF) membranes, and dense membranes, e.g. integrally skinned membranes or thin-film composites (TFC), used as reverse osmosis (RO) and nanofiltration (NF) membranes.[14–16] UF and MF membranes have in general a single chemical composition (normally polymeric) but a gradient of porosity. In contrast to this, composite membranes consist of a thin selective layer on top of a microporous support (a phase separation membrane) that provides mechanical stability.

Microfiltration (MF) and ultrafiltration (UF) follow a separation mode based on particle sieving through the membrane pores. MF membranes have larger pores (0.1 – 5 μm) and they typically remove suspended particles, cellular materials, and microbial pathogens like bacteria. UF membranes (pores between 0.01 and 0.1 μm) are designed to retain macromolecules, such as organic matter and smaller pathogens like viruses.[17]
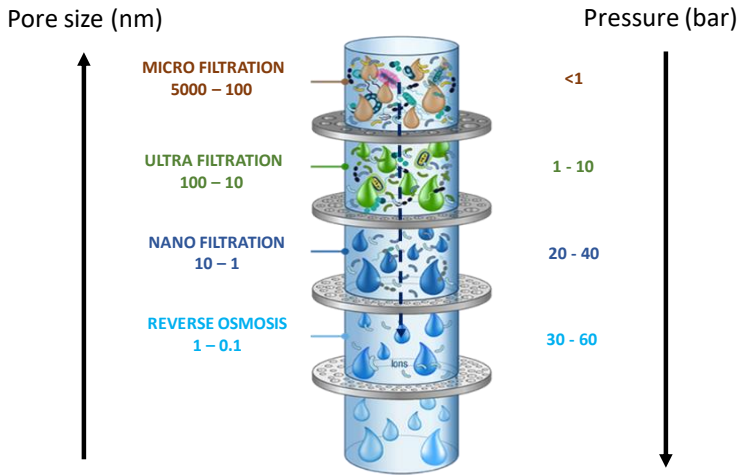
Figure 1.1 | Schematic drawing of the pressure-driven processes for water filtration including microfiltration (MF), ultrafiltration (UF), nanofiltration (NF) and reverse osmosis (RO). The processes are classified based on the size of the solutes that are retained. The main function of MF membranes is to remove suspended particles and microbial pathogens. UF membranes are designed to retain macromolecules and smaller pathogens, such as viruses. NF membranes can effectively remove scale-forming ions, such as calcium and magnesium, and can partially reduce salinity. RO membranes are designed for desalination being non-porous and can remove nearly all ions in addition to uncharged solutes.[18]

TFC membranes are extensively used for molecule-selective filtrations using RO and NF. Such membranes consist of an anisotropic cross-sectional structure with a thin selective layer on top of microporous support made of a different material that provides mechanical stability.[16] This architecture ensures high water permeation with a minimized resistance of the barrier for the permeating species. The porous supports are normally made of polymeric materials that include polyethersulfone (PES), polyacrylonitrile (PAN), polypropylene (PP), polyvinylidene fluoride (PVDF) or polyimide (PI). Among these support materials, polysulfones (PSf) are preferred because their hydrophilicity increases water flux. The current state-of-the-art membrane technology is based on cross-linked polyamides as selective layer formed by interfacial polymerization. [14,15,19] The thin layer of the TFC is usually formed *in situ* at the surface of the support by mixing two monomeric solutions, typically a diamine and a diacid chloride monomer.[14,16] These polyamide membranes can achieve high water permeability and salt rejection that, combined with good mechanical and thermal stability, makes them the standard and the most used systems for desalination.[20]

By far the most widely used membranes in the industry are made of organic polymers due to their processability and low cost.[21] Polymer membranes with different pore sizes for their use in different separation processes are typically based on the same materials, that are processed under different conditions or prepared with different methods. Depending on the application, there are various configurations of NF membranes that have been commercially developed, from which flat-sheet and hollow fiber membranes are used most.[19]

In NF and RO filtration, separation processes take place based on molecular size as well as interactions between membrane and solute, such as charge-charge interactions or hydrophobic/hydrophilic interactions. Depending on the specific membrane, transport is then governed by convection and or solution-diffusion.[22] RO membranes are so dense that they are considered "non-porous" (effective pore size between 0.1 and 1 nm). Molecular transport in RO is governed by solution-diffusion where components dissolve in the membrane, diffuse through statistically distributed, dynamic free volume elements in the membrane and desorb at the permeate side. The applied pressure must exceed the osmotic pressure of the solution to create a driving force over the membrane. NF membranes exhibit a filtration performance between RO and UF because they are considered porous but more mechanisms than size exclusion are now taking place. NF commonly filters species ranging between 1 and 10 nm such as organic molecules, some viruses and even salts. NF and RO have been proven to be effective in the removal of molecular-sized solutes.[21,23–26] However, NF reduces costs because of the lower energy consumption due to the decrease in pressure needed (RO shows permeability values from 1 to 10 $L \cdot m^{-2} \cdot h^{-1} \cdot bar^{-1}$, while NF has permeabilities of 10 - 20 $L \cdot m^{-2} \cdot h^{-1} \cdot bar^{-1}$).[27]

NANOFILTRATION MEMBRANE
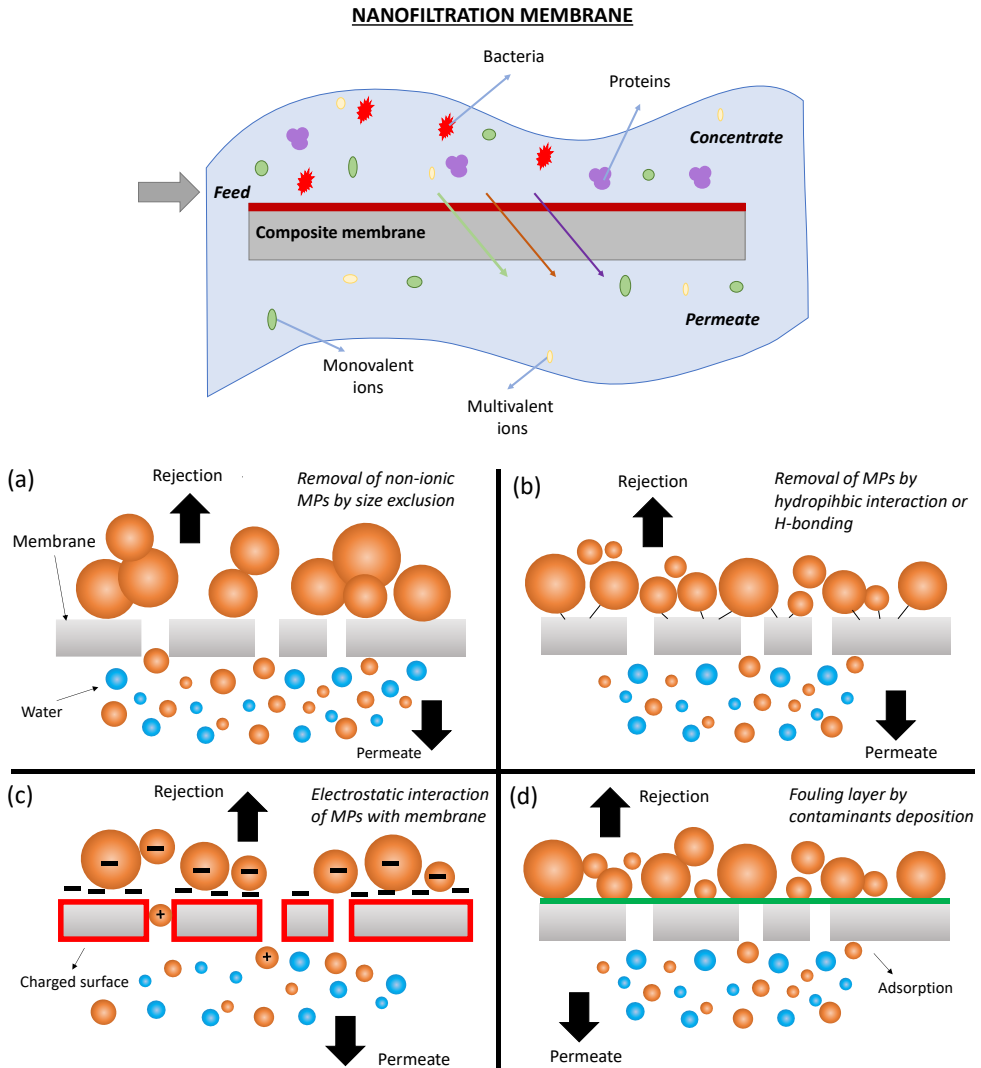
Figure 1.2 | Schematic representation of a NF membrane showing the solutes that can be permeated and retained. The different mechanisms that are involved in MPs removal using a NF membrane are shown; a) size exclusion, b) hydrophobic interactions, c) electrostatic interactions and d) adsorption. Depending on the compounds, removal efficiencies are associated to the physico-chemical properties, film properties, and membrane functioning conditions. Figures adapted with permission from ref. [21]. Copyright © 2017 Rights managed by Taylor & Francis and ref. [8]. Copyright © 2020 Elsevier B.V. All rights reserved.

Among the different types of membranes, especially NF membranes are commonly used for the effective removal of molecular-sized solutes from aqueous

streams.[14,15,22] In this thesis, the interest is focused on the development of improved NF membranes with pore sizes in the nm range to selectively remove small organic micropollutants from water. Due to the organic nature of these emerging contaminants, they can interact with the membrane, making the filtration process a result of different separation mechanisms involved. Therefore, even though in NF the mayor mechanism of actuation is physical sieving (size-based), the rejection of trace organic pollutants involves in addition the participation of 3 main interactions: size/steric exclusion, electrostatic repulsion (polar and charged compounds) and adsorption via hydrophobic interactions as shown in **Figure 1.2.**[24] Together, all these mechanisms determine the rejection and thus the selectivity of the filtration process.

1.2. New materials for water filtration membranes

Current commercial membranes face several challenges, among which the trade-off between permeability and selectivity is an intrinsic limitation that is difficult to address.[11,28,29] The lack of uniformity in pore size and shape in commercial asymmetric NF membranes with a dense morphology limits the selectivity in the filtration of solutes. The wide pore size distribution is a result of the disordered structures that are created in the polymerization process and limits the sharpness of the molecular weight cut-off of the membrane resulting in a lower rejection selectivity. Moreover, for the removal of the new emerging toxic pollutants in water, smaller pores are desired for which control over the molecular design of the selective layer of the membrane is necessary.[30] Controlling the pore size at the nanometer range and having a homogeneous pore size distribution is essential to facilitate the production of highly selective membranes with high water permeability combined with high retention.[31]

Many new organic, inorganic and hybrid materials have been utilized in the search for high-performance nanoporous membranes with improved filtration properties.[17],[32] Inorganic materials like zeolites or ceramics provide with highly ordered nanostructures with high porosity, large surface areas and uniform pore sizes.[33],[34] Stability, durability and mechanical strength are properties offered by these membranes that are often used for microfiltration.[10] However, due to their high operational costs and poor processability, ceramic membranes have found less widespread acceptance in the industry yet except for gas separations or as support for hybrid membranes.[35]

State-of-the-art, commercially available polymer membranes makes use of a limited range of different polymers only.[10] Recent advances in synthetic strategies,

combined with the formation well-defined structures by molecular self-assembly potentially opens routes to true control over pore size and functionality (**Figure 1.3**).[36]
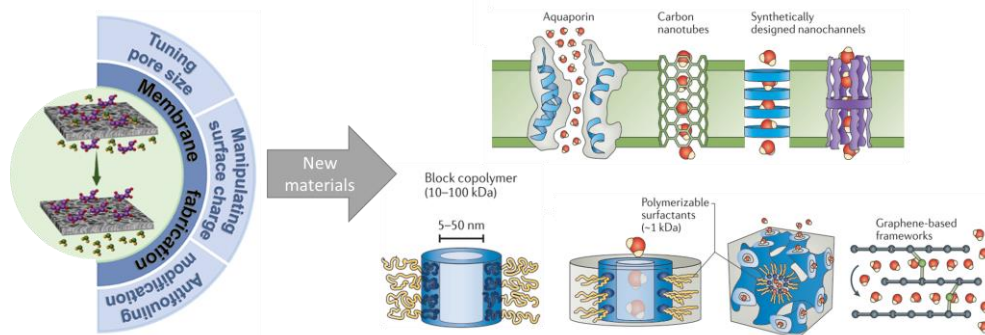
Figure 1.3 | The state of the art in membrane research is focused on the optimization of membrane selectivity by controlling pore size and nanostructure. The new generation nanoporous materials for selective membranes using molecular-level design are shown. The top-right panel shows discrete channels formed on a thin film by including aquaporins, carbon nanotubes and self-assembled cyclic organic molecules. In the bottom-right panel, selective layers are shown that consist of cylindrical channels, or of interconnected channels in a cubic morphology of surfactants and block-copolymers. As well it is shown a selective membrane based on a multilayer graphene-based material. Figures were adapted with permission from [36]. Copyright © 2016. Macmillan Publishers Limited.

Nature, with its huge diversity of molecular structures, chemical processes and systems is a nearly limitless source of inspiration for the design of better membranes. Direct incorporation of biological building blocks can also provide unique selectivity and functionality to polymer-based membranes with good processability and stability.[37] For instance, the design of water channels is gaining importance and one of the most effective biological systems are aquaporins. Aquaporins (AQPs) are an extensive family of water channel proteins present in the cells of many living organisms. The pores are around 7 nm long and are involved in the transport of ions and protons across the phospholipidic bilayer membrane of the cells.[38] These natural water channels have unique properties in terms of high permeability of water and extreme selectivity towards other molecules and ions. The use of AQPs in synthetic membranes aims to enhance the water permeability and to increase the rejection of all other species, while keeping the chemical and mechanical stability and the high processability of normal polymeric membranes. Many studies have shown that AQP containing membranes pottentially have better filtration performance, but these hybrid natural/synthetic filtration systems are still in the research stages, far from commercial application in RO/NF industrial filtration processes.[32]

Nanochannels have also been created *via* supramolecular interactions (H-bonding and $\pi - \pi$ stacking) using purely synthetic building units such as cyclic peptides or rigid organic macrocycles.[40,41] Some of the challenges to develop such membranes are related to the scalability of the methods and the alignment and formation of robust selective channels with the desired balance in water-solute transport. Potentially much more useful is the self-assembly of surfactants and block-copolymers, a topic that will be discussed in **section 1.3**.

Since the discovery of the striking electrical and mechanical properties of graphene, this 2D carbon-based material has been extensively investigated. Graphene sheets are atomically smooth and thin, which makes them promising materials for membrane separations, especially for desalination purposes.[42] Two main modes of graphene have been proposed for membranes: nanoporous graphene forms or graphene frameworks, both based on the size-selective exclusion of solutes. For a perfect monolayer sheet, bigger nanometric defects must be created, for example via plasma etching or bombing with ions and electrons, to allow the intentional passage of water and rejection of specific solutes.[43,44] Because of the very low thickness of this monoatomic layer, projected simulations show water permeability values 10^2–10^3 times greater than current RO membranes. High hydrophilicity permits higher water fluxes also in other forms of carbon such as graphene nanoparticles (NPs) or carbon nanotubes (CNTs), creating new low-energy consuming membranes with high potential and effectiveness due to the ultra-high water transport and controlled salt rejection.[45] Graphene frameworks are refered to as multi-layered laminates of graphene sheets with a space of around 1 nm between the sheets. The smoothness of the layer permits an ultra-fast flow through the graphene channels created, analogous to CNTs. Moreover, the use of graphene oxide (GO) appears as an interesting alternative for the utilization of carbon-based materials for separation purposes.[45] The creation of stacked flakes of GO or reduced GO with spaces accesible for water and humidity, results in rapid permeation of ions.[46]. Nevertheless, industrial scaling up remains a challenge due to intrinsic impediments such as the difficulties in managing the defect formation in monolayer graphene membranes, the high hydrophobicity, and large size impediments in multi-layered systems.

1.3   Nanofiltration membranes based on self-assembled nanostructures

Self-assembly is a bottom-up process in which molecules organize spontaneously into supramolecular structures with a reduction of free energy of the system as the driving force.[47] It is a very versatile way to obtain nanostructures with well-defined pores for

molecular-level separations.[48] The building unit determines in this case the pore size leading to uniform and homogeneous porosity in the structures which gives great potential for separation processes. The control over the morphology and the virtually uniform pore size distribution in self-assembled membranes, improves the quality of the sieving process. Moreover, a very interesting feature is the possibility to modify the chemical environment in the pores by introducing chemical functionality in order to tune the selectivity. Membranes with tuneable pores may provide an important advantage over commercial ones: selectivity of the NF process in such membranes will not only be the result of well-defined pores but also of the specific interactions between the membrane and the solutes. This provides a way to decouple the typically inherent inverse relation between flux and rejection for current NF membranes.

The self-assembly of block copolymers (BCPs) through microphase separation is a well-established method to prepare nanomaterials with well-defined patterns for their applications in electronics,[49] nanolithography[50], and of course, nanoporous membranes.[51] More recently, BCPs have found their place as the next-generation nanopatterning materials due to the possibility of creating many morphologies in a very precise and predictable way.[52,53] In the membrane field, the self-assembly of well-designed molecular building units has opened new perspectives due to the possibility to get better structuration with well-defined and homogeneous pore morphology and narrow pore size distribution with additional functionalities (**Figure 1.4**).[36,54–57] These robust structures bring the possibility to achieve small cut-off sizes and high permeabilities on filtration due to their controlled pore arrangement and morphology, which can be easily tuned in the nanoscale.[58] First reported BCP membranes made of PEO and PET were applied in blood dialysis[59] but higher selectivity and permeability were reached by using PEBAX, decreasing fouling and giving good mechanical stability.[54] Filtration properties have been optimized by post-functionalization of the porous structure to give better selectivity, antifouling properties, and improved lifetime and resistance.[60] However, the real challenge for these self-assembled materials is the achievement of pore sizes below 2 nm,[60] which is the smallest size that has been attained with block-copolymers because of the existing limitations of the block length. Self-assembly of smaller pores would bridge the gap between ultrafiltration (UF) and nanofiltration (NF).[56,61] To reach smaller pore sizes, other chemistries must be adopted.
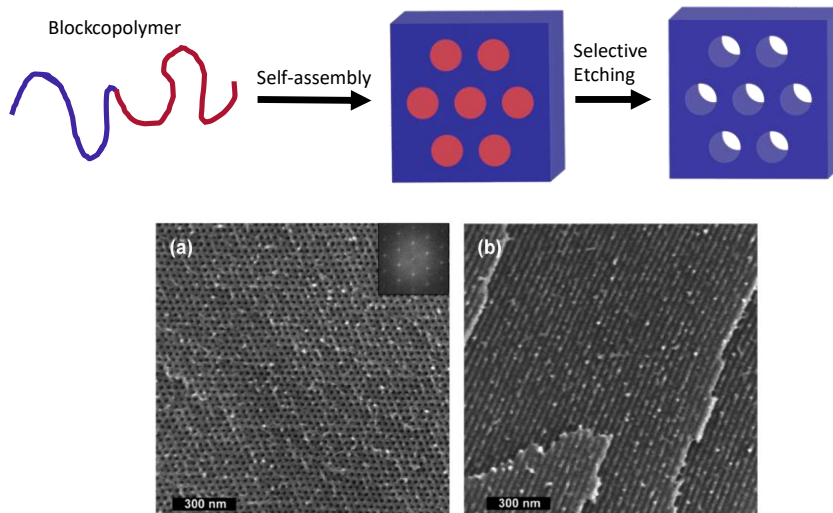
Figure 1.4 | Up; Schematic representation of the formation of nanoporous polymeric materials from ordered block copolymers. Reprinted (adapted) with permission from ref. [57] Copyright © 2008. American Chemical Society. Down; SEM images of nanoporous PS-PDMA materials (a) perpendicular and (b) parallel to the direction of pore alignment. Reprinted (adapted) with permission from ref. [53] Copyright © 2005. American Chemical Society.

1.3.1. LC-based nanoporous structures

On a smaller length scale, liquid crystals (LCs) can self-organize in well-ordered nanostructures with access to even smaller pores than block copolymers.[62,63] Liquid crystalline molecules so-called "mesogens" combine the mobility of isotropic liquids with the orientational order of a solid.[64] These mesogens are classified based on the shape of the molecules, normally calamitic (rod-shape) and discotic (disk-shaped) as shown in **Figure 1.5**. Three common morphologies with different degrees of order can be built from the self-assembly of the mesogens: columnar, lamellar, and bicontinuous, that yield nanoporous structures achieving nanometer dimensions. The organization of the molecules varies with temperature (thermotropic LCs)[65] or, in lyotropic LCs with the solvent content, usually water.[66]
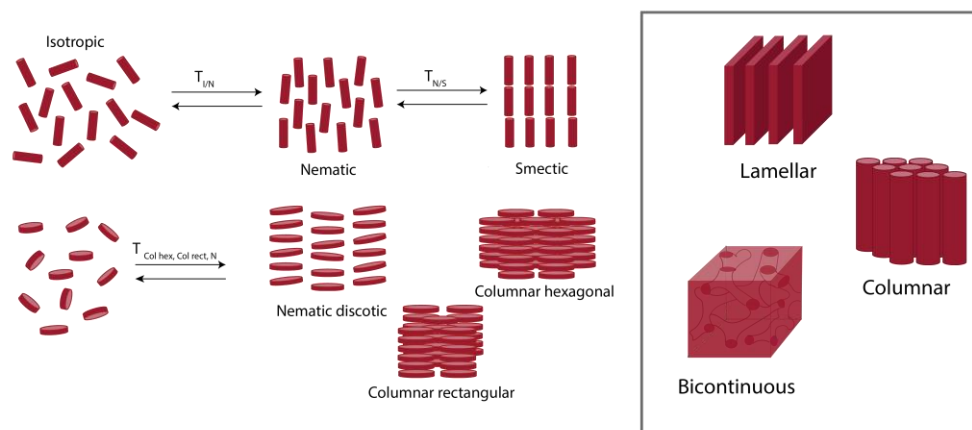
Figure 1.5 | Schematic representation of the different morphologies used in LC membranes depending on the type of mesogen used. 2D pores can be obtained with lamellar lattices based on smectic mesophases and discotic mesogens can give hexagonal or rectangular arrangements with 1D pores. The formation of 3D pores is easy using bicontinuous mesophases.

Recently, the interest in self-assembled LCs has focused on their application as nanoporous materials for separation purposes. The formation of nanostructured LC networks can be for instance driven by the self-organization of the mesogens.[67] This process can be controlled by the molecular design of the building units, whose selection is crucial to get the desired morphology.

Columnar mesophases give 1D pores, with a higher orientational order than the other nanostructures. They can be built from the self-assembly of "wedge-shaped" amphiphilic molecules via nanoscale segregation of the hydrophobic and hydrophilic parts.[68] These systems tend to form cylindrical or rod-like structures with polar groups arranged in the center.[69] For instance, nanoporous materials with ionic channels in a well-defined geometry have been prepared from the self-assembly of sulfonated liquid crystals with different counterions for potential application as ionic membranes.[70–72] Columnar LCs form in situ porous structures governed by the amount of solvent or temperature variations (for lyotropic or thermotropic systems, respectively), together with ionic interactions between the molecules. However, porosity in thermotropic LC-based polymers can also be created after crosslinking. For instance, cylindrical structures can be prepared from disk-shaped molecules typically containing aromatic cores surrounded by flexible alkyl chains that give mobility to the system. LC hydrogen-bonded complexes between benzoic acid derivatives and an aromatic template molecule in the center are well-known to form columnar mesophases.[73,74] An elegant method to create porous structures with a specific pore size is based on the use of a discotic system containing a template molecule that is removed after the fixation of a

columnar structure. This idea was first developed in 2001: the use of an H-bonded benzotri(imidazole) core template molecule led to the formation of hexagonal ordered channels in a crosslinked matrix.[75] Later on, this approach was used to prepare CLC-based nanoporous films with selective binding to ions (**Figure 1.6**). A supramolecular 3:1 complex between polymerizable benzoic acid derivatives and 1,3,5-tris(1H-benzo[*d*]imidazole-2-yl)benzene (**TB**) as template molecule was used as a mesogenic discotic unit for the formation of the columnar lattice.[76] In the following sections, examples of improved membranes based on these approaches will be further discussed. The versatility of self-assembled LCs as materials to be produced on large scale at low costs places them ahead in terms of their applicability in membrane technology.
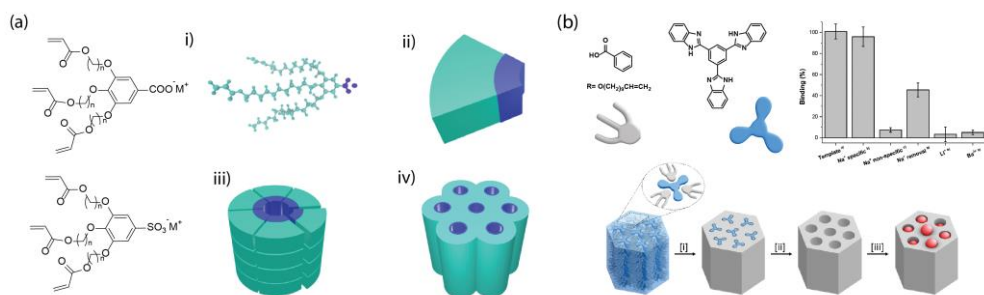
Figure 1.6 | a) Schematic illustration of the self-assembly of LLC monomers with sulfonate and carboxylate moieties i) that exhibit a wedge-shaped structure ii) and stack on top of each other with the polar heads inside iii) forming columnar (hexagonal) mesophases. Reprinted (adapted) with permission from ref. [71]. Copyright © 2018. American Chemical Society. b) Nanoporous materials based on a supramolecular complex with a gallic acid-derived monomer and tris-benzimidazole template. Representation of the monomer self-assembly, polymerization, template removal, and selective ion uptake. Size-selective adsorption of ions as measured by using a quartz crystal microbalance. Adapted from ref [76], under the terms of a Creative Commons Attributtion Non-Commercial License CC BY-NC.

1.3.3 Nanoporous membranes based on polymerized LCs

The highly ordered crosslinked nanostructures with pore sizes below 1 nm that are obtained from the self-assembly of LCs can be used in a wide variety of applications.[51,77] Due to their robustness and stability, polymerized LCs have attracted attention for their use in the preparation of membranes with pore sizes between 0.5 and 2 nm, which potentially opens the window for separations at the molecular level.[78] In addition, the use of bottom-up approaches gives control over the pore functionality, which allows the membrane to distinguish between ions and molecules similar in size or charge but with different affinities.

In recent years, substantial progress has been made in the development of LC membranes for desalination and removal of small organic molecules from water. Among the previously mentioned different morphologies in which the mesogens can arrange, the anisotropy present in 1D columnar mesophases gives a higher order that is advantageous for the formation of uniform pores and thus membranes with higher water flux. However, to achieve this improved performance, unlike for bicontinuous phases, alignment of the columns is needed. Therefore, even though 1D geometries are in principle preferred, there is more work reported based on 3D membranes because of the higher processability they offer.[79–84]

The development of LC-based water filtration membranes started with potential polymerizable lyotropic LCs deposited as a thin selective layer onto a porous support to create a TFC membrane, since free-standing films could not withstand high pressures. These membranes showed high salt rejection values (95% for NaCl and 99% for $MgSO_4$ and $CaCl_2$) and size selectivity for charged and uncharged solutes but low permeability values (<0.5 $L·m^{-2}·h^{-1}·bar^{-1}$), which are insufficient to manage industrial water feeds.[79,85–87] The low permeability obtained is due to the large thickness of the selective layers and transport deficiency of the nanochannels, caused by a lack of order and pore alignment perpendicular to the support. This last issue can be addressed in multiple ways e.g. by application of a magnetic field[88] or the use of sacrificial alignment layers[89] forcing the creation of hexagonal porous networks.
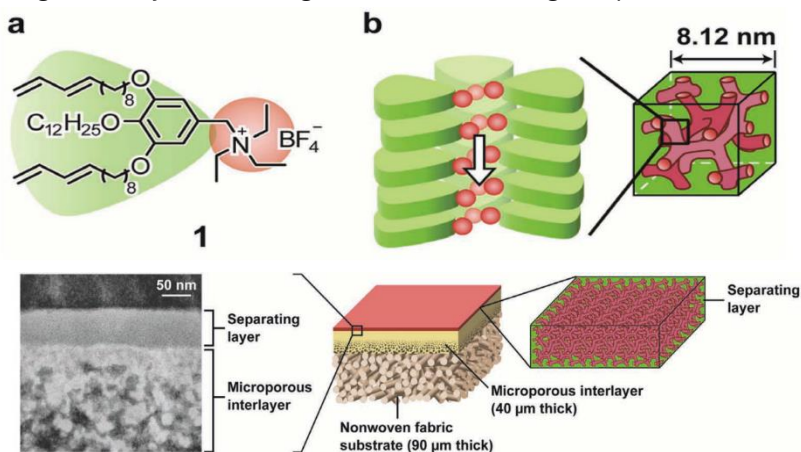
Figure 1.7 | Chemical structure of the wedge-shaped LC molecule 1 and self-assembled cubic bicontinuous structure forming ion nanochannels of molecule 1. A thin layer of 50 nm is formed on top of a porous support to form the filtration membrane. Adapted from ref [81], licensed by John Wiley and Sons, INC. (Hoboken, NJ, USA)

This research line was continued in the same direction but exploiting thermotropic LCs for the fabrication of membranes for salt removal. The following work showed that nano-segregation of wedge-shaped amphiphilic molecules with polar cationic groups

leads to the formation of a bicontinuous cubic mesophase with 3D-interconnected ionic channels (**Figure 1.7**).[80] By spin-coating the LC material on a porous support, a nanocomposite membrane with a 100 nm selective layer with reasonable salt-rejection was obtained (pore size < 1 nm). Virus rejection was further studied by filtration of a Qβ bacteriophage, accomplishing almost total rejection with values up to 99.99%.[81] The modification of the cationic part of the molecule, the morphology changed to a more ordered columnar hexagonal mesophase. This columnar arrangement (1D) is more preferred for membranes because of its easier access to the channels, which resulted in this case in expected higher water flux.[82]

Different molecular designs were further investigated to improve the filtration performance, for instance using a two-component columnar LC system to enlarge the pore size. By mixing the original LC monomer and an ionic liquid moiety, a columnar mesophase was formed and fixated by photopolymerization. Pores were created by removal of the ionic liquid yielding a membrane with almost 100% virus rejection and higher water fluxes than the previous analogous system.[83]

The versatility of self-assembled LCs has led to the design of a strategy that enables highly selective cleavage with light to generate uniform and ordered pores without the destruction of the polymer network.[84] This permitted the formation of defect-free membranes with carboxylate groups inside the pores that exhibited total rejection of the same virus (**Figure 1.8**). 2D morphologies were explored by the same group in order to decrease the pore size and get higher performance membranes.[90] The use of smectic LC nanostructured membranes allowed total virus removal, enhanced water permeability and salt rejection.[91] Nevertheless, charge and size selectivity at a size scale below virus sizes was not further studied. Only a few examples on LC-based composite membranes reported charge and size selectivity of small organic dyes in water but water fluxes were low (1-2 L·m^{-2}·hr^{-1}·bar^{-1}).[92,93]
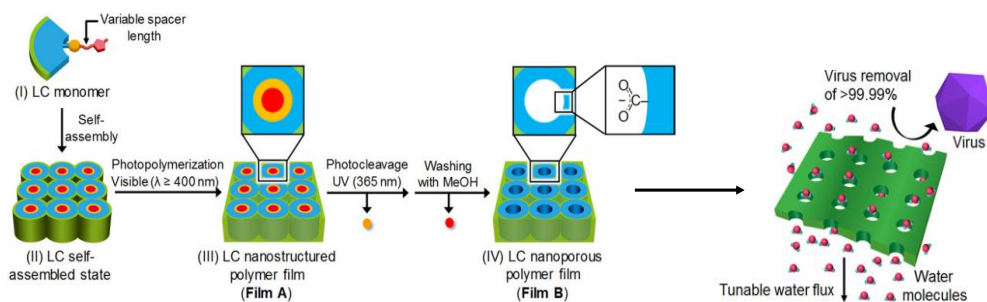
Figure 1.8 | Schematic representation to obtain nanoporous films from the fixation with UV light of nanostructured polymerizable LCs with a columnar arrangement. By photocleavage of an ionic part followed by cleaning with MeOH, pores are created homogeneously in the structure. Rejection of almost 100% of F-coliphage Qβ virus is

reached with high water fluxes. Reprinted (adapted) with permission from ref. [90]. Copyright © 2019. American Chemical Society.

1.4 Improving membrane properties: stability, functionality, and alignment.

A large variety of self-assembled morphologies allows the formation of porous membranes with selectivity towards molecular and ionic solutes in water. Also, the use of polymerizable LCs ensures good control over the molecular design and organization of building blocks within the nanostructure, hence pore size and functionalities can be easily tuned. The next steps in membrane optimization at the molecular level comprise the development of versatile systems with tunable properties such as selectivity for specific small organic molecules for instance.

1.4.1 Optimization of photo-polymerization as the crosslinking method

Polymerizable groups in the LC molecules allow the fixation of self-assembled morphologies by covalent crosslinking through a thermal photopolymerization reaction.[62,94–96] Among the functional groups used for crosslinking, acrylates are most common due to their easy synthesis and fast and localized photo-polymerization that leads to the formation of highly crosslinked and stable polymers.[94] However, thermal and chemical instability (hydrolysis of the ester groups) and uncontrolled polymerization are drawbacks that limit the application of acrylates.

Alkenes are attractive alternative groups to overcome those issues. The chemical stability of alkenes is higher than that of acrylates and their hydrophobicity matches with the alkyl chains in mesogens.[97] Highly crosslinked nanoporous films can be obtained using acyclic diene metathesis (ADMET).[76,98] However, at higher temperatures the catalyst used in ADMET decomposes, which makes it difficult to complete the crosslinking process.
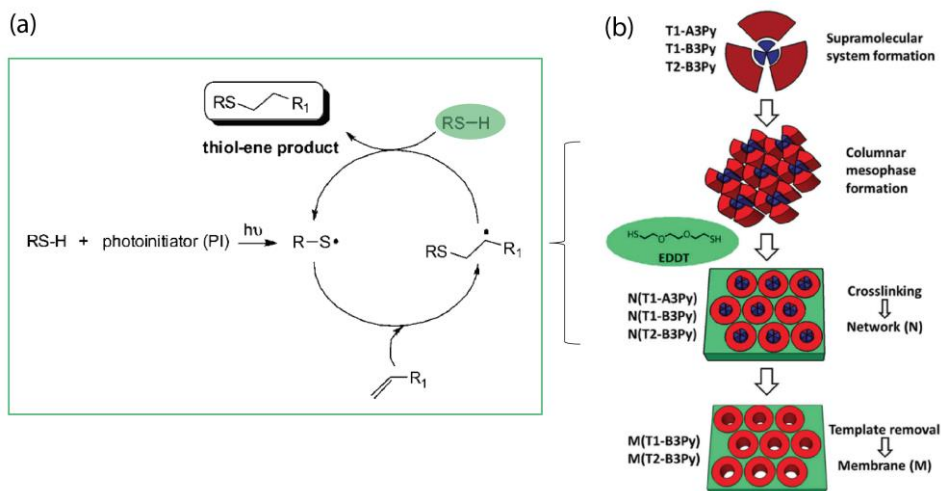
Figure 1.9 | On the left, scheme of a basic thiol-ene photopolymerization: photoinitiator deprotonates the thiol creating a radical that can react with the double bond creating another radical that can keep on reacting. Adapted from [100]. Copyright 2010 The Royal Society of Chemistry (RSC). On the right, chemical structure of the templates and the promesogenic units of the supramolecular systems and schematic representation of the preparation of the nanoporous membranes by thiol crosslinking and template removal. Adapted from ref. [102]. Copyright 2010 The Royal Society of Chemistry (RSC).

Thiol-ene chemistry has been used extensively for the preparation of well-defined polymeric materials.[99] Thiol-ene coupling occurs either *via* a free-radical mechanism or a Michael addition, where a single thiol reacts with a single ene to yield the product. Both mechanisms are extremely efficient, but radical addition polymerization is preferred for network formation because it allows controlled and homogeneous crosslinking. Moreover, a light-mediated thiol-ene radical reaction exhibits benefits such as time and location specificity which allows its application as a powerful and versatile method to crosslink and produce stable networks.[100,101] The preparation of elastomeric templated porous materials using the thiol-ene approach instead of using the most commonly used photopolymerization of acrylates was reported by Gracia et. al. (**Figure 1.9**).[102] Using this cross-linking strategy, hydrolysis of the esters is avoided and the polymers become mechanically and thermally more stable. The use of additional thiol crosslinkers offers an alternative method to easily fixate networks into robust and stable materials. However, its application for the fabrication of filtration membranes has not been reported yet.

1.4.2 Homeotropic alignment of pores in columnar mesophases

Membrane filtration performance can be improved by increasing permeability while maintaining selectivity. This is directly related to the thickness of the selective layer and the pore arrangement in that layer. Especially, the orientation of the pores in the direction of the flux is desired. Liquid crystals show order and mobility and, more specifically, the anisotropy of columnar LCs creates a directional dependency of the properties of the material. Columnar nanostructures are arranged by a self-assembly process driven by attractive interactions between the aromatic molecules and the hydrophobic tails *via* π-π, electrostatic interactions between ionic moieties or non-covalent like H-bonding. Therefore, the orientation of columnar mesophases can be modulated by controlling these interactions or using an external trigger. Once preferential stacking of the disks is reached, the alignment of columns towards one direction in the network is possible. An ideal columnar LC-based thin-film membrane possesses oriented pores over the whole material to allow the passage of the flow without impediment. Columnar mesophases can align on a surface in two different ways: planar and homeotropic. A planar orientation of the columns is easy to reach by shearing the sample on a substrate. However, a continuous and homogeneous homeotropic alignment with the columnar axis perpendicular to the surface is more desirable for the fabrication of high flux membranes.[103,104] Getting vertically aligned pores across the whole membrane is challenging for columnar liquid crystals but a small number of methods have been demonstrated to be successful.

Among the best known approaches to homeotropically align columnar mesophases for fabrication of porous materials are: chemical modification of surfaces or the application of magnetic fields.[88,105,106] In the first method, which is most commonly applied, the surface energy of the substrate is tuned to favor homeotropic alignment of the columns. A non-modified glass surface gives a planar or random orientation of the columns while a properly modified surface can orient the columns vertically. This is based on the affinity regarding the polarity of the materials and surface energy: when polarity of the surface matches with the outside of the disc, a planar orientation is favoured while when there is matching with the inside of the disc, the apolar tails point upwards and a homeotropic monolayer is formed. For instance, highly homeotropically aligned pores in thin films can be obtained using a charged sacrificial layer of poly(sodium 4-styrenesulfonate) (PSS) on the surface (**Figure 1.10 a**). [107] When a hydrophobic material such as octadecyl-trimethoxy silane (OTMS) is used as a sacrificial layer, a planar alignment is observed instead due to the hydrophobic interactions with the lateral alkyl chains.

Polyethylene glycol (PEG) has been widely used in surface modification, specifically to eliminate protein absorption due to steric interactions that prevent direct contact.[108] This fact has inspired the development of a new method to engineer

interfaces of LCs with orientational ordering by including EG mesogens as dopants. [109] The idea was recently applied to create homogeneous homeotropic alignment of columnar LCs by the addition of an analogous mesogen dopant with PEG chains (**Figure 1.11 b**).[110] This approach offers a simple way to enhance the transport and absorption properties of porous materials without interfering in the LC self-assembly necessary to build up the nanostructure.
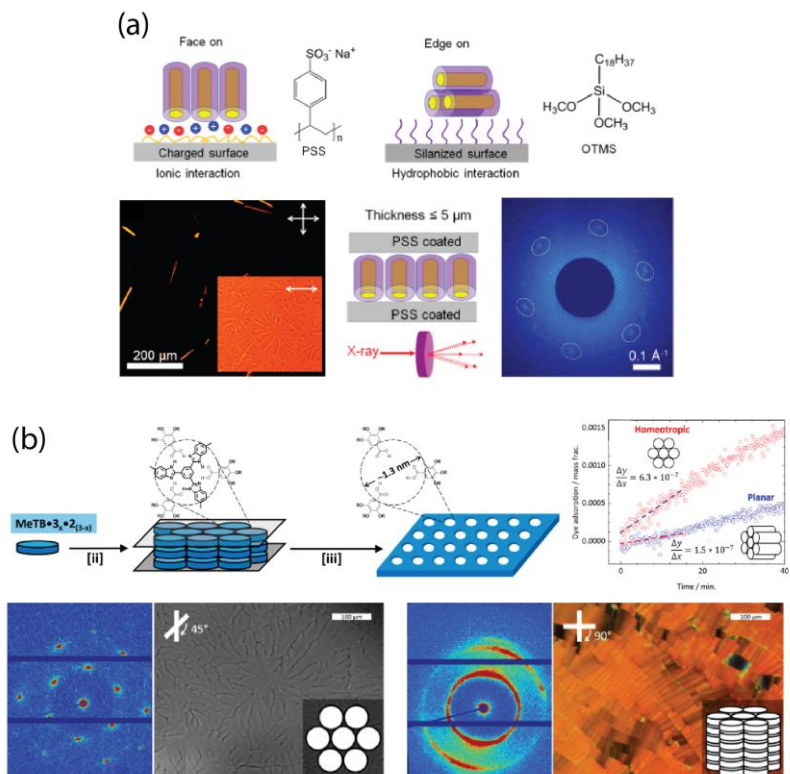
Figure 1.10 | (a) Schematic illustration of face-on or edge-on orientation of the supramolecular columns depending on different surface properties of the substrates resulting in ionic or hydrophobic interactions between the surface and the columns. Vertical alignment of Col_h phase in a thick film confined by poly(sodium 4-styrenesulfonate) (PSS)-coated surfaces was confirmed with POM and SAXS. Reprinted (adapted) with permission from ref. [107]. Copyright © 2017. American Chemical Society. (b) Representation of the self-assembly process of the supramolecular complex by mixing with dopant giving homeotropic alignment of discotic LC phase between glass slides that are kept after fixation of the LC with light followed by the formation of nanopores by template removal. 2D X-ray diffractogram of both homeotropic and planar samples is confirmed by POM and X ray diffraction. The homeotropically aligned film gives more uptake overtime of the positive dye methylene blue than the planar film. Reprinted (adapted) with permission from ref. [110]. Copyright © 2018. American Chemical Society.

1.4.3 Post-modification to bring versatility to nanoporous membranes

The synthesis of new self-assembled materials (liquid crystals) is a difficult, time-consuming, and costly process that in the end has molecular design limitations. To overcome those issues, post-modification of LC membranes is appealing as an alternative way to change the structure and properties of the membranes after their fabrication, by changing the chemistry inside the pores.[111] In filtration, the interplay between pore size and the chemical environment plays an important role in the interaction with solutes. Therefore, pore functionalization becomes a way to change the filtration properties of the membrane.[112] LC-based nanoporous materials can be modified using different approaches, from which two are highlighted as they have been more often applied: i) covalent modification of the pore interior and ii) ion exchange of counterions in ionic membranes.

The functionalization of porous films based on both columnar and smectic liquid crystals has been already reported following the first modification method (**Figure 1.11a,b**).[111,113] The strategy consists of the covalent modification of the functional groups in the molecular structure to change the pore size and the chemical properties such as hydrophobicity, ionic interactions, etc. The reversible modifications of the porous structure (enlargements or decrease of the spacings in the network) resulted in changes in dye absorption, which underscores the versatility of the approach to further tailor transport and diffusion properties in membranes with control over the pore size and functionalities. Yet, this approach has not been applied to water filtration systems.

Going one step further, anion exchange membranes based on lyotropic LCs have been successfully modified by exchanging the counterion inside the pores.[114] The variation of the counterion has an strong influence on the rejection of solutes: substitution with larger and more charged anions (from Cl^- to SO_4^{2-}) reduces the effective pore size, leading to higher rejection values of small organic molecules from water. Nevertheless, this approach has an important drawback: as ionic exchange can occur spontaneously in aqueous solutions containing ionic species, it can interfere with the filtration process. This issue can be solved with the fixation of the exchanged counterion part, yielding a permanently modified network with different rejection properties than the original system.[115] (**Figure 1.11c**).
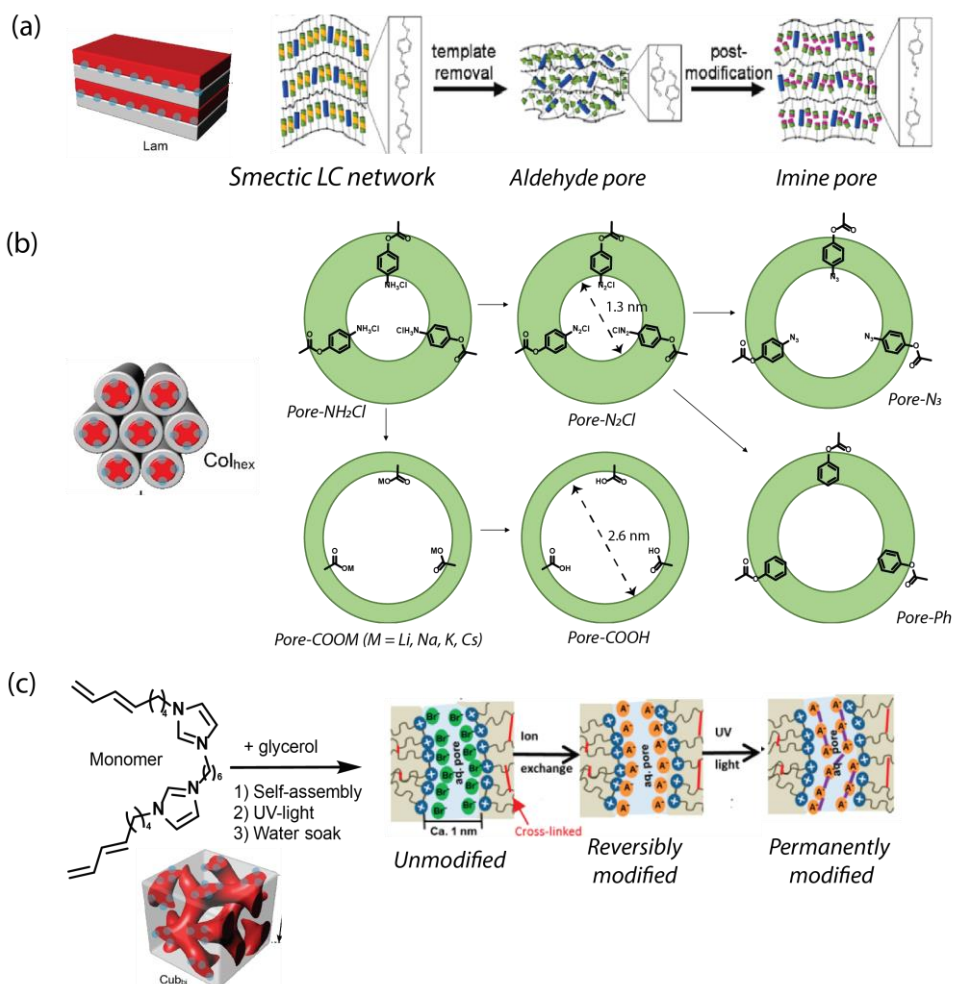
Figure 1.11 | Examples of pore modification of nanoporous materials for different morphologies and purposes: a) nanoporous films based on smectic LC with a lamellar-based structure where aldehyde groups inside the pores are converted into imine, b) columnar based nanoporous polymers with modified functionalities by different covalent chemistries and c) ionic LC membranes with cubic nanostructure with modified pores via ion exchange of counterions inside. Reprinted (adapted) with permission from references [111,113,115]. Copyright © 2017 and 2019. Americal Chemical Society.

1.5 Conclusions and future perspectives

With increasing industrial and human activities, new emerging toxic organics appear in surface water and endanger our health, making the production of clean water more challenging. To address this global issue of water scarcity, effective and sustainable

separation methods to ensure clean water are exploited. Due to its low energy consumption, low use of harsh chemicals and easy processing and scaling up, membrane technology offers a feasible way to purify water and to recover of valuable compounds.[7] To reach molecular separations, the design of new materials with well-defined and ordered porous structures with tunable functionalities is desirable.

To improve water quality, next-generation membranes with enhanced selectivity should be developed. Thus, design at a molecular level of thin and defect-free active layers is required for which 2D materials promise showed high water permeability and rejection values when proper order is reached. Self-assembly of liquid crystals has demonstrated to be an efficient approach to create nanostructures with well-defined morphologies providing membranes with tuneable permeability and selectivity in a controlled manner. The crosslinking of these highly ordered networks with pore sizes below 1 nm increases their mechanical strength and allows their use as membranes for molecular separation. The good processability and variety of morphologies of polymerized LCs make them potentially attractive for highly selective and highly permeable water filtration membranes for micropollutants and salt rejection.

Over the last years, novel approaches and molecular designs for improvement of polymerized LC-based nanoporous materials were explored, focusing on well-defined, ordered and oriented pores to improve properties towards their application as NF membranes with better selectivity and permeability. As a next step, LC membrane pore size needs to be reduced as well as permeability and selectivity need to be increased using the molecular design of the structures. Now it is time to fill this gap by exploring chemical modification of the membranes to achieve tuneable selectivity in order to control the filtration process.

1.6 Aim and Outline of this thesis

In this doctoral Thesis, we make use of the self-assembly of liquid crystals to achieve control over the molecular organization and pore formation with defined sizes and chemical functionalities. We attempt to develop new filtration membranes based on polymerizable liquid crystals for the purification of water. Our strategy is the use of self-assembled columnar liquid crystals to achieve control over the molecular organization and pore formation with defined sizes and chemical functionalities. The columnar nanostructure is formed by the self-assembly of sulfonate monomers and is easily fixated with light. In the process to get the supported membranes, some challenges need to be faced: thin selective layers on top of porous support that gives mechanical strength to get a robust membrane with high permeability, the absence of defects in the layer, the proper orientation of the channels and the modification of the pore to change filtration properties of the membrane.

In **Chapter 2**, the development of a new water purification membrane for the removal of organic pollutants in water is presented. As a strategy, we make use of templated columnar liquid crystal-bearing sulfonic acid groups in a self-assembled discotic molecule. A composite membrane with a defect-free thin layer of **Sulfac₃TB** on top of PES was obtained. Water filtration tests demonstrated a flux around 2 L·m⁻²·h⁻¹·bar⁻¹ and molecular selectivity for neutral and charged solutes. A molecular weight cutoff (MWCO) of around 5000 g/mol correlates with the expected pore size from the **TB** template molecule around 1.5 nm.

In **Chapter 3**, the modification of membrane properties by changing the functionalities at the pore walls was studied. In the first part, the molecular design of a discotic complex **Benzac₃TB** containing COO- moieties allowed the formation of analogous membranes to the sulfonate membranes in Chapter 2. Filtration studies confirmed that the higher interaction of COO- with cations results in poorer transport properties than sulfonated membranes. In the second section, the covalent transformation of the sulfonate functionalities in the pores of membranes in Chapter 2 was accomplished. Three different sulfonamides were obtained which led to a slight variation of the pore size selectivity of the new membranes, affecting MWCO, water permeability and selectivity.

Photo-switchability of templated porous systems was studied in **Chapter 4**. Polymer films were formed from the complex of **Azoac₃TB** and morphological and photo-responsible properties were determined. The uptake kinetics of Rhodamine 6g were studied showing an 8-fold difference between *trans* and *cis* isomers of the porous film. This establishes the basis for the application of a dynamic system in membrane filtration.

In **Chapter 5,** based on the molecular and photo-switching properties studied in Chapter 4 and the membrane design in Chapter 2, a photo-switchable membrane for water filtration is investigated. The use of a discotic complex **Azosulf₃TB** system with azo moieties permits the isomerization *trans-cis-trans* with irradiation. The isomeric membranes presented different pore sizes, different water flux and different rejection of small molecules in a reversible way.

The preparation of wedge-shaped liquid crystalline sulfonate salts containing different counterions is presented in **Chapter 6**. The structural and thermal properties of the columnar nanostructures change depending on the counterion used, which determines the pore size of the network. Compared to the membranes based on complexation with the TB template, the salt-based liquid crystals result in membranes that are easier to produce because there is no need for a template molecule and present a lower isotropization temperature that simplifies annealing. A new **NEt₄Sulf** membrane was produced and tested in comparison with the membrane of Chapter 2. The membrane has a smaller pore, resulting in a slightly lower permeability while enabling the retention of smaller molecules such as mono- and oligosaccharides.

Lastly, **Chapter 7** offers an epilogue of the work presented. An optimization process is described to define the limits of the membranes presented in the earlier Chapters. New molecular designs and fabrication parameters are explored to study their influence on the filtration performance: the presence of N-H bonds in the molecular structures, the thickness of the active layer and coating methods are studied as variable parameters.

Finally, an overall outlook for applications is given, highlighting the important achievements on new materials with improved characteristics and the next steps to be taken that involve new methodologies to scale up the laboratory scale processes developed in this Thesis.

1.7 References

[1] P. Burek, Y. Satoh, G. Fischer, M. T. Kahil, A. Scherzer, S. Tramberend, L. F. Nava, Y. Wada, S. Eisner, M. Flörke, N. Hanasaki, P. Magnuszewski, B. Cosgrove, D. Wiberg, *Water Futur. Solut.* **2016**, 1.

[2] Arthur Dahl, *Micropollutants*, **2009**.

[3] A. Gogoi, P. Mazumder, V. K. Tyagi, G. G. Tushara Chaminda, A. K. An, M. Kumar, *Groundw. Sustain. Dev.* **2018**, *6*, 169.

[4] I. Mohmood, C. B. Lopes, I. Lopes, I. Ahmad, A. C. Duarte, E. Pereira, *Environ. Sci. Pollut. Res.* **2013**, *20*, 1239.

[5] I. Ali, *Chem. Rev.* **2012**, *112*, 5073.

[6] M. A. Shannon, P. W. Bohn, M. Elimelech, J. G. Georgiadis, B. J. Mariñas, A. M. Mayes, *Nature* **2008**, *452*, 301.

[7] K. Peinemann, *Membranes for Water Treatment*, Wiley-VCH, **2010**.

[8] N. K. Khanzada, M. U. Farid, J. A. Kharraz, J. Choi, C. Y. Tang, L. D. Nghiem, A. Jang, A. K. An, *J. Memb. Sci.* **2020**, *598*, 117672.

[9] D. M. Stevens, J. Y. Shu, M. Reichert, A. Roy, *Ind. Eng. Chem. Res.* **2017**, *56*, 10526.

[10] R. W. Baker, *Membrane Technology and Applications*, 2nd ed., Wiley, **2006**.

[11] M. Ulbricht, *Polymer (Guildf).* **2006**, *47*, 2217.

[12] M. K. Purkait, M. K. Sinha, P. Mondal, R. Singh, *Introduction to Membranes*, Vol. 25, **2018**.

[13] G. Srikanth, *Chem. Eng. World* **1999**, *34*, 55.

[14] J. E. C. and R. J. Petersen, *Thin-film composite reverse-osmosis membranes: origin, developments and recent advances*, ACS Symposium Series, Vol. 153, **1981**.

[15] W. J. Lau, S. Gray, T. Matsuura, D. Emadzadeh, J. Paul Chen, A. F. Ismail, *Water Res.* **2015**, *80*, 306.

[16] R. J. Petersen, *J. Memb. Sci.* **1993**, *83*, 81.

[17] A. Lee, J. W. Elam, S. B. Darling, *Environ. Sci. Water Res. Technol.* **2016**, *2*, 17.

[18] D. Li, H. Wang, *J. Mater. Chem.* **2010**, *20*, 4551.

[19] A. Sagle, B. Freeman, *Futur. Desalin. Texas* **2004**, 1.

[20] D. F. N. M. for W. D. Li, H. Wang, *Functional Nanostructured Materials and Membranes for Water Treatment*, 1st ed., Wiley-VCH, **2013**.

[21] S. Tul Muntha, A. Kausar, M. Siddiq, *Polym. - Plast. Technol. Eng.* **2017**, *56*, 841.

[22] C. Bellona, J. E. Drewes, P. Xu, G. Amy, *Water Res.* **2004**, *38*, 2795.

[23] S. S. Madaeni, *Nanofiltration Membranes*, Springer, Berlin, Heidelberg, **2015**.

[24] V. A. Yangali, *Rejection of emerging organic contaminants by nanofiltration and reverse osmosis membranes:Effects on fouling, modelling and water reuse* (Ed.: Group, T. and F.), CRC Press, **2010**.

[25] Y. Yoon, P. Westerhoff, J. Yoon, S. A. Snyder, *J. Environ. Eng.* **2004**, *130*, 1460.

[26] Y. Yoon, P. Westerhoff, S. A. Snyder, E. C. Wert, *J. Memb. Sci.* **2006**, *270*, 88.

[27] M. Mulder, *Basic Principles of Membrane Technology*, Vol. 2, Kluwer Academic, **1996**.

[28] M. Stolov, V. Freger, **2019**, *53*, 2618−2625.

[29] J. Kucera, **2019**, *9*, 111.

[30] N. Bolong, A. F. Ismail, M. R. Salim, T. Matsuura, *Desalination* **2009**, *239*, 229.

[31] J. Radjenović, M. Petrović, F. Ventura, D. Barceló, *Water Res.* **2008**, *42*, 3601.

[32] X. Qu, P. J. J. Alvarez, Q. Li, *Water Res.* **2013**, *47*, 3931.

[33] Y. Peng, Y. Li, Y. Ban, H. Jin, W. Jiao, X. Liu, W. Yang, .

[34] R. Zhang, S. Ji, N. Wang, L. Wang, G. Zhang, J. Li, **2014**, 9775.

[35] Pall Porous Inorganic Media Guide, .

[36] J. R. Werber, C. O. Osuji, M. Elimelech, *Nat. Rev. Mater.* **2016**, *1*, 15.

[37] Y. xiao Shen, P. O. Saboe, I. T. Sines, M. Erbakan, M. Kumar, *J. Memb. Sci.* **2014**, *454*, 359.

[38] A. Engel, T. Walz, P. Agre, *Curr. Opin. Struct. Biol.* **1994**, *4*, 545.

[39] C. Tang, Z. Wang, I. Petrinić, A. G. Fane, C. Hélix-Nielsen, *Desalination* **2015**, *368*, 89.

[40] R. Hourani, C. Zhang, R. Van Der Weegen, L. Ruiz, C. Li, S. Keten, B. A. Helms, T. Xu, *J. Am. Chem. Soc.* **2011**, *133*, 15296.

[41] X. Zhou, G. Liu, K. Yamato, Y. Shen, R. Cheng, X. Wei, W. Bai, Y. Gao, H. Li, Y. Liu, F. Liu, D. M. Czajkowsky, J. Wang, M. J. Dabney, Z. Cai, J. Hu, F. V. Bright, L. He, X. C. Zeng, Z. Shao, B. Gong, *Nat. Commun.* **2012**, *3*, 948.

[42] N. Song, X. Gao, Z. Ma, X. Wang, Y. Wei, C. Gao, *Desalination* **2018**, *437*, 59.

[43] L. Chen, G. Shi, J. Shen, B. Peng, B. Zhang, Y. Wang, F. Bian, J. Wang, D. Li, Z. Qian, G. Xu, G. Liu, J.

Zeng, L. Zhang, Y. Yang, G. Zhou, M. Wu, W. Jin, J. Li, H. Fang, *Nature* **2017**, *550*, 1.

[44] J. S. Bunch, S. S. Verbridge, J. S. Alden, A. M. Van Der Zande, J. M. Parpia, H. G. Craighead, P. L. McEuen, *Nano Lett.* **2008**, *8*, 2458.

[45] J. Lyu, X. Wen, U. Kumar, Y. You, V. Chen, R. K. Joshi, *RSC Adv.* **2018**, *8*, 23130.

[46] H. H. Huang, R. K. Joshi, K. K. H. De Silva, R. Badam, M. Yoshimura, *J. Memb. Sci.* **2019**, *572*, 12.

[47] K. Thorkelsson, P. Bai, T. Xu, *Nano Today* **2015**, *10*, 48.

[48] F. Nabeel, T. Rasheed, M. Bilal, H. M. N. Iqbal, *Sep. Purif. Technol.* **2019**, *215*, 441.

[49] H. C. Kim, S. M. Park, W. D. Hinsberg, I. R. Division, *Chem. Rev.* **2010**, *110*, 146.

[50] K. Nickmans, A. P. H. J. Schenning, *Adv. Mater.* **2018**, *30*, 1703713.

[51] J. Lugger, D. Mulder, R. Sijbesma, A. Schenning, *Materials (Basel).* **2018**, *11*, 104.

[52] C. M. Bates, F. S. Bates, *Macromolecules* **2017**, *50*, 3.

[53] J. Rzayev, M. A. Hillmyer, *J. Am. Chem. Soc.* **2005**, *127*, 13373.

[54] S. P. Nunes, *Macromolecules* **2016**, *49*, 2905.

[55] T. Vidil, N. Hampu, M. A. Hillmyer, *ACS Cent. Sci.* **2017**, *3*, 1114.

[56] H. Yu, X. Qiu, N. Moreno, Z. Ma, V. M. Calo, S. P. Nunes, K. Peinemann, **2015**, *54*, 13937.

[57] D. A. Olson, L. Chen, M. A. Hillmyer, *Chem. Mater.* **2008**, *20*, 869.

[58] K. V. Peinemann, *Procedia Eng.* **2012**, *44*, 214.

[59] W. Rums, *New Synthetic Membranes for Dialysis . I .*, Vol. 3, **1964**.

[60] P. Bengani-Lutz, E. Converse, P. Cebe, A. Asatekin, *ACS Appl. Mater. Interfaces* **2017**, *9*, 20859.

[61] C. Sinturel, F. S. Bates, M. A. Hillmyer, *ACS Macro Lett.* **2015**, *4*, 1044.

[62] T. Kato, N. Mizoshita, K. Kishimoto, *Angew. Chemie - Int. Ed.* **2005**, *45*, 38.

[63] J. Kloos, N. Joosten, A. Schenning, K. Nijmeijer, *J. Memb. Sci.* **2020**, *620*, 118849.

[64] S. J. Cowling, *Handbook of Liquid crystals, Vol. 1, Part III*, Wiley-VCH, **2014**.

[65] W. H. de J. Ger Vertogen, *Thermotropic Liquid Crystals, Fundamentals*, 1st ed., Springer Berlin Heidelberg, **1988**.

[66] Peter S. Pershan, *Phys. Today* **1982**, *35*, 34.

[67] I. K. Shishmanova, *Smectic nanoporous networks : properties and hierarchical strategies towards applications*, **2013**.

[68] U. Beginn, L. Yan, S. N. Chvalun, M. A. Shcherbina, A. Bakirov, M. Moller, *Liq. Cryst.* **2008**, *35*, 1073.

[69] B. J. Coscia, J. Yelk, M. A. Glaser, D. L. Gin, X. Feng, M. R. Shirts, *J. Phys. Chem. B* **2019**, *123*, 289.

[70] H. Zhang, L. Li, M. Möller, X. Zhu, J. J. H. Rueda, M. Rosenthal, D. A. Ivanov, *Adv. Mater.* **2013**, *25*, 3543.

[71] J. J. Hernandez Rueda, H. Zhang, M. Rosenthal, M. Möller, X. Zhu, D. A. Ivanov, *Eur. Polym. J.* **2016**, *81*, 674.

[72] X. Zhu, M. A. Scherbina, A. V. Bakirov, B. Gorzolnik, S. N. Chvalun, U. Beginn, M. Möller, *Chem. Mater.* **2006**, *18*, 4667.

[73] A. Kraft, A. Reichert, R. Kleppinger, *Chem. Commun.* **2000**, *12*, 1015.

[74] R. G. and T. Beatriz Feringán, Pilar Romero,Jose Luis Serrano, *Chem. - A Eur. J.* **2015**, *21*, 8859.

[75] H. K. Lee, H. Lee, Y. H. Ko, Y. J. Chang, N. K. Oh, W. C. Zin, O. Kim, *Angew. Chemie - Int. Ed.* **2001**, *40*, 2669.

[76] G. M. Bögels, J. A. M. Lugger, O. J. G. M. Goor, R. P. Sijbesma, *Adv. Funct. Mater.* **2016**, *26*, 8023.

[77] A. P. H. J. Schenning, Y. C. Gonzalez-Lemus, I. K. Shishmanova, D. J. Broer, *Liq. Cryst.* **2011**, *38*, 1627.

[78] D. L. Gin, W. Gu, B. A. Pindzola, W. J. Zhou, *Acc. Chem. Res.* **2001**, *34*, 973.

[79] M. Zhou, P. R. Nemade, X. Lu, X. Zeng, E. S. Hatakeyama, R. D. Noble, D. L. Gin, **2007**, *129*, 9574.

[80] M. Henmi, K. Nakatsuji, T. Ichikawa, H. Tomioka, T. Sakamoto, M. Yoshio, T. Kato, *Adv. Mater.* **2012**, *24*, 2238.

[81] N. Marets, D. Kuo, J. R. Torrey, T. Sakamoto, M. Henmi, H. Katayama, T. Kato, *Adv. Healthc. Mater.* **2017**, *6*, 1700252.

[82] T. Sakamoto, T. Ogawa, H. Nada, K. Nakatsuji, M. Mitani, B. Soberats, K. Kawata, M. Yoshio, H. Tomioka, T. Sasaki, M. Kimura, M. Henmi, T. Kato, *Adv. Sci.* **2018**, *5*, 1.

[83] K. Hamaguchi, D. Kuo, M. Liu, T. Sakamoto, M. Yoshio, H. Katayama, T. Kato, *ACS Macro Lett.* **2019**, *8*, 24.

[84] M. Gupta, Y. Suzuki, T. Sakamoto, M. Yoshio, S. Torii, H. Katayama, T. Kato, *ACS Macro Lett.* **2019**, *8*, 1303.

[85] M. Henmi, K. Nakatsuji, T. Ichikawa, H. Tomioka, T. Sakamoto, M. Yoshio, T. Kato, *Adv. Mater.* **2012**, *24*, 2238.

[86]   M. Zhou, T. J. Kidd, R. D. Noble, D. L. Gin, *Adv. Mater.* **2005**, *17*, 1850.

[87]   B. M. Carter, B. R. Wiesenauer, R. D. Noble, D. L. Gin, *J. Memb. Sci.* **2014**, *455*, 143.

[88]   X. Feng, M. E. Tousley, M. G. Cowan, B. R. Wiesenauer, S. Nejati, Y. Choo, R. D. Noble, M. Elimelech, D. L. Gin, C. O. Osuji, *ACS Nano* **2014**, *8*, 11977.

[89]   E. Pouzet, V. De Cupere, C. Heintz, J. W. Andreasen, D. W. Breiby, M. M. Nielsen, P. Viville, R. Lazzaroni, G. Gbabode, Y. H. Geerts, *J. Phys. Chem. C* **2009**, *113*, 14398.

[90]   D. Kuo, M. Liu, K. R. S. Kumar, K. Hamaguchi, K. P. Gan, T. Sakamoto, T. Ogawa, R. Kato, N. Miyamoto, H. Nada, M. Kimura, M. Henmi, H. Katayama, T. Kato, *Small* **2020**, *16*, 5.

[91]   K. Hamaguchi, R. Ichikawa, S. Kajiyama, S. Torii, Y. Hayashi, J. Kumaki, H. Katayama, T. Kato, *ACS Appl. Mater. Interfaces* **2021**, *13*, 20598.

[92]   S. J. A. Houben, S. A. van Merwijk, B. J. H. Langers, B. M. Oosterlaken, Z. Borneman, A. P. H. J. Schenning, *ACS Appl. Mater. Interfaces* **2021**, *13*, 7592.

[93]   Y. Zhang, R. Dong, U. R. Gabinet, R. Poling-skutvik, N. K. Kim, C. Lee, O. Q. Imran, X. Feng, C. O. Osuji, *ACS Nano* **2021**, *15*, 8192.

[94]   D. Liu, D. J. Broer, *Langmuir* **2014**, *30*, 13499.

[95]   H. Yang, Y. J. Lv, B. P. Lin, X. Q. Zhang, Y. Sun, L. X. Guo, *J. Polym. Sci. Part A Polym. Chem.* **2014**, *52*, 1086.

[96]   P. G. Breed, J. A. Ramsden, J. M. Brown, *Can. J. Chem.* **2001**, *79*, 1049.

[97]   B. P. Hoag, D. L. Gin, *Macromolecules* **2000**, *33*, 8549.

[98]   K. B. Wagener, J. M. Boncella, J. G. Nel, *Macromolecules* **1991**, *24*, 2649.

[99]   C. E. Hoyle, C. N. Bowman, *Angew. Chemie - Int. Ed.* **2010**, *49*, 1540.

[100]   A. B. Lowe, *Polym. Chem.* **2010**, *1*, 17.

[101]   H. Yang, M. X. Liu, Y. W. Yao, P. Y. Tao, B. P. Lin, P. Keller, X. Q. Zhang, Y. Sun, L. X. Guo, *Macromolecules* **2013**, *46*, 3406.

[102]   I. Gracia, P. Romero, J. L. Serrano, J. Barberá, A. Omenat, *J. Mater. Chem. C* **2017**, *5*, 2033.

[103]   S. Kumar, *The liquid crystal book series. Chemistry of Discotic Liquid Crystals. From monomers to polymers* (Ed.: CRC Press, T. and F. G.), **2011**.

[104]   G. Wang, C. J. Garvey, H. Zhao, K. Huang, L. Kong, *Membranes (Basel).* **2017**, *7*, 37.

[105]   M. Yoshio, T. Kagata, T. Hoshino, T. Mukai, H. Ohno, T. Kato, *J. Am. Chem. Soc.* **2006**, *128*, 5570.

[106]   X. Feng, S. Nejati, M. G. Cowan, M. E. Tousley, B. R. Wiesenauer, R. D. Noble, M. Elimelech, D. L. Gin, C. O. Osuji, *ACS Nano* **2016**, *10*, 150.

[107]   X. Feng, K. Kawabata, G. Kaufman, M. Elimelech, C. O. Osuji, *ACS Nano* **2017**, *11*, 3911.

[108]   A. Halperin, *Langmuir* **1999**, *15*, 2525.

[109]   Z. Yang, J. K. Gupta, K. Kishimoto, Y. Shoji, T. Kato, N. L. Abbott, *Adv. Funct. Mater.* **2010**, *20*, 2098.

[110]   J. A. M. Lugger, D. J. Mulder, S. Bhattacharjee, R. P. Sijbesma, *ACS Nano* **2018**, *12*, 6714.

[111]   S. Bhattacharjee, J. A. M. Lugger, R. P. Sijbesma, *Macromolecules* **2017**, *50*, 2777.

[112]   Q. C. Xia, W. J. Yang, F. Fan, M. Ji, Y. Wang, Z. Y. Wang, X. L. Cao, W. Xing, S. P. Sun, *Nano Lett.* **2020**, *20*, 8185.

[113]   D. J. Mulder, L. M. W. Scheres, J. Dong, G. Portale, D. J. Broer, A. P. H. J. Schenning, *Chem. Mater.* **2017**, *29*, 6601.

[114]   S. M. Dischinger, M. J. McGrath, K. R. Bourland, R. D. Noble, D. L. Gin, *J. Memb. Sci.* **2017**, *529*, 72.

[115]   M. J. McGrath, S. H. Hardy, A. J. Basalla, G. E. Dwulet, B. C. Manubay, J. J. Malecha, Z. Shi, H. H. Funke, D. L. Gin, R. D. Noble, *ACS Mater. Lett.* **2019**, *1*, 452.

Chapter 2

Sulfonated polymerized liquid crystal nanoporous membranes for water purification
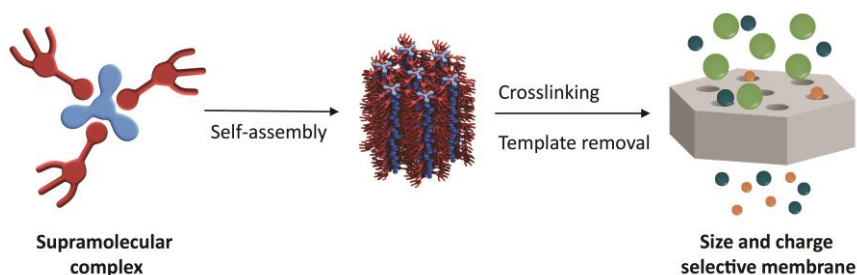
Abstract | New isoporous nanofiltration composite membranes were fabricated by photo-polymerization of thin films of the hexagonal columnar mesophase formed by the supramolecular complex **Sulfac₃TB**. This was followed by deposition on a polyethersulfone (PES) porous support and removal of the template molecule. The membranes had an average permeability of 2.3 L·m^{-2}·h^{-1}·bar^{-1} and a sharp molecular weight cut-off of around 5000 g·mol^{-1} based on PEG filtration. The full rejection of Bovine Serum Albumin and Green Fluorescent proteins and their flux recovery suggested the absence of defects on the active layer of the membrane. The filtration of charged molecules presented total rejection for molecules larger than 1000 g·mol^{-1} and a size-charge selectivity with higher rejection for cationic molecules due to ionic interactions with the pore walls. These interactions mean absorption within the membrane, which affects the rejection of neutral solutes such as Riboflavin and PEG 3000, being less relevant for smaller molecules.

2.1 Introduction

Due to their robustness and stability, polymerized liquid crystals (LCs) have attracted attention for their use in the preparation of membranes with pore sizes between 0.5 and 2 nm, which gives them the potential for molecular level separations.[1] In addition, the use of this bottom-up approach gives control over the pore functionality, which makes possible to have a more specific distinction in the separation process between ions and molecules similar in size or charge. Substantial progress has been made recently in the application of these polymerized LCs as separation systems in filtration membranes, especially for desalination and removal of organic micropollutants from water.[2–9] Among the different morphologies in which the mesogens can arrange (e.g. columnar, lamellar, cubic,...),[10] the anisotropy present in columnar mesophases gives a higher order that is advantageous for the formation of uniform pores and thus membranes with higher water flux.[7]

An elegant method to create porous structures with a specific pore size was firstly reported by Kim. et al. by removing a template molecule from a columnar structure.[11] It is shown that columnar mesophases can be obtained from LC Hydrogen-bonded complexes between benzoic acid derivatives and template aromatic molecules in the center.[12–14] This specific strategy to obtain nanoporous polymerized liquid crystals has been further explored by other groups. More specially, the fabrication of free-standing films with size and charge selectivity for alkali metal ions and organic molecules has been previously reported with 3:1 complexes between gallic acid derivatives and aromatic templates such as melamine (M) or tris(triazolyl)triazine (T)[15] and 1,3,5-Tris(1 H-benzo[*d*]imidazol-2-yl)benzene (TBIB).[16],[17] Further work on homeotropic alignment of the nanoporous films was reported, where absorption of dyes increases compared to planar-oriented films.[18] Important advances in the template strategy have shown the creation of perfectly oriented columnar pores in thin films[19] and the optimization of the thickness of supported membranes to improve the filtration performance in future applications.[20] Up to now, only water permeability has been measured in these systems but rejection and selectivity data of various solutes in water are not yet available.

Here, we moved beyond the state of the art of template strategy to develop a polymerized columnar LC-based water purification membrane for the size and charge selective separation of organic solutes (**Figure 2.1**). We make use of the stronger electrolyte sulfonic acid instead of previously used carboxylic acids to reduce interactions with cations and to increase the water permeability of the membranes.[21,22] A wedge-shaped sulfonic acid monomer derivative **Sulfac** is used to complex to the 1,3,5-tris(6-methyl-1H-benzo[*d*]imidazole-2-yl) benzene (**TB**) template into a discotic supramolecular unit. The alkene functionalities of the sulfonated

monomer are crosslinked, and the template molecule is removed resulting in pores of around 1.3 nm size with sulfonate groups in the interior.
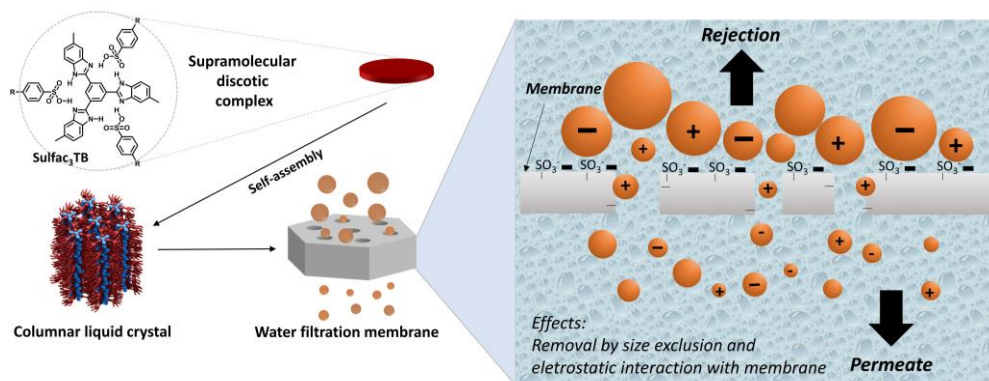
Figure 2.1 | On the left, schematic representation of the supramolecular discotic complex **Sulfac₃TB** which leads to a columnar arrangement that finally is used to fabricate the supported NF membrane. On the right the filtration through the selective layer is represented with SO_3 groups in the pores which create electrostatic interactions and pore size sieving as main process.

2.2 Synthesis and characterization of supramolecular complex Sulfac₃TB

For the formation of the supramolecular complex **Sulfac₃TB**, the sulfonic acid derivative monomer **Sulfac** and the core template **TB** were prepared separately. The synthesis of the template, 1,3,5-tris(6-methyl-1H-benzo[d]imidazole-2-yl) benzene, was performed as reported by Lugger et a*l.*[23] The new sulfonic derivative **Sulfac** was synthesized in four steps following the synthetic route depicted in **Scheme 2.1**.
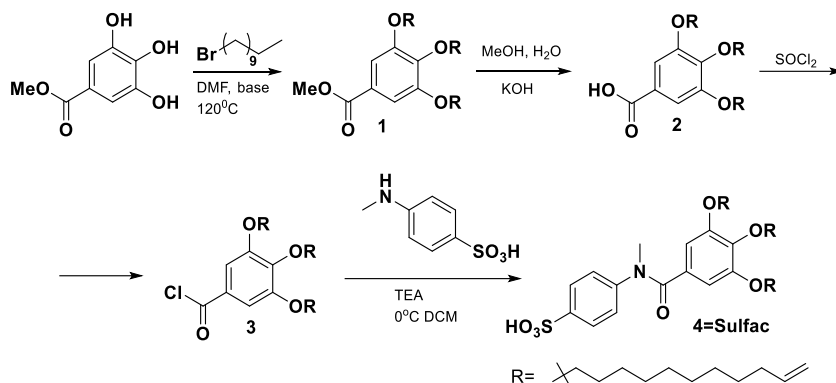
Scheme 2.1. | Synthetic route for the synthesis of **Sulfac**.

First, the three phenolic groups of methyl gallate were alkylated with 11-bromo-1-undecene followed by deprotection of the carboxylic acid according to a literature procedure to give compound **2**.[17] The acid chloride **3** was formed quantitatively with thionyl chloride and coupled with N-methyl sulfanilic acid in DCM with trimethylamine as a base, yielding the desired compound **Sulfac**. The thermal and liquid crystalline properties of **Sulfac** were investigated with differential scanning calorimetry (DSC), polarizing optical microscopy (POM) and X-ray scattering. **Sulfac** was found to be liquid crystalline when visualized under the POM at room temperature with micro-meter sized domains in a typical conic texture (**Figure 2.2a**). This texture is characteristic of columnar mesophases with small domains.[24] A transition peak from isotropic to LC at 57 ^{0}C (ΔH= 3.48 J·g^{-1}) in the heating cycle of the DSC was observed (**Figure 2.2b**). The medium angle X-ray scattering pattern (MAXS) of **Sulfac** (**Figure 2.2c**) showed peaks with a ratio of q values 1:√3:2:√7… corresponding to a Col$_{hex}$ phase with a lattice parameter *a* of 3.84 nm^I (**Figure 2.2d**).

---

^{I} $d_{100} = \frac{2\pi}{q} = a \; x \; \cos 30° \, ; a = \frac{2d}{\sqrt{3}}$
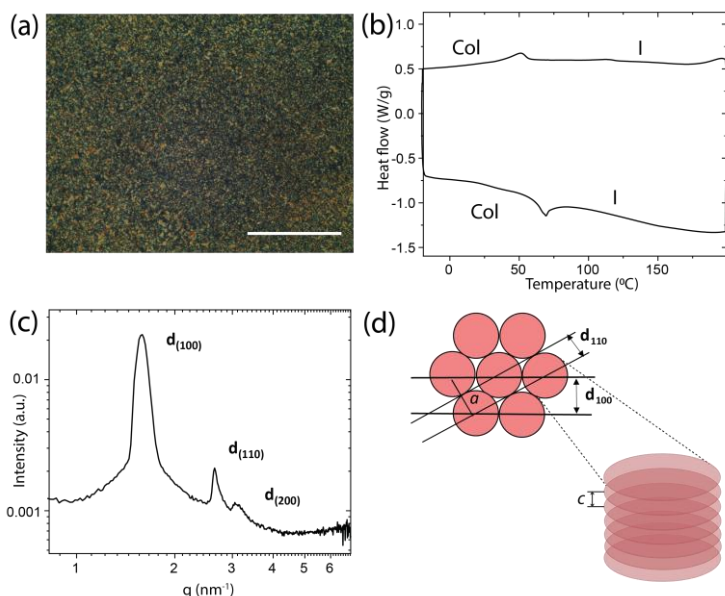
Figure 2.2 | a) POM picture of **Sulfac** at room temperature. Scale bar 100 μm; b) 2nd cycle on DSC of **Sulfac** at 5 ^{0}C/min; c) MAXS pattern of **Sulfac** at room temperature after annealing and d) schematic illustration of the hexagonal columnar lattice

To obtain the 3:1 complex, **Sulfac** was mixed with **TB** as a template (**Figure 2.3a**): to suppress phase separation of the template from the mixture a small excess of **Sulfac**, was used. Mixing of **Sulfac** and **TB** in a 3.2:1 ratio in EtOH:CHCl$_3$ (1:4) afforded the supramolecular complex **Sulfac$_3$TB**. Liquid crystallinity of the complex was studied under POM, where a focal conic texture with micro-meter size domains, as for **Sulfac**, was obtained after heating the sample to 150 ^{0}C and cooling to room temperature (**Figure 2.3b**). The mesophase appears only after hours, regardless of cooling rate with a predominantly homeotropic alignment and randomly ordered planar domains. DSC data (**Figure 2.3c**) showed two transition peaks in the second heating cycle; a glass transition at low temperatures below 0 ^{0}C and isotropization at 55 ^{0}C. X-ray diffraction measurements at room temperature (**Figure 2.3d**) confirmed the existence of a columnar hexagonal mesophase for the complex with a ratio of 1:√3:2... of the principal diffraction peaks giving a lattice parameter *a* of 4.47 nm. A peak related to the interdisc distance at higher q values was absent, identifying this mesophase as disordered columnar hexagonal, Col$_{hd}$.

(a)

(b)

(c)

(d)
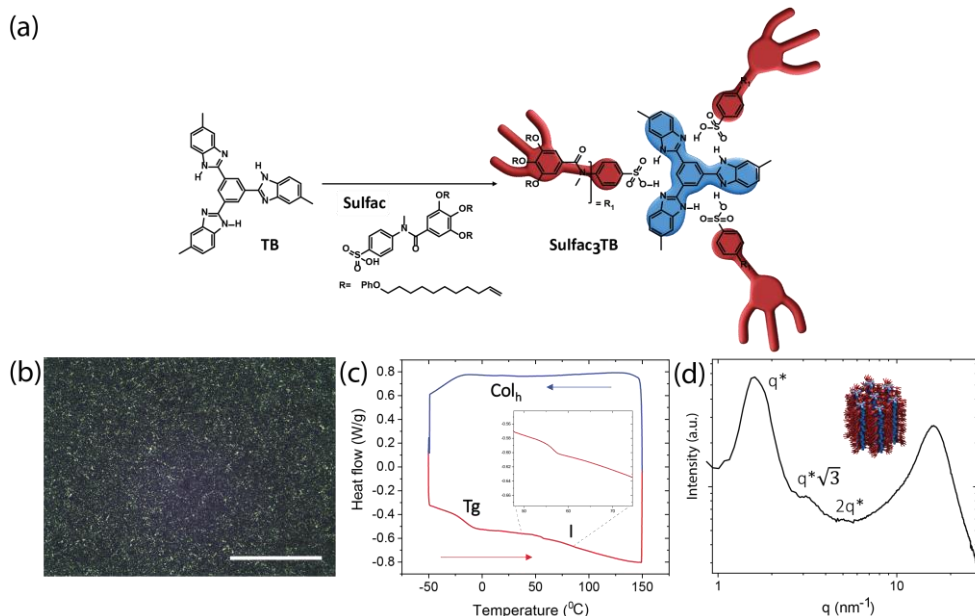
Figure 2.3 | a) Representation of **Sulfac₃TB** complex; b) POM at room temperature after cooling at 50 ^{0}C/min of **Sulfac₃TB**. Scale bar 500 μm; c) DSC of the second cycle at 10 ^{0}C/min of the complex with heating cycle in red and cooling in blue and d) WAXS pattern of the complex at room temperature.

2.3.1 Formation of self-standing LC polymer films of Sulfac₃TB

Nanoporous LC films were prepared *via* thiol-ene reaction, a light-induced radical polymerization in which a thiol group reacts with an alkene to give homogeneously crosslinked networks (**Figure 2.4a**). The thiol-ene reaction is compatible with a wide range of functional groups which is important for the fabrication of membranes with functionalized nanopores.[25]

A solution containing **TB**, **Sulfac**, 10-decanedithiol as the cross-linker (1.5 dithiol molecule per molecule of **Sulfac** to have a ratio 1:1 of thiol:ene) and Irgacure 819 as initiator, was drop-cast onto a clean glass substrate. Free-standing yellow-transparent films were obtained by photo-polymerization and subsequent removal from the glass surface by floating in an aqueous NaCl solution. The obtained self-standing films were characterized by FT-IR to confirm a successful of the photopolymerization by the disappearance of the terminal double bonds (=C-H bending vibration at 908 cm^{-1}) as shown in **Figure 2.4b**. Both POM and X-ray diffraction confirmed the retention of the columnar hexagonal lattice after the polymerization (**Figure 2.4c** and **Figure 2.4d**) with narrower peaks on the WAXS pattern indicating a slightly higher order. The lattice spacing d$_{(100)}$ increased from 3.90 to 4.65 nm in the polymer due to the introduction of the crosslinker in the network. Removal of the template was performed by gently

shaking the free-standing films in DMSO for 3h. Qualitatively, removal of the fluorescent template can be followed by eye, since under 366 nm UV light the as-made film is yellow-green but turns blue after removal of the template (**Figure 2.4e**). Quantitative removal of **TB** after three extractions with DMSO was confirmed with UV-VIS spectroscopy to determine the concentration of template in the solution (**Figure 2.4f**).
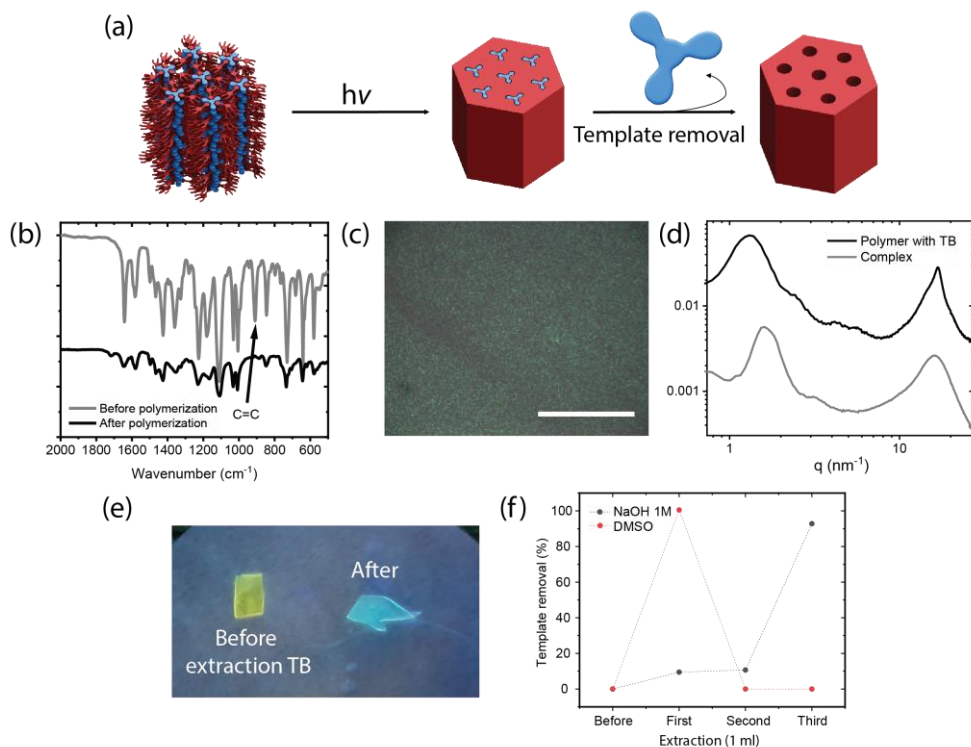
Figure 2.4 | a) Schematic representation of the crosslinking *via* photo-polymerization through thiol-ene chemistry and template removal from the polymerized material; b) comparison of the complex mixture before (grey) and after polymerization (black) on FT-IR; c) POM of the texture of a photopolymerized film. Scale bar 100 µm; d) WAXS pattern before and after polymerization; e) visualization of the films with and without **TB** under UV light and f) % of **TB** removal after 3 extractions in DMSO and NaOH 1M.

2.3 Membrane fabrication and characterization

To develop NF membrane with reproducible performance, the use of a proper support and a technique that produces thin and homogeneous films are essential. Due to its high permeability, a microporous polyethersulfone (PES) UF membrane was used as support. The fabrication of the columnar LC membranes was carried out using photo-polymerization and following a reported transfer method.[3,26] It consists of coating a

glass surface with the LC and transferring by pressing and heating the active layer to the porous support. Spin coating was used in order to achieve the deposition of thin layers to get a higher water flux of the membrane.[27]

i) PVA coated glass   ii) LC spin coated   iii) PES transference with pressure and heat

iv) Photopolymerization   v) Recovery of membrane in water   vi) Supported membrane
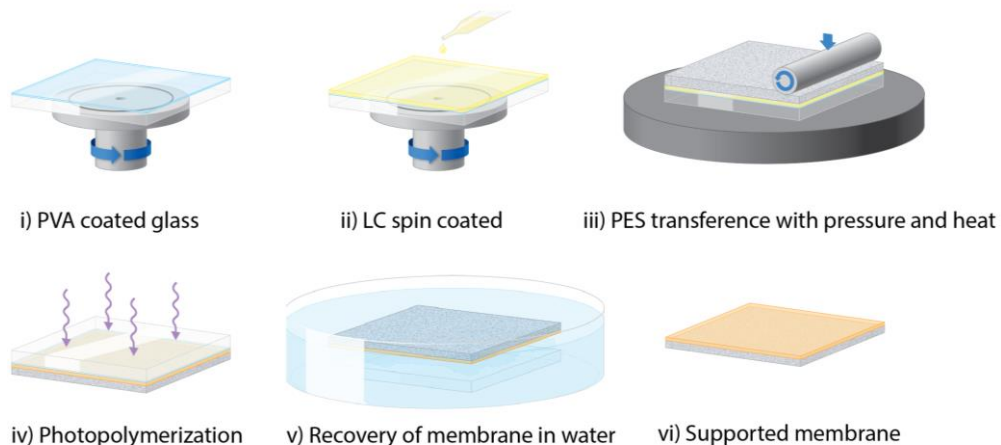
Figure 2.5 | Schematic illustration of the membrane fabrication by spin coating (ii) and PES transference (iii) followed by photopolymerization (iv) and membrane recovery in water (v).

Glass plates were cleaned with acetone and isopropanol under sonication for 10 minutes in a bath. Solutions for spin coating were prepared by mixing the sulfonic acid monomer **Sulfac** (3.2 equivalents) with the template (**TB**, 1 equivalent) and 1,10-decanedithiol (4.6 equivalents) in DCE/EtOH (8:2 v/v) in a 10 wt. % concentration. Finally, Bis(2,4,6-trimethylbenzoyl)-phenylphosphineoxide (Irgacure 819, 3 wt.%) was added as initiator. A sacrificial layer of polyvinyl alcohol (PVA) was used which was spin-coated from a 10wt% aqueous solution onto clean glass at 1500 rpm for 60 s (**Figure 2.5i**). Then the monomer mixture was spin-coated on top at 2500 rpm for 30 s (**Figure 2.5ii**). The resulting LC/PVA was transferred to a polyethersulfone (PES) support. The "sandwich" was heated to 70 ^{0}C and hand-pressed with a steal roller to help the transfer (**Figure 2.5iii**). After further cooling to room temperature, the membrane was polymerized with UV light for 15 min with 8 mW·cm^{-2} of intensity giving a thin active layer on top of the PES support (**Figure 2.5iv**). The glass and PVA sacrificial layer were removed by immersing the composite membrane in water and the obtained membrane was dried in a vacuum oven at 40 ^{0}C (**Figure 2.5vi**). High-resolution Scanning Electron Microscopy (HR-SEM) micrographs of the surface and cross-section were taken. The top view shown in **Figure 2.6b** confirmed that the nanostructured filtration layer covered the PES surface completely without micrometer-scale defects. The successful transference of the LC to the PES support was confirmed in **Figure 2.6c**, where an average thickness of the active layer of

approximately 200 nm on top of the thick, porous PES support was shown. The obtained **Sulfac₃TB** membrane was released from the glass by dissolving the PVA layer with water.
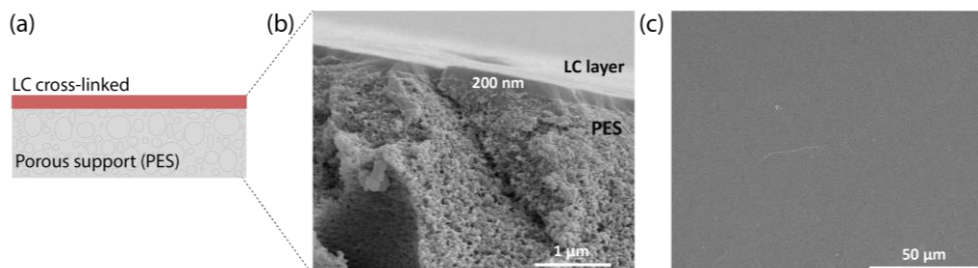
Figure 2.6 | a) Representation of the supported membrane composition; b) HR-SEM top view of the active layer surface and c) HR-SEM cross-section showing the active layer of 200 nm thickness.

Pure water filtration tests

The permeability of the **Sulfac₃TB** membrane was determined measuring the flux of pure water at different pressures (1–5 bar) using a 20 ml custom-made, stainless steel, stirred "Amicon type" dead-end filtration cell of 1.5 cm diameter (**Figure 2.7**).[28] Ultrapure water was permeated through the membrane until the flux remained stable for at least one hour (**Figure 2.8a**). From a linear fit of flux J vs pressure P as represented in **Figure 2.8b**, the permeability P [L·m⁻²·h⁻¹·bar⁻¹] was calculated following:

$$P = \frac{J}{\Delta P} \text{ (eq. 1.1)}$$

The pure water permeability was determined to be 2.36 ± 0.27 L·m⁻²·h⁻¹·bar⁻¹ while for the bare PES support the permeability was 106 ± 3.92 L·m⁻²·h⁻¹·bar⁻¹. This indicates that the active layer is the dominant factor in the overall membrane performance and that the PES support is not significantly affecting the permeability.
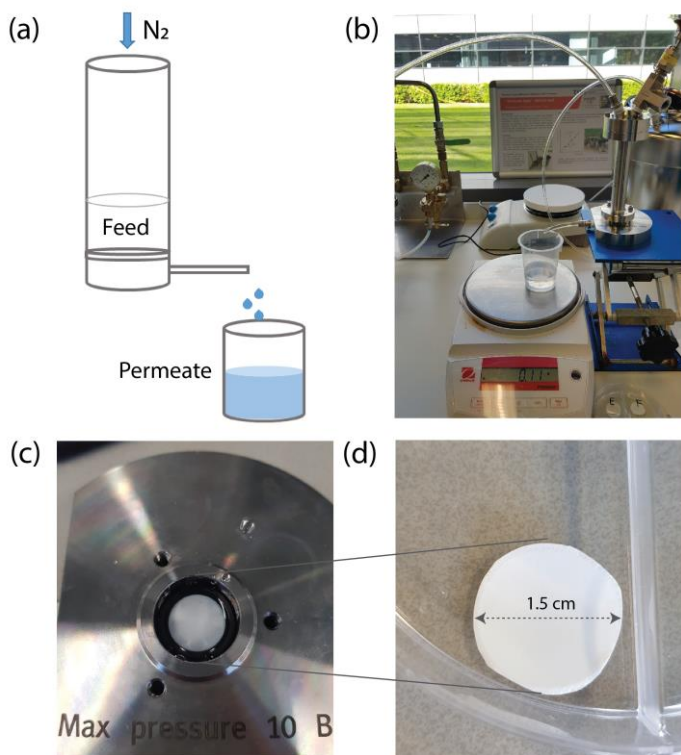
Figure 2.7 | a) Schematic representation of filtration process; b) real set up of an Amicon Cell connected to a nitrogen gas inlet. The permeate is collected and weighted in a digital balance; c) at the bottom of the cell, on the platform with the reservoir for the water, a membrane is placed and protected with a rubber ring on top; d) zoom-in of the membrane sample used with a diameter of 1.5 cm.
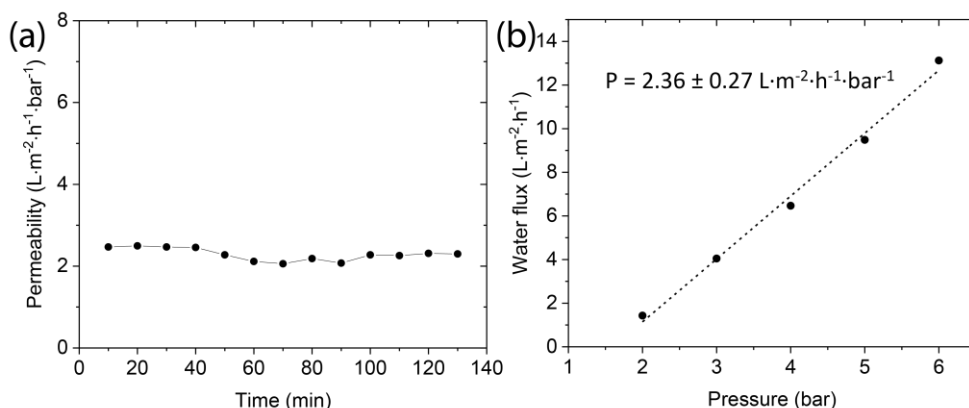
Figure 2.8 | a) Plot of water permeability vs time and b) Relation between water flux vs pressure from which the permeability value P was is obtained.

Theoretical permeability was calculated to compare with **Sulfac₃TB** membrane. We assumed a flow through an ideally homeotropically aligned monodomain of a columnar hexagonal mesophase,[29] as described in previous studies on similar LC-based nanocomposite membranes[2]:

$d_1 = 4.65$ nm
$d_2 = 1.3$ nm (TB diameter)
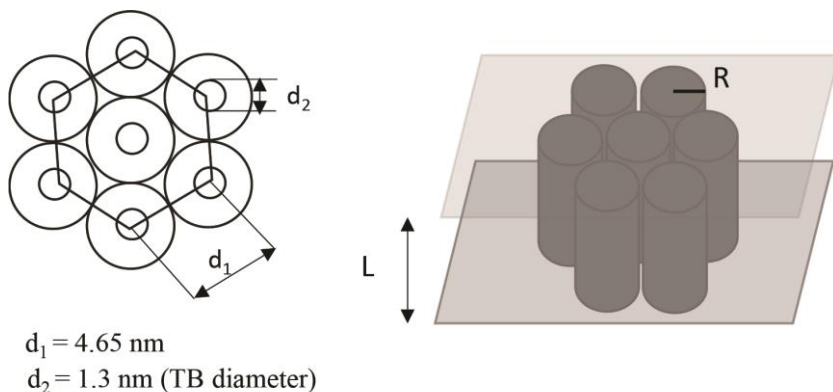
Figure 2.9 | Representation of a hexagonal lattice with the characteristic parameters and representation of the homeotropic orientation for a theoretical water flux.

Theoretical water flux, Q [L·m⁻²·h⁻¹·bar⁻¹] was calculated using the Hagen-Poiseuille equation:

$$Q = \frac{\pi\varepsilon(\Delta P)R^4}{8\mu L} \text{ (eq. 1.2)}$$

The length of all cylinders was assumed to be equal to the thickness of the film (L [m]). The porosity (ε) of the mesophase is related to the distance between the cylinders d_1:

$$\varepsilon = \frac{2}{\sqrt{3d_1{}^2}} \text{ (eq. 1.3)}$$

The pressure difference ΔP is 1 bar, R is the characteristic radius and equal to the ratio of d_2/d_1 and μ is the viscosity of the medium, in this case, water $0.89\cdot10^{-3}$ Pa·s⁻¹.

The permeability of **Sulfac₃TB** membrane is close to that of current commercial NF membranes[30] (between 1 and 10 L·m⁻²·h⁻¹·bar⁻¹), as indicated in **Table 2.1** and similar to the values of recent LC-based membranes reported by the groups of Kato, Osuji and Schenning.[4,6,8,9,20]

Table 2.1 | Comparison of permeability values for commercial NF membranes and our membrane:

LC-based membranes	Reference	Support	Permeability ($L\ m^{-2}\ h^{-1}\ bar^{-1}$)
Sulfac₃TB	This work	Composite PES	2.3
Cub_bic*	[4]	Composite PS	0.17
Col_h*	[6]	Composite PS	2, 3.5
SmA*	[8],[9]	Composite PS	2.8, 0.95
Col aligned**	[20]	Composite PEEK	1.8
Commercial membranes*	*Membrane*	*Material*	
NF90	Dow FilmTec	Polyamide TFC	6.6
NF200	Dow FilmTec	Polyamide TFC	4.2
N30F	Microdyn-Nadir	Polyethersulfone	5.6
NP030	Microdyn-Nadir	Polyethersulfone	1.8
TFC-HR	Koch	Polyamide TFC	3.5
DK	GE Osmonics	Polyamide TFC	5.5

*values based on 400 nm LC layer

**value based on 750 nm LC layer

***from ref. [30]

The theoretical permeability was calculated for a 200 nm thick membrane with a perfect homeotropic alignment of the pores (calculated pore density $\varepsilon = 6.73\cdot10^{16}\ m^{-2}$) with a diameter of 1.3 nm. This value is the estimated pore size from the calculated diameter for the template molecule with Chem3D software for an analogous system (ref [16]). Experimental pore size determination is not straightforward since available methods are not capable of determining sizes of a few nm. The commonly used N_2 adsorption isotherm (BET) provides information about all pores in the membrane, not just active pores but also dead-end pores and those of the PES support under the separating layer. Porometric methods such as porometry, permporometry and mercury porometry depend on filling of pores with liquid, which requires excessively high pressures well above 100 bar. Pore filling using capillary condensation has a limit of a few nm, making this approach also inappropriate for pores with sizes around a nanometer. Therefore, experimentally determined pore sizes are not useful to interpret filtration behaviour.

The obtained water permeability value is 6.8 $L\cdot m^{-2}\cdot h^{-1}\cdot bar^{-1}$, which is clearly in the same order of magnitude as the experimental. The experimental permeability is 35% of the theoretical value, while the membrane was impermeable before template removal. In a planar orientation, the membrane would have none or very low permeability. Therefore, we conclude that the remarkably high flux of pure water

(similar to NF commercial membranes) suggest that a significant fraction of the pores connects bottom and top of the active layer.

Protein rejection

The ability of the **Sulfac₃TB** membrane to reject bigger, globular solutes was checked with the filtration of aqueous solutions containing two proteins, bovine serum albumin (BSA) and green fluorescence protein (GFP), with molecular weights of 66 kDa and 40 kDa respectively (6 and 5 nm size [31]). Rejection was determined once the steady-state of both proteins was reached with the stabilization of the flux (**Figure 2.10c**). The analysis of UV-Vis data comparison between permeate and feed solutions showed that 99.6% of the BSA protein and 99.2% of GFP were rejected (**Table 2.2**). Due to the big size of the solutes the flux, the very high number on rejection confirmed a defect-free membrane with pores smaller than 2 nm. Moreover, the filtration of BSA resulted in a reduction of the permeability from 2.39 to 0.82 [$L \cdot m^{-2} \cdot h^{-1} \cdot bar^{-1}$], with nearly complete (>90%) recovery of flux when the protein solution was again replaced by pure water (**Figure 2.10d**), indicating the resistance to fouling of the membrane that could permanently block the pores.

Table 2.2 | Rejection % of BSA and GF proteins as solutes when steady state is reached.

Solute	Rejection (%)
BSA	99.6% ± 0.15%
GFP	99.2% ± 0.41%
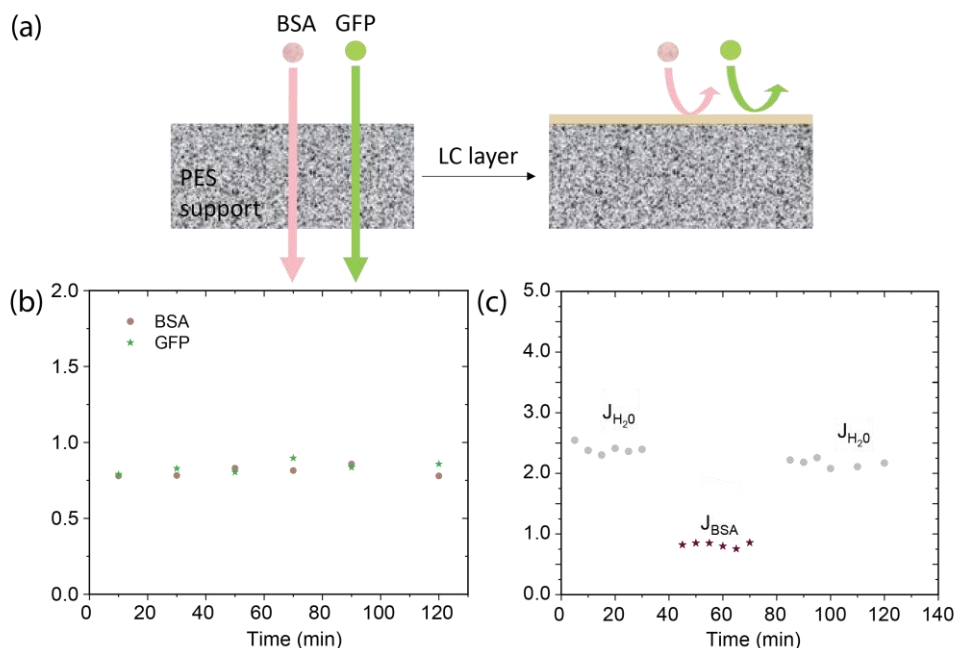
Figure 2.10 | a) Filtration process of the proteins through the porous support and the composite membrane; b) Permeability of the solutions of both BSA and GF proteins upon time showing a stable flow and c) Flux vs time for pure water followed by BSA solution, and pure water, respectively.

MWCO determination and salt rejection

The rejection of different average molecular weights (M_n) polyethylene glycol (PEG) ranging from 600 to 20000 g·mol^{-1} was measured to determine the molecular weight cut-off (MWCO) of the membrane. By definition, MWCO is the molecular weight at which 90% of the solute is retained. The **Sulfac₃TB** membrane showed a MWCO value of 5000 g·mol^{-1} PEG (**Figure 2.11a**). This value corresponds to a hydrodynamic radius (R_h) of 1.7 nm as calculated from the relation between molecular weight and hydrodynamic radius for PEG, given by **equation 1.4**.[32]

$$R_h = 0.06127 \cdot Mn^{0.3931} (\text{eq. 1.4})$$

In principle, we could expect a smaller R_h at the MWCO following the calculated molecular size of the **TB** template (1.3 nm). However, the observed R_h at the MWCO (**Figure 2.11c**) is not in conflict with the estimated pore size, considering the fact that the PEG coils do not have a fixed size and can pass through pores with a smaller radius than R_h.[33]

Table 2.3 | Calculated rejection values for the different Mn PEG used, with the corresponding pore hydrodynamic radius that are related to pore sizes of the membrane:

M_n (g·mol^{-1})	R_h (nm)	Retention (%) ± error
1500	1.08	43.4 ± 0.92
3000	1.42	50.1 ±1.31
4000	1.59	74.6 ± 0.51
4600	1.68	83.2 ± 3.09
7000	1.99	96.2 ± 0.94
10000	2.29	97.8 ± 2.02
20000	3.01	99.8 ± 0.11

The rejection of salts with mono or divalent cations was determined for NaCl and MgSO$_4$ and plotted against time showing rejections of less than 10% (**Figure 2.11b**). Clearly, these inorganic salts are not retained by the membrane because the pore size (estimated to be 1.3 nm) is bigger than the ionic radius of the ions (Na$^+$=0.102, Cl$^-$ =0.181 nm, Mg^{2+}=0.072 and SO$_4^{2-}$=0.290)[34] making the coordination by the sulfonate groups in the pore walls weak.
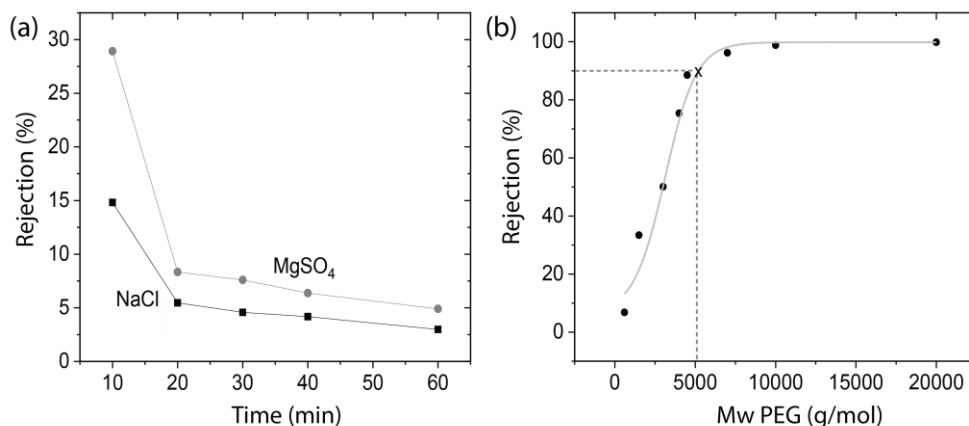
Figure 2.11 | a) Rejection of the monovalent salt NaCl and the divalent salt MgSO$_4$ as a function of time; b) MWCO curve of the **Sulfac₃TB** membrane. Solute: PEG.

Size and charge selectivity

Size and charge selectivity of the **Sulfac₃TB** membrane for small organic molecules was further tested with the filtration of a series of different sizes of anionic, neutral, zwitterionic and cationic dyes with molecular weights between 186 and 1299 g·mol^{-1}

(**Table 2.4**, **Figure 2.12a**). Aqueous solutions of the dyes were filtered separately through the membrane and permeate solutions were collected once a steady-state for rejection and flux was reached.

Table 2.4 | Dyes used in the filtration test, molecular characteristics and rejection values:

Dye	Charge	Mw (g·mol⁻¹)	Molecular width* (nm)	Rejection (%)
PhCy	-4	892.25	1.42	99.8
Pyr	-3	455.37	0.99	77.4
OG	-2	406.38	1.07	23.1
F	-1	330.27	0.92	16.9
RhB	+-	442.57	1.14	50.9
Rib	0	376.36	1.04	17.4
MB	+1	284.4	0.58	77.1
CV	+1	372.45	1.12	88.1
DMBP	+2	186.26	0.98	35.7
AB	+4	1157.06	2.26	99.3

largest dimension orthogonal to the long axis of the molecule

Analysis of the obtained data showed the influence of the charges and sizes of the dyes on their rejection. The effect is more noticeable for the cationic dyes: the large dye **AB**, (M_W = 1157 g·mol⁻¹) was fully rejected, while for cationic dyes smaller than the estimated pore size, **CV**, **MB** and **DMBP**, rejection decreased considerably with decreasing size (Mw) of the molecule. Moreover, the rejection values of the cationic dyes with different charges follow the same MWCO curve (green trend line in **Figure 2.12b**), which lies above the data for the dyes without charge (**Rib** and **RhB**). This suggests an effect of positive charge, but a limited role of overall charge on rejection. Similarly, rejection of anionic dyes increased gradually with molecular size: from 17% rejection of the smallest dye Fluorescein (**F**) (Mw = 330 g·mol⁻¹) to total rejection of the large dye **PhtCy** (Mw= 892 g·mol⁻¹). However, unlike for cationic dyes, there was little effect of the negative charge on rejection since the rejection values of the anionic dyes are lower and lie on a steeper curve (orange line in **Figure 2.12c**) than the cationic dyes. For example, the rejection of monocationic **MB** is 77%, much higher than for monoanionic **F**, although the molecular weights of the ions are similar (284 vs 330 g·mol⁻¹). The neutral dye Riboflavin (**Rib**) and the zwitterionic dye Rhodamine B (**RhB**) follow the same tendency.

(a)

Methylene blue
(MB)

Crystal violet
(CV)

Dimethyl bipyridine
(DMBp)

Alcian blue
(AB)

Fluorescein
(F)

Orange G
(OG)

Pyranine
(Pyr)

Phtalocyanine tetrasulfonate
(PhtCy)

Rhodamine B
(RhB)

Riboflavin
(Rib)

(b)

(c)
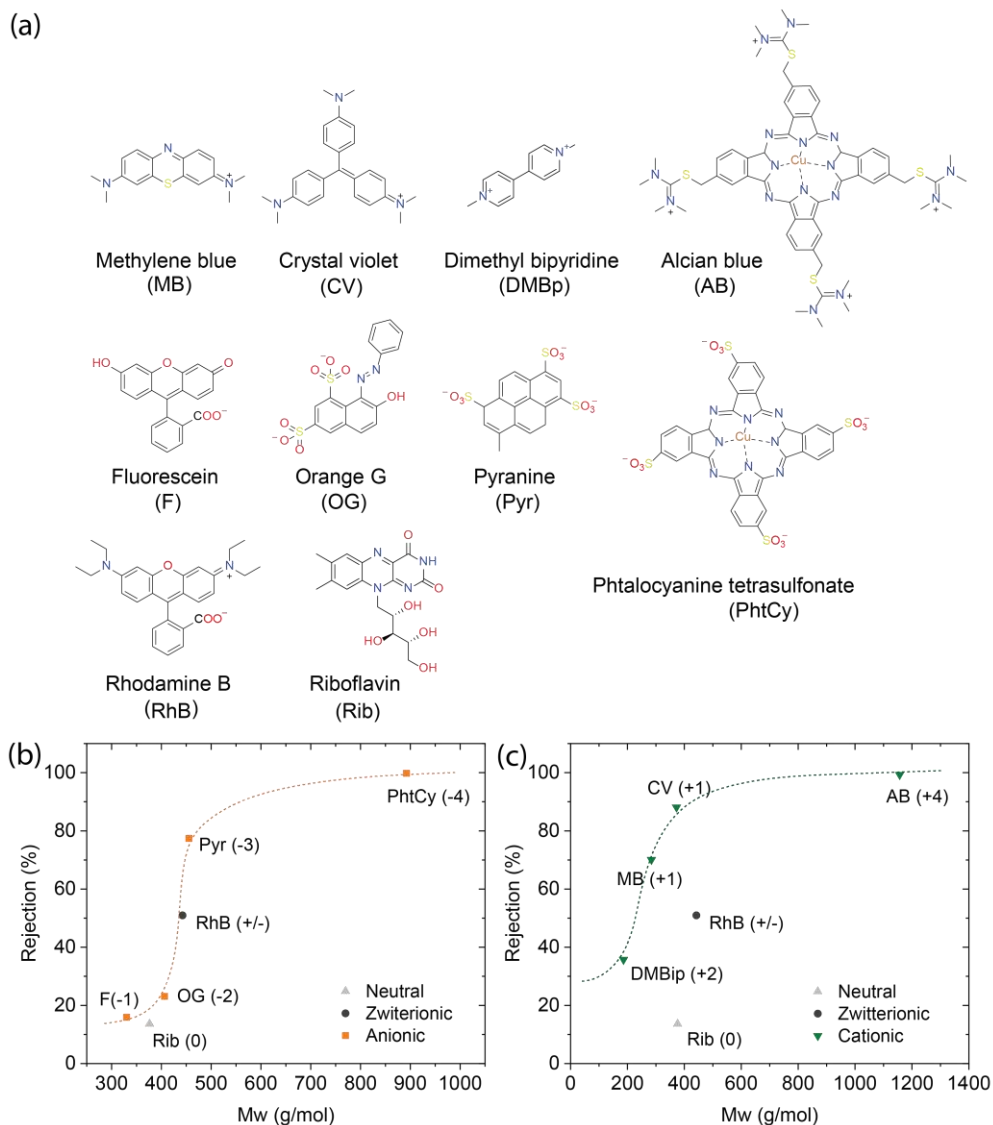
Figure 2.12 | a) Molecular structures of the different dyes used; b) plot with rejection values vs molecular weight for anionic dyes and c) for cationic.

Therefore, it is proposed that the higher rejection of cationic dyes is caused by their absorption in the pores *via* electrostatic interaction with the sulfonate groups. The absorption of the molecules inside the pores leads to a smaller effective pore diameter, as has been previously shown for absorption of counterions at the pore wall of lyotropic LC membranes.[35] This hypothesis is supported by several observations: The large dye **AB** (Mw = 1157 g·mol^{-1}) was totally rejected and partially adsorbed at the

surface, which could be observed with the coloration of the surface of the membrane. During the filtration of a smaller mono cationic dye **CV,** the rejection increased from an initial value of 60% to 80% at the steady-state. The strong coloration of the whole membrane after the filtration process and the low concentration of dye in the retentate solution confirmed the absorption of the dye within the membrane. Thus, on the filtration of a cationic dye with a molecular size similar to or smaller than the pore size, absorption occurs, increasing the rejection of the dye upon time. The observed behaviour was studied in more detail by checking the influence of the presence of cationic dyes on the rejection of other molecules using a feed mixture containing the cationic dye **MB** and the neutral solute PEG 3000 or **Rib**. **Table 2.5** gives the rejection and flux values at the steady-state of the solutes. Comparing data with and without **MB**, a lower flux it is observed for the mixture and a higher rejection, more remarkably for PEG 3000 (from 50% to 75%), which confirms there is an influence of cationic dyes in the retention of, in this case neutral molecules, when they are together in a mixture.

The reason might be related to the proposed slowdown process inside the pores of the membrane when cationic solutes are filtered due to the charge interactions which "decreases the apparent pore size". We attribute these results to the molecular size: **Rib** is not big enough to be affected while PEG 3000 is in the steeper part of the MWCO curve for PEG rejection.

Table 2.5 | Rejection and flux values at steady state for the filtration of neutral solutes PEG 3000 and **Rib** in the presence and without cationic **MB**.

	Without MB		With MB	
	Rib	*PEG 3000*	*Rib*	*PEG 3000*
Permeability **(L·m^{-2}·h^{-1}·bar^{-1})**	2.0	1.9	0.7	0.7
Rejection (%)	17.4	50.1	21.6	74.6

In conclusion, the presented **Sulfac$_3$TB** membrane is size-selective and rejects cations more strongly than anions of similar size due to absorption within the pores *via* electrostatic interactions with SO$_3^-$ groups. The membrane presents an average MWCO between 400 and 700 g·mol^{-1} for charged solutes and total rejection for both charges is reached for molecules with a diameter larger than 1.4 nm, in excellent agreement with the estimated pore size of 1.3 nm.

2.4 Conclusions

In this Chapter, we presented the application of a template-pore strategy to develop a new isoporous NF membrane for water purification consisting of a supramolecular

columnar LC selective layer on top of a porous PES support. The retention of the columnar hexagonal structure after its fixation by photo-polymerization permitted the removal of the template molecule leading to the formation of controlled-sized nanometer pores with sulfonate functionalities.

The thin LC film was successfully attached on top of the porous PES support. The absence of defects was checked with the nearly complete (>99%) rejection of globular proteins suggesting the good quality of the membrane. This resulted in membranes with a nearly full rejection of large solutes and permeability values similar to those reported for commercial and literature NF membranes. The columnar organization of pores with a homogenous size gave steep size-dependent retention for the filtration of PEG with a MWCO of 5000 $g \cdot mol^{-1}$ corresponding to a hydrodynamic radius of 1.7 nm. In addition, the presence of SO_3^- functionalities created a charge selectivity on the rejection process besides the size sieving effect, lowering the MWCO to around 1000 $g \cdot mol^{-1}$ for charged solutes. Moreover, the charges played an important role: rejection is higher for cationic dyes than anionic ones with the same molecular size due to a decrease of the effective pore size created by the absorption of the first ones in the membrane. This is a result of the interaction of positive charges with the anionic sulfonate groups at the pore walls.

In this Chapter, a new approach to obtain a polymerized LC-supported membrane for the selective removal of small organic molecules from water is provided. The template-pore strategy permits the creation of well-organized porous columnar structures with controlled size. The presence of charged functionalities within the pores introduces specific interactions that modulate the selectivity on the filtration of charged and uncharged solutes.

2.5 Experimental section

2.5.1. Materials and methods

All the reagents and solvents for synthesis were purchased from Sigma-Aldrich or TCI America. The ultrafiltration PES support, PES UF (30 kDa MWCO) was purchased from Sartorius Stedim Biotech, monodispersed PEG with a polydispersity of ~ 1.05 was purchased from Agilent. Ultrapure water was used for all filtration experiments.

NMR spectra were recorded at room temperature on a Bruker FT-NMR spectrometer AVANCE III HD-NanoBay (400 MHz, Bruker UltraShield magnet, BBFO Probehead, BOSS1 shim assembly) in $CDCl_3$. Chemical shifts are given in ppm with respect to tetramethylsilane (TMS, 0 ppm). MALDI-TOF-MS analysis was performed on a Bruker speed autoflex operated in reflectron mode with a positive voltage polarity, 500 shots. ATR FT-IR spectra were recorded at room temperature on a PerkinElmer Spectrum Two spectrometer equipped with a universal attenuated total reflectance (ATR) sampling accessory. Polarized Optical Microscopy (POM) was performed with a Jeneval

microscope equipped with crossed polarizers and a Linkam THMS 600 heating stage. Differential Scanning Calorimetry (DSC) measurements were performed in hermetic T-zero aluminium sample pans using a TA Instruments Q2000−1037 DSC instrument equipped with an RCS90 cooling accessory. Transition temperatures and enthalpies were typically determined from the first cooling and second heating run using Universal Analysis 2000 software (TA Instruments). X-ray scattering measurements were performed on a Ganesha lab instrument equipped with a Genix-Cu ultralow divergence source producing X-ray photons with a wavelength of 0.154 nm and a flux of $1 \cdot 10^8$ photons s^{-1}. Diffraction patterns were collected using a Pilatus 300 K silicon pixel detector with 487 × 619 pixels of 172 μm^2 in size, placed at a sample to detector distance of 91 mm (wide-angle, WAXS), or 500 mm (medium angle, MAXS). On the obtained diffraction patterns an azimuthal integration was performed using SAXSGUI software, to calculate the intensity against the scattering vector q, where q = (4π/ λ)sin ϑ (ϑ is the angle of incidence and λ is the wavelength). The beam center and the q-range were calibrated using silver behenate (d$_{(100)}$ = 1.076 nm; 5.839 nm) as a reference. The d$_{(300)}$ was used for calibration. The temperature was controlled with a Linkam HFSX350 heating stage and cooling unit. Measurements were performed on bulk samples sealed in 1.0 mm diameter glass capillaries, 0.01 mm wall thickness (Hilgenberg). UV-VIS experiments were performed on a Jasco V-750 spectrophotometer. All experiments were performed in 10 × 10 mm quartz cuvettes at 20 ^{0}C. Fluorescence experiments were measured using a Spark® Tecan 10M. Spectra were recorded using 100 of gain and 50% mirror at 20 ^{0}C. The photopolymerization was performed for 15 min with a mercury lamp (Omnicure s2000, emitting at 320−500 nm). The intensity was approximately 8 mW·cm^{-2} at the sample surface. HR-SEM was measured with Quanta 3D FEG (FEI/TFS) with EDT secondary detector. Samples were sputter-coated with a thin layer of gold using a Balzer Union SCD 040 sputter device. The conductivity of the feed and permeate solutions was measured with a C319 Consort conductivity meter.

2.5.2 Detailed experimental conditions

Film fabrication

Clean glass substrates (3 x 3 cm) were prepared by washing with acetone and isopropanol and finally dried. The nanoporous materials were made by making a solution containing **TB** (1 equivalent), **Sulfac** (3.2 equivalents), 1,10-decanedithiol as the cross-linker (1.5 dithiol molecule per molecule of **Sulfac** to have a ratio 1:1 of thiol:ene) in CHCl₃/MeOH (9:1 v/v) with a final concentration of (50 mg ml^{-1}). Finally, Bis(2,4,6-trimethylbenzoyl)-phenylphosphineoxide (Irgacure 819, 3 wt.%) was added as a photo-initiator. 100-200 μL of the solution was bar coated manually (gap of 100 μm) on the clean glass substrate at 70°C to evaporate the solvent of the mixture. The

sample was photo-polymerized using an EXFO Omnicure S2000 lamp with 8 mW·cm^{-2} of intensity, for 10 minutes, resulting in a yellow-transparent non-soluble self-standing polymer film. Lastly, after rinsing with pure water, the sample was dried in a vacuum oven at 40 °C.

TB removal

Complete removal of **TB** was checked with UV-Vis spectroscopy by measuring the amount of template in the solution. Two samples of film of 1 mg each were extracted 3 times in 2ml of both NaOH 1 M and DMSO. Absorption at 315 nm was measured with UV/Vis and converted into concentration with the calibration curves previously determined. Taking into account the volume of the cuvette (2 ml) and the molecular weight of TB the amount of TB in the film was calculated.

For NaOH:
$$\text{mg TB} = \frac{\text{Abs}}{0.05535} \text{ x 2 ml x 426,48}$$

For DMSO:
$$\text{mg TB} = \frac{\text{Abs}}{0.06023} \text{ x 2 ml x 426,48}$$

The amount of TB was calculated for 1mg of polymer:

$$\text{SulfAc x 3} + \text{TB} + 4.5 \text{ x dithiol} = 796.16 \text{ x } 3 + 426.48 + 206.41 = 3021.37$$
$$\% \text{ of TB in the polymer} = 426.48/3021.37 = 14.11 \%$$

Taking the observed amount of TB on each extraction the % of TB that has been removed was calculated as:

$$\% \text{ TB removed} = \frac{\text{TB each extraction}}{0.14} \text{ x 100}$$

Water filtration

Samples of the membrane were cut to the desired size and pre-cleaned with deionized water. For each filtration test, a membrane was placed in the cell which was filled with ultrapure water (total volume of 20 ml) and was pressurized with nitrogen at the desired pressure Samples that after 2h under a pressure of 5 bar showed a water flux of zero were considered defect free. After that, the membranes were shaken in 1M aqueous NaOH for 3 hours to remove the template and subsequently were rinsed with water. Permeate weight was measured *in triplo* increasing P from 1 to 5 bar. The permeate at each pressure was collected once a steady-state flux was reached and

was converted to volume to obtain the water flux (J [L·m^{-2}·h^{-1}]),[36] which was proportional to the pressure difference.

All measurements were performed using at least two different membranes to ensure reproducibility.

Salt rejection

2 g·L^{-1} aqueous solutions of NaCl and MgSO$_4$ were used for filtration tests in the Amicon cell set-up described above. 15 ml of feed solution was introduced in the cell and filtered through the membrane at 4 bar and samples were collected every 10 minutes from the beginning of the process. The conductivity of the feed and permeate solutions was measured with a C319 Consort conductivity meter. The concentration was determined from the calibration curve previously determined for both salts:

$$\sigma_{NaCl} = 1.945\,[C]$$
$$\sigma_{MgSO_4} = 0.759\,[C]$$

(where the salt concentration [C] is given in g·L^{-1} and conductivity σ in μS·cm^{-1})
Rejection (R) was calculated from the difference of feed (C$_F$) and permeate (C$_P$) concentrations:

$$R\,(\%) = \frac{C_F - C_P}{C_F}\,x\,100\,(\%)$$

Protein rejection

A solution of 1 g·L^{-1} of BSA was prepared in PBS buffer. 50 nM solution of GFP was prepared from 5 mM stock solution by dissolving 50 μL in PBS buffer to have a neutral pH (IP$_{BSA}$ = 4.7, IP$_{GFP}$ = 5.9). First pure water flux was filtered to clean the membrane and once a stable flux was reached, the cell was emptied and filled with 10 ml of the protein feed solution. Filtration was carried out at a pressure of 4 bar where 4 samples of 1 ml of permeate were collected from which the first one was discarded to avoid mixtures with residual water below the membrane in the cell. BSA samples were immediately measured with UV-Vis spectroscopy between 240 and 400 nm in a quartz microcuvette (peak absorption at 280 nm). For the GFP solutions, the fluorescence intensity of the emission at 510 nm was measured with excitation at 488 nm. Rejection of the solute was calculated from the UV intensity of the maxima (I) in UV absorbance for BSA and fluorescence intensity for GFP of the feed (F) and the permeate (P) solutions:

$$R\,(\%) = \frac{I_F - I_P}{I_F}\,x\,100\,(\%)$$

The flux in both processes was measured every 10 minutes for 2h to confirm the steady-state. Moreover, to check the recovery of the initial water flux, pure water was filtered after the filtration of BSA and flux was measured over time.

MWCO determination

The MWCO was determined by measuring the rejection of polyethylene glycol (PEG). Membranes were subjected to Polyethylene glycol (PEG) filtrations at 4 bar using the same Amicon cell. Aqueous solutions in ultrapure water were made containing 8 PEGs with a number of average molecular weights (M_n) ranging from 600 to 20000 g·mol^{-1} with a concentration of 0.5 g·L^{-1} for each polymer. 10 ml of 2 solutions of 4 different Mn PEG (from 600 to 4000 and from 4500 to 2×10^4 g·mol^{-1}) were filtered separately and 3 fractions of 1 ml of permeate solution were collected. The composition of the feed and the permeate solutions was analysed by size exclusion chromatography (SEC) in DMF. The collected fractions of 1 ml of each permeate sample were evaporated separately and dissolved in 1 ml of DMF. For each analysis, 10 µL of the sample was injected into the SEC, which ran at 10 ml·min^{-1}. The concentration of PEG was detected with a photodiode array detector (PDA). The corresponding calibration curve is applied to convert the rejection time to molecular weight. The average peaks obtained from each solution were normalized to the peak of PEG 600 g·mol^{-1}, which was shown to pass through the supported membrane without rejection (Hydrodynamic radius of the coil, R_h = 0.81 nm) in a single filtration experiment of this Mn PEG. The rejection (R) was calculated from the difference of the maximum intensity of the peaks of the feed (F) and permeate (P) as:

$$R\,(\%) = \frac{I_F - I_P}{I_F}\,x\,100\,(\%)$$

Dye-Size and charge selectivity

A series of different dyes with molecular weights between 186 and 1299 g·mol^{-1} were used for filtration tests. 50 µM aqueous solutions of the dyes were filtered separately at 4 bar of pressure in the Amicon setup. Once a steady-state was reached, samples of the permeate were collected *in triplo* to determine the average rejection. Samples were immediately measured in UV-Vis between 300 and 600 nm in a quartz microcuvette. Rejection (R) of the solute was determined by comparing the intensity (I) of the maxima of each dye in UV absorbance of the feed (F) and the permeate (P) solutions using equation 6. The filtration of a mixture containing Riboflavin and Methylene Blue was performed in the same way and the rejection of Riboflavin was calculated as described above.

2.5.3. Synthetic procedures

Methyl 3,4,5-tris(undec-10-en-1yloxy) benzoate (1)

To a stirred solution of methyl gallate (2.1 g; 11.5 mmol; 1 equiv.) in DMF was added K_2CO_3 (15.9 g; 115 mmol, 10 equiv.) and 11-bromo-undecene (8.85 g, 40 mmol, 3.3 equiv.). The suspension is heated to reflux at 100 °C overnight under Argon. When completed the solution is cooled down to ambient temperature, filtered and evaporated. The residue was extracted with EtAc/water, dried and filtered. After the removal of the solvent was further purified by flash column chromatography in SiO_2 with Heptane/EtAc, 7:3 to 1:1 obtaining compound **1** as a white solid, 78% yield. ^{1}H-NMR (CDCl₃, 400 MHz) δ 7.25 (s, 2H, 2x CH arom.), 5.81 (ddt, J = 16.9, 10.3, 6.6 Hz, 3H, 3x CH₂=CH-), 5.06 – 4.86 (dd, 6H, 3x CH₂=CH-), 4.01 (td, J = 6.5, 2.6 Hz, 6H, 3x CH₂-CH₂-O), 3.88 (s, 3H, CH₃O), 2.04 (dt, J = 7.0 Hz, 6H, -CH₂-CH₂=CH), 1.78 (dp, J = 22.0, 7.6, 7.2 Hz, 6H, 3x CH₂-CH₂-O), 1.55 – 1.12 (m, 43H, alkyl chain). ^{13}C-NMR (CDCl₃, 100 MHz) δ 166.93, 152.81, 142.35, 139.19, 124.66, 114.12, 114.11, 108.00, 73.46, 69.15, 52.11, 33.84, 33.82, 31.89, 30.33, 29.66, 29.57, 29.54, 29.46, 29.42, 29.37, 29.30, 29.20, 29.15, 28.98, 28.95, 26.07, 26.05, 25.81, 22.70.

3,4,5-tris(undec-10-en-1-yloxy) benzoic acid (2)

A solution of **1** (3 g, 1.56 mmol, 1 equiv.) in MeOH/H₂O 3:1 is treated with KOH (2.13 g, 37.91 g, 8.1 equiv.) and heated with reflux overnight. After completion, the mixture is cooled down and neutralized to pH 2 with HCl 3M and extracted with EtAc. The product is a white powder that is cleaned with water and filtered. Quantitative yield. ^{1}H-NMR (CDCl₃, 400 MHz) δ 7.31 (s, 2H, 2x CH arom.), 5.81 (ddt, J = 16.9, 10.2, 6.7 Hz, 3H, 3x CH₂=CH-), 5.06 – 4.87 (m, 6H, 3x CH₂=CH-), 4.03 (m, J = 6.8 Hz, 6H, 3x CH₂-CH₂-O), 2.12 – 1.97 (m, 6H, CH₂-CH₂=CH), 1.79 (dp, J = 22.3, 7.6, 7.1 Hz, 6H, 3x CH₂-CH₂-O), 1.58 – 1.22 (m, 42H, alkyl chain). ^{13}C-NMR (CDCl₃, 100 MHz) δ 170.01, 152.86, 143.10, 139.18, 123.37, 114.12, 108.54, 73.53, 69.19, 33.82, 30.33, 29.66, 29.56, 29.54, 29.46, 29.37, 29.28, 29.20, 29.15, 28.98, 28.95, 26.06, 26.04. FT-IR: 1686 cm^{-1} (C=O str.), 1641 cm^{-1} (C=C str.)

3,4,5-tris(undec-10-en-1-yloxy) benzoyl chloride (3)

Compound **2** (1 g, 1.6 mmol, 1equiv.) was reacted directly with SOCl₂ (3 ml) for 1h at room temperature. The excess of SOCl₂ was evaporated with membrane pump rotavapor for half an hour to give compound **3** quantitatively. ^{1}H-NMR (CDCl₃, 400 MHz): δ = 7.30 (s, 2H, 2 x CH arom.), 5.80 (ddt, 3H, 3 x CH₂ = CH-CH₂), 5.01-4.92 (dd, 6H, 3 x CH₂ = CH), 4.02 (m, 6H, 3 x CH₂-CH₂-O), 2.05 (m, 6H, 3 x CH₂ = CH-CH₂), 1.78 (m, 6H, 3 x CH₂-CH₂-O), 1.31 (m, 36H, 18 x CH₂- CH₂-CH₂). ^{13}C-NMR (CDCl₃, 100 MHz) δ 167.72, 152.86, 144.75, 127.28, 114.14, 73.72, 69.36, 67.65, 33.83, 33.81, 30.32,

29.63, 29.55, 29.52, 29.49, 29.44, 29.34, 29.19, 29.14, 29.05, 28.97, 28.94, 28.71, 26.03, 25.97, 25.56, -5.97. FT-IR: 1750 cm^{-1} (C=O str.), 693 cm^{-1} (C-Cl str.)

4-(N-methyl-3,4,5-tris(undec-10-en-1-yloxy) benzamido) benzenesulfonic acid (Sulfac)

Compound **3** (1.4056 g, 2.30 mmol, 1 equiv.) was dissolved in 3 ml of DCM at 0 °C. Then 4-(methylamino) benzenesulfonic acid (0.500 g, 2.68 mmol, 1.2 equiv.) and triethylamine (0.45 g, 4.46 mmol, 2 equiv.) were dissolved in another round bottom flask in DCM (2 ml). The amine solution was slowly added to the solution with compound **3**. The solution was left stirring overnight at room temperature. After completion of the reaction, the solvent was evaporated. The residue was dissolved in water and extracted with chloroform, dried with MgSO$_4$ and filtered. The solvent was evaporated and compound **4** was obtained as a white crystal with 67% yield. Further purification was performed by an ion exchange resin to get the sulfonic acid. The residue was dissolved in ethanol and charged through the ion exchange resin (Amberlite IR-120 hydrogen form). The solvent was evaporated, and product was dried in vacuum oven at 120 ^{0}C to obtain **Sulfac** as a brown waxy material in quantitative yield.^{1}H-NMR (CDCl$_3$, 400 MHz) δ 7.78 (d, J = 7.3 Hz, 2H, 3,5-benzene-H), 7.18 (d, J = 7.5 Hz, 2H, 2,6-benzene-H), 6.56 (s, 2H 2,6-benzene-H), 5.80 (ddt, J = 16.9, 10.3, 6.6 Hz, 3H, 3x CH$_2$=CH-), 5.04 – 4.88 (m, 6H, 3x CH$_2$=CH-), 3.92 (t, J = 6.7 Hz, 2H, 1x CH$_2$-CH$_2$-O), 3.79 (t, J = 6.3 Hz, 4H, 2x CH$_2$-CH$_2$-O), 3.44 (s, 3H, -NCH$_3$), 2.03 (q, J = 7.1 Hz, 6H, 3x -CH$_2$-CH$_2$=CH), 1.69 (tq, J = 14.8, 9.2, 7.8 Hz, 6H, 3x -CH$_2$-CH$_2$-O), 1.51 – 1.20 (m, 46H, alkyl chain). ^{13}C-NMR (CDCl$_3$, 100 MHz) δ 170.53, 152.44, 146.54, 143.04, 139.46, 139.20, 130.08, 127.11, 126.15, 114.11, 114.09, 107.64, 73.34, 68.97, 38.59, 33.83, 30.29, 29.67, 29.59, 29.56, 29.53, 29.48, 29.41, 29.36, 29.28, 29.20, 29.17, 28.98, 28.96, 26.06, 26.03. FT-IR: 1642 cm^{-1} (C=O str., secondary amide), 1377 cm^{-1} (S=O str.) Maldi-ToF MS: m/z calculated for C$_{40}$H$_{66}$O$_5$ (M^{-1})$^+$: 794,51 found: 794,52.

2.6 References

[1]   D. L. Gin, W. Gu, B. A. Pindzola, W. J. Zhou, *Acc. Chem. Res.* **2001**, *34*, 973.

[2]   M. Zhou, T. J. Kidd, R. D. Noble, D. L. Gin, *Adv. Mater.* **2005**, *17*, 1850.

[3]   M. Henmi, K. Nakatsuji, T. Ichikawa, H. Tomioka, T. Sakamoto, M. Yoshio, T. Kato, *Adv. Mater.* **2012**, *24*, 2238.

[4]   N. Marets, D. Kuo, J. R. Torrey, T. Sakamoto, M. Henmi, H. Katayama, T. Kato, *Adv. Healthc. Mater.* **2017**, *6*.

[5]   T. Sakamoto, T. Ogawa, H. Nada, K. Nakatsuji, M. Mitani, B. Soberats, K. Kawata, M. Yoshio, H. Tomioka, T. Sasaki, M. Kimura, M. Henmi, T. Kato, *Adv. Sci.* **2018**, *5*, 1.

[6]   K. Hamaguchi, D. Kuo, M. Liu, T. Sakamoto, M. Yoshio, H. Katayama, T. Kato, *ACS Macro Lett.* **2018**, 24.

[7]   M. Gupta, Y. Suzuki, T. Sakamoto, M. Yoshio, S. Torii, H. Katayama, T. Kato, *ACS Macro Lett.* **2019**, *8*, 1303.

[8]   D. Kuo, M. Liu, K. R. S. Kumar, K. Hamaguchi, K. P. Gan, T. Sakamoto, T. Ogawa, R. Kato, N. Miyamoto, H. Nada, M. Kimura, M. Henmi, H. Katayama, T. Kato, *Small* **2020**, *16*, 2001721.

[9]   S. J. A. Houben, S. A. van Merwijk, B. J. H. Langers, B. M. Oosterlaken, Z. Borneman, A. P. H. J. Schenning, *ACS Appl. Mater. Interfaces* **2021**, *13*, 7592.

[10]   W. H. de J. Ger Vertogen, *Thermotropic Liquid Crystals, Fundamentals*, 1st ed., Springer Berlin Heidelberg, **1988**.

[11]   H. K. Lee, H. Lee, Y. H. Ko, Y. J. Chang, N. K. Oh, W. C. Zin, O. Kim, *Angew. Chemie - Int. Ed.* **2001**, *40*, 2669.

[12]   A. Kraft, A. Reichert, R. Kleppinger, *Chem. Commun.* **2000**, *12*, 1015.

[13]   J.-F. Xiong, S.-H. Luo, J.-P. Huo, J.-Y. Liu, S.-X. Chen, Z.-Y. Wang, *J. Org. Chem.* **2014**, *79*, 8366.

[14]   R. G. and T. Beatriz Feringán, Pilar Romero,Jose Luis Serrano, *Chem. - A Eur. J.* **2015**, *21*, 8859.

[15]   A. Concellón, A. P. H. J. Schenning, P. Romero, M. Marcos, J. L. Serrano, *Macromolecules* **2018**, *51*, 2349.

[16]   J. A. M. Lugger, D. J. Mulder, S. Bhattacharjee, R. P. Sijbesma, *ACS Nano* **2018**, *12*, 6714.

[17]   G. M. Bögels, J. A. M. Lugger, O. J. G. M. Goor, R. P. Sijbesma, *Adv. Funct. Mater.* **2016**, *26*, 8023.

[18]   S. Bhattacharjee, J. A. M. Lugger, R. P. Sijbesma, *Chem. Commun.* **2018**, *54*, 9521.

[19]   X. Feng, K. Kawabata, G. Kaufman, M. Elimelech, C. O. Osuji, *ACS Nano* **2017**, *11*, 3911.

[20]   O. Q. Imran, N. K. Kim, L. N. Bodkin, G. E. Dwulet, X. Feng, K. Kawabata, M. Elimelech, D. L. Gin, C. O. Osuji, *Adv. Mater. Interfaces* **2021**, *8*, 1.

[21]   K. A. Mauritz, R. B. Moore, *Chem. Rev.* **2004**, *104*, 4535.

[22]   K. Takakura, Y. Ono, K. Suetsugu, M. Hara, S. Nagano, T. Abe, Y. Nagao, *Polym. J.* **2019**, *51*, 31.

[23]   J. A. M. Lugger, R. P. Sijbesma, *ChemistryOpen* **2016**, *5*, 580.

[24]   S. J. Cowling, *Handbook of Liquid crystals, Vol. 1, Part III*, Wiley-VCH, **2014**.

[25]   I. Gracia, P. Romero, J. L. Serrano, J. Barberá, A. Omenat, *J. Mater. Chem. C* **2017**, *5*, 2033.

[26]   R. Vendamme, S. Y. Onoue, A. Nakao, T. Kunitake, *Nat. Mater.* **2006**, *5*, 494.

[27]   D. B. Hall, P. Underhill, J. M. Torkelson, *Polym. Eng. Sci.* **1998**, *38*, 2039.

[28]   Tu. Equipment & Prototype Center, *"Amicon type" stirred cell*.

[29]   R. E. Kesting, *Synthetic polymeric membranes, Chapter 4*, Mc-Graw Hill, **1971**.

[30]   D. Reurink, Enhanced Polyelectrolyte Multilayers for Highly Selective Membranes: From Densification to Aquaporin Water Channels, Twente University, **2020**.

[31]   H. P. Erickson, *Biol. Proced. Online* **2009**, *11*, 32.

[32]   X. Dong, A. Al-Jumaily, I. C. Escobar, *Membranes (Basel).* **2018**, *8*, 23.

[33]   P. Demchick, A. L. Koch, *J. Bacteriol.* **1996**, *178*, 768.

[34]   Y. Marcus, *Biophys. Chem.* **1994**, *51*, 111.

[35]   S. M. Dischinger, M. J. McGrath, K. R. Bourland, R. D. Noble, D. L. Gin, *J. Memb. Sci.* **2017**, *529*, 72.

[36]   M. Mulder, *Basic Principles of Membrane Technology*, Vol. 2, Kluwer Academic, **1996**.

Chapter 3

Pore functionalization in CLC-based nanoporous membranes for water filtration
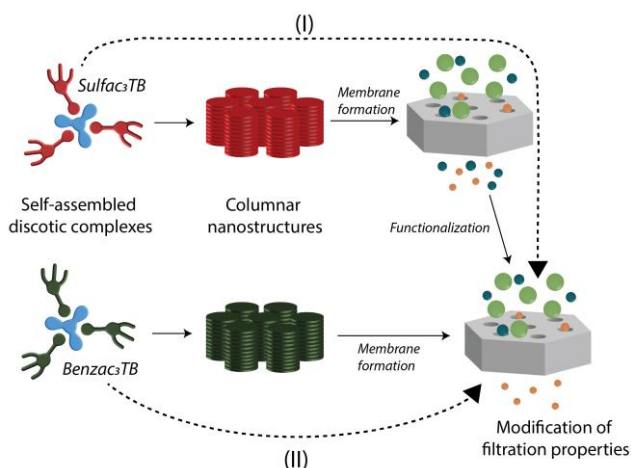
Abstract | Filtration membranes based on self-assembled structures, especially liquid crystal networks, offer the possibility to introduce chemical functionality into the pores. Because pore properties determine the filtration behavior, their modification expands the scope of molecular separation. In this Chapter, two different approaches to modify chemical functionalities at the pore walls in **Sulfac₃TB** membrane from Chapter 2, are reported. First, the synthesis and characterization of the supramolecular complex **Benzac₃TB**, a carboxylic acid analog of **Sulfac₃TB**, is described. The filtration properties of **Benzac₃TB** membrane show lower permeability and higher rejection of neutral and charged solutes due to a smaller pore size than **Sulfac₃TB** membrane. Additionally, there is also an influence of the increased binding strength with ionic species due to the weaker ion pairing of carboxylates than sulfonates. The second part reports the derivatization of the sulfonate groups of **Sulfac₃TB** membranes into sulfonamides. The functionalization with 3 differently substituted amines gave membranes with reduced pore size. Despite the incomplete conversion of sulfonate groups, the rejection of charged and neutral solutes changed considerably. Chemical derivatization is shown to be a versatile way to modify the filtration properties of membranes for the molecular separation of solutes from water.

3.1 Influence of ionic functionalities within the pores: SO_3^- vs COO^-

Over the last years, molecular sieving membranes have become a potential solution to face growing issues of water contamination.[1],[2] Especially, the increasing amount of toxic trace organic pollutants is seriously threatening access to clean water. Due to the trade-off between selectivity and permeability of existing membranes, new materials are explored to get highly selective membranes with improved permeation performance.[3],[4] The development of membranes by molecular design is a powerful tool to control pore size and chemical functionalities at the pore wall, both having a decisive role in the selectivity of the filtration process. Polymerized liquid crystals have attracted attention as materials with satisfactory performance in membranes for desalination and removal of organic micropollutants from water.[5–8] In Chapter 2, self-assembled thermotropic liquid crystals with columnar morphologies were used to obtain stable nanoporous films after the removal of porogen templates, and their application as active layer in composite filtration membranes was demonstrated. It was additionally shown that the presence of sulfonate functionalities in the pores provides good permeability and absorption/rejection of charged molecules, which increases the retention compared to neutral solutes. The use of other functional groups can modify those interactions and therefore the rejection properties: e.g. carboxylic acids form stronger ion pairs than sulfonic acids,[9] represented by the equilibrium depicted in **Scheme 3.1**.[10]

$$\textbf{Dissociated} \qquad\qquad \textbf{Associated}$$

$$COO^- + X^+ \; \underset{\longleftarrow}{\longrightarrow} \; COOM$$

$$SO_3^- + X^+ \; \overset{\longrightarrow}{\longleftarrow} \; SO_3M$$
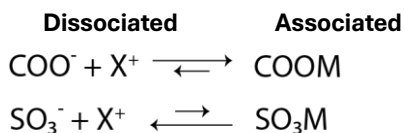
Scheme 3.1 | Ion pairing equilibrium of carboxylate and sulfonate salts.

Previous studies of absorption properties in porous films based on liquid crystalline systems with COO^- functionalities have shown strong binding of small metal cations (Li^+ and Na^+) or organic cationic dyes.[11],[12] The uptake of cations in the membrane is the result of ion-pairing. On the other hand, ion exchange membranes containing SO_3^- groups are used for to their capability to exchange cations easily because of weak ion pairing.[13][14][15] As a consequence, the binding strength with cationic solutes is lower than for carboxylates. Applied to filtration processes, the interaction with ions or other charged solutes will differ using either sulfonate or carboxylate, producing different rejection/transport properties. For instance, when association with ions increases, the permeance of the membrane may be reduced.

To study the influence of acid functionalities on the permeability, ion transport and retention of the membranes, the performance of **Benzac₃TB** membrane is compared to the analogous **Sulfac₃TB** membrane (**Figure 3.1**). To this end, a supramolecular columnar liquid crystal **Benzac₃TB** with carboxylate functionalities was first synthesized and characterized. The formation of the new nanoporous system from the self-assembly of the complex was studied as well.
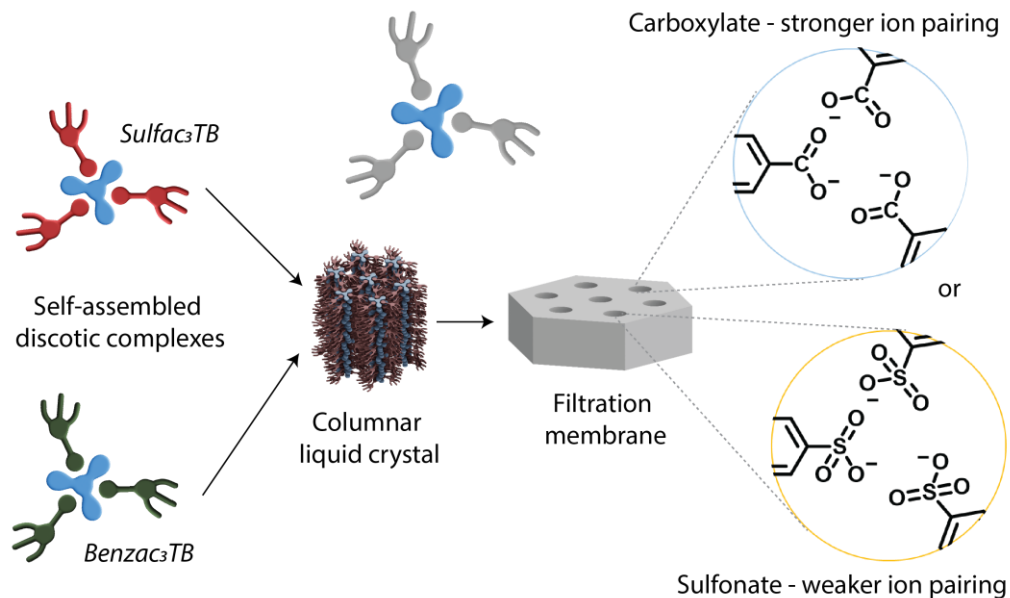
Figure 3.1 | Schematic representation of the formation of a membrane based on a columnar liquid crystal consisting of a discotic supramolecular complex containing either COO⁻ or SO₃⁻ functionalities.

3.1.1 Synthesis and characterization of the 3:1 supramolecular complex Benzac₃TB

For the formation of the **Benzac₃TB** supramolecular complex, **TB** was also used as template molecule and **Benzac** monomer was synthesized as depicted in **Scheme 3.2**.
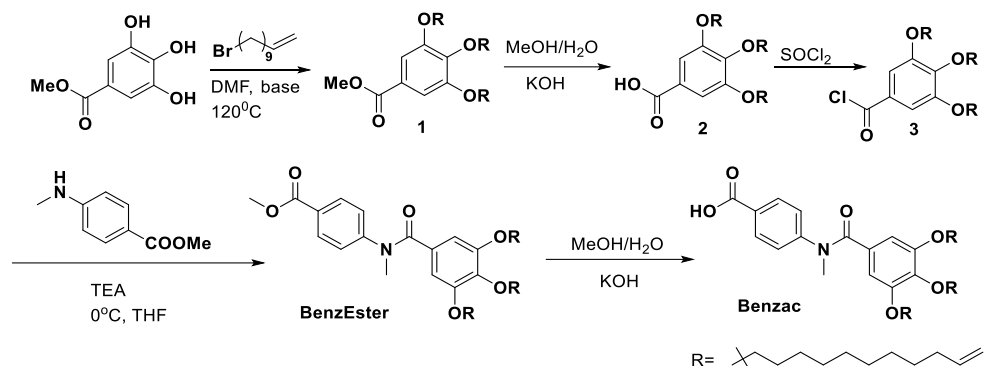
Scheme 3.2: | 5-step synthetic route for **Benzac**.

Alkylation of the three phenolic groups of methyl gallate with 11-bromo-1-undecene followed by deprotection of the carboxylic acid yielded compound **2**. Acid chloride **3**, obtained quantitatively by treatment of **2** with thionyl chloride, was coupled with N-methyl benzoate in THF with trimethylamine as a base, to give **BenzEster**. Finally, the deprotection of the ester with KOH in a mixture of MeOH and water gave the desired compound **Benzac**, after acidification of the reaction mixture with aqueous HCl and precipitation in water. The thermal and liquid crystalline properties were studied using Polarized Optical Microscopy (POM) and Differential Scanning Calorimetry (DSC). Under the POM, the material showed a typical texture for columnar mesophases after heating and cooling to room temperature (**Figure 3.2a**). Although in the heating cycle of the DSC traces more than one mesophase was observed in addition to a recrystallization peak below 0 ^{0}C (**Figure 3.2b**), a single mesophase was formed at room temperature during the cooling. This phase was confirmed to be hexagonal columnar with X-ray diffraction (**Figure 3.2c**). The pattern showed very narrow peaks even in the high-q region which revealed the nearly crystalline order of the molecules in the mesophase.
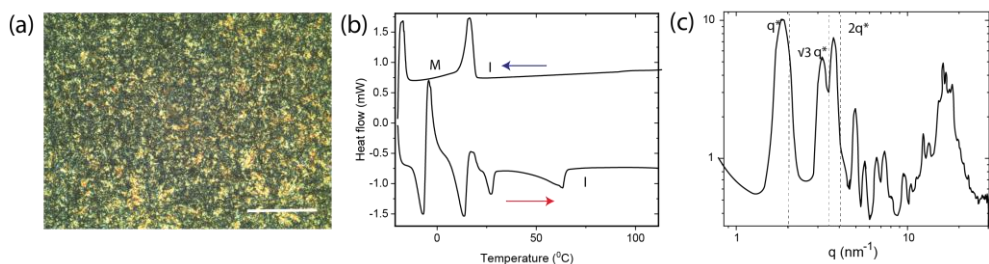
Figure 3.2 | a) POM picture of **Benzac** at RT. Scale bar 100 µm; b) 2nd cycle on DSC of **Benzac** at 5°C/min and c) WAXS pattern of **Benzac** at room temperature after annealing.

Benzac and TB were dissolved in a CHCl₃:MeOH (9:1) mixture as described for **Sulfac₃TB** in Chapter 2 to afford the supramolecular complex **Benzac₃TB** via H-bonding. FT-IR showed a new band at 3264 cm⁻¹ from the vibration of the N-H⁺ bond and a shift of the C=O bond to higher wavenumber (from 1675 to 1690 cm⁻¹), which confirmed the H-bond formation (**Figure 3.3a**).[11]

The thermal and liquid crystal properties of the complex were further investigated in the same way as for **Benzac**. Under the POM at room temperature after heating and cooling down, **Benzac₃TB** presented a typical texture of a randomly oriented columnar mesophase with small domains (**Figure 3.3b**). Upon cooling, DSC traces of **Benzac₃TB** showed a transition from isotropic to mesophase at 36 °C and crystallization at 18 °C (**Figure 3.3c**) which suggested that the molecule is liquid crystalline at room temperature. X-ray diffraction was performed at room temperature to determine the type of mesophase of **Benzac₃TB**. The diffraction pattern showed the ratio 1, √3, 2, √7,... as for **Sulfac₃TB,** which corresponds to a hexagonal columnar mesophase (**Figure 3.3d**). Hence, the discotic complex arranges in columns with a hexagonal packing with a calculated lattice parameter a = 4.07 nm from the first diffraction peak q_{100}, approximately 10% shorter than for **Sulfac₃TB** (a = 4.47 nm).
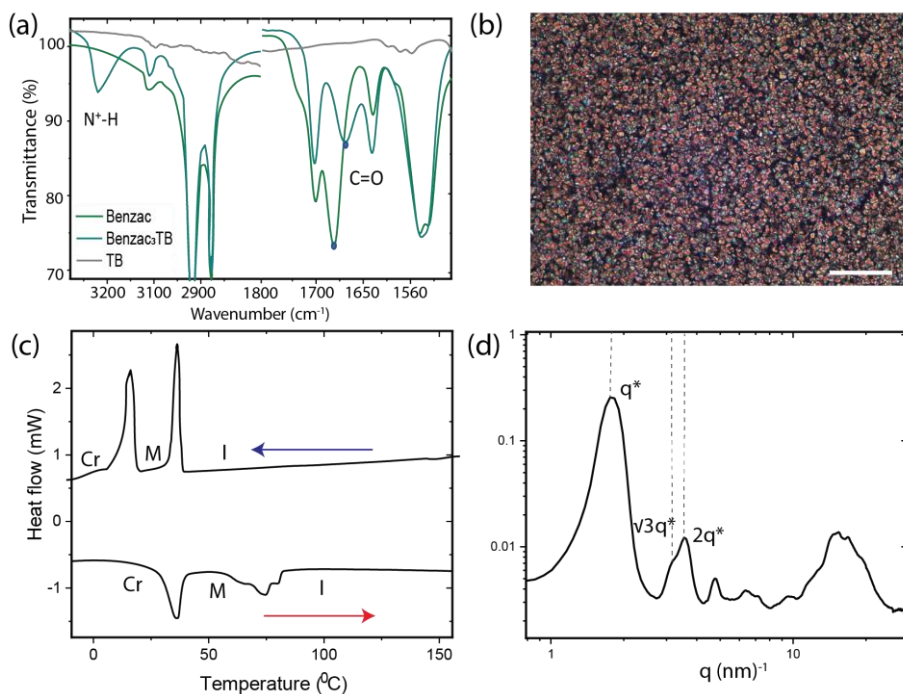
Figure 3.3 | a) FT-IR spectra comparing before and after complexation of **Benzac** with **TB**; b) POM at RT after cooling at 50 °C/min of **Benzac₃TB**. Scale bar 50 µm; c) DSC of the second cycle at 10 °C/min of the complex with heating cycle in red and cooling in blue and d) WAXS pattern of the complex at room temperature.

3.1.2 Crosslinking of Benzac₃TB

Benzac₃TB films were obtained by crosslinking using a photoinduced thiol-ene reaction. A mixture of **Benzac** (3.1 equiv.), **TB** (1 equiv.), 1,10-decanedithiol (4.6 equiv.) as a crosslinker and 2 wt.% of Irgacure 819 photo-initiator was drop-cast from THF, and the solvent was evaporated. Irradiation with UV light for 10 minutes resulted in transparent and flexible polymers films. Completion of the crosslinking reaction was confirmed by FT-IR spectroscopy (**Figure 3.4a**). After exposure to UV light for 10 minutes, the characteristic vibration band of the alkene double bonds at 908 cm^{-1} had disappeared. X-ray diffraction measurements at room temperature showed an increase of the lattice parameter from a = 4.07 to 5.58 nm due to the presence of the dithiol crosslinker. The columnar lattice is not well-defined after the crosslinking compared to the bulk sample (**Figure 3.4b**). The broad peaks hinder the identification of more diffraction peaks needed to assign the type of mesophase. The template molecule **TB** was quantitatively removed by extraction from the film by shaking in DMSO for 2 hours. Removal was confirmed with the disappearance of the N-H$^+$ band in the FT-IR spectrum. Moreover, a color change from yellow to blue of the film under 366 nm irradiation confirmed the removal of the fluorescent **TB** template (**Figure 3.4c**).[16]
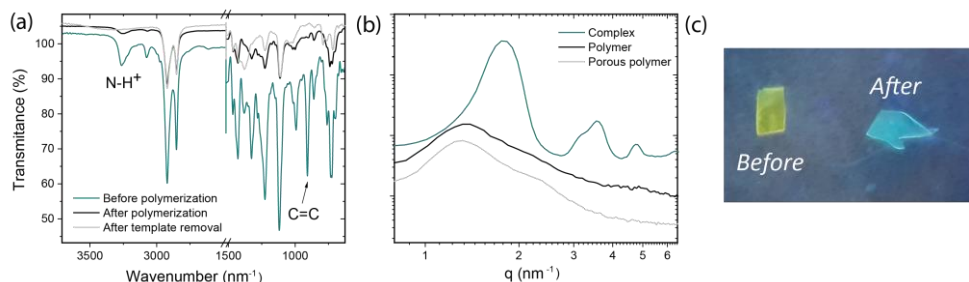
Figure 3.4 | a) FT-IR spectra comparing before and after crosslinking, which is confirmed by the disappearance of the C=C vibration peak; b) X-ray diffraction confirmed the decrease of the lattice distance in the columnar arrangement with the crosslinking but after template removal, mesophase conformation stays, with less order though and c) change of color from yellow to blue of the polymer film under 366 nm excitation that confirmed the removal of the template.

3.1.3 Membrane formation and characterization

Composite **Benzac₃TB** membranes were prepared as previously described for **Sulfac₃TB** membranes in Chapter 2, using polyethersulfone (PES) with molecular weight cut-off of 30 kDa as support. In order to be able to compare the filtration properties, membranes of both complexes **Sulfac₃TB** and **Benzac₃TB** were prepared under identical conditions (i.e. concentration and spin coating speed) to get similar

layer thicknesses. HR-SEM pictures in **Figure 3.5** show that the thickness of the active layer is lower than 500 nm, well attached to the support as a well-differentiated 2-layer-composite with no penetration of the mixture into the PES support.
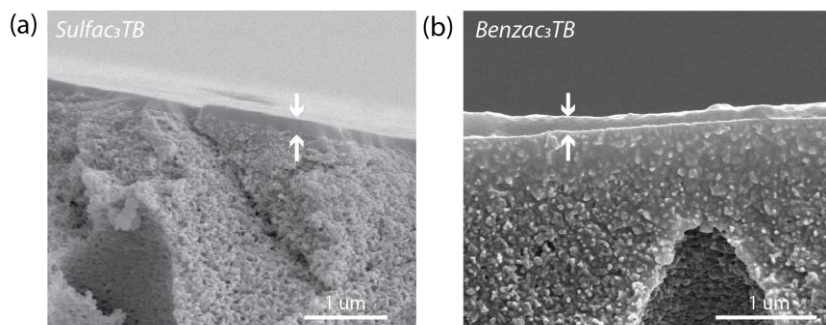
Figure 3.5 | Cross-section micrographs from HR-SEM measurements showing active layers of around 200 nm thickness for both **Sulfac₃TB** (a) and **Benzac₃TB** (b) membranes.

Water permeability and solute rejection

Water permeability measurements showed similar but slightly lower values for the **Benzac₃TB** membrane (2.14 L·m^{-2}·h^{-1}·bar^{-1}) than for the **Sulfac₃TB** membrane (2.36 L·m^{-2}·h^{-1}·bar^{-1}) as depicted in **Figure 3.6a**.

The rejection curves of different PEG with different molecular weights represented in **Figure 3.6b** showed a slightly lower MWCO value for **Benzac₃TB** membrane than for **Sulfac₃TB** membrane (4400 g·mol^{-1} and 4600 g·mol^{-1} respectively). This corresponds to hydrodynamic radii of 1.4 and 1.7 nm,[17] in line with the lower water flux previously obtained for the **Sulfac₃TB** membrane.
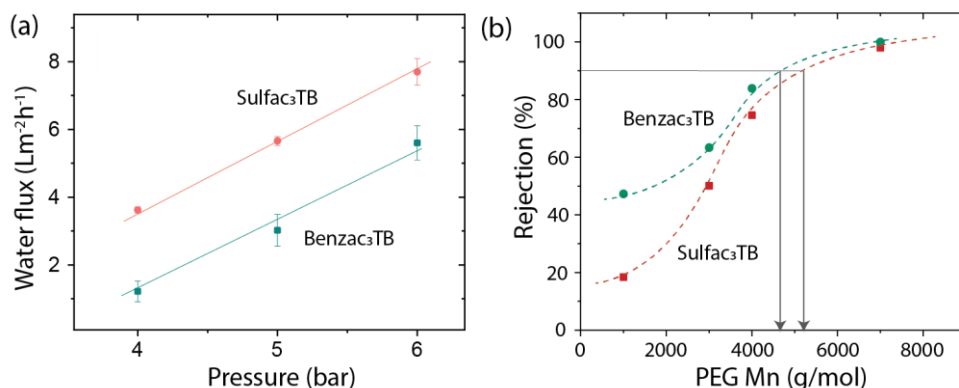
Figure 3.6 | a) Water flux versus applied pressure of both membranes: b) MWCO rejection curve for the filtration of different M_n PEGs showing higher rejection for the **Benzac₃TB** membrane. Hydrodynamic radius equivalent to $R_h = 0.06127 \cdot M_n^{0.3931}$

Aqueous solutions of NaCl, MgSO$_4$ and CaCl$_2$ (1 g·L^{-1}) were filtered with both membranes to investigate the rejection and transport properties of ionic species. Even though rejection values of both membranes are low (<40%) compared to commercial membranes,[18] larger rejection values for **Benzac₃TB** membrane were measured, as shown in **Figure 3.7a**. This is mainly caused by the smaller pore size but also because of the salt absorption process that takes place due to the stronger ion pairing with COO$^-$ than with SO$_3^-$.[10] For both membranes, a trend of increasing rejection was observed: Na<Mg<Ca in line with ion-pairing strength and retention of these ions by ion-exchange resins.[13,19] In the pores of **Benzac₃TB** membrane, exchange is slower, increasing the rejection of the cations and decreasing the difference in rejection between them. The differences in cation rejection between the membranes are a result of differences in pore size and ion pair strength of the anionic pore wall functionalities.

Strong ion pairing with Ca^{2+} may significantly influence membrane transport, and the permeability values of both membranes for pure water, a 2M CaCl$_2$ aqueous solution and pure water after salt permeation are reported in **Figure 3.7b**. Water fluxes were measured after reaching a stable state (J$_w$). The solution of the salt was filtered afterward to get the permeate salt flux (J$_p$) and finally, water was filtered again to identify the recovery flux (J$_r$). Due to its smaller pore size, **Benzac₃TB** membrane gave lower water fluxes than **Sulfac₃TB** membrane. The quantitative relative flux reduction (FRF) and flux recovery ratio (FRR) was additionally compared for both membranes[20]:

$$RFR = 1 - J_P/J_W \times 100$$
$$FRR = J_R/J_W \times 100$$

While for the **Sulfac₃TB** membrane a flux reduction of 7% and a recovery of 98 % was obtained, the **Benzac₃TB** membrane showed values of 68% and 67% respectively. These results suggest strong association of Ca^{2+} ions to the carboxylate groups in the **Benzac₃TB** membrane. This causes a significant decrease in permeability whereas the effect of Ca^{2+} on the permeability of the **Sulfac₃TB** membrane is small and almost completely reversible due to the weaker ion pairing of this ion with the sulfonate groups.
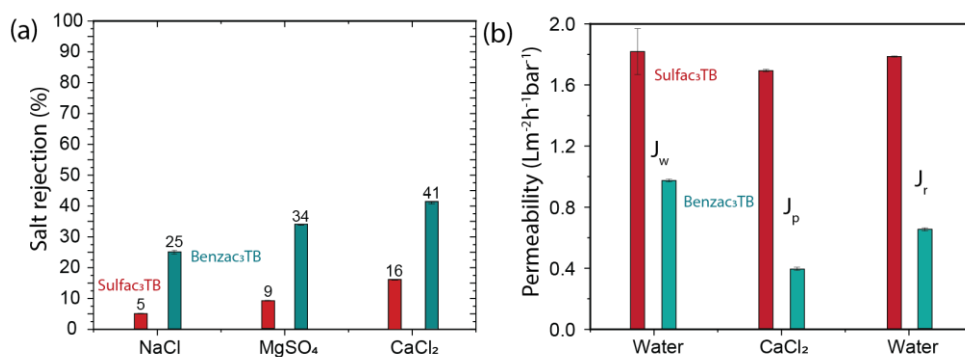
Figure 3.7 | a) Rejection of NaCl, MgSO$_4$ and CaCl$_2$ for both **Sulfac$_3$TB** and **Benzac$_3$TB** membranes; b) Average value of the permeability for the filtration of pure water followed by a 2M aqueous solution of CaCl$_2$ and water again.

Filtration of small neutral and charged molecules

The rejection of charged and neutral small organic molecules was determined in order to investigate the effect of the COO$^-$ and SO$_3^-$ anionic functionalities on the filtration properties of the membranes. Aqueous solutions (50 µM) of the following dyes were prepared to be filtered separately over both membranes: anionic fluorescein (**F**) and orange G (**OG**); cationic methylene blue (**MB**) and crystal violet (**CV**) and neutral riboflavin (**Rib**) (**Figure 3.8**). The rejection values obtained for the **Benzac$_3$TB** membrane in comparison with **Sulfac$_3$TB** membrane are listed in **Table 3.1**. In all cases, higher rejection values were obtained with the **Benzac$_3$TB** membrane. This is ascribed to differences in pore size as well as to ion exchange effects. The differences in rejection for larger dyes **OG**, **CV**, and neutral **Rib** indicate an important role for size. Also, the comparable rejection values for **F** and **Rib** indicates weak effect of ionic interactions with anionic solutes next to the values for **F** and **OG**, with a small difference that can be explain by size change.

With cationic solutes, a clear effect of ion pairing between the anionic pore wall functionalities and the dyes is found; both **Sulfac$_3$TB** and **Benzac$_3$TB** have a higher rejection of the cationic dyes **MB** and **F** than of the similar sized neutral **Rib.**
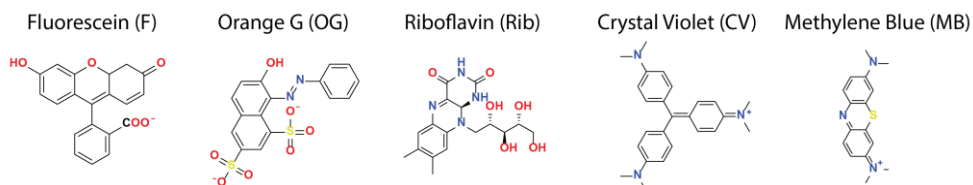
Figure 3.8 | Molecular structures of the dyes used for filtration experiments.

Table 3.1 | Rejection values and molecular information of neutral and ionic dyes, comparing both membranes.

Dye	Charge	Mw (g·mol^{-1})	Molecular dimensions (nm)	Rejection Sulfac$_3$TB (%)[*]	Rejection Benzac$_3$TB (%)
F	-1	330.27	1.03 x 0.92	16.9	36.5
OG	-2	406.38	1.26 x 1.07	23.1	51.1
Rib	0	376.36	1.35 x 1.04	17.4	41.6
CV	+1	372.45	1.23 x 0.97	88.1	99.9
MB	+1	284.4	1.31 x 0.58	69.1	85.0

[*]*Values from Chapter 2*

Lastly, the filtration of a solute with a molecular size similar to the pore was investigated for both membranes. With matching size and functionality, high selectivity values have been observed. As an example, it has been reported that a porous materials made with melamine as a template can selectively absorb this molecule after its removal from the network,[21] with good recyclability of the material for absorption processes. As a proof of principle, the filtration of an aqueous solution of **TB,** the template molecule used to form the complexes, was tested for both membranes (**Figure 3.9**). Pure water was first filtered measuring the flux to reach an initial J_{H2O}. The water was then replaced with a 100 µM solution of **TB** in H_2O:MeOH (9:1) and the flux was measured till it reached a stable value (J_{TB}). Finally, pure water was filtered again. The relative flux reduction (RFR) showed a higher value for the **Benzac$_3$TB** membrane than for the **Sulfac$_3$TB** membrane (93.9% and 33.3% respectively).

As both **Benzac$_3$TB** and **Sulfac$_3$TB** membranes were prepared with **TB** as template, the reduction of the flux in both membranes is explained by binding of this molecule with the sulfonate and carboxylate groups in their neutral form. Since sulfonates are weaker bases than carboxylates, formation of a complex with the template in the pores of is more favorable for **Benzac$_3$TB** membrane. The effect of template binding in each membrane is the blocking of the pores, which in the **Benzac$_3$TB** membrane, is strong enough to reduce the flux to nearly zero.
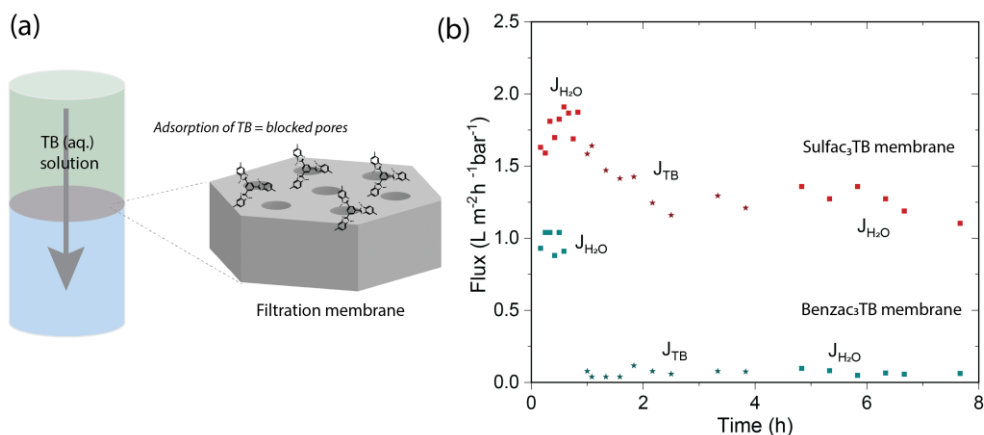
Figure 3.9 | a) Representation of the **TB** filtration process in the membrane and the blocking of the pores due to absorption; b) Plot of normalized flux (to 1 bar of applied pressure) vs time for the filtration of water, an aqueous solution of **TB** (1M) and the final recovery of water flux.

Concluding for this section, the preparation and characterization of **Benzac₃TB** complex was successfully performed. Thermal and structural characterization confirmed that the material exhibited a columnar hexagonal mesophase. A crosslinked network of the liquid crystal was efficiently applied on porous support to yield filtration membranes after the removal of the template molecule. Compared to the analogous **Sulfac₃TB** membrane the **Benzac₃TB** membrane has a lower permeability and higher rejection of all charged and neutral solutes due to a combination of a smaller pore size and stronger ion pairing of carboxylate groups to cations. This last feature results in strong binding with $CaCl_2$. The experiments establish that in membranes with a similar architecture, sulfonic acid functionalized pores provide better transport of aqueous solutions of cationic species, while the differences in rejection of neutral and anionic dyes can be ascribed to pore size differences between **Sulfac₃TB** and **Benzac₃TB** membranes.

3.2 Covalent modification of sulfonate groups to sulfonamides

The possibility to modify the chemical functionalities of the pores broadens the scope of membranes because of their high involvement in the rejection process of the organic components and pollutants in water.[22] As demonstrated in the previous **section 3.1**, fixed functionalities inherent to the molecular structure of the monomeric units in the liquid crystal determine the chemical environment of the pores of the membrane which directly influences the interactions of the solutes with the pore. However, tuning functionalities inside the pores of membranes remains a challenge.

In recent years, post-modification processes have emerged as useful strategies to change the chemistry on the interior of the pores in nanoporous materials *in situ*.[23]

Several efforts to tailor the functionalities in porous materials have been reported in literature. Covalent chemical modification of the functional groups can be used to change the size of the pore and its chemical properties such as hydrophobicity, or the strength of ionic interactions.[23,24] The versatility showed by this approach shows its potential for future use in specific applications. In a noncovalent approach the exchange of counterions in the interior of pores has been used to modify salt rejection in ionic membranes for water filtration.[6,25] Nevertheless, stability is not guaranteed in these types of systems, since exchange can spontaneously occur in aqueous solutions with higher ionic strength. This can be addressed by polymerization of the exchanged counterions to achieve stable but irreversible modification.[26]
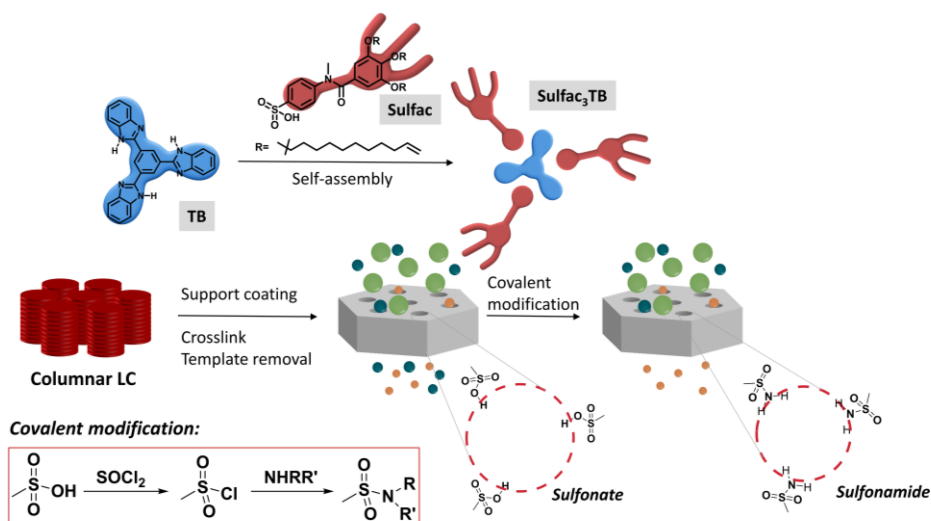
Figure 3.10 | Illustration of the membrane formation and functionalization. Supported membranes are based on a self-assembled discotic complex that yields porous columnar structures. The system is covalently modified by converting the sulfonic groups inside the pores into sulfonamides in a 2-step process.

In this regard, **Sulfac₃TB** membranes described in Chapter 2 can be modified chemically by post-modification of the sulfonic acid groups to sulfonamides. In the following sections, the formation of three modified membranes is reported, each with a different type of sulfonamide group that modifies the charge and size of the pores and therefore influences the filtration properties of the membrane (**Figure 3.10**).

3.2.1 Formation of crosslinked Sulfac$_3$TB films and modification

The modification of **Sulfac$_3$TB** membrane was first attempted in self-standing films and was later applied to supported membranes. Following the procedure of Chapter 2, nanoporous films were prepared via thiol-ene photoreaction. The conversion of the sulfonate groups attached to the pore walls of the films to sulfonamides was performed by a condensation reaction between the amine and the activated sulfonyl chloride derivative. As shown in **Figure 3.11a**, samples of the nanoporous films were first treated with thionyl chloride in DCM for 2h at room temperature, turning brown (Step 1). After drying at 50 ^{0}C in the oven, they were subsequently treated with diethylamine (DEA) in THF overnight (Step 2). After rinsing with deionized water and drying, brown/orange films were obtained. Conversion to sulfonamide was followed with FT-IR as depicted in **Figure 3.11b**. A shift of the S=O stretching vibration band to higher wavenumber values after the activation with SOCl$_2$ (from 1361 to 1382 cm^{-1}) was observed. The conversion to the sulfonamide group was confirmed with a shift back to a lower wavenumber of 1359 cm^{-1}.[27] Changes of morphology were studied with X-ray diffraction on films before and after functionalization. In **Figure 3.11c** the SAXS patterns of both the pristine porous polymer and the DEA-functionalized polymer are shown. For the pristine polymer, peaks with relative q values of 1, $\sqrt{3}$, 2, etc., were observed, corresponding to a columnar hexagonal lattice. After functionalization, the distance of the lattice parameter is smaller (higher q$_{100}$) and a columnar arrangement can no longer be established because the higher order reflections peaks at $\sqrt{3}$q* and 2q* have disappeared.
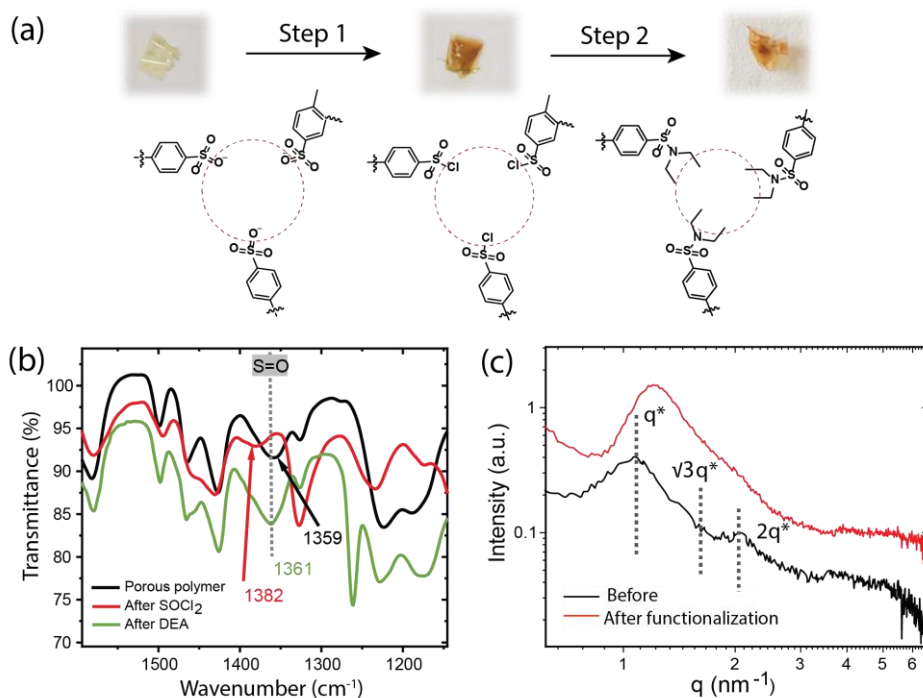
Figure 3.11 | a) 2-step synthetic route to convert sulfonates into sulfonamides consisting of: 1, chlorination of sulfonate groups with SOCl₂ in DCM and 2, amidation with DEA in THF; b) FT-IR comparison patterns before and after each step and c) SAXS pattern before and after functionalization.

The chemical conversion from sulfonate (negatively charged) to sulfonamide (neutral) creates a less polar environment inside the pores which could affect the absorption properties of the material. To study the polarity of the pore interior, absorption of a cationic and an anionic dye was followed with UV-Vis spectroscopy upon time. Samples of modified and unmodified porous films were first treated with HCl (1M) and subsequently were immersed for 20h in aqueous solutions of the anionic dye fluorescein (**F**) and the cationic crystal violet (**CV**) separately. **F** was not absorbed by the unmodified film (same color solution in scheme **Figure 3.12b**) unlike for the cationic **CV,** which was strongly absorbed, leading to a loss of all the purple color from the solution (**Figure 3.12a**) due to the absorption of the dye. For the DEA-functionalized films, a different behavior was observed: **F** was absorbed (loss of color showed in **Figure 3.12b**) while the absorption of **CV** decreased (slight loss of color in scheme **Figure 3.12a**). Additionally, the absorption intensity values obtained were converted into dye uptake (in mmol per sample). After 20 hours, as it is depicted in the plots of **Figure 3.12**, the uptake of **F** increases from 0 to 0.1 mmol dye/mmol film and

decreases for **CV** from 0.2 to 0.1. This means that a functionalization of half of the sulfonate groups into sulfonamides is reached. These results are explained by the presence of SO_3 groups in the unmodified films and the conversion into SO_2DEA groups after modification. For the first situation, the repulsion/absorption effect is very strong due to the negative charge of the sulfonate groups. In the second situation, different processes occur for each dye: cationic **CV** is less absorbed due to the decrease of sulfonate groups which also lowers the repulsion of anionic **F**. This, in addition to its small size, produces its absorption after modification of the film.

Therefore, with the results of FT-IR and UV vis absorption experiments, it was confirmed that the covalent modification of sulfonate groups influences the chemical environment of the pores.
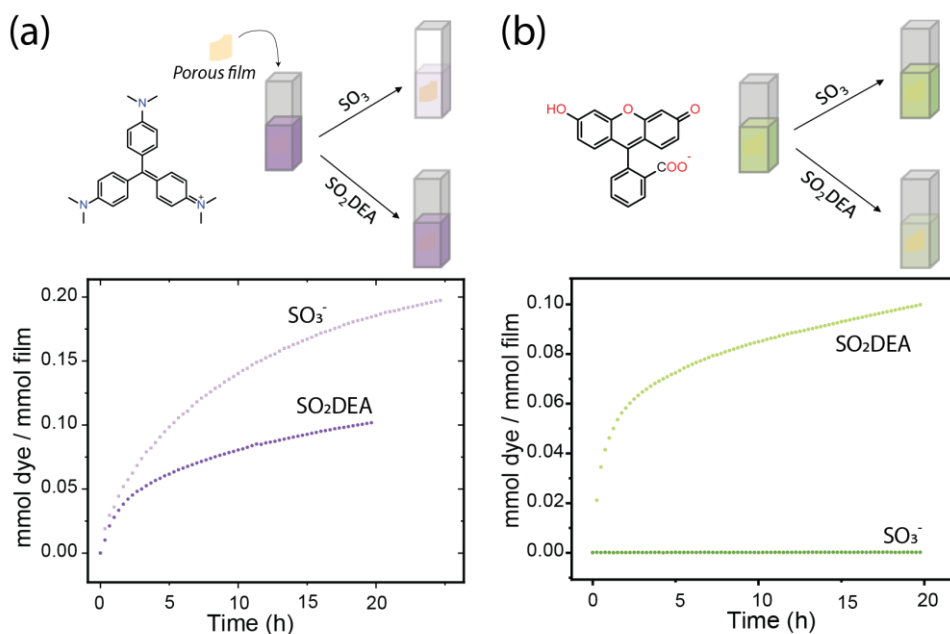
Figure 3.12 | UV-Vis plots of absorption process upon time of a) cationic dye **CV** and b) anionic **F** of self-standing film samples before and after functionalization with DEA. The solutions after 20 h showed more or less color depending on the absorption of the dye in the film.

3.2.2 Preparation and modification of PVDF supported Sulfac₃TB membranes

For the membranes presented in **section 3.1**, polyethersulfone (PES) was selected as a support due to its high hydrophilicity and good adhesion to the active layer. However, the chemical resistance of PES is low (it is not resistant to strong acidic/basic or chlorinated solvents). Therefore, hydrophilic modified polyvinylidene fluoride (PVDF) was used as support in membrane modification to sulfonamides. PVDF membranes are resistant to a large variety of chemicals and have good water permeability.[28,29]

Thin-film supported membranes were fabricated by directly spin-coating a solution of the liquid crystal complex, the photo-initiator and the crosslinker (see Chapter 2) on the surface of the commercial PVDF support that was mounted on a glass slide (**Figure 3.13a**). The sample was then photopolymerized to crosslink the liquid crystalline network by exposure to UV light. The cross-section of the obtained membrane was visualized with HR-SEM showing a dense layer with a thickness of around 400 nm attached to the support (**Figure 3.13b**).
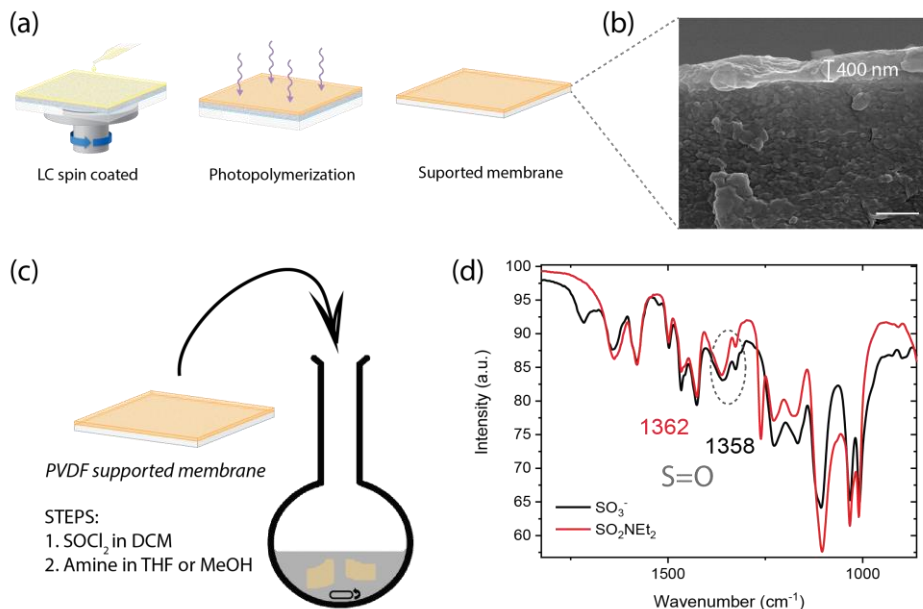
Figure 3.13 | a) Schematic representation of membrane fabrication by spin coating and photo-polymerization; b) HR-SEM cross-section image of the non-functionalized membrane. Scale bar 400 nm; c) Set-up for membrane modification in solution and d) FT-IR before and after complete functionalization with DEA.

Pristine samples of PVDF-supported membranes were functionalized following the same procedure as for the nanoporous films (**Figure 3.13c**). Once the template was removed by soaking the membranes in DMSO for 2h, the membrane was properly rinsed with deionized water and dried. The first reaction step for the functionalization was the reaction with thionyl chloride in DCM for 2h. After drying at 40 ^{0}C, the second step was carried out by stirring overnight in 10 ml of THF and 1 ml of diethylamine or isobutylamine. A third sample was prepared by reaction with ammonia in methanol.

3.2.3 Filtration properties of modified membranes

Water permeability

The filtration properties of the membranes were tested in a custom-made Amicon stirred dead-end filtration setup. Pure water flux of the different membranes was measured after reaching a stable flux at 4 bars for 1h. In **Table 3.2** the permeability values of the functionalized membranes are shown in comparison with the unmodified membrane (with SO_3^- groups). A big decrease in the water permeability occurs after coating the support (permeability of 60 $L \cdot m^{-2} \cdot h^{-1} \cdot bar^{-1}$) due to the presence of a dense layer which reduces the water flux. Furthermore, functionalized membranes exhibited lower permeability values, as a result of the possible reduction of the pore size caused by the presence of the sulfonamides inside. In fact, the membranes functionalized with di-substituted amides showed lower values of permeability suggesting smaller pore sizes with bulky amides.

Furthermore, the quality of the membranes was checked with the rejection of bovine serum albumin protein (BSA, 6 nm diameter) with a size much larger than the pores of the selective layers. The high rejection values above 96% for both the unmodified membrane and the functionalized membranes confirmed the presence of a nearly defect-free thin-film layer.

Table 3.2 | Comparison of permeability values and protein rejection for the unmodified and the 3 functionalized membranes with error within the samples tested:

Membrane	Permeability ($L \cdot m^{-2} \cdot h^{-1} \cdot bar^{-1}$)	BSA protein rejection (%)
SO_3^-	4.72	98.9 ± 0.57
SO_3NH_2	3.67	96.4 ± 0.79
SO_3DEA	2.62	98.1 ± 0.57
$SO_3isobutyl$	2.83	96.2 ± 0.03

MWCO determination

The MWCO of the membranes was estimated from the filtration of a series of PEGs with different M_n. By definition, the MWCO corresponds to the molecular weight at which 90% of the solute is rejected. The MWCO rejection curves obtained for the different functionalized membranes are shown in **Figure 3.14**. R_h values shown in **Table 3.3** were calculated from the relation of molecular weight with the hydrodynamic radius of a PEG coil. A decrease in pore size for all the functionalized sulfonamide

membranes compared with the unmodified membranes was observed. Bulkier amides gave a lower MWCO: the pore size for isobutylamide is the smallest due to the large size of the isobutyl group, while the primary sulfonamide formed by the addition of ammonia shows the biggest pore size among all the functionalized membranes.
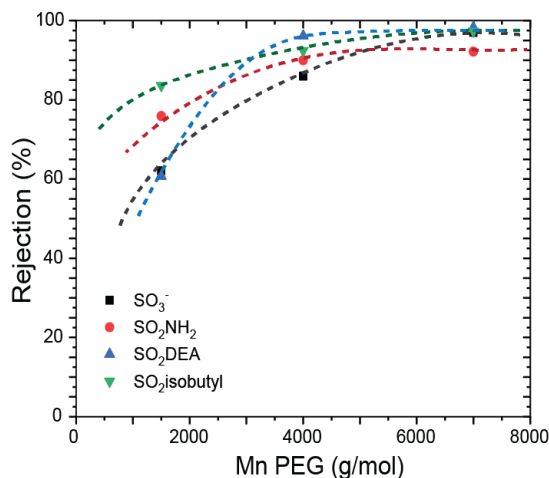
Figure 3.14 | MWCO curves of the sulfonate and the three sulfonamide membranes.

Table 3.3 | MWCO values (g·mol^{-1}) with the corresponding calculated hydrodynamic radius (nm) for the unmodified and functionalized membranes:

Membrane	MWCO (g·mol^{-1})	R_h (nm)*
SO_3^-	4.6×10^3	1.68
SO_2NH_2	3.8×10^3	1.56
SO_2DEA	3×10^3	1.42
$SO_2isobutyl$	2.8×10^3	1.38

$^*R_h = 0.06127 \times Mn^{0.3931}$

Charge and size selectivity

The rejection of charged and neutral small organic dyes was determined to investigate the effect of the functionality modification on the charge and pore size of the membranes. Aqueous solutions of charged and neutral dyes with similar molecular weights between 332 and 452 g·mol^{-1} were prepared separately with a concentration

of 50 μM (**Figure 3.8**). Anionic fluorescein (**F**) and orange G (**OG**), cationic crystal violet (**CV**) and neutral riboflavin (**Rib**) were selected.

In the free-standing films studied in **section 3.2.1**, approximately half of the SO_3 groups were converted to sulfonamide, and we use this value as an estimate for the conversion of the sulfonate groups in the supported membranes as well. The unreacted SO_3 groups can still interact with cationic dyes (absorption) and this will influence the transport properties. The rejection values obtained from the permeate solutions of each membrane are plotted in **Figure 3.15** and **Table 3.4**. The unmodified membrane shows low rejection of anionic **F**. Functionalized membranes showed a modest increase in rejection due to the small size of the dye relative to the pore size of the membranes.
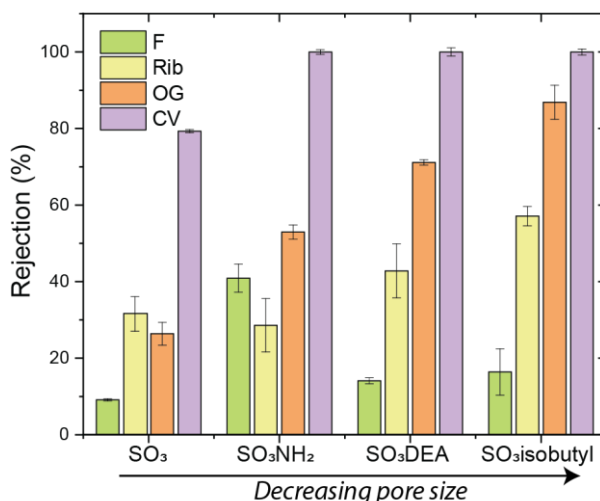
Figure 3.15 | Rejection values of the organic dyes for each membrane.

Because they are larger, anionic **OG** and neutral **Rib** are more strongly rejected than **F** by the non-modified membrane. The larger of the two, **OG** is rejected more than **Rib**. The modified membranes showed stronger rejection for both dyes with bulkier amides presenting higher values. These results are in line with the decrease of the membrane pore sizes. For larger pore sizes (unmodified membrane) the rejection values of **OG** and **Rib** are similar because both molecules are much smaller than the pore. However, for the membrane with smallest pore size (isobutylsulfonamide) discrimination between the larger **OG** and **Rib** is stronger, since the molecular size is closer to the pore size. The cationic dye **CV** is 80% rejected by the unmodified membrane due to the absorption inside the pores caused by ionic interactions. Due to incomplete functionalization of the SO_3 groups, absorption still occurs after functionalization, in

addition to rejection due to the reduction in pore size, resulting in near complete rejection of **CV** by the modified membranes.

Table 3.4 | Rejection % of a series of anionic, neutral and cationic small organic dyes:

Dye	F	Rib	O G	C V	Permeability $(L \cdot m^{-2} \cdot h^{-1} \cdot bar^{-1})$
Charge	-1	0	-2	+1	-
Mw (g·mol^{-1})	330.27	376.36	406.38	372.45	-
Molecular dimensions (nm)	1.03 x 0.92	1.35 x 1.04	1.07 x 1.21	1.23 x 0.97	-
Rejection (%)					
SO_3^-	9.10	32.8	26.4	79.3	4.72
SO_3NH_2	40.9	28.6	52.9	>99	2.97
SO_3DEA	14.1	42.8	71.1	>99	3.67
SO_3isobutyl	16.4	57.1	86.8	>99	2.83

Summarizing this section, it was shown that the covalent functionalization of sulfonate into sulfonamide groups produces a reduction in pore size resulting in lower water permeability, lower MWCO values and higher rejection of charged and neutral dyes. Even though the rejection process is driven by size exclusion, the incomplete functionalization of the sulfonate groups produces additional absorption/repulsion of cationic dyes.

3.3 Conclusions

In this Chapter, two different ways to change the chemical functionalities inside the pores of the membranes in Chapter 2 are described. The use of different functional groups results in variation of rejection and transport properties due to the large influence of the pore functionalities.

In the first section, an analogous monomer **Benzac** containing carboxylate functionalities was synthesized and characterized to form the supramolecular complex **Benzac₃TB**. Columnar nanostructures were obtained and used to develop supported membranes in the same way as **Sulfac₃TB** membranes in Chapter 2. The

comparison of the filtration properties showed for **Benzac₃TB** membrane lower permeability and higher rejection of ionic compounds like salts, anionic dyes and the template molecule **TB** due to a smaller pore size (MWCO) and stronger ion pairing of carboxylate groups. The experiments show that sulfonate groups result in superior transport properties due to less binding of cations.

The second section shows an interesting approach to post-modify the membrane pores via covalent chemical modification the sulfonate groups. Transformation *via* a 2-step reaction of sulfonate to sulfonamide groups was first carried out in self-standing films. The confirmation of the functionalization allowed us to apply it as a modification method of the porous system of a thin layer in a PVDF supported membrane. Even with incomplete conversion of approximately half of the sulfonate groups to sulfonamides, pronounced effects on the permeability and rejection properties were measured due to a decrease of the pore size by functionalization congruous with the size of the amide. The smaller pore size reduces permeability and increases rejection of neutral and charged organic molecules, mainly based on size effects.

A control of the filtration properties of LC-based membranes is possible by tuning the pore functionalities, proven here as a promising approach. This can be addressed by molecular design of the building block in the nanostructure or by in situ post-modification. The last strategy shows more interest as offers more versatility to directly change the properties of already produced membranes.

3.4 Experimental section

3.4.1. Materials and methods

Reagents and solvents for synthesis were purchased from Sigma-Aldrich or TCI America. The UF PES and PVDF supports (30 kDa MWCO) were purchased from Sartorius Stedim Biotech and Synder Filtration, respectively. Monodispersed PEGs with a polydispersity of around 1.05 were purchased from Agilent. Ultrapure water was used for all filtration experiments. NMR-spectra were recorded at room temperature on a Bruker, FT-NMR spectrometer AVANCE III HD-NanoBay (400MHz, Bruker UltraShield magnet, BBFO Probehead, BOSS1 shim assembly) in either acetone-d_6 or CDCl$_3$. The chemical shifts are given in ppm and the coupling constants as J in Hz. FT-IR spectra are measured on a Perkin Elmer Spectrum One spectrometer equipped with an attenuated total reflectance (ATR) sampling accessory. MALDI-TOF mass spectra were obtained on a PerSeptive Biosystems Voyager-DE PRO spectrometer with α-cyano-4-hydroxycinnamic acid as a matrix. Flash column chromatography was carried out using silica gel. Polarized optical microscopy (POM) images were recorded Jeneval microscope equipped with crossed polarizers and Polaroid CCD camera and a Linkam

THMS 600 heating stage. DSC measurements were performed in aluminum sample pans using a TA instruments Q1000. All runs were performed with heating and cooling rates of 10 K min^{-1}. X-ray scattering measurements were performed on a Ganesha lab instrument equipped with a Genix-Cu ultralow divergence source producing X-ray photons with a wavelength of 0.154 nm and a flux of $1 \cdot 10^8$ photons s^{-1}. Diffraction patterns were collected using a Pilatus 300 K silicon pixel detector with 487 × 619 pixels of 172 µm^2 in size, placed at a sample to detector distance of 91 mm (wide-angle, WAXS), or 500 mm (medium angle, MAXS). The beam center and the q-range were calibrated using silver behenate (d$_{(100)}$ = 1.076 nm; 5.839 nm) as a reference. The d$_{(300)}$ was used for calibration. Measurements were performed on film samples at RT. UV-Vis experiments were performed on a Jasco V-750 spectrophotometer. All experiments were performed in 10 × 10 mm quartz cuvettes at 20 ^{0}C. The photopolymerization was performed for 15 min with a mercury lamp (Omnicure s2000, emitting at 320−500 nm). The intensity was approximately 22 mW·cm^{-2} at the sample surface. HR-SEM was measured with Quanta 3D FEG (FEI/TFS) with EDT secondary detector. Samples were sputter-coated with a thin layer of gold using a Balzer Union SCD 040 sputter device. The conductivity of the feed and permeate solutions was measured with a C319 Consort conductivity meter.

3.4.2. Detailed experimental conditions

Sample preparations

Self-standing films

For section **3.2**, self-standing films were made membranes were prepared as follows: clean glass substrates (3 x 3 cm) were prepared by washing with acetone and isopropanol and finally dried. The nanoporous materials were made by making a solution containing **TB** (1 equivalent), **Benzac** (3.2 equivalents), 1,10-decanedithiol as the cross-linker (1.5 dithiol molecule per molecule of **Benzac** to have a ratio 1:1 of thiol:ene) in CHCl$_3$/MeOH (9:1 v/v) with a final concentration of (50 mg·ml^{-1}). Finally, Bis(2,4,6-trimethylbenzoyl)-phenylphosphineoxide (Irgacure 819, 3 wt%) was added as photo-initiator. 100-200 µL of the solution was bar coated manually (gap of 100 µm) on the clean glass substrate at 70°C to evaporate the solvent of the mixture. The sample was photo-polymerized using an EXFO Omnicure S2000 lamp with 8 mW·cm^{-2} of intensity, for 10 minutes, resulting in a yellow-transparent non-soluble self-standing polymer film. Lastly, after rinsing with pure water, the sample was dried in a vacuum oven at 40 °C.

For section **3.3**, self-standing films were prepared with the same conditions detailed in Chapter 2. Functionalization was performed following a 2-step reaction procedure. Pieces of 2 x 2 cm of the dried film were immersed in DCM (10 ml) and thionyl chloride was added (1 ml). The solution was let stir for 2 h at room temperature.

After this time, when the sulfonyl chloride is formed, the samples were rinsed with water and dried in the oven at 40 ^{0}C. Consequently, they were immersed in THF (10 ml) and diethylamine was added dropwise (1 ml). The reaction was left overnight, stirring at room temperature. When the reaction was completed, the samples were rinsed with THF and water and dried.

Supported membranes

For section **3.2**, polyether sulfone (PES) membranes were prepared as previously detailed in Chapter 2 (experimental section 2.4.2) using **Benzac** instead of **Sulfac**. Membranes of section **3.3** were prepared of complex **Sulfac₃TB** using polyvinylidene fluoride (PVDF) as support. Clean glasses of 3 x 3 cm were covered by PVDF using double-sided tape as flat as possible. Solutions for spin coating were prepared by mixing the sulfonic acid monomer (3.2 equivalents) with the template (**TB**, 1 equivalent) and 1,10-decanedithiol (4.6 equivalents) in DCE/EtOH (8:2 v/v) in a 10 wt. % concentration. Finally, Bis(2,4,6-trimethylbenzoyl)-phenylphosphineoxide (Irgacure 819, 3 wt.%) was added as the initiator. The mixture was spin-coated on top of PVDF at 1500 rpm for 60 s. The membrane was polymerized with UV light for 15 min with 8 mW·cm^{-2} of intensity giving a thin layer of around 400 nm of the LC phase-coated onto a PVDF support. Functionalization of the membranes of **section 3.3** was done following the same procedure as for the films: pieces of 2 x 2 cm of membranes were made to react with thionyl chloride in DCM for 2h. After rinsing with water and drying, 3 samples were reacted separately with three different amines (diethylamine, isobutylamine and ammonia) in THF overnight. After rinsing the samples and dry in the oven, the membranes were ready to use for filtration experiments.

Dye absorption in films

Samples of films from **section 3.3** were used for absorption experiments in aqueous solutions of crystal violet and fluorescein separately. Pieces of 1 mg of non-functionalized and functionalized samples were immersed in 50 µM solutions. UV-Vis was measured on the maximum absorbance wavelength of the dyes overtime for 20h. The intensity was converted to mmol of dye per sample to estimate the % of sulfonate groups that are functionalized.

Filtration tests

Filtration tests were performed using a 20 ml custom-made, stainless steel, stirred "Amicon type" dead-end filtration cell of 1.5 cm diameter. Samples of the membrane were cut to the desired size and pre-cleaned with deionized water. For each filtration test, a membrane was placed in the cell that was filled with ultrapure water (total

volume of 20 ml). The cell was closed and subsequently pressurized with nitrogen at the desired pressure.

The permeability of the membranes was determined by measuring the flux of pure water at different pressures (3–6 bar) *in triplo* for 2 membranes. Pure water was filtered for 2 h to stabilize the flux.

Protein rejection was determined with the filtration of aqueous solutions (50 µM) of BSA and GFP in PBS. With the cell previously cleaned with water, the filtration was carried out at a pressure of 4 bar where 4 samples of 1 ml of permeate were collected from which the first one was discarded to avoid mixtures with residual water below the membrane in the cell.

The MWCO of the membranes was determined by measuring the rejection of polyethylene glycol (PEG). Membranes were subjected to PEG filtrations at 4 bar in the Amicon cell. Aqueous solutions in ultrapure water were made containing PEGs with number average molecular weights (M_n) ranging from 600 to 10000 $g \cdot mol^{-1}$ with a concentration of 0.5 $g \cdot L^{-1}$ for each polymer. A series of different dyes with different molecular weights and charges were used for filtration tests: Fluorescein, Riboflavin, Methylene Blue, Crystal Violet and Orange G were selected. 50 µM aqueous solutions of the dyes were filtered separately at 4 bar pressure in the Amicon setup. For the salt rejection experiments 2 $g \cdot L^{-1}$ aqueous solutions of NaCl, $MgSO_4$ and $CaCl_2$ were used. Additionally, the flux of $CaCl_2$ solution was measured to determine the flux reduction and recovery. The filtration procedure and the rejection calculation of all these experiments were done as described in previous Chapter 2.

Synthetic procedures

Compound **Benzac** of **section 3.2** was synthesized following the synthetic route of **scheme 1**. The intermediate compounds (**1**), (**2**) and (**3**) were prepared as detailed in Chapter 2.

Methyl 4-(methyl(3,4,5-tris(undec-10-en-1-yloxy)phenyl)amino)benzoate (Benzester):
Acid chloride (**3**) (1.4056 g, 2.30 mmol, 1 equiv.) was dissolved in 3 ml of DCM at 0 ^{0}C. Then methyl 4-(methylamino)benzoate (0.455 g, 2.76 mmol, 1.2 equiv.) and triethylamine (0.46 g, 4.6 mmol, 2 equiv.) were dissolved in another round bottom flask in DCM (2 ml). The amine solution was slowly added to the solution with compound **3**. The solution was left stirring overnight at room temperature. After completion of the reaction, the solvent was evaporated. The residue was dissolved in water and CH_3Cl, extracted with CH_3Cl, dried with $MgSO_4$ and filtered. The solvent was evaporated to yield a white solid crystal. ^{1}H-NMR (CDCl$_3$, 400 MHz) δ = 7.91 (d, 2H, 3,5-benzene-*H*), 7.10 (s, 2H, 2,6-benzene-*H*), 6.50 (d, 2H, 2,6-benzene-*H*), 5.82 (m, J = 16.9, 10.1, 6.6, 3.4 Hz, 3H, 3x CH$_2$=C*H*-), 5.01 – 4.92 (m, 6H, 3x C*H$_2$*=CH-), 3.88 (t, J = 6.6 Hz, 2H, 1x

CH$_2$-C*H$_2$*-O), 3.70 (t, J = 6.5 Hz, 4H, 2x CH$_2$-C*H$_2$*-O), 3.50 (s, 3H, -CH$_3$), 2.05 (q, J = 7.3 Hz, 8H, 4x -C*H$_2$*-CH$_2$=CH), 1.65 (m, J = 14.4, 6.6 Hz, 8H, 3x -C*H$_2$*-CH$_2$-O), 1.38 – 1.28 (m, 42H, alkyl chain). ^{13}C-NMR (CDCl$_3$, 100 MHz) δ = 170.53, 152.44, 146.54, 143.04, 139.46, 139.20, 130.08, 127.11, 126.15, 114.11, 114.09, 107.64, 73.34, 68.97, 38.59, 33.83, 30.29, 29.67, 29.59, 29.56, 29.53, 29.48, 29.41, 29.36, 29.28, 29.20, 29.17, 28.98, 28.96, 26.06, 26.03.

4-(methyl(3,4,5-tris(undec-10-en-1-yloxy)phenyl)amino)benzoic acid (Benzac):

To hydrolyze the ester into the correspondent benzoic acid, **Benzester** (1.7 g, 2.28 mmol, 1 equiv.) was dissolved in a mixture MeOH:H$_2$O 3:1 (18 ml) with KOH as a base (1.02 g, 18.25 mmol, 8 equiv.) and left overnight under reflux. The solution was extracted 1 time with chloroform and washed 2 times with HCl and NaCl respectively. The solvent was evaporated and dried over a vacuum to yield a white powder crystal. ^{1}H-NMR (CDCl$_3$, 400 MHz) δ = 7.97 (d, 2H, 3,5-benzene-*H*), 7.30 (s, 2H, 2,6-benzene-*H*), 7.11 (d, 2H 2,6-benzene-*H*), 5.82 (m, J = 16.9, 10.1, 6.6, 3.4 Hz, 3H, 3x CH$_2$=C*H*-), 5.06 – 4.89 (m, 6H, 3x C*H$_2$*=CH-), 3.89 (t, J = 6.6 Hz, 2H, 1x CH$_2$-C*H$_2$*-O), 3.71 (t, J = 6.5 Hz, 4H, 2x CH$_2$-C*H$_2$*-O), 3.52 (s, 3H, -NC*H$_3$*), 3.32 (q, J = 7.3 Hz, 8H, 4x -N-C*H$_2$*-CH$_3$), 2.03 (q, J = 6.7 Hz, 6H, 3x -C*H$_2$*-CH$_2$=CH), 1.81 – 1.75 (m, 12H, 3x -C*H$_2$*-CH$_2$-O), 1.65 (m, 8H, 3x -C*H$_2$*-CH$_2$-O), 1.47 – 1.30 (m, 58H, alkyl chain). ^{13}C-NMR (CDCl$_3$, 100 MHz) δ = 170.98, 170.07, 152.69, 152.32, 142.99, 139.04, 131.01, 129.32, 125.91, 123.33, 113.95, 108.38, 107.84, 73.37, 68.84, 38.04, 33.65, 30.16, 29.40, 29.20, 28.96, 28.78, 25.89.

3.5 References

[1]   A. P. H. J. Schenning, Y. C. Gonzalez-Lemus, I. K. Shishmanova, D. J. Broer, *Liq. Cryst.* **2011**, *38*, 1627.

[2]   J. Lugger, D. J. Mulder, R. Sijbesma, A. Schenning, *Materials (Basel).* **2018**, *11*, 104.

[3]   J. R. Werber, C. O. Osuji, M. Elimelech, *Nat. Rev. Mater.* **2016**, *1*, 15.

[4]   K. Zuo, K. Wang, R. M. DuChanois, Q. Fang, E. M. Deemer, X. Huang, R. Xin, I. A. Said, Z. He, Y. Feng, W. Shane Walker, J. Lou, M. Elimelech, X. Huang, Q. Li, *Mater. Today* **2021**, *50*, 516.

[5]   D. L. Gin, W. Gu, B. A. Pindzola, W. J. Zhou, *Acc. Chem. Res.* **2001**, *34*, 973.

[6]   B. M. Carter, B. R. Wiesenauer, R. D. Noble, D. L. Gin, *J. Memb. Sci.* **2014**, *455*, 143.

[7]   M. Henmi, K. Nakatsuji, T. Ichikawa, H. Tomioka, T. Sakamoto, M. Yoshio, T. Kato, *Adv. Mater.* **2012**, *24*, 2238.

[8]   M. Gupta, Y. Suzuki, T. Sakamoto, M. Yoshio, S. Torii, H. Katayama, T. Kato, *ACS Macro Lett.* **2019**, *8*, 1303.

[9]   Y. Marcus, G. Hefter, *Chem. Rev.* **2006**, *106*, 4585.

[10]   P. D. Helmenstine, Anne Marie, *Acid Dissociation Constant Definition: Ka.*, **2020**.

[11]   G. M. Bögels, J. A. M. Lugger, O. J. G. M. Goor, R. P. Sijbesma, *Adv. Funct. Mater.* **2016**, *26*, 8023.

[12]   S. Bhattacharjee, J. A. M. Lugger, R. P. Sijbesma, *Chem. Commun.* **2018**, *54*, 9521.

[13]   Yoshino Tanaka, *Ion exchange membranes. Fundamentals and applications*, 2nd ed., Elsevier science, **2015**.

[14]   A. H. Avci, T. Rijnaarts, E. Fontananova, G. Di Profio, I. F. V. Vankelecom, W. M. De Vos, E. Curcio, *J. Memb. Sci.* **2019**, *595*, 117585.

[15]   C. Klaysom, B. P. Ladewig, G. Qing, M. Lu, L. Wang, *Functional Nanostructured Materials and Membranes for water filtration, Chapter 6* (Ed.: Mikel Duke, D. Z. and R. S.), 1st ed., Wiley-VCH Verlag, **2013**.

[16]   J.-F. Xiong, S.-H. Luo, J.-P. Huo, J.-Y. Liu, S.-X. Chen, Z.-Y. Wang, *J. Org. Chem.* **2014**, *79*, 8366.

[17]   X. Dong, A. Al-Jumaily, I. C. Escobar, *Membranes (Basel).* **2018**, *8*, 23.

[18]   M. A. Abdel-Fatah, *Ain Shams Eng. J.* **2018**, *9*, 3077.

[19]   T. Hosokawa, *J. Synth. Org. Chem.* **1984**, *42*, 173.

[20]   R. Zhou, P. Ren, H. Yang, Z. Xu, *J. Memb. Sci.* **2014**, *466*, 18.

[21]   Z. Z. Nie, B. Zuo, L. Liu, M. Wang, S. Huang, X. M. Chen, H. Yang, *Macromolecules* **2020**.

[22]   Q. C. Xia, W. J. Yang, F. Fan, M. Ji, Y. Wang, Z. Y. Wang, X. L. Cao, W. Xing, S. P. Sun, *Nano Lett.* **2020**, *20*, 8185.

[23]   S. Bhattacharjee, J. A. M. Lugger, R. P. Sijbesma, *Macromolecules* **2017**, *50*, 2777.

[24]   D. J. Mulder, L. M. W. Scheres, J. Dong, G. Portale, D. J. Broer, A. P. H. J. Schenning, *Chem. Mater.* **2017**, *29*, 6601.

[25]   S. M. Dischinger, M. J. McGrath, K. R. Bourland, R. D. Noble, D. L. Gin, *J. Memb. Sci.* **2017**, *529*, 72.

[26]   M. J. McGrath, S. H. Hardy, A. J. Basalla, G. E. Dwulet, B. C. Manubay, J. J. Malecha, Z. Shi, H. H. Funke, D. L. Gin, R. D. Noble, *ACS Mater. Lett.* **2019**, *1*, 452.

[27]   Sigma Aldrich, *IR Spectrum Table and Chart*.

[28]   I. Sanitary, M. Membrane, *Synder filtration. Industrial membrane catalog*.

[29]   Synder Filtration, *V3 (PVDF 30000 Da)*.

Chapter 4

Nanoporous films with photo-switchable absorption kinetics based on a columnar LC
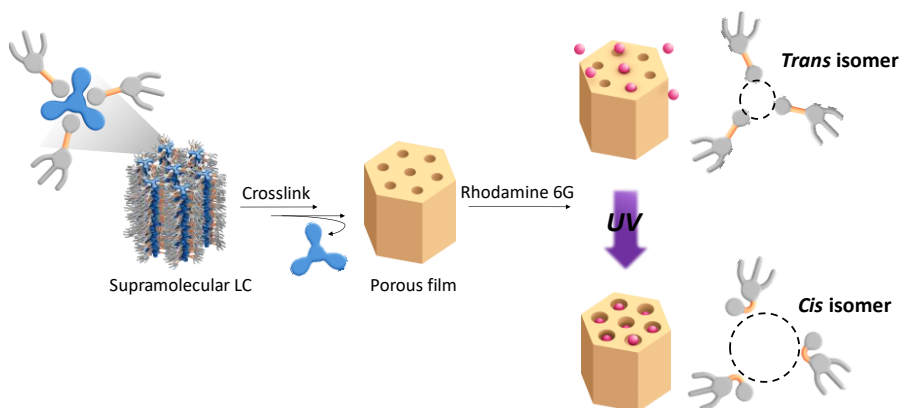
Abstract | A photo-responsive nanoporous polymer film has been produced from the templated self-assembly of a columnar liquid crystal containing azo units. The LC supramolecular complex **Azoac₃TB** was crosslinked via thiol-ene photo-polymerization keeping the columnar morphology. Subsequent removal of the template yielded nanoporous polymer films with pores of approximately 1 nm in diameter. The photo-switchable properties of the azo system were tested in solution for the monomer **Azoac** and in the porous films, showing a reversible *trans-cis* isomerization. At room temperature, the cis isomer was sufficiently long-lived to establish a difference in dye absorption kinetics of the two isomers. The cationic dye rhodamine 6G was bound to both isomers, but the rate of binding to films enriched in the cis isomer was 8 times faster. This dynamic photo-responsive system can be applied for selective *on-demand* transport applications in porous materials.

4.1 Introduction: use of azo-benzenes to develop photo-switchable materials

Intensive study of nanoporosity in different types of materials over the last decade has led to improved performance in applications such as separation membranes, catalysis, drug delivery, etc.[1–3] The use of self-assembled organic building blocks to develop nanoporous materials is an elegant approach to address well-defined structures with uniform pore distribution.[4] Selectivity, absorption kinetics and absorption capacity are often better than in inorganic nanoporous materials like silica or zeolites, which have better long-term stability but are more difficult to process.[5,6] Applying external stimuli such as light to soft organic nanostructured materials permits tuning features like absorption kinetics and selectivity.[7] This can be achieved by the incorporation of light-responsive molecular moieties in the pores that can photo-switch between two isomers, promoting the alteration of pore dimension and polarity.[8,9] Azobenzenes, stilbenes, and acylhydrazones are light-responsive compounds that isomerize reversibly when irradiated with light.[10–12] Among these units, azobenzenes are the most convenient building blocks, since their synthesis is relatively straightforward, and photo-isomerization is brought about by convenient light sources with wavelengths of ~ 400 nm, whereas stilbene and acylhydrazone are switched by light of shorter wavelengths.[13]

Azobenzenes usually isomerize from *trans* to *cis* when irradiated with 300-400 nm UV light, while *cis* to *trans* isomerization is stimulated by irradiation at > 400 nm wavelength.[14] The *trans* isomer is also formed by the thermal relaxation of the *cis* form since this isomer is thermodynamically more stable.[15,16] Reversible isomerization of azobenzene compounds can lead to changes in polarity, photochromic pK_a or binding strength to other molecules.[17] When the azo moiety is part of a receptor molecule, reversible isomerization may change the size of the binding site, affecting the selectivity towards molecules of different sizes.[18] Azobenzenes have been applied for instance as photo-responsive units in nanoporous films based on liquid crystalline supramolecular networks, where the number of binding sites and pore dimensions increased upon irradiation with UV light due to *trans*-*cis* isomerization of the azo groups.[19]

As shown in Chapter 2, columnar LCs can be prepared from a 3:1 supramolecular complex between a tris-benzimidazolyl benzene (**TB**), as template molecule, and three monomeric units of wedge-shaped sulfonic acids (**Sulfac**) giving C_3-symmetric supramolecular disks which stack into columns. The introduction of azo moieties in the molecular building units of the columnar nanostructure, more specifically, in the pore surroundings, will likely lead to a photo-responsive material with dynamic pores that can close and open with the application of light due to the change in polarity of the azo groups.
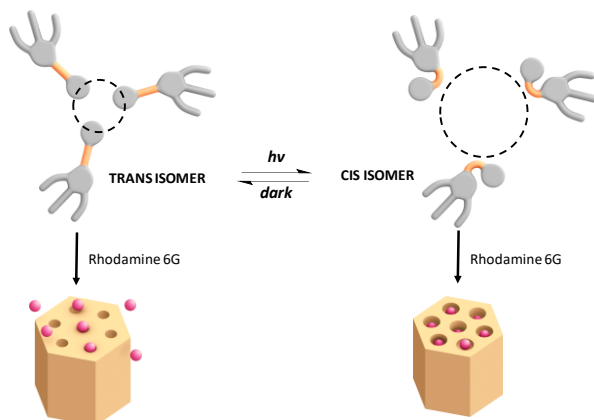
Figure 4.1 | Isomerization of azo moieties with UV light in a porous material changes pore size and absorption rate**.**

Herein we present the synthesis and characterization of a photo-switchable nanoporous film based on a wedge-shaped azo derivative Azoac, containing carboxylic functionalities which form a disk-shaped 3:1 supramolecular complex with the template molecule TB (Figure 4.1). The formed complex self-assembles into a columnar mesophase that is fixated by crosslinking with a thiol-ene reaction, and removal of the template leads to the formation of a nanoporous material. Previously in the group, it has been established that the pores in similar materials without photo-switchable moieties have a fixed selectivity for the binding of charged dyes.[20] In the current work, we establish that photo-switching between *trans* and *cis* isomeric states of the azo moieties in the porous material influences the absorption kinetics of the cationic dye rhodamine 6G.

4.2 Synthesis and characterization of Azoac$_3$TB complex

The synthesis of 4-((2,3,4-tris(undec-10-en-1-yloxy)phenyl)diazenyl)benzoic acid (**3**) was performed in three steps as shown in **Scheme 4.1**.
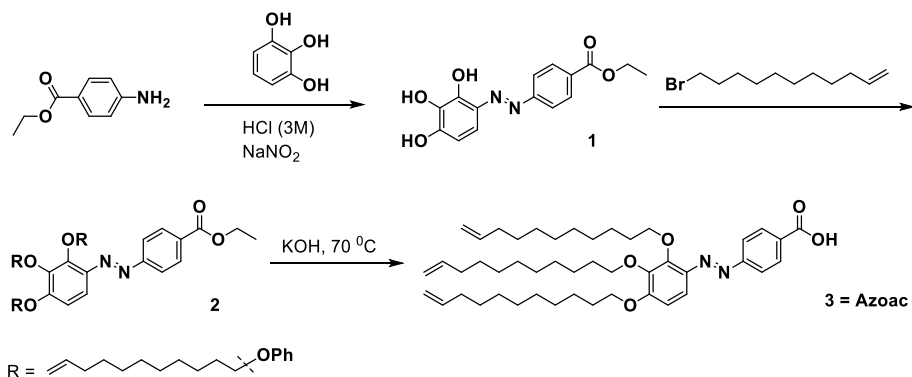
Scheme 4.1 | Synthesis of wedge-shaped azo derivative **3** (**Azoac**)

First, ethyl 4-aminobenzoate was diazotised with sodium nitrite to give the corresponding diazonium salt. The azo product, 4-((3,4,5-trihydroxyphenyl)diazenyl)benzoate (**1**) was obtained by reacting the freshly prepared diazonium salt with 1,2,3-tris(hydroxybenzene) (pyrogallol).[21] ^{1}H-NMR showed that substitution took place at the 4-position of pyrogallol due to the electron-donating nature of the hydroxy groups, favoring substitution at the *ortho* and *para* positions.[22] Alkylation of the phenolic hydroxy groups with 11-bromo-1-undecene yielded the tris-alkene ester **2**, which was hydrolyzed with aqueous potassium hydroxide, followed by acidification with aqueous hydrochloric acid to give photo-switchable acid **Azoac**. ^{1}H-NMR showed that only the thermodynamically more stable *trans* isomer was present. In bulk, molecules of **Azoac** are present as H-bonded dimers, as indicated by the broadened C=O stretch band at 1686 cm^{-1} (**Figure 4.2c**).[23] Dimerization of the fan-shaped molecule promotes liquid crystallinity, and polarized optical microscopy (POM) and Differential Scanning Calorimetry (DSC) showed that pure **Azoac** is liquid crystalline between 25°C and 130°C (**Figure 4.2a,b**).
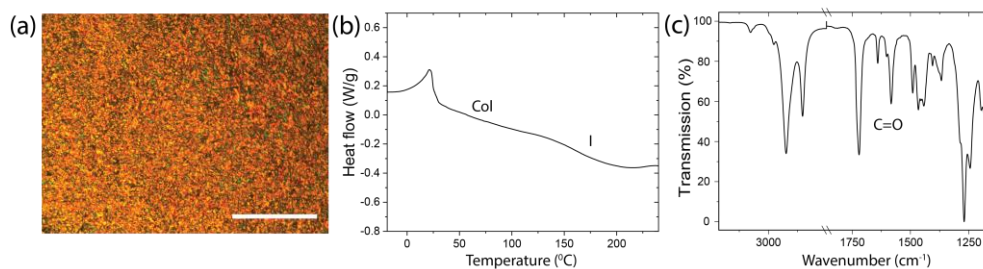
Figure 4.2 | a) cross-polarized micrograph of the mesophase formed after heating to isotropic and cooling to room temperature of **Azoac**. Scale bar 100 µm; b) DSC traces of 2nd cooling cycle of pure **Azoac** at 10^{0}C/min and c) FT-IR spectrum of alkene ester **2**.

Mixing **TB** with 3 equiv. of **Azoac** afforded a H-bonded 3:1 *C$_3$*-symmetric complex (**Figure 4.3a**) as is evident from the FT-IR spectrum in which the C=O band shifted from

1686 cm^{-1} to 1674 cm^{-1}, and a new band appeared at 3250 cm^{-1} (**Figure 4.3b**), which was assigned to the imidazolium N^+-H stretching vibration. The presence of a mesophase was established with POM and DSC. However, at a 3:1 ratio of **Azoac** and **TB**, the formation of needle-shaped crystals was observed after annealing, indicating phase separation of the template. Using 3.2 equivalents of **Azoac** prevented crystallization of **TB** and resulted in a clean Col_{hex} LC-phase with fan-shaped texture in POM (**Figure 4.3c**) below 50°C in DSC (**Figure 4.3d**). The X-ray diffractogram showed peaks with q-ratios of $1:\sqrt{3}:2:\sqrt{7}$ (**Table 4.1** and **Figure 4.3e**) confirming the presence of a Col_{hex} mesophase with a lattice parameter a of 3.76 nm. The WAXS diffractogram shows a diffraction peak corresponding to an inter-disk distance c of 0.38 nm, identifying the mesophase as ordered columnar hexagonal (Col_{ho}).
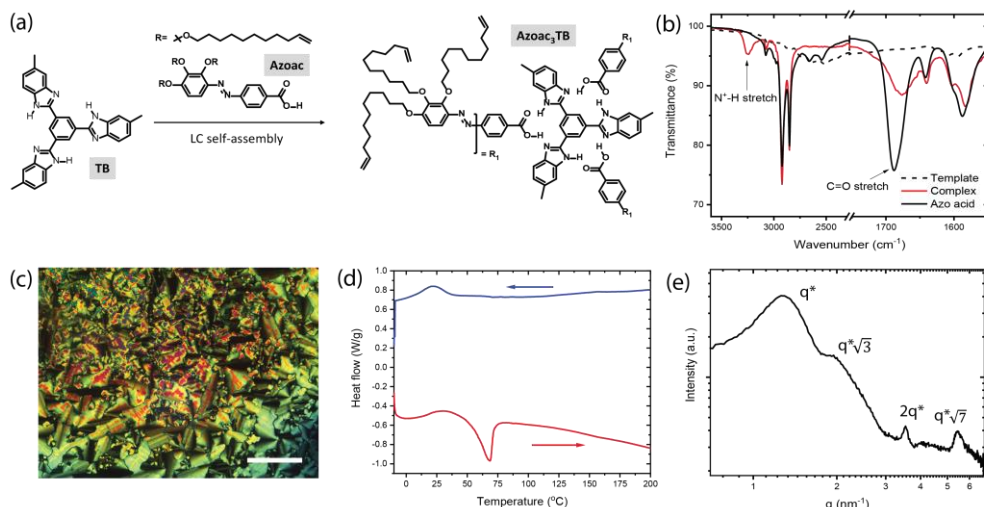
Figure 4.3 | a) Formation of the supramolecular discotic complex **Azoac₃TB** via H-bonding; b) IR spectra of **Azoac**, **TB** and the 3:1 mixture indicating the formation of an H-bonded complex; c) POM image of a 3.2:1 mixture of **Azoac** and **TB** at room temperature. Scale bar 100 µm; d) DSC traces of 2nd heating and cooling cycle of **Azoac₃TB** at 10°C/min and e) WAXS diffractogram of **Azoac₃TB** at room temperature.

Table 4.1 | XRD data of **Azoac₃TB** at room temperature after annealing:

Peak	q (nm⁻¹)	hkl	d_{obs} (nm)	d_{calc} (nm)	Structural parameter
1	1.93	100	3.25	3.25	a = 3.76 nm
2	3.36	110	1.87	1.88	
3	3.87	200	1.62	1.62	
4	5.02	210	1.25	1.23	
5	5.79	220	1.08	1.08	
6	19.04	001	0.33		c = 0.38 nm

4.3. Formation and characterization of photo-switchable nanoporous films

4.3.1 Photo-isomerization of Azoac₃TB in solution and films

Polymer films obtained from the liquid crystal phase must be highly crosslinked in order to obtain nanoporosity after template removal. Columnar mesophases of a similar non-photo-switchable system with carboxylic acids have previously been crosslinked with acyclic diene metathesis (ADMET) polymerization of tris-alkenyl benzoic acids using Grubbs' 2nd gen. catalyst.[20,24] A similar approach with the complex of **TB** with **Azoac** was not successful due to the low degrees of polymerization achieved.[25]

As an alternative crosslinking method, the photochemical thiol-ene click reaction (**Figure 4.4a**), already used in the previous Chapters was more successful. Drop cast films (thickness 0.5-1 µm) of the complex with 10-decanedithiol (DDT) and 2 wt.% Irgacure 819 photoinitiator[26,27] were irradiated with UV light for 15 minutes, using a 405 nm cut-off filter to prevent *trans*-*cis* isomerization of the azo group. Alkene conversion was estimated to be 82 %, based on the intensity of the =C-H bending band at 907 cm^{-1} in the FTIR spectrum (**Figure 4.4b**).[28] Finally, a porous polymer was obtained after removal of the **TB** template by soaking the film in DMSO for 3 h, followed by two additional washing steps with water and extensive drying in vacuo. FT-IR showed full disappearance of the N$^+$-H stretching band at 3250 cm^{-1}, and a shift of the C=O stretching vibration of the carboxylic acid from 1676 cm^{-1} to 1689 cm^{-1}, confirming the template removal. X-ray diffractograms were taken to verify retention of the columnar order after the cross-linking and the removal of the template (**Figure 4.4c**). Polymerization did not affect the Col$_{hex}$ order, but the lattice spacing d$_{(100)}$ increased from 3.76 nm of the pure **Azoac₃TB** complex to 4.33 nm of the polymer due to the presence of the crosslinker. When the **TB** template was removed, the spacing increased to 4.52 nm (**Figure 4.4c**, grey line). A reflection from the interdisc distance at wide angles is absent in the diffractogram, indicating disordered stacking in the polymerized material.[29]
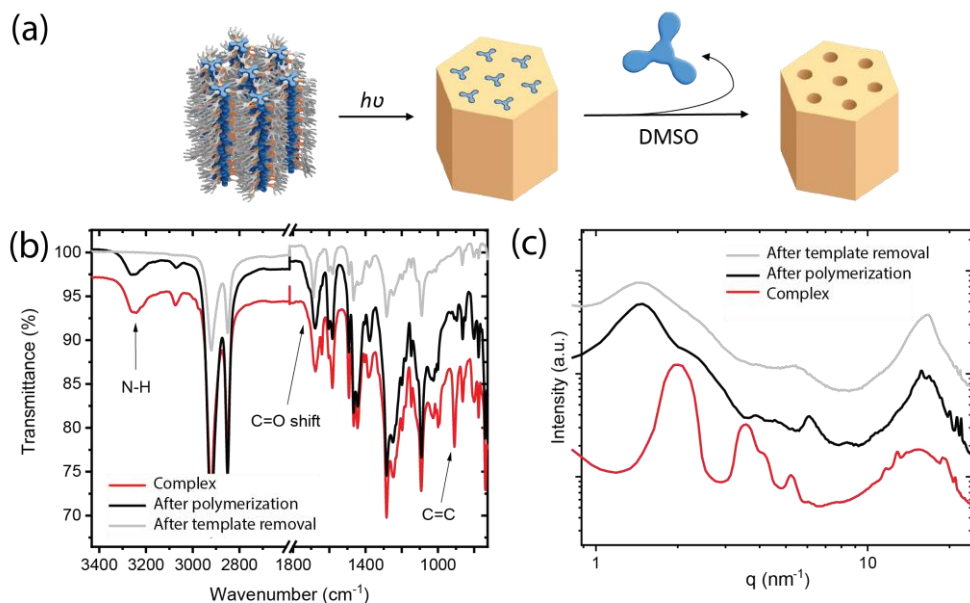
Figure 4.4 | a) Crosslinking of the film by photo-polymerization and consecutive removal of the **TB** template molecule; b) FT-IR spectra of the **Azoac$_3$TB** complex before and after polymerization. The arrow indicates the nearly complete disappearance of the =C-H stretching band of the double bond. After removal of the template, the N-H band disappears and carbonyl band shifts; c) Wide angle X-ray diffractograms (WAXS) of the polymerization mixture (red), after polymerization (black) and after the removal of the **TB** (grey).

4.3.2 Photo-isomerization of Azoac$_3$TB in solution and films

Trans to *cis* photo-isomerization of **Azoac** in solution was monitored with UV-Vis spectroscopy and the *cis-trans* thermal relaxation was monitored with both UV-Vis and ^{1}H-NMR spectroscopy. The UV-Vis spectrum shows an intense $\pi \to \pi^*$ absorption band at 377 nm corresponding to the *trans* isomer and a much weaker n $\to \pi^*$ band at 465 nm (**Figure 4.5a**).[16] Upon irradiation of the solution with 365 nm UV light the intensity of the π - π^* transition band at 377 nm decreased strongly, indicating *trans* to *cis* isomerization. After approximately 1 minute, a photo-stationary state was reached. Irradiation of the solution with 450 nm blue light (350 mA) resulted in an increase of the 377 nm absorption band and a slight decrease at 465 nm as the result of *cis*-to-*trans* photo-isomerization (**Figure 4.5b**), showing that isomerization is photochemically reversible with a photo-stationary state that depends on the irradiation wavelength.[30]
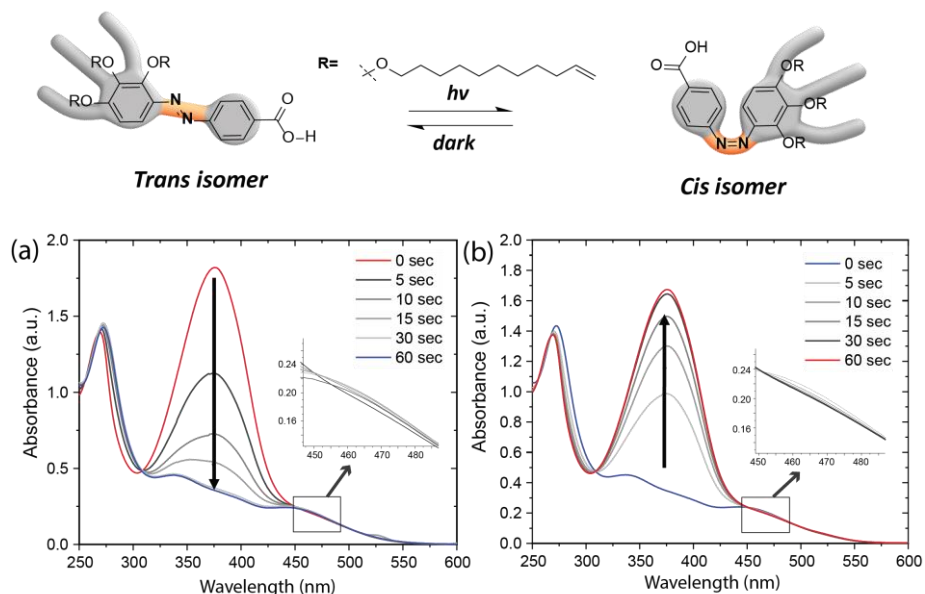
Figure 4.5 | UV-Vis spectra of **Azoac** in CHCl$_3$ after UV irradiation for various times. a) Irradiation at 365 nm; b) Irradiation at 450 nm.

Excitingly, photo-isomerization studies on thin films of the porous polymer revealed that the azo-benzene still switched from *trans* to *cis* under these conditions. Upon irradiation of a thin film (~ 0.5 µm) at 365 nm the intensity of the band at 377 nm decreased by 40 % in 1.5 h (**Figure 4.6**), at which time a photo-stationary state had been reached. When this *cis*-enriched film was irradiated at 450 nm light conversion to the *trans* isomer only took a few minutes.
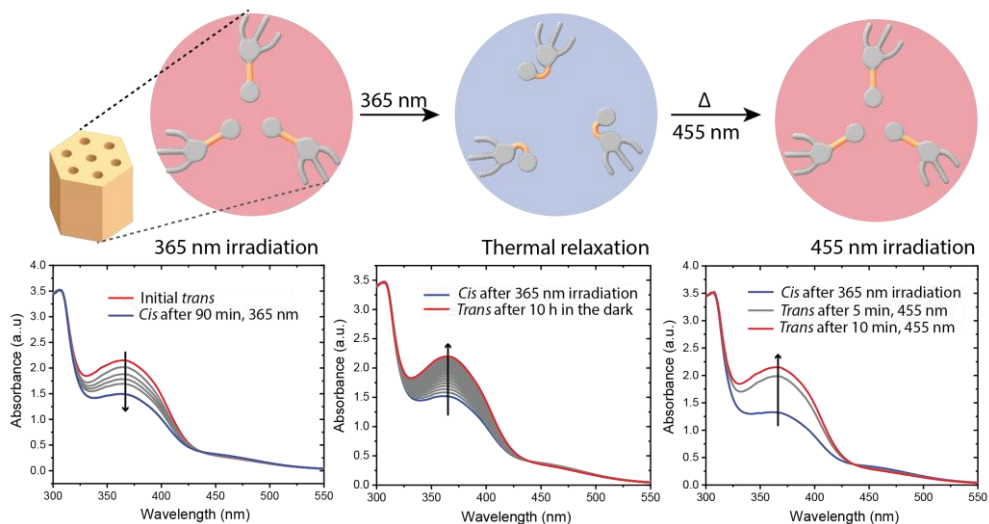
Figure 4.6 | UV-Vis spectra of **Azoac₃TB** films of irradiation at 365 nm for 1.5 h to reach the *cis* isomer, thermal relaxation for 10 h reaching total conversion to *trans* isomer and after 10 minutes of 455 nm with a total recovery of the *trans* population.

Thermal relaxation of the azobenzene was investigated to obtain the half-life of the *cis* isomer. A solution of **Azoac** in chloroform (100 mM) was irradiated at 365 nm for 10 minutes. By monitoring the absorption on UV-Vis of the recovery of the band at 377 nm the half-life of the *cis* isomer was calculated. The data were fitted with the equation for half-life (**eq. 4.1**) that follows an exponential model:

$$N(t) = N_0 * (0.5)^{\frac{t}{t_{0.5}}} \quad \text{(eq. 4.1)}$$

Where N(t) represents the amount of *cis* at time = t, N_0 the amount at t = 0, t the time (h) and $t_{0.5}$ represents the half-life time (h) at a specific temperature.

A half-life for the *cis* isomer of 13.8 h at room temperature was obtained (**Figure 4.7a**), in line with lifetimes for *cis-trans* isomerization of similar azo compounds.[31] In the same way, when the *cis*-enriched film was allowed to relax back thermally at room temperature in the dark, the absorption band at 377 nm increased with a half-life of 8.6 h, significantly faster than in solution (**Figure 4.7b**).
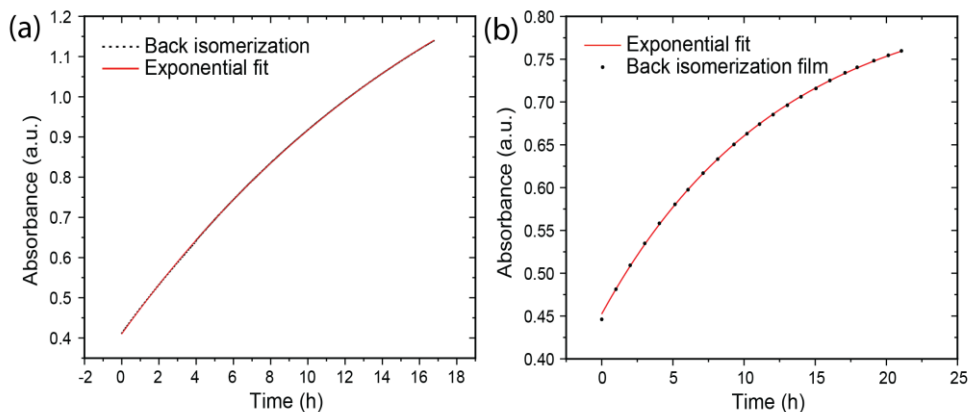
Figure 4.7 | Thermal relaxation curve measured at room temperature at 377 nm and its exponential fitting curve for a) **Azoac** in solution and b) polymer film of the crosslinked network.

The shorter half-life for relaxation of the *cis* to *trans* isomerization in the polymer is related to a restriction of free volume. Initially, the network is disposed to accommodate the *trans* isomer. Hence, photo-isomerization to the *cis* isomer is slower than in solution because of the restricted movement. The *cis* isomer is in a

sterically strained environment, favoring thermal relaxation to the more stable *trans*-form.[32–34] Although the half-life of the *cis* form is significantly lower in the polymer, the films are sufficiently stable to study dye absorption in the pure *trans* and in the *cis* enriched films separately.

The conservation of the columnar structure was confirmed with WAXS; samples of the film were measured before irradiation of 365 nm and after to compare *cis* and *trans* isomerization states. The same pattern was obtained but a slight shift to bigger distances was observed due to the enlargement of the lattice after irradiation.

4.3.3 Uptake of rhodamine 6G in porous films

Trans to *cis* isomerization in the porous polymer is expected to result in increased pore size, as shown in **Figure 4.1**. Isomerization does not only result in larger pores but the pores are also expected to become more polar because molecular symmetry is reduced.[35] To verify these predictions, absorption was tested of the cationic dye rhodamine 6G, with dimensions of 1.35 nm × 1.06 nm, similar to the pore diameter. *Cis*-enriched films were obtained by irradiation at 365 nm for 1.5 h. Samples of 0.5 mg of the *trans* or *cis*-enriched porous polymer films (thickness 1 µm) were immersed in a solution of Rhodamine 6G in a quarz cuvette of 1 cm thickness. Dye absorption was followed by monitoring the decrease of light absorption at 474 nm, the rhodamine 6G absorption maximum while taking care to keep the films away from the light path. To analyze the absorption rates, the concentrations were plotted and smoothed over 20 points (**Figure 4.8a**). Both types of films absorbed dye, but with significantly different uptake rates, with initial absorption in the *cis*-enriched film approximately 2 times higher after 10 hours. Reversibility of the uptake behavior was tested by comparing dye absorption in *trans* films with absorption in films that were irradiated to create the *cis* enriched state, and then were thermally relaxed for 10 h before measuring the dye uptake. **Figure 4.8b** shows that the absorption rates for both routes are equal.

After 45 h, the *cis*-enriched film had bound 0.036 mmol of dye per mg of film, corresponding to approximately 1 dye molecule per 6 **Azoac** units which is the same as two **Azoac₃TB** complexes, while for the *trans* polymer*,* approximately half of that amount was adsorbed. The maximum amount of dye absorbed, based on the size of the molecule, may be assumed to correspond to one rhodamine cation per **Azoac₃TB** complex.
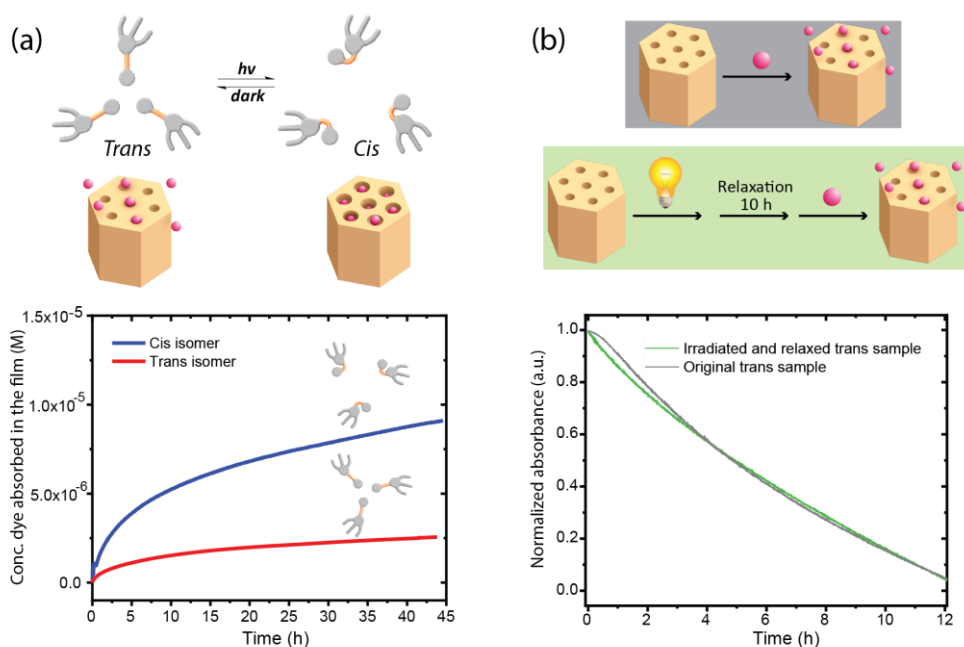
Figure 4.8 | a) Scheme of the absorption of Rhodamine 6G in both isomer films and plot showing the concentration (M) of the dye absorbed in the pores for both *trans* and *cis* films. b) Schematic figure and plot of the absorbance of rhodamine 6G normalized for *trans* films before and after irradiation and relaxation back.

The absorption rate of rhodamine 6G was fitted using a Fickian diffusion model[36] (**eq. 2**) with the diffusion coefficient of adsorbate in the film as the single fitting parameter. The Fickian transport model correlates the adsorption profile of the dye, in this case, Rhodamine 6G in a single pore of the porous material with the decrease in concentration in solution.

$$C_b(t) = \int_{x=0}^{x=l/2} C_0 \left(1 - erf\frac{x}{\sqrt{4\,\mathcal{D}_F t}}\right) dx \quad \text{(eq. 4.2)}$$

With C_b as the concentration of the dye (mg/L) in the solution at y(t). c_0 concentration dye at t(0), t time (s), x the pore length (um) and $\mathcal{D}$ the adsorption coefficient of the adsorbate.

Eq. 4.2 was fitted to the batch adsorption curves obtained for the cis and the trans isomers (**Figure 6.9a**) by applying a range of diffusion coefficients. The best fit value was determined by minimizing the sum S of absolute weighted difference between the measured and fitted data points (**eq. 4.3**)

$$S = \sum_{i=1}^{N} \left| \frac{(y_i - f(x_i))}{y_i} \right| \qquad \text{(eq. 4.3)}$$

With y_i as the concentration of the dye (mg/L) in the solution at t, $f(x_i)$ concentration dye calculated according to **eq. 4.2**, and S the sum of absolute weighted deviations between $f(x_i)$ and y_i. The fitting procedure was performed on a reduced number of data points (20 from the initial 100) to shorten the fitting time. The equilibrium concentration of the dye (c_{eq}) was obtained by extrapolating **eq. 4.2** to infinite time c_b (t=∞).
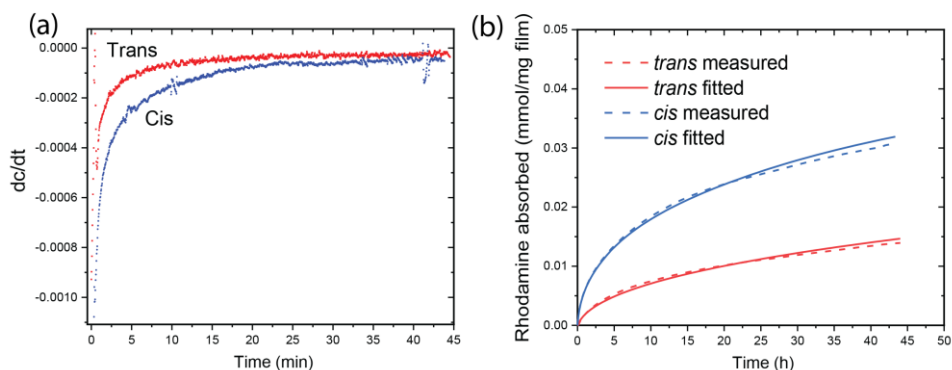
Figure 4.9 | a) Overlay of absorption measurements of rhodamine 6G vs. time in porous films of *trans* and *cis* -enriched isomers with fitted Fickian transport equation using the optimized D_F, C_0 at t = 0; b) Absorption of rhodamine 6G vs. time in the porous film in its native *trans* state and after irradiation + relaxation.

The data of the initial 45 minutes (2600 seconds) of the absorption measurements, when little isomerization has taken place, was used for the fitting. The decreasing concentration values of dye in the solution were taken into account for the calculation of the diffusion coefficients of rhodamine 6G for each isomer (**Figure 4.9b**). The best fit for the diffusion coefficients D_F (**Table 4.2**) gave an approximately 8 times higher absorption rate for the *cis*-enriched material than for the *trans* polymer. Since the *cis* isomer has a limited lifetime, and absorption equilibrium had not been reached after 48 hours, it is not feasible to determine the equilibrium absorptions of cis and trans isomers individually.

Table 4.2 | Optimal parameters from fitting with the Fickian transport equation.

Isomer	Time (s)	$D_F (10^{-5} \cdot \mu m^2 \cdot s^{-1})$
Trans	0 - 2600	0.290
Cis	0 - 2600	2.278

Pore length 0.5 microns, D_F = diffusion coefficient of the adsorbate.

4.4 Conclusions

A light-responsive nanoporous polymer film was prepared based on a columnar discotic liquid crystal formed by a new 3:1 hydrogen-bonded complex **Azoac₃TB** containing azobenzene moieties. The columnar morphology was retained after thiol-ene polymerization, and nanometer-sized pores were created by the removal of the template. *Trans-cis* photo-isomerization in the solid was slower than in solution, while thermal and photochemical *cis-trans* isomerization was faster than in solution. Absorption of rhodamine 6G was faster in the *cis* enriched films than in the *trans* films, confirming the initial hypothesis that pore size increases upon irradiation due to the isomerization of the azo moieties in the nanoporous structure. The change in absorption kinetics opens the possibility to apply these materials as light-controlled filtration membranes.

4.5 Experimental section

4.5.1 Materials and methods

Chemicals and solvents were purchased from Sigma-Aldrich or bio-solve and used as received unless stated otherwise. NMR-spectra were recorded at room temperature on a Bruker, FT-NMR spectrometer AVANCE III HD-NanoBay (400MHz, Bruker Ultra Shield magnet, BBFO Probehead, BOSS1 shim assembly) in either acetone-d6 or CDCl₃. The chemical shifts are given in ppm and the coupling constants as J in Hz. FT-IR spectra are measured on a Perkin Elmer Spectrum One spectrometer equipped with an attenuated total reflectance (ATR) sampling accessory. MALDI-TOF mass spectra were obtained on a PerSeptive Biosystems Voyager-DE PRO spectrometer with α-cyano-4-hydroxycinnamic acid as a matrix. Flash column chromatography was carried out using silica gel. POM images were obtained on a Jeneval microscope equipped with crossed polarizers, a Linkham THMS 600 heating stage, and a Polaroid DMC le CCD camera. DSC measurements were performed in aluminium sample pans using TA instruments Q1000. All runs were performed with heating and cooling rates of 10 K·min^{-1}. UV-Vis experiments were performed on a Jasco V-750 spectrophotometer. All experiments were performed in 10 x 10 mm quartz cuvette at 20°C. Irradiation experiments were done with a CS2010 UV curing led system equipped with a M450LP1 (450nm) LED or M365LP1c (365 nm). A filter for azo is used to avoid isomerization from *trans* to *cis* in the polymerization process.

4.5.2 Detailed experimental conditions

Sample preparations

Clean glass substrates (3 x 3 cm) were prepared by washing with acetone and isopropanol followed by drying. The nanoporous materials were made by making a solution of 4-((2,3,4-tris(undec-10-en-1-yloxy)phenyl)diazenyl)-benzoic acid 3 (3.2 equiv.) and 1,10-decanedithiol (4.8 equiv.) in $CHCl_3$/MeOH (9:1 v/v) and adding this solution to the required amount of 1,3,5-tris(5-methyl-1H-benzo[*d*]imidazol-2-yl)benzene (**TB**, 1 equiv.) (50 mg·ml^{-1}). Finally, Bis(2,4,6-trimethylbenzoyl)-phenylphosphineoxide (Irgacure 819, 3 wt.%) was added as a photoinitiator. 100-200 µL of the solution was cast on a clean glass substrate of 3 x 3 cm and spin-coated at 2000 rpm for 30 seconds. The temperature was then raised to 70 ^{0}C and the sample was photo-polymerized using an EXFO Omnicure S2000 lamp with 8 mW·cm^{-2} of intensity for 10 minutes using a 405 nm cut-off filter. The sample resulted in a bright orange non-soluble polymer that was released from the glass as a self-standing film. Then, the sample was placed in DMSO and shacked for 3h to remove the template. Lastly, the DMSO was extracted, and the sample was dried in a vacuum oven at 40 ^{0}C.

UV-Vis switching experiment

The photo-initiated switching between *trans* and *cis* was measured by making a solution of 3 in 10 ml chloroform (93.01 µM). The UV-Vis spectrum was measured with a baseline set for chloroform. *Trans* to *cis* switching was measured by irradiating with 365 nm UV-light (700 mA) for respectively 5, 10, 15, 30, 60 seconds and measuring a new UV-Vis spectrum after each irradiation time. *Cis* to *trans* switching was measured by first irradiating the sample for 2 minutes with UV-light (365 nm) and then irradiating the sample 5, 10, 15, 30 and 60 seconds with the blue light of 450 nm (350 mA) and measuring the UV-Vis spectra.

The photo and back isomerization between *trans* and *cis* of the polymer were measured in solid-state onto glass substrates via UV-Vis spectroscopy. The baseline is set for the clean glass. *Trans* to *cis* switching was measured by irradiating with 365 nm UV light (700 mA) for 4h and taking a new UV-Vis spectrum every 5, 10, or 20 minutes in the end due to the stabilization. *Cis* to *trans* back switching was measured by first irradiating the sample for 4 hours with UV-light (365 nm) and then in the dark a spectrum was taken every 30 minutes for 9 hours.

Cis - trans decay experiment

Cis - trans decay experiments were performed by irradiating a solution of **Azoac** in chloroform (20 mg/10 ml) and a sample of the polymer film of **Azoac₃TB** (1 cm^2) with UV-light of 365 nm (700 mA) for 5 minutes and 1.5 h respectively. The intensity in UV-

Vis at 377 nm was measured upon time every minute to get the decay curve, fitted with the exponential model of the half-life.

Dye-Selectivity tests

Measurements were done in a quartz cuvette and stirred at 400 rpm. Concentrations were calculated from the molar extinction coefficient of Rhodamine 6G at 474 nm using Lambert-Beer's Law in water. The mass of the films was weighed on a microbalance before the measurement. The volume was kept constant at 3 ml. For adsorption measurements, the initial concentration of the dye was 10 µM (40 mg·L^{-1}) and the absorbance was measured every minute for 10 h. Measurements were done over time at room temperature for a sample before irradiation (*trans* isomer) and after irradiation with UV-light for 6 hours (*cis* isomer).

Synthetic procedures

Ethyl (E)-4-((2,3,4-trihydroxyphenyl)diazenyl) benzoate (1):

The synthesis and characterization of tris-benzimidazolyl benzene core (**TB**) has been reported.[22] To a stirred solution of ethylaminobenzoate (5.71 g; 34.5 mmol; 1.0 equiv.) in H_2O (17 ml), 23 ml of a 3M HCl (2.0 equiv.) was added. A solution of $NaNO_2$ (2.87 g; 41.6 mmol; 1.2 equiv.) in H_2O (15 ml) was added dropwise to the solution. The mixture was stirred for 30 minutes at a temperature below 5°C. Then pyrogallol (4.44 g; 35.2 mmol; 1.0 eq) was added and was reacted for 1 h (<5 °C). After completion of the reaction, saturated $NaHCO_3$ was added to reach pH ~ 6 and the suspension was filtered to obtain a solid. The solids were washed 3 times with 50 ml water and then freeze-dried. The crude compound was purified by flash column chromatography (chloroform/EtOH, 99:1 to 9:1, in 20 CV) to obtain a dark brown solid (938 mg, 10%). ^1H-NMR (acetone-d_6, 400 MHz): δ= 8.18 (d, 2H, J = 8.8 Hz, 2 × CH arom.), 7.95 (d, 2H, J = 8.7 Hz, 2 × CH arom.), 7.39 (d, 1H, J = 9.0 Hz, CH arom.) 6.68 (d, 1H, J = 9.0 Hz, CH arom.), 4.39 (q, 2H, J = 7.1 Hz and 14.3 Hz , O-CH_2-CH_3), 1.40 (t, 3H, J = 7.1 Hz, CH_3-CH_2). ^{13}C-NMR (acetone-d_6, 100 MHz): δ= 165.9, 157.0, 152.3, 140.1, 136.3, 132.3, 130.2, 122.9, 118.4, 119.1, 110.2, 60.9, 14.1.

Ethyl (E)-4-((2,3,4-tris(undec-10-en-1-yloxy)phenyl)diazenyl) benzoate (2):

To a stirred solution of **1** (400 mg; 1.32 mmol; 1.0 equiv.) in DMF (10.5 ml), K_2CO_3 (1.927 g; 13.9 mmol; 10.0 equiv.) and 11-bromo-1-undecene (1.008 g; 4.32 mmol; 3.3 equiv.) were added. The resulting mixture was heated at 110°C overnight, cooled to room temperature and after removing the solvent under vacuum evaporation, it was purified by flash column chromatography (heptane/ethyl acetate 97:3) to obtain **2** as an orange oil (569 mg, 57%) ^1H-NMR (CDCl$_3$, 400 MHz): δ = 8.17 (d, 2H, J = 8.8 Hz, 2 × CH arom.), 7.91 (d, 2H, J = 8.6 Hz, 2 × CH arom.), 7.50 (d, 1H, J = 9.2 Hz, CH arom.), 6.70 (d, 1H, J = 9.3 Hz, CH arom.), 5.81 (m, 3H, CH_2=CH-CH_2), 4.95 (dd, 6H, J = 10.3 Hz and 17.1 Hz,

3 × CH$_2$=CH), 4.40 (q, 2H, J = 7.1 Hz and 14.2 Hz, O-CH$_2$-CH$_3$), 4.25 (t, 2H, J = 65 Hz , O-CH$_2$-CH$_2$), 4.05 (m, 4H, O-CH$_2$-CH$_2$), 2.04 (m, 6H, 3 × O-CH$_2$-CH$_2$-CH$_2$), 1.83 (m, 6H, 3 × CH-CH$_2$-CH$_2$), 1.51 (m, 6H, 3 × CH$_2$-CH$_2$-CH$_2$), 1.42 (t, 3H, J = 7.2 Hz, CH$_3$-CH$_2$), 1.32 (m, 30H, 15 × CH$_2$-CH$_2$-CH$_2$). ^{13}C-NMR (CDCl$_3$, 100 MHz): δ = 166.1, 157.0, 155.6, 153.2, 142.2, 141.0, 139.2, 131.5, 130.5, 122.5, 114.2, 111.6, 107.7, 76.3, 74.0, 68.9, 61.1, 33.8, 30.4, 29.7, 29.6, 29.5, 29.4, 29.3, 29.2, 29.1, 29.0, 28.9, 28.7, 28.5, 26.2, 25.8. ATR FT-IR: 3077, 2978, 2924, 2853, 1718, 1639, 1582, 1490, 1466, 1438, 1404, 1365, 1270, 1242, 1196, 1174, 1148, 1091, 1016, 992, 908, 862, 801, 772, 722, 696, 630, 599, 559, 522 cm^{-1}. MALDI-TOF MS: m/z calculated for C$_{48}$H$_{74}$N$_2$O$_5$ (M+H)$^+$: 759.57 found : 759.59, (M+Na)$^+$: 781.55, found : 781.57.

(E)-4-((2,3,4-tris(undec-10-en-1-yloxy)phenyl)diazinyl) benzoic acid (Azoac):

A solution of ethyl-4-((2,3,4-tris-(undec-10-en-1-yloxy)phenyl)diazenyl)benzoate **2** (470 mg; 0.62 mmol; 1.0 equiv.) in EtOH/MeOH/H$_2$O (6:3:1 v/v, 30 ml) was treated with KOH (311 mg; 5.54 mmol; 8.9 equiv.) and heated to reflux (70 °C) for 5 hours. After completion of the hydrolysis 5.5 ml of 1M HCl was added to reach pH around 3. The resulting solids were washed with H$_2$O (3 × 10 ml) and then freeze-dried to obtain the final compound as an orange powder (314 mg, 69%). ^{1}H-NMR (CDCl$_3$, 400 MHz): δ = 8.24 (d, 2H, J = 8.6 Hz, 2 × CH arom.), 7.94 (d, 2H, J = 8.6 Hz, 2 × CH arom.), 7.52 (d, 1H, J = 9.2 Hz, CH arom.), 6.71 (d, 1H, J = 9.3 Hz, CH arom.), 5.81 (m, 3H, CH$_2$=CH-CH$_2$), 4.96 (m, 6H , 3 × CH$_2$=CH), 4.25(t, 2H, J = 6.5 Hz, O-CH$_2$-CH$_2$), 4.06(m, 4H, O-CH$_2$-CH$_2$), 2.04 (m, 6H, CH$_2$-CH$_2$-CH$_2$), 1.83 (m, 6H, CH-CH$_2$-CH$_2$), 1.58 (m, 6H, CH$_2$-CH$_2$-CH$_2$), 1.32(m, 30H, CH$_2$-CH$_2$-CH$_2$). ^{13}C-NMR (CDCl$_3$, 100 MHz): δ = 171.2, 157.1, 156.1, 153.3, 142.2, 141.1, 139.2, 131.2, 130.4, 122.6, 114.1, 111.7, 107,8, 74.0, 69.0, 33.8, 30.4, 30.3, 29.7, 29.6, 29.5, 29.4, 29.3, 29.2, 29.1, 29.0, 26.2, 26.1. ATR FT-IR: 3079, 2977, 2921, 2850, 2659, 2540, 1684, 1640, 1600, 1586, 1491, 1466, 1443, 1419, 1382, 1282, 1248, 1197, 1152, 1095, 1039, 1011, 990, 964, 909, 863, 832, 800, 772, 756, 719, 697, 672, 656, 630, 549, 524, 508, 482 cm^{-1}. MALDI-TOF MS: m/z calculated for C$_{46}$H$_{70}$N$_2$O$_5$ (M+H)$^+$: 731.54, found : 731.55.

.

4.6 References

[1]   E. A. Jackson, M. A. Hillmyer, *ACS Nano* **2010**, *4*, 3548.
[2]   L. A. Curtiss, N. A. Monteiro-riviere, *Nanomedicine and Nanobiotechnology* **2009**, *1*, 568.
[3]   A. Mozalev, S. Magaino, H. Imai, **2001**, *46*, 2825.
[4]   A. P. H. J. Schenning, Y. C. Gonzalez-Lemus, I. K. Shishmanova, D. J. Broer, *Liq. Cryst.* **2011**, *38*, 1627.
[5]   Ł. Laskowski, M. Laskowska, N. Vila, M. Schabikowski, A. Walcarius, *Molecules* **2019**, *24*, 1.
[6]   K. Na, M. Choi, R. Ryoo, *Microporous Mesoporous Mater.* **2013**, *166*, 3.
[7]   F. Ercole, T. P. Davis, R. A. Evans, *Polym. Chem.* **2010**, *1*, 37.
[8]   H. M. D. Bandara, S. C. Burdette, *Chem. Soc. Rev.* **2012**, *41*, 1809.
[9]   M. K. Purkait, M. K. Sinha, P. Mondal, R. Singh, *Introduction to Membranes*, Vol. 25, **2018**.
[10]   F. Leyssner, S. Hagen, J. Dokic, P. Saalfrank, M. V Peters, S. Hecht, T. Klamroth, P. Tegeder, **2010**, 1231.
[11]   P. C. Yang, C. L. Lee, W. C. Chen, C. Y. Lin, *Can. J. Chem. Eng.* **2013**, *91*, 1513.
[12]   D. J. Van Dijken, P. Kovar, S. P. Ihrig, S. Hecht, **2015**.
[13]   Optical Switching and Image Storage by Means of Azobenzene Liquid-Crystal Films Author (s): Tomiki Ikeda and Osamu Tsutsumi Published by : American Association for the Advancement of Science Stable URL : http://www.jstor.org/stable/2887854 Optical Switc, **2017**, *268*, 1873.
[14]   M. Poprawa-smoluch, J. Baggerman, H. Zhang, H. P. A. Maas, L. De Cola, A. M. Brouwer, **2006**, 11926.
[15]   P. J. Coelho, C. M. Sousa, M. C. R. Castro, A. M. C. Fonseca, M. M. M. Raposo, 1.
[16]   E. Merino, M. Ribagorda, *J. Org. Chem.* **2012**, *8*, 1071.
[17]   T. Fukaminato, E. Tateyama, N. Tamaoki, *Chem. Commun.* **2012**, *48*, 10874.
[18]   M. Natali, S. Giordani, **2012**, 4010.
[19]   H. P. C. Van Kuringen, Z. J. W. A. Leijten, A. H. Gelebart, D. J. Mulder, G. Portale, D. J. Broer, A. P. H. J. Schenning, *Macromolecules* **2015**, *48*, 4073.
[20]   G. M. Bögels, J. A. M. Lugger, O. J. G. M. Goor, R. P. Sijbesma, *Adv. Funct. Mater.* **2016**, *26*, 8023.
[21]   F. De Ciencias, U. De Valladolid, P. Vasco, D. De Fı, F. De Ciencia, **2010**, *II*, 8904.
[22]   R. K. Balasainath, Regiospecific Synthesis of Ortho Substituted Phenols, Western Kentucky University, **2011**.
[23]   J. Dong, Y. Ozaki, K. Nakashima, **1997**, *9297*, 1111.
[24]   K. B. Wagener, J. M. Boncella, J. G. Nel, *Macromolecules* **1991**, *24*, 2649.
[25]   N. Gimeno, P. Formentín, J. H. G. Steinke, R. Vilar, **2007**, 918.
[26]   C. E. Hoyle, C. N. Bowman, *Angew. Chemie - Int. Ed.* **2010**, *49*, 1540.
[27]   I. Gracia, P. Romero, J. L. Serrano, J. Barberá, A. Omenat, *J. Mater. Chem. C* **2017**, *5*, 2033.
[28]   C. Decker, K. Moussa, *Die Makromol. Chemie* **1988**, *189*, 2381.
[29]   M. Gupta, S. P. Gupta, S. K. Pal, *J. Phys. Chem. B* **2017**, *121*, 8593.
[30]   Z. Li, Y. Zhang, L. Zhu, T. Shen, H. Zhang, **2010**, *1*, 1501.
[31]   J. García-amorós, D. Velasco, *Beilstein J. Org. Chem* **2012**, 1003.
[32]   C. S. Paik, H. Morawetz, *Macromolecules* **1972**, *5*, 171.
[33]   G. C. Henk J. Haitjema, Gijs L. von Morgen, Y. Yong Tan, *Macromolecules* **1994**, *27*, 6201.
[34]   A. Miniewicz, H. Orlikowska, A. Sobolewska, S. Bartkiewicz, *Phys. Chem. Chem. Phys.* **2018**, *20*, 2904.
[35]   J. Henzl, M. Mehlhorn, H. Gawronski, K. H. Rieder, K. Morgenstern, *Angew. Chemie - Int. Ed.* **2006**, *45*, 603.
[36]   J. A. M. Lugger, Nanoporous films from discotic liquid crystals, PhD Thesis, Eindhoven, **2018**.

Chapter 5

Photo-switchable nanofiltration membranes based on columnar LC with azo moieties
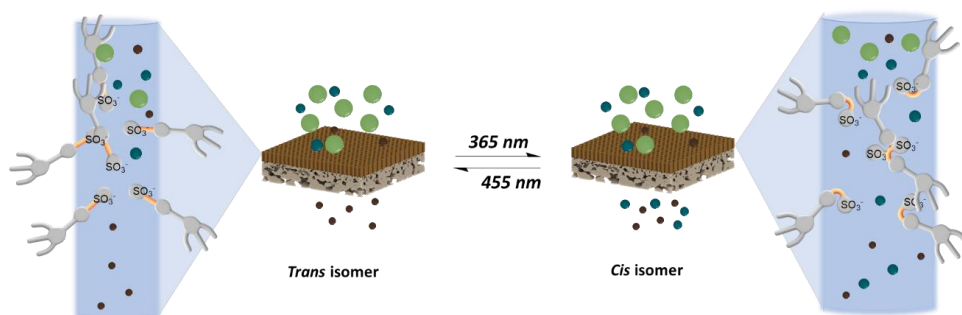
Abstract | In this Chapter, a reversible and photo-switchable water filtration membrane based on templated liquid crystals is presented. The membrane is fabricated by crosslinking a columnar network, which is obtained by the self-assembly of a discotic supramolecular complex containing an azo photo-responsive moiety **SulfAzo₃TB**, on top of a porous support. Due to the reversibility and the stability of the photoswitched isomers in the crosslinked system, the filtration performance of the membrane in each isomeric state could be evaluated. The results showed a light-induced reversible change in the water permeability and MWCO: pore size increases for *cis* isomer (1.4 nm) and decreases after relaxation back to *trans* (1.2 nm). The reversibility of the rejection properties is studied with the filtration of organic dyes: a size and charge based selectivity is proven, and more epecifically, with on-demand passage of Rhodamine B by light irradiation. The results show this material as a potential recyclable light-controlled separation system, that could be further applied to the selective filtration of certain contaminants in water.

5.1 Introduction: photo-responsive pores of membranes containing azo molecules

Smart materials are of increasing importance due to their ability to change properties under the influence of external stimuli.[1] The use of light, a versatile stimulus that can be applied locally and rapidly, has proven to be a clean and non-destructive manner to switch molecules between different states.[2] The incorporation of these molecules to give light-responsive materials has been exploited with significant benefits in many fields including drug delivery, sensing, remote actuators and robotics, microfluidics, data storage and water treatment.[2–4] The photo-switchable molecular moieties, isomerize reversibly upon irradiation at specific wavelengths, leading to changes of material properties on demand.[5] As reported in Chapter 4, azobenzenes are light-responsive compounds that reversibly isomerize from *trans* to *cis* by irradiation and revert to the *trans* form by thermal relaxation, accompanied by changes in geometry, polarity, and electrical properties.[6,7] Due to the stability, versatility and robustness of these chromophores, they have been included as photo-responsive moieties in materials where light produces changes in properties such as wettability, binding, shape, color, alignment, etc.[8][9] These light-induced changes in such polymers allow their application for instance as molecular actuators for soft-robotics,[10] up-take and release guests as drug delivery systems[11,12] or for biomimetic modification of surface properties,[13] among others.

The strong interest in sustainability and energy-saving in recent years has increased the need for efficient separation of molecular mixtures. Due to the efficient response to light stimuli and the easiness and economic benefits of photo-switching processes, the integration of molecular photo-switches in porous materials for their application as separation systems is highly appealing in many fields such as healthcare, wastewater treatment, food, medicine, catalysis, sensing, etc.[5,14] Nanoporous materials have shown changes in absorption selectivity towards molecules of different sizes due to changes in pore size and polarity.[15–18] In light-responsive membranes properties such as the diffusion and transport of solutes through the pores can be tuned with simple irradiation.[19–22] Photo-responsive membranes can be made either by incorporation of molecular photo-switches during their synthesis, or by grafting photo-responsive polymers on the membrane surface after their preparation. As an example of the first strategy, molecular recognition materials with photo-switchable properties have been made by molecular imprinting, allowing specific binding interactions with target molecules.[23] The grafting strategy, on the other hand, has been used to tune wettability and other surface properties to create self-cleaning or antifouling membranes.[24] The pores in a photo-switchable membrane can also act as photoresponsive valves allowing the regulated transport of molecules. Gating channels with reversible opening and closing have been successfully developed using

polyelectrolyte and inorganic nanoporous membranes containing azo moieties. However, photo-switching has not been used as a dynamic process that permits control over the passage of solutes in water filtration membranes yet.[25–28]

In Chapter 2, the use of columnar liquid crystals (CLCs) to develop supported membranes for water filtration with charge and size selectivity in the filtration of organic molecules was shown. Moreover, the photo-switchable properties of porous films of a similar templated system containing azo moieties, **Azoac₃TB,** were described in Chapter 4. In the current Chapter, the development of a photo-responsive filtration membrane based on a new supramolecular columnar liquid crystal **SulfAzo₃TB** is reported with full characterization of the photo-induced isomerization of the supramolecular system in solution and the crosslinked network. The photo-isomerization of the azo moieties in the membrane leads to stable, yet reversible changes in pore size that last for several hours, hence controlling the selectivity towards small organic molecules in the membrane with light (**Figure 5.1**). The results shown here, pave the path towards a dynamic separation system for water purification.
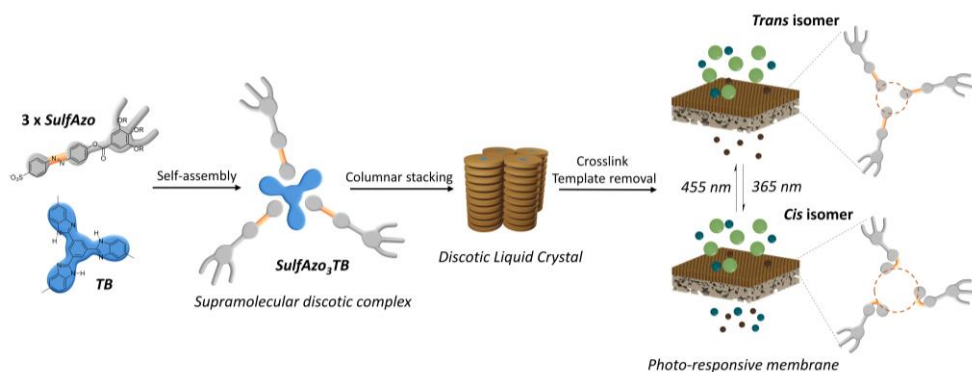
Figure 5.1 | Schematic representation of the photo-switchable supramolecular complex formation, which forms a columnar mesophase that is transferred into support and crosslinked with UV light. The *trans-cis* isomerization of azo moieties with UV light in the filtration membrane changes the permeability of solutes.

5.2 Design and characterization of SulfAzo₃TB complex

5.2.1 Synthesis and characterization of Azoac

The supramolecular complex **SulfAzo₃TB** is composed of two molecules: a tris-benzimidazolyl benzene core molecule (**TB**), that acts as the template, and the wedge-shaped monomer **SulfAzo** containing an azo moiety and double bonds in the alkyl chains for later crosslinking. Both molecules were synthesized separately: **TB** was

synthesized as previously reported[29] and **SulfAzo** was prepared following a 3-step synthetic route shown in **Scheme 5.1**.
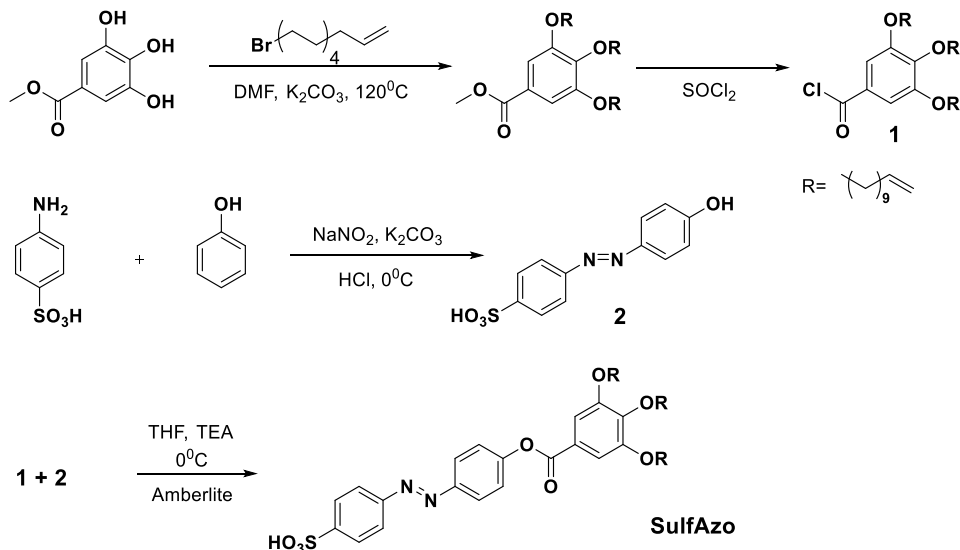
Scheme 5.1 | Synthesis of wedge-shaped azo derivative **SulfAzo.**

Acid chloride derivative **1** was obtained from the alkylation of the hydroxyl groups of methyl gallate with 11-bromo-1-undecene followed by chlorination of the tris-alkene ester (see Chapter 2). The diazonium salt for diazo coupling was prepared by the diazotization of p-aminobenzene sulfonate with sodium nitrite. Subsequently, this salt was reacted with phenol to yield azo product **2** as an orange powder after precipitation and drying under vacuum.[30] Finally, compounds **2** and **1 reacted in** THF and TEA to give the salt of **SulfAzo**. After ion-exchange on Amberlite IR 120 (acidic form) the photo-switchable sulfonic acid (**SulfAzo**) was obtained.

Polarized optical microscopy (POM) and Differential scanning calorimetry (DSC) were used to study the thermal and liquid crystalline properties of the compound. Similar compounds are reported to be liquid crystalline due to the amphiphilicity of the wedge-shaped molecules that promote specifically columnar arrangements in supramolecular complexes.[31],[32] The results of the DSC and POM indicated the formation of a mesophase in the cooling cycle at 70 ^{0}C and a cold crystallization in the heating at 10 ^{0}C; hence **SulfAzo** is liquid crystalline at room temperature (**Figure 5.2a and 5.2b).** X-ray diffraction studies showed the formation of a columnar rectangular mesophase room temperature after annealing **(Figure 5.2c).**
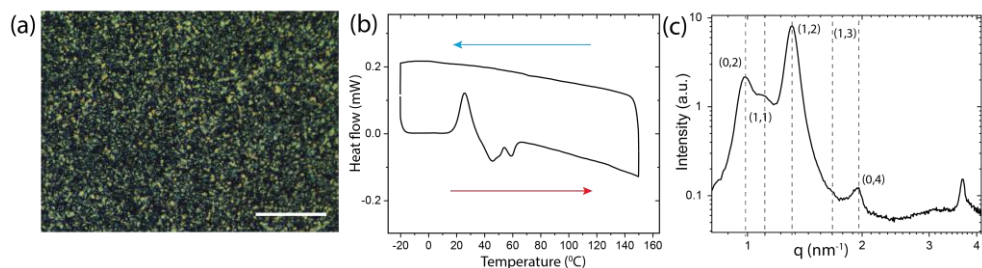
Figure 5.2 | a) Polarized light micrograph of **SulfAzo** (and molecular structure illustration) at room temperature with a scale bar of 50 μm; b) DSC of the second cycle of **SulfAzo** at 10 °C/min and c) MAXS pattern of **SulfAzo** after thermal annealing.

5.2.2 Formation of SulfAzo₃TB complex

A mixture of **TB** with 3.2 equiv. of **SulfAzo** afforded a H-bonded 1:3 complex (**Figure 5.3a**) as is evidenced from a new band at 3250 cm⁻¹ in the FT-IR spectrum (**Figure 5.3b**), which corresponds to the imidazolium N^+-H stretching vibration.[33] The addition of a small excess (3.2 instead of 3 equiv.) of **SulfAzo** prevented phase separation of crystalline **TB**.[33] The observation of the complex under the POM at room temperature showed a mosaic-like shaped texture typical for columnar mesophases (**Figure 5.3c**). X-ray diffraction data showed the formation of a columnar rectangular mesophase after annealing at 80 °C (**Table 5.1**).
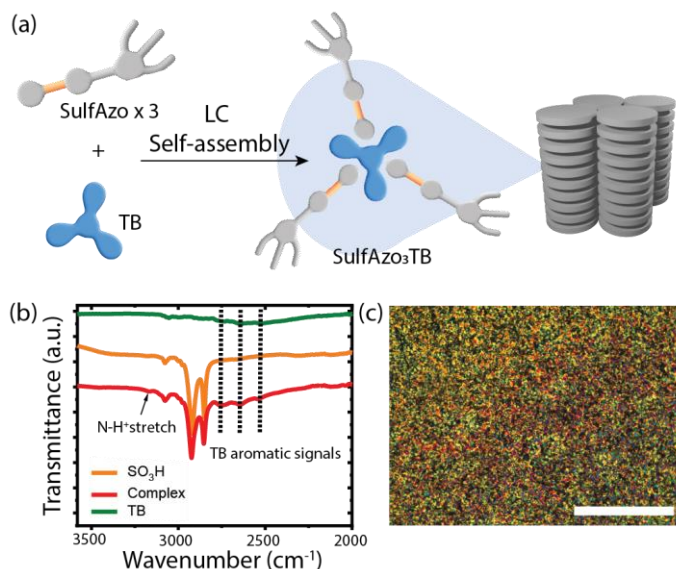
Figure 5.3 | a) Formation of the supramolecular discotic complex **SulfAzo₃TB** via H-bonding; b) IR spectra of **SulfAzo**, **TB** and the 3:1 mixture indicating the formation of a H-bonded complex; c) cross-polarized light micrograph of a 3.2:1 mixture of **SulfAzo** and **TB** at room temperature with a scale bar of 50 μm.

Table 5.1 | XRD data of **SulfAzo$_3$TB** at 80^{0}C after annealing:

Temperature	q (nm^{-1})	d$_{exp}$ (nm)	d$_{calc}$ (nm)	h	k	Lattice parameters (nm)
80^{0}C	1.14	5.32	5.32	0	1	Columnar rectangular
	1.31	4.79	4.79	1	0	
	2.35	2.73	2.86	0	2	a=4.79
	3.56	1.79	1.77	2	0	b=5.32

5.2.3 Formation of nanoporous films by photo-polymerization

Nanoporous polymer films were obtained from the columnar mesophase of the complex using the photochemical thiol-ene click reaction as crosslinking method (**Figure 5.4a**).[34] A mixture containing 1 equiv. of **TB**, 3.2 equiv. of **SulfAzo**, 4.5 equiv. of 1,10-decanedithiol as crosslinker, and 2 wt.% Irgacure 819 photoinitiator in CHCl$_3$:EtOH (9:1) was cast in glass molds (1 mm × 1 mm). The solvent was slowly evaporated in a heating plate at 70 ^{0}C, and the drop-cast films (thickness 0.5-1 μm) were irradiated with UV light for 15 minutes. The obtained dry films (**Figure 5.4b**) showed under the POM typical textures of a columnar mesophase (**Figure 5.4c**). The disappearance of the C=C bending band at 907 cm^{-1} in the FTIR spectrum indicated almost full conversion of the alkene groups (**Figure 5.4d**).[35] Finally, a porous polymer was obtained after removal of the **TB** template by soaking the film in DMSO for 2 h, followed by a washing step with water and drying in vacuum. FT-IR showed full disappearance of the N$^+$-H stretching band at 3250 cm^{-1}, confirming template removal.

WAXS studies were carried out to check the retention of the columnar order after crosslinking and removal of the template (**Figure 5.4e**). Polymerization affected the columnar order with a shift of the lattice spacing d$_{010}$ from 4.42 nm to 4.84 nm, indicating a 10% increase in periodicity. When the **TB** template was removed, the q-value of the first maximum increased further to 5.08 nm. A reflection from the inter-disk distance at wide angles is slightly visible as a shoulder at *d*=0.34 nm for the polymerized material, indicating some order in the stacking of the columns.
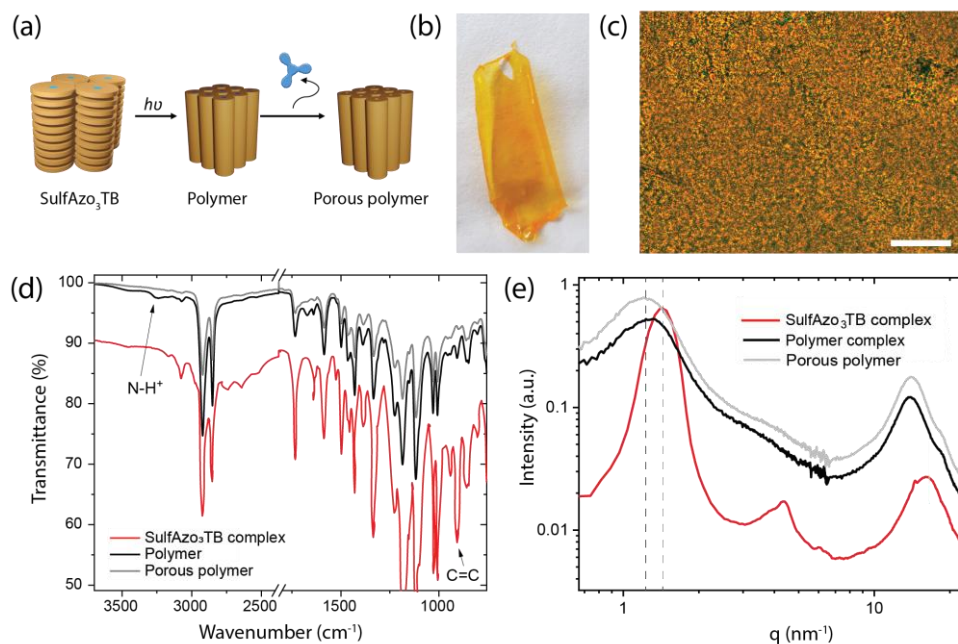
Figure 5.4 | a) Crosslinking of the columnar mesophase and consecutive removal of the **TB** template molecule; b) Sample of the polymer film; c) POM picture of the film showing a mosaic-like texture with small domains. Scale bar is 50 μm; d) FT-IR spectra comparing **SulfAzo₃TB** before and after polymerization where the =C-H stretching band of the double bond disappeared. After removing **TB**, the peak corresponding to N-H⁺ also disappeared; e) 1D WAXS of the polymerization mixture (red), after polymerization (black) and after template removal (grey).

5.2.4 Photo-isomerization of the monomer in solution and of the fixed complex in nanoporous films

Photo-isomerization of the azo group is responsible for inducing changes in the pores. Isomerization was studied in the monomer as well as in the thin film as their photophysical properties can be different.[18] The UV-Vis spectrum of a 100 μM chloroform solution of **SulfAzo** showed an intense $\pi \rightarrow \pi^*$ absorption band at 325 nm corresponding to the *trans* isomer and a much weaker $n \rightarrow \pi^*$ band at 465 nm (red curve, **Figure 5.5**).[36] Upon irradiation of the solution with 365 nm UV light the intensity of the $\pi - \pi^*$ transition band at 325 nm decreased strongly, indicating *trans-cis* isomerization. After 15 minutes, a photo-stationary state was reached (blue curve, **Figure 5.5**) with the decrease of the 325 nm absorption band and a slight increase at 440 nm as the result of *trans-cis* photo-isomerization. The sample was let relax back in the dark, showing an increase of the 325 nm band but the total conversion was not reached, and only 52% of the population of the *trans* isomer was recovered after 20h.

This suggests that longer times are needed for the full recovery of the *trans* isomerization form. However, by irradiation of the solution with 455 nm blue light, the process was accelerated, reaching the complete recovery of the *trans* population in only 15 minutes (dashed line **Figure 5.5**).

In order to study both states of a photo-switchable membrane, the lifetime of each *trans* and *cis* isomers must be sufficient. Therefore, the thermal relaxation of the azobenzene was investigated for **SulfAzo** to obtain the lifetime of the *cis* isomer by monitoring the change in absorption at 325 nm. The data was fitted with the exponential model used in Chapter 4, yielding a lifetime for the *cis* isomer of 7.1 h at room temperature (**Figure 5.7.a**). The observed reversibility of the isomerization process and the lifetime value obtained are in line with the compound shown in Chapter 4.[18]
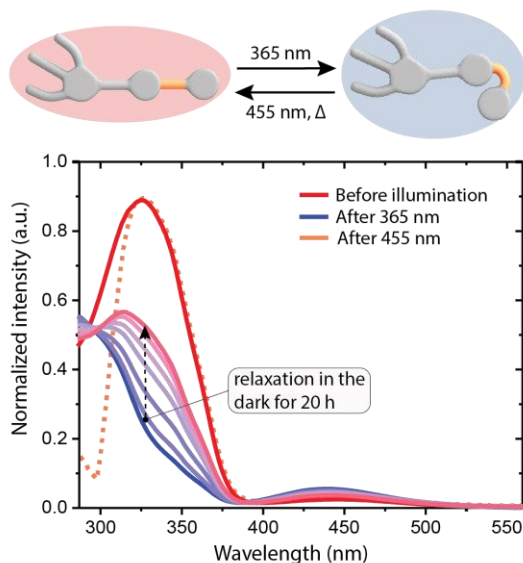
Figure 5.5 | UV-Vis spectra of **AzoSulf** in CHCl₃ after 365 nm light irradiation for 15 minutes, after thermal relaxation up to 20 h and after 455 nm irradiation for 15 minutes (dashed line).

The photo-switchable characteristics were also studied in thin films (thickness ~ 0.5 µm) of the porous polymer with **SulfAzo₃TB** complex (**Figure 5.6**), revealing a similar behavior than for **SulfAzo** in solution. Upon irradiation at 365 nm, the intensity of the band at 325 nm decreased to *cis* in 1 h, a bit longer than in solution due to the restricted movement in the crosslinked network. When the *cis*-enriched film was allowed to relax back thermally at room temperature in the dark, the initial *trans* state was not reached even for long times (after 36 h there is still 50% of *cis* isomer present). The thermal relaxation data was plotted and fitted with an exponential model in the

same way as for the monomer in solution showing a lifetime of 5.7 h (**Figure 5.7**). *Cis-trans* isomerization was complete after only 15 minutes when the film was irradiated with 455 nm light. The slightly shorter lifetime of the *cis* isomer in the polymer compared to in solution is related to a restriction of the molecular movement in solid state, as observed in similar networks.[18,37,38] However, lifetime of each state was sufficient to study the filtration properties in supported membranes in the pure *trans* and the *cis* enriched films separately.
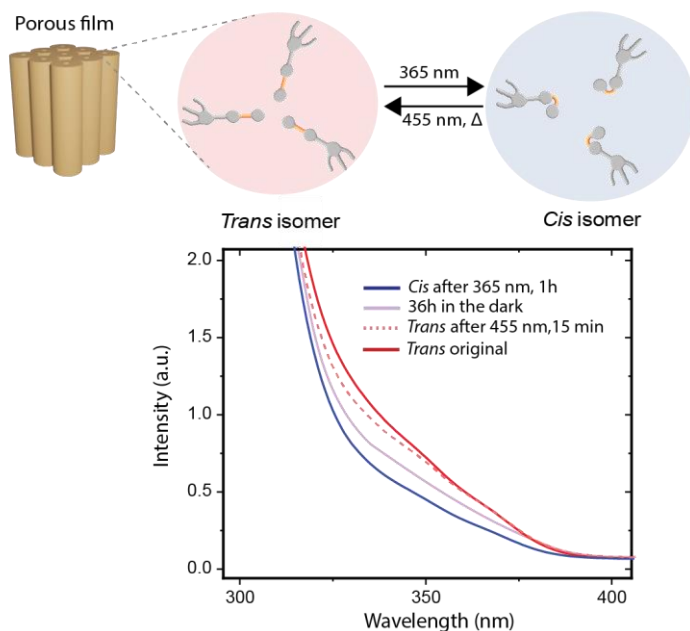
Figure 5.6 | UV-Vis spectra of **SulfAzo₃TB** films of irradiation at 365 nm for 1 hour to reach the *cis* isomer, thermal relaxation for 36 h without reaching total conversion to *trans* isomer and after 15 minutes of 455 nm with a total recovery of the *trans* population.
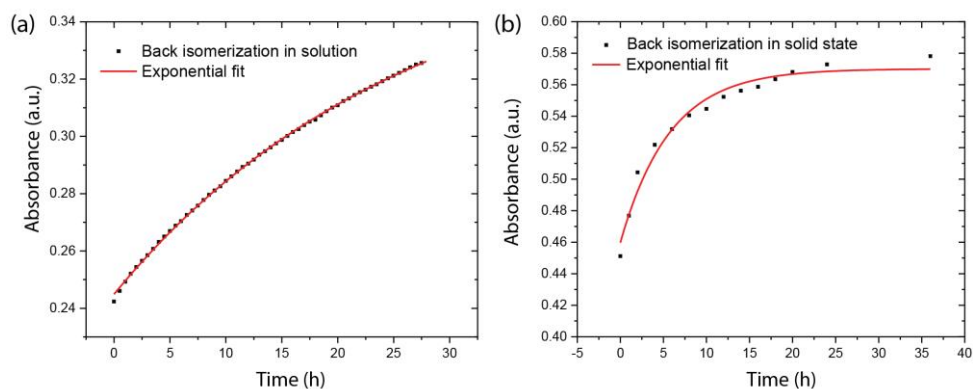
Figure 5.7 | Plot of the absorbance vs time at 325 nm in the dark at room temperature of a) **Sulfac** in $CHCl_3$ and b) porous film of crosslinked **Sulfac$_3$TB** system in black and fitting to exponential decay curves in red.

X-ray diffraction measurements of the films were performed to study whether the photoisomerization process affected the morphology of the network at room temperature. In **Figure 5.8** the WAXS pattern of the nanoporous film before and after irradiation at 365 nm is shown. An increase of the lattice parameter (lower q value for the first diffraction peak) was observed after photoisomerization to the *cis* isomer (from d_{010} = 4.39 nm to 5.38 nm). When the film was irradiated with 455 nm light to go back to the *trans* isomer, the initial lattice spacing was almost recovered (*a trans* back = 4.79 nm). These results confirm that the reversibility of the isomerization process translates to a reversible change of the nanostructure with light irradiation, which is probably related to a change in pore size.
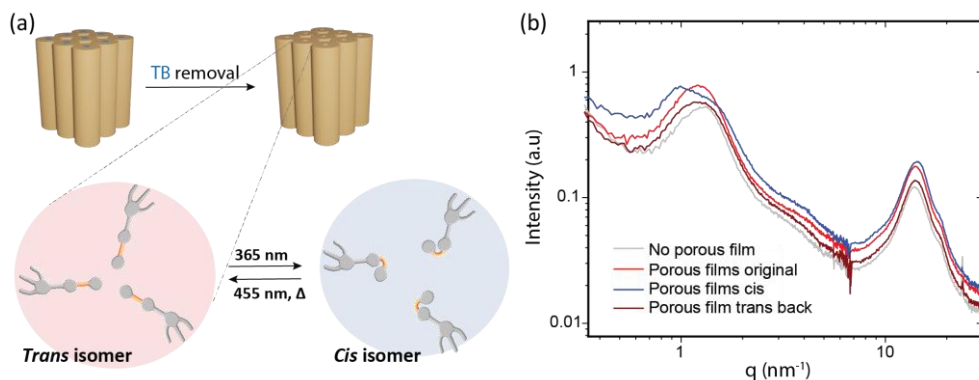
Figure 5.8 | a) Schematic representation of photoswitching of azo moieties in the porous polymer, b) WAXS pattern of the polymer before and after UV irradiation corresponding to the *trans* and *cis* state respectively at room temperature.

5.3 Membrane formation and filtration performance

Polyethersulfone (PES)-supported membranes for water filtration were fabricated by following the process detailed in Chapter 2 (**Figure 5.9a**). High-resolution Scanning Electron Microscopy (HR-SEM) showed an average thickness of the active layer of approximately 300 nm. This film was successfully transferred to a porous PES support layer of around 300 μm thickness (**Figure 5.9b**).

(a)

1. Spin coating LC mixture
on PVA-coated glass

2. Transfer to PES support
applying heat and pressure

3. UV photo-polymerization
to crosslink network

(b)
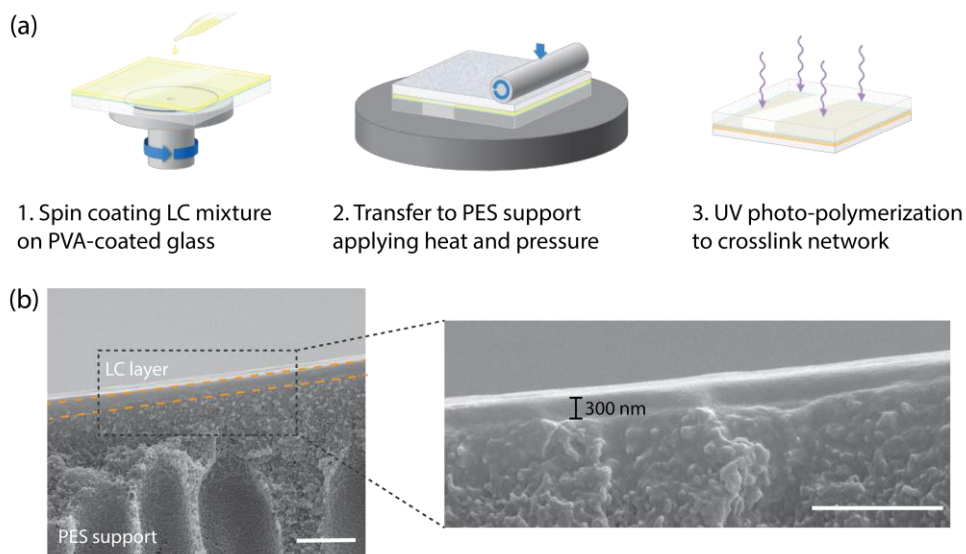
Figure 5.9 | a) Membrane fabrication process where the LC solution is spin-coated and later transferred to a PES support and b) Zoom out and zoom in HR-SEM images showing a perfectly defined and attached 300 nm active layer on top of the support with scale bars of 1 μm and 500 nm respectively.

5.3.1 Effect of photo-switching on filtration properties

The long lifetime of 5.7 h for the *cis* isomer makes it possible to study filtration in these isomeric states of the membrane, while accelerated and complete isomerization back to the *trans* state by irradiation at 455 nm allows for repeated switching between states. To verify the photo-responsiveness of the membrane, filtration tests were performed before and after UV and blue light irradiation as represented in **Figure 5.10**. The membrane was irradiated inside the filtration cell alternatingly with 365 nm and 455 nm light for 1h and 15 minutes respectively. The flux of pure water was measured over time for the different states of the membrane for 3 cycles (**Figure 5.10b**). A reproducible and stable pattern of higher and lower values of water flux (0.78 ± 0.004 and 0.64 ± 0.019 L·m^{-2}·h^{-1}·bar^{-1}) was observed for *cis* and *trans* states respectively, confirming that the flux is dependent on the state of the polymer and that this behavior is indeed reversible upon irradiation with a specific wavelength.
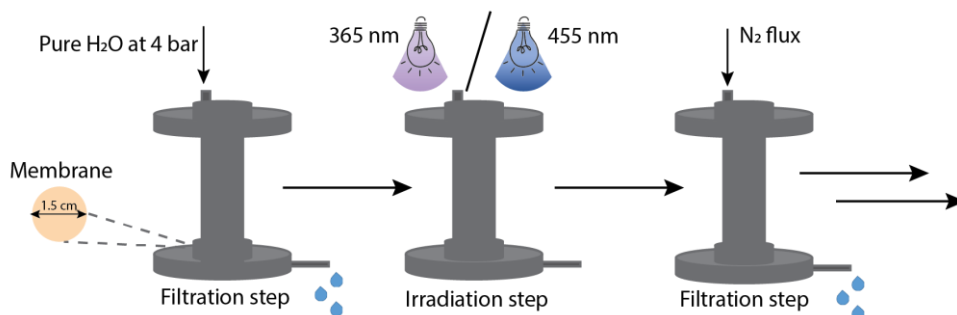
Figure 5.10 | (a) Schematic illustration of the filtration process with irradiation steps to switch *on-off* each isomerization state in the membrane.

The molecular weight cut-off (MWCO) of the membrane, which is the molecular weight at which 90% of a solute is rejected, was determined in both isomerization states. Filtration tests of a mixture of four PEGs with an M_n ranging from 600 to 7000 g·mol^{-1} were performed with both the *cis* and the *trans* state. The PEG rejection curves for the membrane before and after irradiation at 365 nm (*trans* followed by *cis*) and after irradiation with 455 nm light (back to *trans*) are represented in **Figure 5.11b**. At a specific PEG molecular weight, always a higher retention was obtained for the membrane in the *trans* state due to its smaller pore size. In line with this, over the full MWCO range, a higher MWCO value was observed for the *cis* state (~ 4000 g·mol^{-1}) compared to the *trans* state (~ 2000 g·mol^{-1}), which is in full agreement with the higher permeability for the *cis* membrane as shown in **Figure 5.11a**. Additionally, after the relaxation back to the *trans* state, a lower MWCO value was obtained again, very close to the initial value of the rejection curve in the *trans* state and confirming the reversibility of the process.

These observations are in line with the hypothesized changes in pore size due to the opening of the structure after isomerization from *trans* to *cis* . MWCO values of 1.2 nm and 1.6 nm are calculated for the *trans* and *cis* membranes respectively from relation between M_n PEG and pore size given by **equation 4** in Chapter 2.[39] Additionally, it is important to remark that the change in polarity in the azo surroundigs after isomerization can also affect the filtration process, as it was observed in Chapter 4 for the kinetics of absorption of Rhodamine 6G.
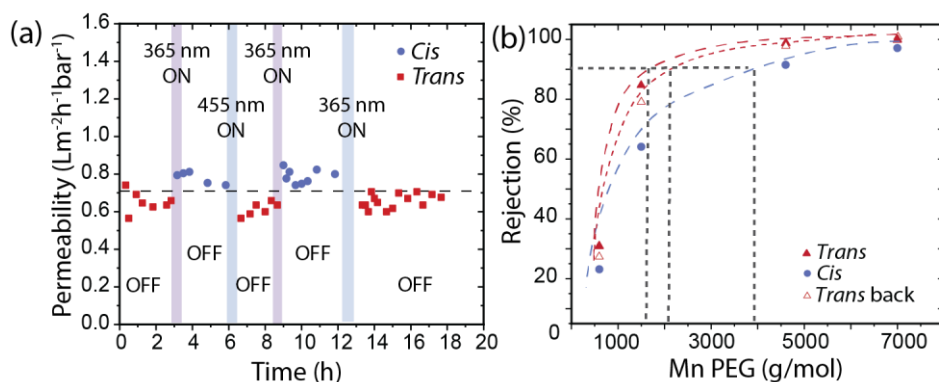
Figure 5.11 | a) Plot of pure water permeability as a function of time of the membrane while alternating UV (365 nm) and blue light (455 nm) to get *trans* and *cis* states; b) MWCO curves for the membrane in the initial *trºans* state (red filled triangles), after 1h of 365 nm irradiation in *cis* state (blue circles) and after 15 minutes of 455 nm in *trans* state back (red open triangles).

The effect of the isomeric state of the membrane (*cis* or *trans*) on the rejection of small organic molecules was also investigated (**Figure 5.12**). The filtration of aqueous solutions (50 µM) of 3 molecules of similar size, Riboflavin (**Rib**, 1.02 nm), Rose Bengal (**RB**, 1.08 nm) and Rhodamine B (**RhB**, 1.14 nm), was performed. In all cases, rejection in the *cis* membrane is lower, irrespective of the size of the dyes. The rejection increases again when the membrane is isomerized back to its *trans* state. The change in rejection between the *cis* and the *trans* state is for the largest dye (**RhB**), probably because the pore size of the *trans* state (1.2 nm) is close to the size of this dye (1.14 x 1.63 nm). The smaller dyes, **Rib** and **RB**, show a weaker dependence on the isomerization state. Rejection of the neutral dye **Rib**, especially in the *cis* state, is lower than that of the anionic **RB** as a result of the repulsion between the negatively charged **RB** and the sulfonate groups within the pores, in line with the observations in Chapter 2. The slightly higher transport for the *trans* state after irradiation than the initial *trans* can be attributed to incomplete recovery of the *trans* isomer after irradiation with 455 nm. These observations suggest that the strongest effects of pore size modulation can be expected for molecules that are close in size to the pore size of the membrane.
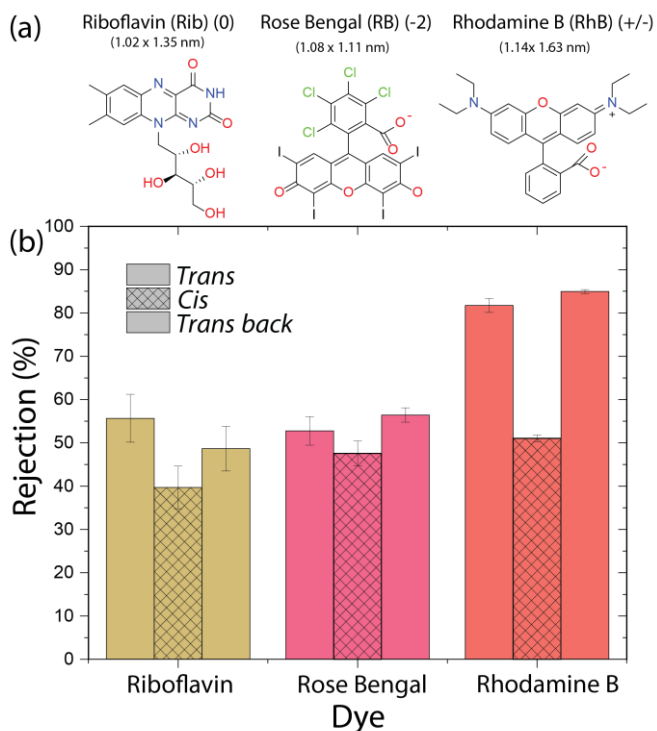
Figure 5.12 | a) Molecular structures of the riboflavin, Rhodamine B and Rose Bengal; b) Plot of the rejection % through the membrane before, after irradiation at 365 nm and after relaxation back to *trans* with 455 nm light.

5.4 Conclusions

In this Chapter, a reversible photo-switchable water filtration membrane based on a polymerized LC is presented. The supramolecular discotic liquid crystal (**SulfAzo₃TB**) containing azo moieties was used as the photo-responsive system. Crosslinking of the columnar network formed followed by the removal of the **TB** template led to a nanoporous material that was used as the active layer in a filtration membrane. The long lifetime of the *cis* isomer in solid state (5.7 h) allowed the study of the filtration properties of the membrane in each isomeric state. Light-induced reversible changes in the water permeability and the molecular transport of organic solutes were confirmed, proving this membrane as an effective light-controlled separation system. An easy and fast way to reverse selectivity and transport properties is offered by this dynamic membrane, which has much potential for water purification purposes. For instance, a possible application could be the selective removal of contaminants on-demand or recovery of valuable components, therefore helping to build up the circular economy we aim for sustainability.

5.5 Experimental section

5.5.1 Materials and methods

Chemicals and solvents were purchased from Sigma-Aldrich or bio-solve and used as received unless stated otherwise. NMR-spectra were recorded at room temperature on a Bruker, FT-NMR spectrometer AVANCE III HD-NanoBay (400MHz, Bruker UltraShield magnet, BBFO Probehead, BOSS1 shim assembly) in either acetone-d_6 or CDCl$_3$. The chemical shifts are given in ppm and the coupling constants as J in Hz. FT-IR spectra are measured on a Perkin Elmer Spectrum One spectrometer equipped with an attenuated total reflectance (ATR) sampling accessory. MALDI-TOF mass spectra were obtained on a PerSeptive Biosystems Voyager-DE PRO spectrometer with α-cyano-4-hydroxycinnamic acid as a matrix. Flash column chromatography was carried out using silica gel. Polarized optical microscopy (POM) images were recorded Jeneval microscope equipped with crossed polarizers and Polaroid CCD camera and a Linkam THMS 600 hot stage. DSC measurements were performed in aluminum sample pans using a TA instruments Q1000. All runs were performed with heating and cooling rates of 10 K min^{-1}. X-ray scattering measurements were performed on a Ganesha lab instrument equipped with a Genix-Cu ultra-low divergence source producing X-ray photons with a wavelength of 0.154 nm and flux of 1×10^8 photons s^{-1}. Diffraction patterns were collected using a Pilatus 300K silicon pixel detector with 487 x 619 pixels of 172 μm^2 in size, placed at a sample to detector distance of 91 mm (wide-angle, WAXS), or 500 mm (medium angle, MAXS). On the obtained diffraction patterns an azimuthal integration was performed, using SAXSGUI software, to calculate the intensity against the scattering vector q, where q=$(4\pi/\lambda)\sin\vartheta$ (ϑ is the angle of incidence and λ is the wavelength). The beam center and the q-range were calibrated using silver behenate ($d_{(100)}$ = 1.076 nm^{-1}; 5.839 nm), as a reference. The $d_{(300)}$ was used for calibration. The temperature was controlled with a Linkam HFSX350 heating stage and cooling unit. Measurements were performed on bulk samples sealed in 1.0 mm diameter glass capillaries (Hilgenberg) or directly on the polymer film. UV-Vis experiments were performed on a Jasco V-750 spectrophotometer. All experiments were performed in 10 × 10 mm quartz cuvette at 20°C and for the solid-state tests, a film of around 1-micron thick spin-coated on glass was used. The photopolymerization for both free-standing film and membrane was performed for 15 min with a mercury lamp (Omnicure s1000, emitting at 320−500 nm) which was provided with a 400 nm cutoff filter (Newport), to avoid the isomerization from *trans* to *cis* of the azobenzene moiety during polymerization. The intensity was approximately 22 mW·cm^{-2} at the sample surface.

5.5.2 Detailed experimental conditions

Film preparations

Clean glass substrates (3 x 3 cm) were prepared by washing with acetone and isopropanol and finally dried. The nanoporous materials were made by making a solution of 4-((2,3,4-tris(undec-10-en-1-yloxy)phenyl)diazenyl)-benzoic acid 3 (3.2 equiv.) and 1,10-decanedithiol (4.8 equiv.) in CHCl$_3$/MeOH (9:1 v/v) and adding this solution to the required amount of 1,3,5-tris(5-methyl-1H-benzo[*d*]imidazol-2-yl)benzene (**TB**, 1 equiv.) (50 mg·ml^{-1}). Finally, Bis(2,4,6-trimethylbenzoyl)-phenylphosphineoxide (Irgacure 819, 3 wt.%) was added as a photo-initiator. 100/200 µL of the solution was cast on a clean glass substrate of 3 x 3 cm and spin-coated at 2000 rpm for 30 seconds. The temperature was then raised to 70 ^{0}C and the sample was photo-polymerized using an EXFO Omnicure S2000 lamp with 8 mW·cm^{-2} of intensity, for 10 minutes, resulting in a bright orange non-soluble polymer. Then, the sample was placed in DMSO and shacked for 3h to remove the template. Lastly, the DMSO was extracted, and the sample was dried in a vacuum oven at 40 ^{o}C.

Membrane Fabrication

Glass plates were cleaned with acetone and isopropanol under sonication for 10 minutes in a bath. Solutions for spin coating were prepared by mixing **SulfAzo** (3.2 equiv.) with **TB** (1 equiv.) and 1,10-decanedithiol (4.6 equiv.) in DCE/EtOH (8:2 v/v) in a 10 wt. % concentration. Finally, Bis(2,4,6-trimethylbenzoyl)-phenylphosphineoxide (Irgacure 819, 3 wt.%) was added as the initiator. A sacrificial layer of PSS was used to avoid de-wetting of the monomer mixture afterward. A 10 wt.% aqueous solution was spin-coated on the clean glass at 1500 rpm for 60 s. Then the monomer mixture was spin-coated on top at 2500 rpm for 30 s. The resulting LC/PSS was *trans*ferred to a polyethersulfone (PES) support. The "sandwich" was heated to 70 ^{0}C and hand-pressed with a steal roller to help the transfer. After further cooling to room temperature, the membrane was polymerized with UV light for 15 min with 8 mW·cm^{-2} of intensity, which was provided with a 400 nm cutoff filter (Newport), to avoid *trans - cis* isomerization of the azobenzene moiety during polymerization.

The glass and PSS sacrificial layer were removed by immersing the composite membrane in water and the obtained membrane was dried in a vacuum oven at 40 ^{0}C.

Water filtration tests

Filtration tests were performed using a 20 ml custom-made, stainless steel, stirred "Amicon type" dead-end filtration cell of 1.5 cm diameter. Samples of the membrane were cut to the desired size and pre-cleaned with deionized water. For each filtration test, a membrane was placed in the cell which was filled with ultrapure water (total volume of 20 ml) and was pressurized with nitrogen at the desired pressure.

The permeability of the membranes was determined by measuring the flux of pure water at different pressures (1–5 bar) in an Amicon Cell set-up used previously. Membranes were previously shaken in NaOH (1M) for 2 hours to remove the template and subsequently were rinsed with water. Pure water was filtered for 2 h to stabilize the flux.

The MWCO of the LC membrane was determined by measuring the rejection of polyethylene glycol (PEG). Membranes were subjected to Polyethylene glycol (PEG) filtrations at 4 bar in the Amicon Cell. Aqueous solutions in ultrapure water were made containing PEGs with number average molecular weights (M_n) ranging from 600 to 10000 g·mol^{-1} with a concentration of 0.5 g·L^{-1} for each polymer.

The filtration procedure and the rejection calculations of these experiments were done as described in previous Chapters (e.g. experimental section 2.6). For all the permeability and filtration tests, permeate solutions were collected in triplo for each sample. At least 2 samples of each type of membrane were tested.

Filtration of neutral and charged organic molecules

Aqueous solutions of the 3 organic dyes (RB, RhB, Rib) with molecular weights between 330 and 892 g·mol^{-1} were used for filtration tests. The solutions (50 μM) were filtered at 4 bar pressure in the Amicon setup. Once a steady-state was reached, samples of the permeate were collected *in triplo* to determine the average rejection. Samples were immediately measured in UV-Vis between 300 and 600 nm in a quartz microcuvette. Rejection (R) of each dye was determined as described in previous Chapters (e.g. experimental section 2.6)

UV-Vis switching experiment

The photoinitiated switching between *trans* and *cis* was measured by making a solution of 3 in 10 ml chloroform (93.01 μM). The UV-Vis spectrum was measured with a baseline set for chloroform. *Trans-cis* switching was measured by irradiating with 365 nm UV light (700 mA) for respectively 5, 10, 15, 30, 60 seconds and measuring a new UV-Vis spectrum after each irradiation time. *Cis-trans* switching was measured by first irradiating the sample for 2 minutes with UV-light (365 nm) and then irradiating the sample 5, 10, 15, 30 and 60 seconds with the blue light of 450 nm (350 mA) and measuring the UV-Vis spectra.

The photo and back isomerization between *trans* and *cis* of the polymer were measured in solid-state onto glass substrates via UV-Vis spectroscopy. The baseline is set for the clean glass. *Trans* to *cis* switching was measured by irradiating with 365 nm UV light (700 mA) for 4h and taking a new UV-Vis spectrum every 5, 10 or 20 minutes in the end due to the stabilization. *Cis-trans* back switching was measured

by first irradiating the sample for 4 hours with UV light (365 nm) and then in the dark a spectrum was taken every 30 minutes for 9 hours.

Cis to trans decay experiment

Cis to *trans* decay experiments were performed by irradiating a solution of **SulfAzo** (13.8 mg) in chloroform (0.7 ml) with UV light of 365 nm (700 mA) for 5 minutes.

Synthetic procedures

The synthesis and characterization of tris-benzimidazolyl benzene core (**TB**) has been reported in literature.[29]

3,4,5-tris(undec-10-en-1-yloxy) benzoyl chloride (1):

To a stirred solution of methyl gallate (2.1 g; 11.5 mmol; 1 equiv.) in DMF was added K_2CO_3 (15.9 g; 115 mmol) and 11-bromo-undecene (3.3 equiv.). The suspension was heated to reflux at 10 ^{0}C overnight under Argon. When completed the solution was cooled down, filtered and evaporated. The residue was extracted with EtAc/water, dried and filtered. After the removal of the solvent was further purified by flash column chromatography in SiO_2 with Heptane/EtAc, 7:3 to 1:1 obtaining a white solid. The compound was acidified with KOH (8.1 equiv.) in a solution of $MeOH/H_2O$ 3:1 and heated with reflux overnight. After completion is cool down and neutralized to pH 2 with HCl 3M and extracted with EtAc. The product appeared as a white powder that was cleaned with water and filtered. The compound was reacted directly with $SOCl_2$ (3ml) for 1h at room temperature. The excess of $SOCl_2$ was evaporated with membrane pump rotavapor for half an hour to give compound 1 quantitatively. ^{1}H-NMR ($CDCl_3$, 400 MHz): δ = 7.30 (s, 2H, 2 x CH arom.), 5.80 (ddt, 3H, 3 x CH_2 = $CH-CH_2$), 5.01-4.92 (dd, 6H, 3 x CH_2 = CH), 4.02 (m, 6H, 3 x CH_2-CH_2-O), 2.05 (m, 6H, 3 x CH_2 = $CH-CH_2$), 1.78 (m, 6H, 3 x CH_2-CH_2-O), 1.31 (m, 36H, 18 x CH_2- CH_2-CH_2). ^{13}C-NMR ($CDCl_3$, 100 MHz) δ = 167.72, 152.86, 144.75, 127.28, 114.14, 73.72, 69.36, 67.65, 33.83, 33.81, 30.32, 29.63, 29.55, 29.52, 29.49, 29.44, 29.34, 29.19, 29.14, 29.05, 28.97, 28.94, 28.71, 26.03, 25.97, 25.56, 5.97. FT-IR: 1750 cm^{-1} (C=O str.), 693 cm^{-1} (C-Cl str.).

(E)-4-((4-hydroxyphenyl)diazinyl)benzenesulfonic acid (2):

To a stirred solution of sulfanilic acid (3.5 g; 20 mmol; 1.0 equiv.) in cold water H_2O (10 ml), 6 ml of 6 M HCl (2.0 equiv.) were added. A solution of $NaNO_2$ (1.5 g; 41.6 mmol; 1.2 equiv.) in H_2O (15 ml) was added dropwise to the solution. The mixture was stirred for 30 minutes at 0°C. Then a solution of phenol (1.9 g; 20 mmol; 1.0 equiv.) in K_2CO_3 (50 ml) was added and was reacted for 2 h (<5°C). After completion of the reaction, HCl was added to reach pH ≈ 2 and the suspension was filtered to obtain a pure yellow solid (2). ^{1}H-NMR (MeOD-d_4, 400 MHz): δ= 8.18 (d, 2H, J = 8.8 Hz, 2 × CH arom.), 7.95 (d, 2H, J = 8.7 Hz, 2 × CH arom.), 7.39 (d, 1H, J = 9.0 Hz, CH arom.) 6.68 (d, 1H, J = 9.0

Hz, CH arom.), 4.39 (q, 2H, J = 7.1 Hz and 14.3 Hz, O-CH$_2$-CH$_3$), 1.40 (t, 3H, J = 7.1 Hz, CH$_3$-CH$_2$). ^{13}C-NMR (MeOD-d$_4$, 100 MHz) δ 172.3, 161.49, 158.89, 154.13, 136.14, 134.58, 130.99, 125.82. HRMS (ESI) m/z: [M + H]$^+$ calc. for C$_{12}$H$_{10}$N$_2$O$_4$S, 278.04; found, 278.42.

(E)-4-((4-((4-(dec-9-en-1-yloxy)-3,5-bis(undec-10-en-1-yloxy)benzoyl)oxy)phenyl)diazinyl)benzenesulfonic acid (SulfAzo):

To a stirred solution of 1 (1 g; 1.0 equiv.) in THF (6 ml) at 0 ^{0}C, a DMF solution (6ml) of compound 2 (0.47 g, 1.1 equiv.) with TEA (0.3 g, 2.0 equiv.) was added slowly and let react stirring overnight at room temperature. After complexation, HCl was added to acidify to pH = 2 and the product was extracted in chloroform. Further purification was done by flash column chromatography (CHCl$_3$/MeOH 80:20) to obtain an orange powder (569 mg, 57% yield). ^{1}H-NMR (CDCl$_3$, 400 MHz): δ = 7.97 (d, J = 8.2 Hz, 2H, CH arom.), 7.93 (s, 2H, CH arom.), 7.88 (d, J = 8.2 Hz, 2H, CH arom.), 7.79 (d, J = 8.2 Hz, 2H, CH arom.), 7.31 (s, 2H, CH arom), 5.82 – 5.66 (ddt, 3H, 3 x CH$_2$ = CH-CH$_2$), 4.99 – 4.78 (dd, 6H, 3 x CH$_2$ = CH), 3.97 (dt, J = 13.3, 6.5 Hz, 6H, 3 x CH$_2$-CH$_2$-O), 1.72 (dt, J = 23.1, 7.3 Hz, 6H, 3 x CH$_2$ = CH-CH$_2$), 1.48 – 1.37 (m, 6H), 1.37 – 1.17 (m, 36H, 18 x CH$_2$-CH$_2$-CH$_2$). ^{13}C-NMR (CDCl$_3$, 100 MHz) δ = 170.98, 153.01-143.08, 139.17, 127.89, 124.42, 123.96, 122.69, 114.30, 108.54, 73.43, 69.23, 33.91-26.15. FT-IR: 30403 cm^{-1} (O-H str.), 1712 cm^{-1} (C=O str.), 1215 cm^{-1} (S=O str.); 906 cm^{-1} (C=C str.); HRMS (ESI) m/z: [M + H]$^+$ calc. for C$_{21}$H$_{38}$N$_4$O$_6$S, 886.52; found, 886.56.

5.6 References

[1]   M. A. C. Stuart, W. T. S. Huck, J. Genzer, M. Müller, C. Ober, M. Stamm, G. B. Sukhorukov, I. Szleifer, V. V. Tsukruk, M. Urban, F. Winnik, S. Zauscher, I. Luzinov, S. Minko, *Nat. Mater.* **2010**, *9*, 101.

[2]   F. Ercole, T. P. Davis, R. A. Evans, *Polym. Chem.* **2010**, *1*, 37.

[3]   A. Goulet-Hanssens, F. Eisenreich, S. Hecht, *Adv. Mater.* **2020**, *32*, 1905966.

[4]   M. Irie, *Photoresponsive polymers*, Vol. 94, Elsevier Ltd, **1990**.

[5]   F. P. Nicoletta, D. Cupelli, P. Formoso, G. de Filpo, V. Colella, A. Gugliuzza, *Membranes (Basel).* **2012**, *2*, 134.

[6]   J. Henzl, M. Mehlhorn, H. Gawronski, K. H. Rieder, K. Morgenstern, *Angew. Chemie - Int. Ed.* **2006**, *45*, 603.

[7]   H. M. D. Bandara, S. C. Burdette, *Chem. Soc. Rev.* **2012**, *41*, 1809.

[8]   R. H. El Halabieh, O. Mermut, C. J. Barrett, *Pure Appl. Chem.* **2007**, *76*, 1445.

[9]   Y. Wei, *Anal. Chim. Acta* **2015**, *900*, 10.

[10]   A. H. Gelebart, D. Jan Mulder, M. Varga, A. Konya, G. Vantomme, E. W. Meijer, R. L. B. Selinger, D. J. Broer, *Nature* **2017**, *546*, 632.

[11]   D. Xia, G. Yu, J. Li, F. Huang, *Chem. Commun.* **2014**, *50*, 3606.

[12]   H. Zhang, W. Tian, R. Suo, Y. Yue, X. Fan, Z. Yang, H. Li, W. Zhang, Y. Bai, *J. Mater. Chem. B* **2015**, *3*, 8528.

[13]   A. H. Gelebart, D. Liu, D. J. Mulder, K. H. J. Leunissen, J. van Gerven, A. P. H. J. Schenning, D. J. Broer, *Adv. Funct. Mater.* **2018**, *28*, 1705942.

[14]   M. K. Purkait, M. K. Sinha, P. Mondal, R. Singh, *Interface Sci. Technol.* **2018**, *25*, 115.

[15]   M. Alvaro, M. Benitez, D. Das, H. Garcia, E. Peris, *Chem. Mater.* **2005**, *17*, 4958.

[16]   C. Wang, R. G. Weiss, *Macromolecules* **2003**, *36*, 3833.

[17]   H. P. C. Van Kuringen, Z. J. W. A. Leijten, A. H. Gelebart, D. J. Mulder, G. Portale, D. J. Broer, A. P. H. J. Schenning, *Macromolecules* **2015**, *48*, 4073.

[18]   J. A. M. Lugger, P. P. Marín San Román, C. C. E. Kroonen, R. P. Sijbesma, *ACS Appl. Mater. Interfaces* **2021**, *13*, 4385.

[19]   Z. Wang, A. Knebel, S. Grosjean, D. Wagner, S. Bräse, C. Wöll, J. Caro, L. Heinke, *Nat. Commun.* **2016**, *7*, 13872.

[20]   T. Kumeria, J. Yu, M. Alsawat, M. D. Kurkuri, A. Santos, A. D. Abell, D. Losic, *Adv. Mater.* **2015**, *27*, 3019.

[21]   E. Glowacki, K. Horovitz, C. W. Tang, K. L. Marshall, *Adv. Funct. Mater.* **2010**, *20*, 2778.

[22]   H. Q. Liang, Y. Guo, Y. Shi, X. Peng, B. Liang, B. Chen, *Angew. Chemie - Int. Ed.* **2020**, *59*, 7732.

[23]   N. Minoura, *Chem. Mater.* **2003**, *15*, 4703.

[24]   S. N. Ramanan, N. Shahkaramipour, T. Tran, L. Zhu, S. R. Venna, C. K. Lim, A. Singh, P. N. Prasad, H. Lin, *J. Memb. Sci.* **2018**, *554*, 164.

[25]   T. Sata, Y. Shimokawa, K. Matsusaki, *J. Memb. Sci.* **2000**, *171*, 31.

[26]   Y. Jiang, L. Heinke, *Langmuir* **2021**, *37*, 2.

[27]   S. K. Kumar, J. D. Hong, *Langmuir* **2008**, *24*, 4190.

[28]   N. Liu, D. R. Dunphy, P. Atanassov, S. D. Bunge, Z. Chen, G. P. López, T. J. Boyle, C. Jeffrey Brinker, *Nano Lett.* **2004**, *4*, 551.

[29]   J. A. M. Lugger, R. P. Sijbesma, *ChemistryOpen* **2016**, *5*, 580.

[30]   and J. E. M. J. Baena, P. Espinet, C. L. Folcia, J. Ortega, **2010**, *49*, 8904.

[31]   X. Zhu, B. Tartsch, U. Beginn, M. Möller, *Chem. - A Eur. J.* **2004**, *10*, 3871.

[32]   K. N. Grafskaia, J. J. H. Rueda, X. Zhu, V. M. Nekipelov, D. V Anokhin, M. Moeller, D. A. Ivanov, *Phys. Chem. Chem. Phys.* **2015**, *17*, 30240.

[33]   G. M. Bögels, J. A. M. Lugger, O. J. G. M. Goor, R. P. Sijbesma, *Adv. Funct. Mater.* **2016**, *26*, 8023.

[34]   C. E. Hoyle, C. N. Bowman, **2010**, *49*, 1540.

[35]   C. Decker, K. Moussa, *Die Makromol. Chemie* **1988**, *189*, 2381.

[36]   E. Merino, M. Ribagorda, *J. Org. Chem.* **2012**, *8*, 1071.

[37]   C. S. Paik, H. Morawetz, *Macromolecules* **1972**, *5*, 171.

[38]   G. C. Henk J. Haitjema, Gijs L. von Morgen, Y. Yong Tan, *Macromolecules* **1994**, *27*, 6201.

[39]   X. Dong, A. Al-Jumaily, I. C. Escobar, *Membranes (Basel).* **2018**, *8*, 23.

Chapter 6

Nanofiltration membranes based on self-assembled wedge-shaped LCs
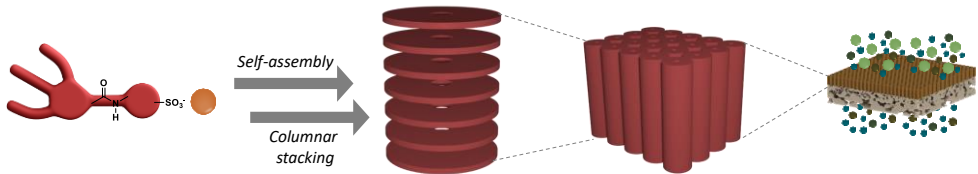
Abstract | In this Chapter, the preparation and characterization of wedge-shaped sulfonate salts with different inorganic and organic counterions is presented. Thermotropic columnar liquid crystals (CLCs) were obtained from the self-assembly of the salts that stacked into columns by nanophase-segregation. The molecular arrangement and the thermal properties could be tuned by changing the counterion. A membrane for water filtration was developed based on the sulfonated salt containing tetraethylammonium (NEt$_4$) counterions after direct deposition on a porous polyether sulfone support and photo-crosslinking of the columnar phase. The membranes, with small pore sizes around 1.2 nm, had a relatively high water permeability (1.43 L·m^2·h^{-1}·bar^{-1}). The membranes had a lower MWCO than analogous membranes made with the larger **TB** template as described in Chapter 2 (3000 vs 5000 g·mol^{-1}). With their small pore size, the membranes selectively reject smaller organic solutes such as saccharides.

.

6.1 Introduction: columnar nanostructures based on wedge-shaped sulfonate salts

The strategy used in the previous Chapters to prepare nanoporous membranes makes use of self-assembly of wedge-shaped sulfonates and a trifunctional aromatic template (**TB**) into 3-member discs that form a columnar liquid crystalline phase by stacking. The removal of the template after fixation of the morphology by polymerization led to the formation of channel-like nanopores of approximately 1.3 nm in diameter, which permitted the filtration of small organic molecules in water with charge and size selectively. The advantages of this strategy rely on the presence of a porous network with a fixed pore size which can be modified with the selection of a different template molecule. However, the removal of the template is an extra step in which the nanostructure can be disrupted. Also, the use of a fixed pore size doesn't provide flexibility to the structure once it is crosslinked. To address more versatility, the approach can be extended to systems with other protonated molecules such as metals or quaternary amines that act as counterions that create the pores. In this case, the "template" is ionic and can be easily changed by ion exchange processes. Moreover, narrower pore sizes can be achieved with small charged counterions. Generally, in these types of complexes, there is a nanophase separation that is based on the confinement of the highly polar ionic parts of the complexes in the interior and the hydrophobic interaction of the alkyl chains in the outer part of the aggregate (**Figure 6.1**).[1] In particular, the highly ionic nature of sulfonates makes them more prone to microphase segregate, forming well-defined channels. It is reported that the use of counterions with different sizes and permanent charges gives potential nanoporous materials with ionic channels in a well-defined geometry that can be used as ion-selective membranes.[2–4]

In the present Chapter, the formation of thermotropic columnar phases from the self-assembly of wedge-shaped sulfonate salts with different counterions is described. The size, shape and charge of the counterion guide the arrangement of the molecules within the liquid crystalline phase and the formation of the pores in the center of the discs. Based on the results, the quaternary ammonium counterion was selected as the best candidate for its application in filtration membranes due to the high order of the mesophase at room temperature. The solubility of the sulfonate salt in methanol allowed the direct coating of a porous support for the fabrication of the membrane. The membrane properties such as water permeability, pore size and rejection of solutes were studied and compared with those of system **Sulfac₃TB** as reported in Chapter 2.
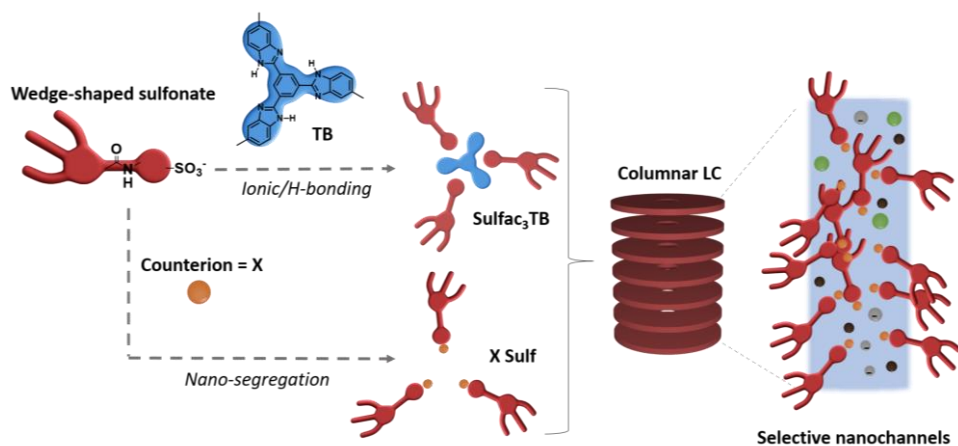
Figure 6.1 | Schematic representation of the formation of disc-shaped complexes from the self-assembly of wedge-shaped molecules with an aromatic core template molecule (**TB**) or with counterions with permanent charge by nano-aggregation. Columnar structures are formed by the stacking of the discotic complexes and act as nano-channels for the mass transport of solutes in water, with selectivity based on steric and Coulombic interactions due to the specific pore size and presence of charged sulfonate groups.

6.2 Synthesis and characterization of sulfonate salts

6.2.1. Variation of pore size by changing counterion

The use of different counterions with the wedge-shaped sulfonate influences the structure of the discs that make up the columns of the liquid crystal phase. The variation in size, shape and charge of the cations guides the pore size. The effect of the counterion on the structure of the liquid crystal phase was studied with three inorganic ions (Na^+, K^+, Mg^{2+}) and with three quaternary ammonium salts (tetraethylammonium, methyl pyridine and dimethyl bipyridine) that were synthesized from the **HNEt$_3$·Sulf** salt presented in Chapter 2, according to **Scheme 6.1** and fully characterized.

Table 6.1 | Counterions properties: charge, Mw and molecular size (ionic diameter for atoms):

Counterion	Charge	Mw (g·mol^{-1})	Ionic size (Å)
Na^+	+1	23.00	1.86
K^+	+1	39.10	2.31
Mg^{2+}	+2	24.31	1.60
$HNEt_3^+$	+1	102.20	4.27
NEt_4^+	+1	130.25	4.75
MPy^+	+1	94.14	3.84
$DMBP^{2+}$	+2	186.26	8.78
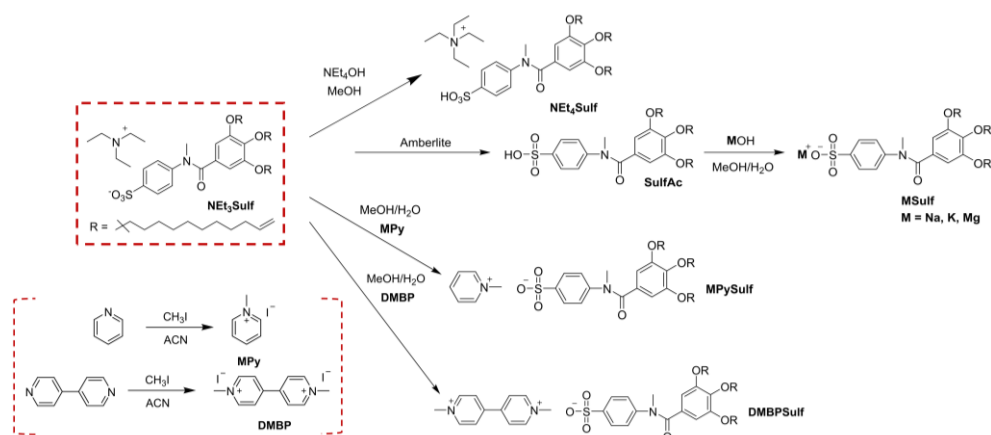
Scheme 6.1 | Synthesis of the different sulfonate salts changing the counterion.

Compound **NEt₄·Sulf** was prepared from **HNEt₃·Sulf** (synthesized as detailed in Chapter 2) by cation exchange with NEt₄OH (1:1 equivalents) in methanol. To produce the inorganic salts, **HNEt₃·Sulf** was first converted to the sulfonic acid using an Amberlite IR120 ion exchange resin. **Sulfac** was obtained as a viscous brown paste. The sulfonated salts **Na·Sulf, K·Sulf, Mg·Sulf₂** were produced by the addition of the corresponding metallic hydroxide in MeOH/H₂O mixture. Salts **MPy·Sulf** and **DMBP·Sulf₂** were obtained quantitatively by reacting **HNEt₃·Sulf** in MeOH/H₂O and the iodide salts of **MPy⁺ and DMBP²⁺** respectively, which were previously synthesized by reaction of pyridine and bipyridine with methyl iodide in acetonitrile under reflux for 1 day, followed by recrystallization.

The morphology and thermal properties of the dried compounds were studied with Polarized optical microscopy (POM) and Differential scanning calorimetry (DSC). First, the samples were observed under crossed polarizers; after heating and reaching the isotropization temperature of each compound, the samples were cooled down at 5⁰C/min. The optical appearance of birefringent textures with fan-shape focal and small needle-like patterns suggested the probable formation of thermotropic columnar mesophases at room temperature (**Figure 6.2**). Some compounds showed bigger domains (**Na·Sulf, NEt₄·Sulf, MPy·Sulf, HNEt₃·Sulf** and **DMBP·Sulf₂**) and specifically for NEt₃ and DMBP salts, the presence of many narrow and radial structures inside the focal shapes indicated the high order of the phase, suggesting crystalline behavior of the compounds.

Table 6.2 summarizes all the transition temperatures and the corresponding enthalpy energies obtained from the second heating cycle of DSC traces. **HNEt₃·Sulf** and **DMBP·Sulf₂** presented peaks with very high enthalpy values; enantiotropic transitions at between 60 to 70 ⁰C and in the case of **HNEt₃·Sulf**, a recrystallization

peak at low temperatures. These results confirmed the previous supposition from the optical observations that **HNEt₃·Sulf** and **DMBP·Sulf₂** are crystalline at room temperature. **NEt₄·Sulf** salt has a transition peak with low enthalpy at room temperature which corresponds to a liquid crystal - isotropic transition. The other salts (**Na**, **K**, **Mg**, and **MPy·Sulf**) showed a mesophase with isotropization above 150 ⁰C and a glass transition above room temperature, meaning that the material is in a frozen state where the molecular order is the same as in the liquid crystalline phase but without the mobility. Additionally, the high transition temperature for **MPy·Sulf** suggested a very stable interaction of the sulfonate salt with **MPy** counterion.
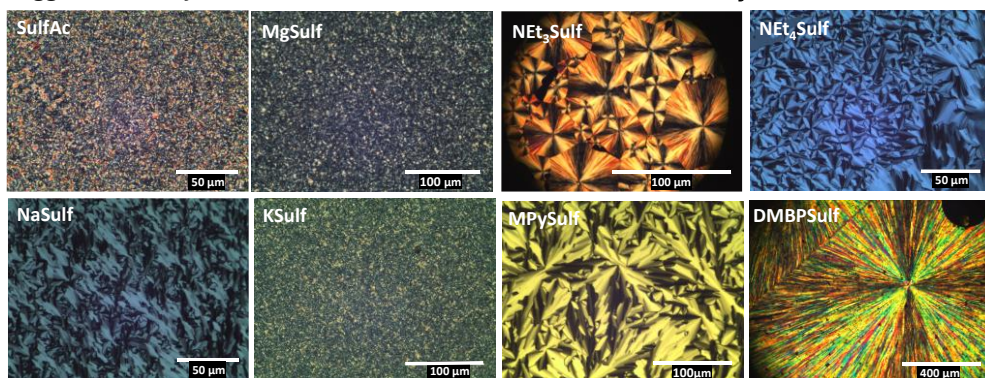
Figure 6.2 | Polarized optical micrographs of the salts at room temperature after heating to isotropic and cooling at 5⁰C/min.

Table 6.2 | Transition temperatures (⁰C) and enthalpies (kJ·mol⁻¹) of the thermotropic transitions measured with DSC for the different salts in the second heating cycle at 10⁰C/min:

	Phase transition	T (⁰C)	ΔH (kJ·mol⁻¹)
	recrystallization	17	5.68
NEt₃·Sulf	melting	29	43.3
	isotropization (M → I)	76	72.9
NEt₄·Sulf	isotropization (M → I)	72	0.48
Na·Sulf	glass transition	89	2.11
	isotropization (M → I)	185	
K·Sulf	glass transition	57	1.58
	isotropization (M → I)	190	
Mg·Sulf₂	glass transition	48	11.4
	isotropization (M → I)	149	

MPy·Sulf	glass transition	155	0.69
	isotropization (M → I)	239	
DMBP·Sulf$_2$	recrystallization	7	74.7
	melting (C → I)	62	47.1

There is an important influence of the counterion on the thermal (transition temperatures and enthalpy) and morphological properties of the material formed (crystallinity). Therefore, for the mesogenic compounds, the type of mesophase formed will be influenced by the counterions and the arrangement of the molecular units within the nanostructure. It is reported that cone-shaped molecules with small polar heads groups aggregate in confined structures such as cubic lattices. Larger head groups give truncated cone shapes that prefer cylindrical and columnar phases. It can also occur that very large counterions of the polar heads in the molecule prefer to stay in the outer part more than confined in the centres.[1,3,4]

The structural arrangement in the mesophase was determined with X-ray diffraction at room temperature after annealing the samples above the corresponding isotropization temperature. The high number of diffraction peaks in the high q range of the WAXS diffractograms of **HNEt$_3$·Sulf** and **DMBP·Sulf$_2$** salts (**Figure 6.3a**) confirmed the presence of a crystalline phase. However, the other compounds showed a broad peak at high q values related to the presence of disordered alkyl chains in liquid crystals or the glassy state. Diffraction peaks at low q values with q-ratios of 1:√3:2:√7 confirmed a columnar hexagonal arrangement with the best-defined patterns for the **NEt$_4$** and **Mg** salts. Even though the compounds with inorganic counterions are in a glassy state at room temperature, they present the same columnar arrangement as for the mesophase.

The observed columnar morphologies are expected to be formed from the stacking of discotic assemblies of our wedge-shaped molecules. The number of wedges per disc (Z) was estimated from the obtained parameters (lattice parameter *a* in **Figure 6.3b**), assuming a density of $\rho = 1 \ g \cdot cm^{-3}$. The relation between the density and lattice parameters is given by $\rho = (M \cdot Z)(N_A \cdot V)$, where M is the molar mass of each compound in g·mol^{-1}, N_A is Avogadro number in mol^{-1} and V is the volume of the unit cell in cm^{-3}. For a columnar hexagonal mesophase V is calculated by the equation $V = \left(\frac{\sqrt{3}}{2}\right) a^2 c \ 10^{-24}$ cm^3, where *c* is the inter disk distance d$_{001}$ which is set as 0.35 nm, an average value for columnar LC´s.[5,6]

For an identical charge of the cation, the lattice parameter *a* increased with the size of the counterion when the charge is the same. The Z value is also influenced by the charge: for the inorganic salts, the Z value increases from 3 for **Na·Sulf** to 5 for **Mg·Sulf$_2$**. The bigger size and charge of Mg^{2+} create more ionic interactions with the sulfonated monomer (both attraction and repulsion between the ions). For the organic salts, **HNEt$_3$·Sulf** aggregates with 3 wedges per disc but **NEt$_4$·Sulf** and **MPy·Sulf** with 4, which

suggests that for bigger counterions, the lattice spacing increases, leaving more space for molecules to confine and increasing Z value. **DMBP·Sulf₂** presents the same number of wedges per disc as **MPy·Sulf**, which can be explained with similar ways of packing where two MPy^+ ions take up roughly the same space as one $DMBP^{2+}$ counterion, in both cases producing a structure with 4 wedges per disc.

Compound	a (nm)	Z	Wedges per disc
SulfAc$_3$TB	4.48	1.26	1
Na	3.96	3.39	3
K	4.32	3.96	4
Mg	4.19	3.85	4
MPy	4.56	4.15	4
DMBP	4.53	4.01	4
HNEt$_3$	3.84	2.88	3
NEt$_4$	4.68	4.19	4
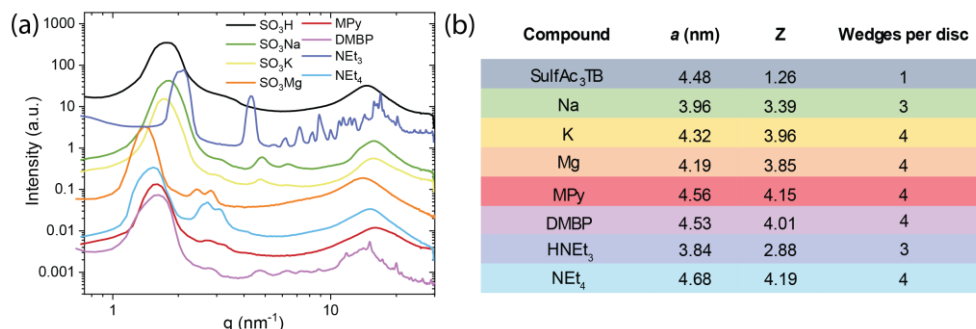
Figure 6.3 | a) WAXS pattern of sulfonate salts measured at room temperature in bulk; b) Lattice parameter *a* and number of molecules (wedges) per disc Z calculated for the sulfonate salts.

When using a template molecule with a specific number of functionalities, a fixed number of molecules per disc is obtained, which is the case of the complex **Sulfac₃TB** (see Chapter 2). It is suggested that the presence of the trifunctional **TB** template molecule provides only site for 3 molecules per disc while with the presence of counterions, there is freedom of arrangements for the molecules, where other factors like size and charge are the driving force of the aggregation.

As conclusions from the thermal and structural characterization of the salts it can be highlighted that:

1. **HNEt₃·Sulf** and **DMBP·Sulf₂** are crystalline at room temperature after annealing. **DMBP·Sulf₂** has a metastable mesophase at low temperatures that crystallizes at 7 ^{0}C, complicating its application in fabrication of nanoporous membranes.
2. The inorganic salts and **MPy·Sulf** have a columnar mesophase but at room temperature, they stay in a glassy state with low mobility. Col$_{hex}$ morphology was retained but the diffraction pattern was broader and less defined.
3. **NEt₄·Sulf** and **Sulfac** exhibit a columnar LC at room temperature but **NEt₄·Sulf** mesophase is more ordered as can be concluded from the narrower diffraction peaks.

6.3 Membrane fabrication and filtration performance

To study its properties on filtration membranes, **NEt₄·Sulf** was selected because of the presence of a columnar mesophase at room temperature, and its relatively low isotropization temperature of 72 ^{0}C. The other complexes are either crystalline at room temperature (**HNEt₃·Sulf** and **DMBP·Sulf₂**), which hampers polymerization, or have a high isotropization temperature, which is a disadvantage in processing before polymerization (see Chapter 7, **section 7.3).**
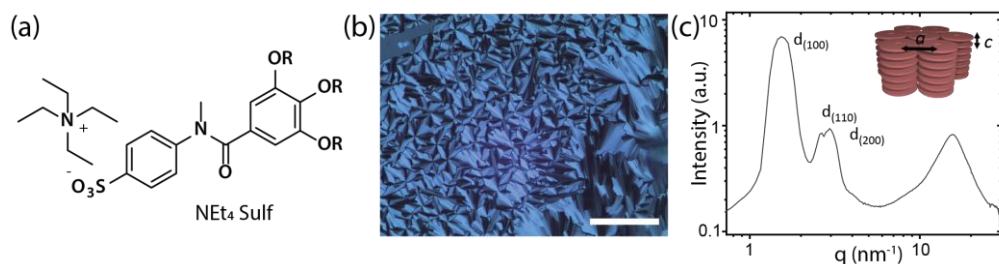
Figure 6.4 | a) Molecular structure of **NEt₄·Sulf**; b) Polarized optical micrograph of **NEt₄Sulf** after heating up to isotropization and cooling at 10^{0}C/min. Scale bar 50 μm; c) WAXS pattern at room temperature after annealing showing peaks with ratio corresponding to a hexagonal lattice.

6.3.1. Fixation of the network by photo-polymerization

Polymer films of the compound were prepared using thiol-ene photo-polymerization by drop-casting a solution in methanol containing **NEt₄·Sulf** (1 equiv.), dithiol crosslinker (1.5 equiv.) and photoinitiator (2 wt.%). Evaporation of the solvent followed by UV light irradiation for 10 minutes led to the formation of a flexible white-transparent film. Crosslinking of **NEt₄·Sulf** salt was confirmed by FT-IR (**Figure 6.5a**) with the disappearance of the peak of C=C stretch vibration band at 908 cm^{-1}.
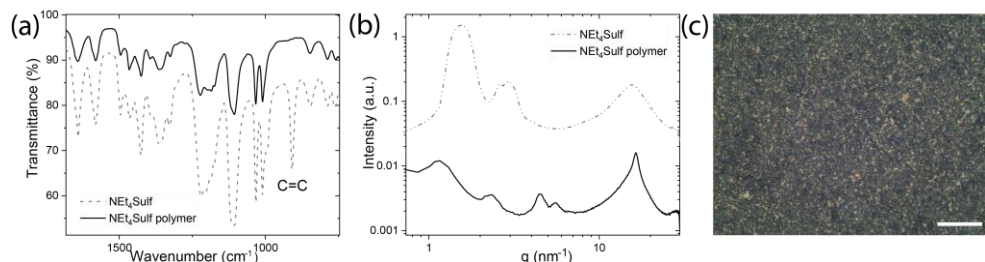
Figure 6.5 | a) FT-IR plot comparison before and after crosslinking of the monomer; b) WAXS pattern of salt in bulk (dotted line) and polymer film at room temperature (black line); c) Polarized optical light micrograph of the polymer film at room temperature. Scale bar 100 μm.

After drying the polymer film under vacuum, POM pictures showed a birefringence texture typical for randomly oriented columnar order with small domains of around 1-10 μm (**Figure 6.5c**). X-ray measurements confirmed that the hexagonal columnar mesophase in bulk was preserved in the polymer (**Figure 6.5b**) with an enlargement of the network due to the addition of the crosslinker (from d_{salt} = 4.08 nm to d_{pol}= 5.28 nm). The number of molecules per disc in the crosslinked network was determined to be as well 4 units. Compared to **Sulfac₃TB** system, the lattice distances *d* are higher (**Table 6.3**) which can be due to the increase in one molecule per disc, making the network larger.

Table 6.3 | WAXS distance parameters of the lattice for both systems before and after polymerization with the calculated number of molecules per disc in bulk:

Compound	d_{100} (nm)	*a* (nm)	wedges per disc (Z)
Sulfac₃TB bulk	3.91	4.51	1 (3:1 complex)
Sulfac₃TB polymer	4.65	5.37	
NEt₄·Sulf bulk	4.08	4.71	4
NEt₄·Sulf polymer	5.28	6.09	

6.3.2 Membrane fabrication and characterization

Polyether sulfone (PES) supported membranes were made by spin coating of a 10 wt.% ethanol solution of compound **NEt₃·Sulf**, 1,10-decanodithiol and Irgacure 819 directly on the PES support using the procedure represented in **Figure 6.6.** As the PES support is resistant to ethanol, direct spin coating of the monomer mixture was possible. This method presents an advantage over the method described for **Sulfac₃TB** membranes in Chapter 2, where first a thin film of the membrane is made, and it is subsequently transferred to the support. Since direct spin coating avoids the transfer of an extremely thin and brittle polymeric film, it is easier to prepare defect-free composite membranes. To temporarily attach the PES support to the glass surface during spin coating, a layer of polyvinyl alcohol (PVA) was used as glue (applied at 1500 rpm, 30 s, 10 wt.% solution in water), facilitating the flatness of the support and helping to have homogeneous coverage. After coating and photo-polymerization of the LC layer, the membranes were detached from the glass support by dissolving the sacrificial PVA layer in water.

i) PVA coated glass   ii) PES support   iii) LC spin coated

iv) Photopolymerization   v) Recovery of membrane in water   vi) Supported membrane
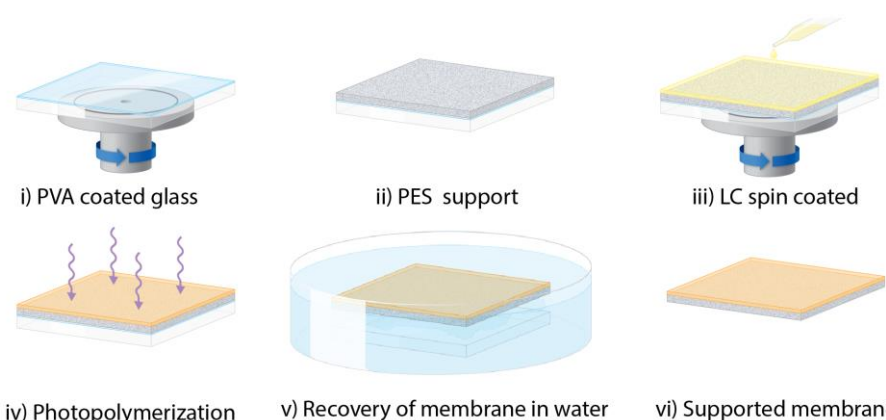
Figure 6.6 | Schematic representation of the fabrication of **NEt₄·Sulf** membranes following a direct spin coating method: i) spin coating of glass with PVA, ii) deposition of PES support, iii) spin coating with monomer solution, iv) photopolymerization and v) release of composite from the glass support.

After washing with deionized water and drying the composite membranes, the thickness of the active layer was visualized and measured with High-Resolution Scanning Electron Microscopy (HR-SEM) (**Figure 6.7**). The micrographs showed the formation of membranes with a well-attached active layer (of around 250 nm thickness) without surface defects and suitable for filtration studies. Unlike previous systems like **Sulfac₃TB** (Chapter 2) or **AzoSulf₃TB** (Chapter 5), the pores are now created as ionic channels by the confinement of the polar groups on the centre of the columnar structures due to the hydration of the sulfonate groups.

Figure 6.7 | a) Composite membrane cut in a circular shape for filtration test; b) HR-SEM top view and c) HR-SEM cross-section showing a thin active layer of 250 nm attached to PES.

6.3.3 Membrane filtration properties

Pure water permeability

The pure water permeability and flux of the **NEt₄·Sulf** membrane (flux at 4 bar) with an active layer thickness of 250 nm were measured as a function of pressure and time

and results were compared to the templated membranes of Chapter 2 with a thickness of 200 nm (**Figure 6.8**).

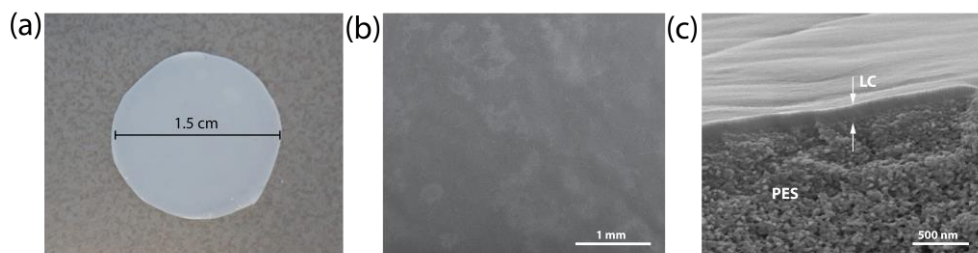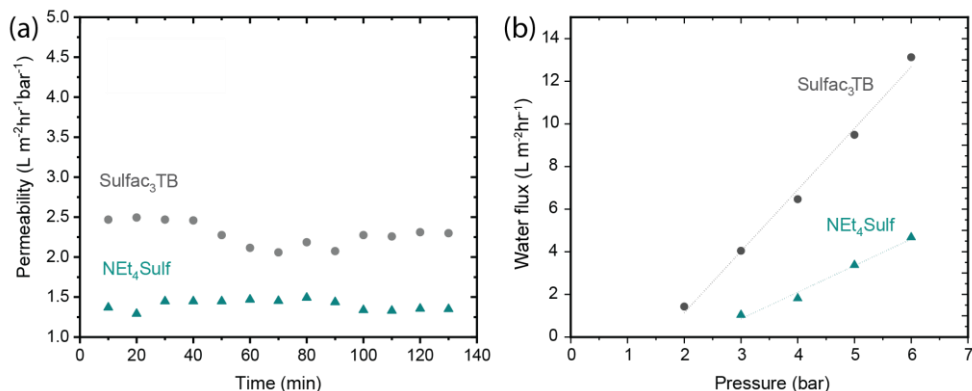**Figure 6.8 |** a) Plot of pure water permeability normalized to 1 bar of applied pressure vs time of **Sulfac₃TB** (grey circles) and **NEt₄·Sulf** (green triangles) membranes and b) Plot of pure water flux vs applied pressure after stabilization of the flow at the maximum pressure.

The permeability of the **NEt₄·Sulf** membrane was about 40% lower than of the **Sulfac₃TB** membrane (1.4 vs 2.3 L·m^{-2}·h^{-1}·bar^{-1}), although the thickness was only 20 % higher. Taking into account the number of wedges per disc (z=4), the theoretical pore size was estimated from the energy-minimized structure of **NEt₄·Sulf** (**Figure 6.9**), corresponding to the ionic channel diameter in the columnar state and was estimated to be about 1.2 nm, which is smaller than the calculated **TB** template size (1.3 nm) representing the pore size in **Sulfac₃TB**.[7]

These results suggest that the lower flux of **NEt₄·Sulf** membranes than that of **Sulfac₃TB** is a result of the smaller pores given by the self-assembled structure with NEt₄ counterions.
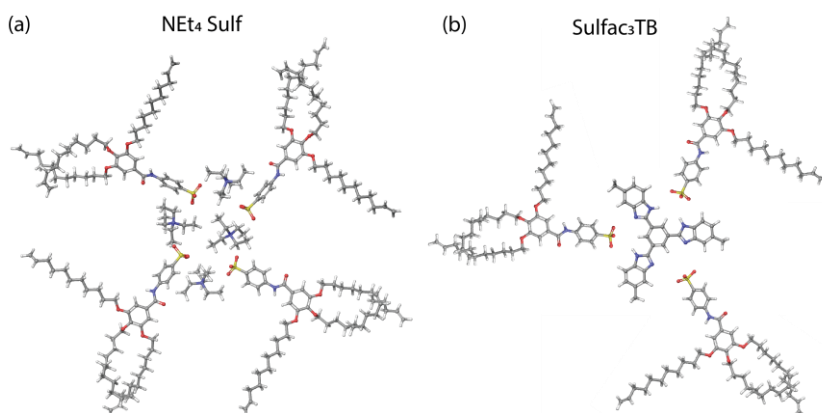
Figure 6.9 | Energy minimized molecular structure of a) **NEt₄·Sulf** with an estimated pore size of 1.2 nm and b) **Sulfac₃TB** with a calculated size of 1.3 nm for **TB**.

The theoretical permeability through the cylindrical pores can be calculated using the Hagen-Poiseuille equation, used in Chapter 2, that assumes a flow through perfectly homeotropically aligned columnar channels.

$$Q = \frac{\pi \varepsilon (\Delta P) R^4}{8 \mu L} \text{ (eq. 6.1)}$$

With R = 0.234 and pore density (ε) of 9.7 10^{-18} cm^{-2} (using the estimated value for the pore diameter d_2 = 1.2 nm), L as the thickness of membrane (250 nm), ΔP = 1 bar and μ (water) = 0.89·10^{-3} Pa·s^{-1}. (See Chapter 2)

The calculated permeability is 2.7 L·m^{-2}·h^{-1}·bar^{-1}, around twice the experimental value, which indicates that – assuming a perfectly aligned, defect active layer – around half of the channels is spanning the active layer. This is slightly higher than in the **Sulfac₃TB** membrane, which had less than 0.4 times the theoretical permeability. It is hypothesized that the slight improvement of the flux is related to a higher fraction of pores aligned with the permeation direction.

Protein rejection

The ability of the membranes to retain different solutes present in water was tested with the filtration of big globular organic molecules, e.g. bovine albumin serum (BSA) and green fluorescence (GF) proteins with sizes of 66 and 33 kDa respectively (6 and 5 nm diameter). The feed solutions were separately subjected to filtration under 4 bar pressure. The permeate solutions were collected *in triplo* (1 ml each) and the concentration of the protein was determined from UV-Vis absorption measurements. The results observed in **Table 6.4** showed nearly complete rejection (>99%) of both proteins. This indicates that the membrane pores are smaller than 5 nm as expected and most importantly that there are very few micro defects in the active layer.

Table 6.4 | Comparison of rejection of BSA and GFP solutions of the **NEt₄·Sulf** membrane and the **Sulfac₃TB** membrane:

Membrane	BSA rejection (%)	GFP rejection (%)
NEt₄ Sulf	99.8	99.3
Sulfac₃TB	99.6	99.2

MWCO determination and salt rejection

To determine the molecular weight cut off (MWCO) of **NEt₄·Sulf** membranes, rejection of polyethylene glycol (PEG) of different M_n (600, 1600, 4600, 7000 and 10000 g·mol^{-1}) was determined. An aqueous solution with a mixture of the different PEGs, at 0.5 g·L^{-1} each, was filtered through the membrane. Permeate solutions of 1 ml were collected and further analyzed with Size Exclusion Chromatography (SEC) to calculate the rejection. The results of these experiments are plotted in **Figure 6.10a**, where it can be

seen that the rejection varies from 62.3 % for PEG with a molecular weight of 600 to 99.4 % for PEG 10000. The MWCO, which corresponds to the molecular weight at which 90 % is rejected, was determined from the plot to be around 3000 g·mol^{-1} with a hydrodynamic radius of 1.3 nm.[8] **Figure 6.10** also shows that the MWCO of the membrane with **Sulfac₃TB** is higher (5000 g·mol^{-1}), corresponding to a hydrodynamic radius of 1.7 nm. These results are in line with the lattice parameter ratio´s obtained from X-ray data in **Table 6.3**: without the template, the **NEt₄·Sulf** self-organized in discotic aggregates with 4 wedge-shaped molecules leaving less space inside than the **TB** template in **Sulfac₃TB**.
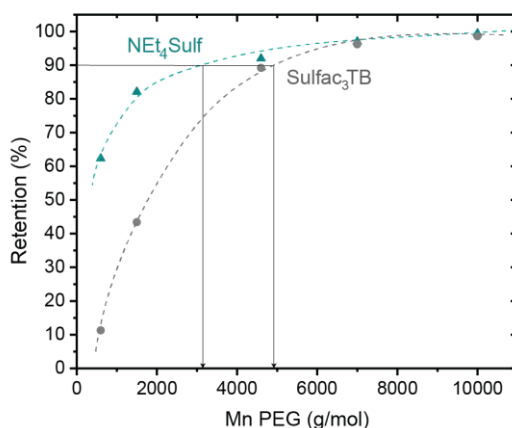
Figure 6.10 | Comparison plots of rejection curves of membranes **NEt₄·Sulf** and **Sulfac₃TB** with PEG ranging between 600 and 10000 g·mol^{-1}. Hydrodynamic radii are calculated as R_h (nm)= $0.06127 \cdot M_n^{0.3931}$.

Ion exchange

There are other reported examples of anion exchange membranes based on similar structures to the one presented in this work. In those membranes the porous structure is formed by the aggregation of the salts with the counterions in the interior of the pores. The pore size is then defined by the size of the channels created in the nanostructure, and determines the transport properties of the membrane.[9],[10]

As the pore formation in the **NEt₄·Sulf** membranes is based on ion exchange, the effect of the counterion in the feed solution on the filtration performance was investigated to understand transport in these membranes. As proof of principle, the exchange of the NEt₄ counterion with dimethyl bipyridinium ion (DMBP^{2+}) was attempted (**Figure 6.11a**). This counterion was used for the exchange as it was earlier proven to form a stable salt **DMBP·Sulf₂** (**Section 6.2**) and due to its big size, effects on permeability, if any, will be more pronounced.

Water flux of **NEt₄·Sulf** membrane was measured over time once a stable value was reached (dark yellow squares of NEt₄⁺(1) in **Figure 6.11b**). After the ion exchange process was completed by soaking overnight the membrane in an aqueous solution of DMBP iodide, it was rinsed with deionized water and the water flux was measured over time. The green plot with circles in **Figure 6.11b** (DMBP²⁺) showed almost half of the flux than for previous membrane. These results suggest that NEt₄⁺ counterions have been replaced by DMBP²⁺ and the bigger size of this last one produces a decrease of the flux. The reversibility of the exchange was confirmed with the recovery of the flux after soaking the membrane in NEt₄Cl. Indeed, the flux was recovered as it is shown by **NEt₄⁺ (2)** in the orange plot with triangles in **Figure 6.11b**.
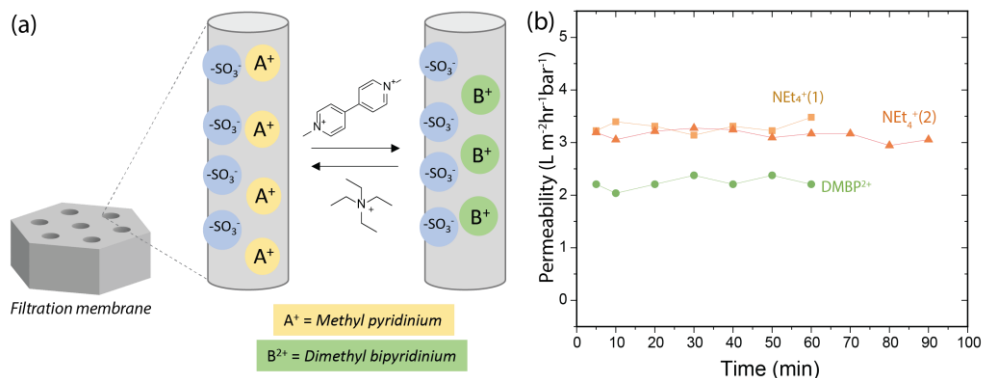
Figure 6.11 | a) Schematic illustration of the ion exchange process in the cylindrical pores of the membrane. In this case, NEt₄ counterions are replaced first by DMBP²⁺, a process that can be reversed back using NEt₄Cl; b) Water permeability vs time for the membrane with NEt₄⁺ counterions (yellow squares), after being exchanged with DMBP²⁺ (green circles) and re-stored with NEt₄⁺ again (orange triangles).

Therefore, the pore size of the membrane changes due to ion exchange process and this suggests that the counterions stay inside the pores of the nanostructure, effectively increasing or decreasing the pore size when using smaller or bigger counterion respectively. The change in pore size results in different transport properties such as water permeability or rejection of solutes, depending on the type of counterion. Obviously, the speed rate of exchange will depend on the ionic strength of the SO₃⁻ groups in the membrane structure relative to the concentration of the counterion. This variable pore size behaviour confirms that the formation of the columnar nanostructure from the wedge-shaped LCs is governed by the presence of counterions that have a strong influence on pore size and therefore filtration properties of the membrane.

Filtration of charged and neutral organic molecules

Continuing with the study of the rejection properties of the **NEt₄·Sulf** membrane, smaller organic molecules were used. Aqueous solutions of charged and neutral dyes with different molecular weights (Mw) were prepared separately with a concentration of 50 μM; anionic fluorescein (**F**), orange G (**OG**) and phtalocyanine copper tetrasulfonate (**PhtCy**), cationic crystal violet (**CV**), zwitterionic Rhodamine B (**RhB**) and neutral Riboflavin (**Rib**) (**Figure 6.12a**) were selected. The rejection values for both **Sulfac₃TB** and **NEt₄·Sulf** membranes are shown in **Table 6.5.**

Both membranes presented both size and charge selectivity based on the rejection values observed. For all the dyes, rejection by the **NEt₄·Sulf** membrane was higher than by the **Sulfac₃TB** membrane (**Figure 6.12b**) entirely in line with the difference in pore size. The big anionic **PhtCy** was totally rejected by both membranes due to the size and the 4 negative charges that cause high repulsion. The cationic dye **CV** was already highly retained by **Sulfac₃TB** membrane due to absorption within the pores by ion pairing with SO_3^- groups (Chapter 2). A slight increase in rejection from 88% to 93% was observed for **NEt₄·Sulf** due to its small pore size. The small anionic dyes **F** and **OG**, were significantly more strongly rejected by the **NEt₄·Sulf** membrane than by the **Sulfac₃TB** membrane (17% to 55% for **F** and 23% to 67% for **OG**). In addition to the differences in pore size, repulsion by a higher density of the SO_3^- groups in the pores (4 per disc vs 3 per disc) may contribute to the differences in rejection of anionic dyes by the two membranes. A similar effect was observed for zwitterionic **RhB**, which followed the same trend as the cationic and anionic dyes of increased rejection by the **NEt₄·Sulf** membrane. Finally, the lack of charges and the small size of **Rib** allowed the passage of the molecule with relatively low rejection based on its size in both membranes with a slight increase (from 17% to 38%) for the **NEt₄·Sulf** membrane.
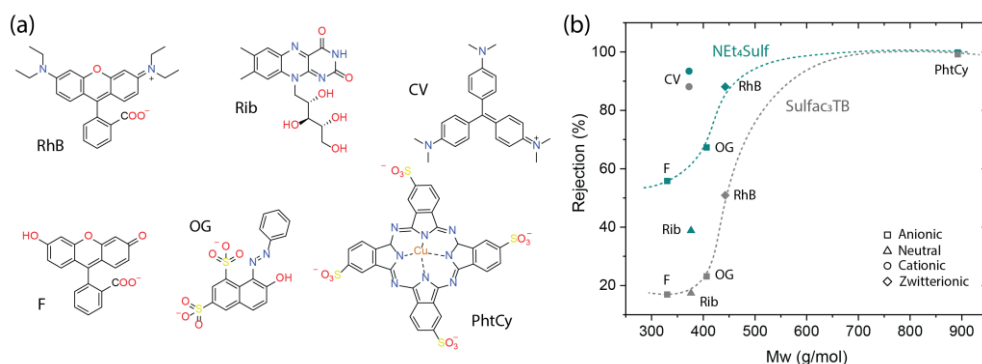

Figure 6.12 | a) Molecular structures of the dyes used in the filtration tests and b) comparison of rejection curves of **NEt₄·Sulf** salt membrane (green) and **Sulfac₃TB** (grey).

In summary, the rejection of dyes increases with molecular weight (and the number of charges for anionic dyes), being higher for cationic dyes and lower for neutral molecules. For all dyes, rejection by the **NEt₄·Sulf** membrane is higher than by the **Sulfac₃TB**, due to the smaller pore size.

Table 6.5 | Dyes used in the filtration test, molecular characteristics and rejection values of dyes by **Sulfac₃TB** and **NEt₄·Sulf** membranes:

Dye	Mw (g·mol^{-1})	Molecular width (nm)	Charge	Retention (%) Sulfac₃TB *	Retention (%) NEt₄·Sulf
F	330.27	0.92	-1	16.9	55.8
OG	406.38	1.07	-2	23.1	67.3
PhtCy	892.25	1.42	-4	99.8	99.2
Rib	376.36	1.02	0	17.4	38.8
RhB	442.57	1.14	±	50.9	88.1
CV	372.45	1.12	+1	88.1	93.4

**Values from Chapter 2*

Because of the smaller pores of the **NEt₄·Sulf** membrane, it was of interest to probe the capability of this membrane to retain molecules with even lower M_w, such as saccharides. Filtration experiments with glucose, sucrose, and raffinose (mono, di, and trisaccharide respectively) showed that retention increases with molecular weight from 10% for glucose to 50% for raffinose (**Table 6.6**). Retention values of neutral molecules of similar size e.g. sucrose and riboflavin were almost the same (37% at M_w 342 g·mol^{-1} for sucrose and 39% at Mw 376 g·mol^{-1} for riboflavin). Remarkably, anionic fluorescein (Mw 342 g·mol^{-1}) has a higher rejection (56%) than similarly sized sucrose (330 g·mol^{-1}) with 37% rejection due to repulsion effects of the negative charges.

Table 6.6 | Average hydrodynamic radius[11] and M_w of the saccharides with their rejection by **NEt₄·Sulf** membrane:

Solute	R_h (nm)	M_w (g·mol^{-1})	Rejection (%)
Glucose	0.73	180.16	16 ± 9.5
Sucrose	0.94	342.30	37 ± 14
Raffinose	1.12	594.51	47 ± 9.4

In conclusion, both membranes show size-selectivity for organic molecules with or without charge but higher rejection values are exhibited by the **NEt₄·Sulf** membrane due to the presence of one more negative charge from the sulfonate group per pore, and the smaller pore size of that membrane compared to the **Sulfac₃TB** membrane.

6.4 Conclusions and outlook

In the first section of this Chapter, the synthesis was presented of a number of wedge-shaped sulfonate salts that form columnar structures by nano-segregation with the polar heads at the core of the discotic aggregates. The morphological and thermal studies showed columnar hexagonal arrangements with lattice parameters that depend on the counterion. This strategy allows tuning of structural and thermal properties of the material by changing the cation of the sulfonate salt.

In the second part, PES-supported membranes for water filtration were prepared from **NEt₄·Sulf**, a salt that was selected for its high stability, order and good solubility. These properties permitted direct coating of the support instead of the transference method used in previous Chapters. A reduced pore size of around 1.2 nm for **NEt₄·Sulf**, compared to 1.3 for **Sulfac₃TB** membranes, was estimated from the network modelling, which correlates with the lower MWCO value obtained in PEG filtration experiments. The **NEt₄·Sulf** membranes can remove small organic solutes from water. Selectivity is based on size sieving with a role for ionic interactions of the sulfonate groups with cationic solutes.

Compared to the template strategy presented in Chapters 2-5, the use of counterions with a permanent charge facilitates the creation of stable nanoporous membranes with on-demand pore sizes and high processability. We have demonstrated that it is possible to select a counterion to modify rejection and transport properties *via* an ion exchange process. However, more work needs to be done to explore the limitations of the binding strength of the counterions inside the pores at different conditions of pH, ionic strength, concentration, etc.

6.5 Experimental section

6.5.1. Materials and methods

All reagents and solvents for synthesis were purchased from Sigma-Aldrich or TCI America. The ultrafiltration support, PES UF (30 kDa MWCO) was purchased from Sartorius Stedim Biotech, monodispersed PEG with a polydispersity of ≈ 1.05 was purchased from Agilent. Ultrapure water was used for all filtration experiments.

NMR spectra were recorded at room temperature on a Bruker FT-NMR spectrometer AVANCE III HD-NanoBay (400 MHz, Bruker UltraShield magnet, BBFO Probehead, BOSS1 shim assembly) in CDCl₃. Chemical shifts are given in ppm from tetramethylsilane (TMS, 0 ppm). MALDI-TOF-MS analysis was performed on a Bruker speed autoflex operated in reflectron mode with a positive voltage polarity, 500 shots. ATR FT-IR spectra were recorded at room temperature on a PerkinElmer Spectrum Two spectrometer equipped with a universal attenuated total reflectance (ATR) sampling accessory. Polarized Optical Microscopy (POM) was performed with a Jenaval

microscope equipped with crossed polarizers and a Linkam THMS 600 heating stage. Differential Scanning Calorimetry (DSC) measurements were performed in hermetic T-zero aluminium sample pans using a TA Instruments Q2000−1037 DSC instrument equipped with a RCS90 cooling accessory. Transition temperatures and enthalpies were typically determined from the first cooling and second heating run using Universal Analysis 2000 software (TA Instruments). X-ray scattering measurements were performed on a Ganesha lab instrument equipped with a Genix-Cu ultralow divergence source producing X-ray photons with a wavelength of 0.154 nm and a flux of $1 \cdot 10^8$ photons s^{-1}. Diffraction patterns were collected using a Pilatus 300 K silicon pixel detector with 487 × 619 pixels of 172 μm^2 in size, placed at a sample to detector distance of 91 mm (wide-angle, WAXS), or 500 mm (medium angle, MAXS). On the obtained diffraction patterns an azimuthal integration was performed using SAXSGUI software, to calculate the intensity against the scattering vector q, where q = (4π/ λ)sin ϑ (ϑ is the angle of incidence and λ is the wavelength). The beam centre and the q-range were calibrated using silver behenate (d$_{(100)}$ = 1.076 nm; 5.839 nm) as a reference. The d$_{(300)}$ was used for calibration. Temperature was controlled with a Linkam HFSX350 heating stage and cooling unit. Measurements were performed on bulk samples sealed in 1.0 mm diameter glass capillaries, 0.01 mm wall thickness (Hilgenberg). UV-Vis experiments were performed on a Jasco V-750 spectrophotometer. All experiments were performed in 10 × 10 mm quartz cuvettes at 20 ^{0}C. Fluorescence experiments were measured using a Spark® Tecan 10M. Spectra was recorded using 100 of gain and 50% mirror at 20 ^{0}C. LC-MS experiments were performed in a Shimadzu LC-2040C liquid crhromatograph mass spectroscometer with a mass detector LCMS-2020. The photopolymerization was performed for 15 min with a mercury lamp (Omnicure s2000, emitting at 320−500 nm). The intensity was approximately 22 mW·cm^{-2} at the sample surface. HR-SEM was measured with Quanta 3D FEG (FEI/TFS) with EDT secondary detector. Samples were sputter coated with a thin layer of gold using a Balzer Union SCD 040 sputter device.

6.5.2 Detailed experimental conditions

Sample preparations

Self-standing films

Clean glass substrates (3 x 3 cm) were prepared by washing with acetone and isopropanol. The nanoporous materials were made by preparing a solution containing **NEt₄·Sulf** (1 equivalent), 1,10-decanedithiol as the cross-linker (1.5 equivalents) and Bis(2,4,6-trimethylbenzoyl)-phenylphosphineoxide (Irgacure 819, 3 wt.%) as photo-initiator in MeOH (50 mg/ml). 100-200 μL of the solution were bar coated manually (gap of 100 μm) on the clean glass plate at 70ºC to evaporate the solvent of the mixture. The samples were photo-polymerized using an EXFO Omnicure S2000 lamp with 8

mW·cm^{-2} of intensity, for 10 minutes, resulting in a white-transparent non-soluble self-standing polymer film of around 1 μm. Lastly, after rinsing with pure water, the samples were dried in a vacuum oven at 40 ^{0}C.

Supported membranes

Glass plates were cleaned with acetone and isopropanol under sonication for 10 minutes in a bath. A glue layer of polyvinyl alcohol (PVA) was spin-coated from a 10 wt.% aqueous solution onto clean glass at 1500 rpm for 60 s. An asymmetric polyethersulfone (PES) layer was pasted on the glass by pressing at 60 ^{0}C. Solutions for spin coating were prepared by mixing NET$_4$Sulf (1 equiv.) 1,10-decanedithiol (1.5 equiv.) as the crosslinker in ethanol in a 10 wt. % concentration. Finally, Bis(2,4,6-trimethylbenzoyl)-phenylphosphineoxide (Irgacure 819, 3 wt.%) was added as initiator. Then the monomer mixture was spin-coated onto the flat PES layer at 2500 rpm for 30 s. The "sandwich" was annealed by heating up to 70 ^{0}C and cooled down to room temperature. The membrane was polymerized with UV light for 15 min with 8 mW·cm^{-2} of intensity. The sample was peeled off from the glass by immersing in water to remove the PVA layer and after dried in a vacuum oven at 40 ^{0}C.

Ion exchange procedure

Circular samples of **NEt$_4$·Sulf** membranes (1.5 cm diameter) are immersed in an aqueous solution of DMBP iodide (1M) and stirred overnight at room temperature. After completion, the samples are rinsed with deionized water to be tested. The re-storage of the membranes to the initial form with NEt$_4^+$ counterions was carried out by soaking now the samples in an aqueous solution of NEt$_4$Cl (2M) overnight.

Filtration tests

Filtration tests were performed using a 20 ml custom-made, stainless steel, stirred "Amicon type" dead-end filtration cell of 1.5 cm diameter. Samples of the membrane were cut to the desired size and pre-cleaned with deionized water. For each filtration test, a membrane was placed in the cell that was filled with ultrapure water (total volume of 20 ml). The cell was closed and subsequently pressurized with nitrogen at the desired pressure.

The permeability of the membranes was determined by measuring the flux of pure water at different pressures (2–6 bar) *in triplo* for 3 samples. Pure water was filtered for 2 h at 5 bar to stabilize the flux.

Protein rejection was determined with the filtration of aqueous solutions (50 μM) of BSA and GFP in PBS. With the cell previously cleaned with water, the filtration was carried out at a pressure of 4 bar where 4 samples of 1 ml of permeate were collected

from which the first one was discarded to avoid mixtures with residual water below the membrane in the cell.

The MWCO of the membranes was determined by measuring the rejection of polyethylene glycol (PEG). Membranes were subjected to PEG filtrations at 4 bar in the Amicon cell. Aqueous solutions in ultrapure water were made containing PEGs with number average molecular weights (M_n) ranging from 600 to 10000 g·mol^{-1} with a concentration of 0.5 g·L^{-1} for each polymer. A series of different dyes with different molecular weights and charges were used for filtration tests: Fluorescein, Riboflavin, Crystal Violet, Orange G and Rhodamine B were selected. 50 µM aqueous solutions of the dyes were filtered separately at 4 bar of pressure in the Amicon setup. The filtration procedure and the rejection analysis of all these experiments (proteins, PEG, dyes) was done as described in previous Chapters (e.g. **section 2.6.2**).

For the rejection measurements of mono, di and tri saccharides, filtration of aqueous solutions was carried out separately at 4 bar and permeate solutions of 1 ml were collected and analysed with LC-Mass Spectroscopy.[12]

Saccharide		Parent ion m/z	Detected ion m/z	Retention time (s)
Glucose	$C_6H_{11}O_6$	180.16	180.16 + 23 (from Na of the matrix)	0.408
Sucrose	$C_{12}H_{21}O_{11}$	342.29	+23	0.358
Raffinose	$C_{18}H_{31}O_{16}$	594.51	+23	0.383

The concentration of the feed solutions was selected according to linearity of the mass intensity detected by the spectrometer. Calibration curves were made for concentrations of 0.5, 0.05 and 0.005 mg/ml of the saccharides and samples with different injection volumes (µl) were measured. Linearity was checked for the 3 concentrations, from which the best one (R-value closest to 1) was chosen. Permeate solutions that were collected were measured and the intensity of the detected peaks was converted into concentration using the calibration curve made for each sugar. Rejections were calculated relative to the feed concentrations.

For all the permeability and filtration tests, permeate solutions were collected *in triplo* for each sample. At least 2 samples of each type of membrane were tested.

Synthetic procedures

SulfAc was synthesized as detailed in Chapter 2:

HNEt₃·Sulf was converted into the sulfonic acid by using an ion exchange resin Amberlyst 15 hydrogen form. The residue was dissolved in ethanol and put through the resin with atmospheric pressure to let the triethylammonium cations exchange with

the protons. The solvent was evaporated and product was dried in vacuum oven at 60 °C to obtain a brown waxy material. ^{1}H-NMR (DMSO-d$_6$, 400 MHz,) δ = 7.54 – 7.41 (m, 2H), 7.13 – 7.07 (m, 2H), 6.50 (s, 2H), 5.78 (ddtd, J = 16.7, 9.8, 6.6, 3.0 Hz, 3H), 5.03 – 4.88 (m, 6H), 3.78 (t, J = 6.3 Hz, 2H), 3.69 (t, J = 6.2 Hz, 4H). ^{13}C-NMR (100 MHz, DMSO-d$_6$) δ 169.26, 152.10, 146.93, 145.23, 138.70, 130.90, 115.05, 72.81, 68.76, 33.67, 30.23, 29.56, 29.50, 29.37, 29.29, 29.23, 29.18, 29.06, 29.04, 28.78, 25.99.

Tetraethylammonium sulfonic acid salt (NEt₄·Sulf)

HNEt₃·Sulf (95 mg, 0.119 mmol, 1 equiv.) and NEt₄OH (14.2 mg, 0.119 mmol 1 equiv.) were dissolved in 5 ml of MeOH and left stirring overnight. A pH paper was used to check the pH to be neutral. The solvent was evaporated and the residue was dissolved in chloroform and was filtered. The chloroform was evaporated, and the product was dried in vacuum oven at 60 ^{0}C to dry the compound. ^{1}H-NMR (CDCl₃, 400 MHz) δ = 7.85 – 7.71 (m, 2H), 7.09 – 6.94 (m, 2H), 6.53 (s, 2H), 5.81 (ddtd, J = 16.9, 10.2, 6.7, 3.5 Hz, 3H), 5.10 – 4.82 (m, 6H), 3.80 (dt, J = 48.6, 6.6 Hz, 6H), 3.42 (s, 3H), 3.35 (q, J = 7.3 Hz, 8H), 2.04 (q, J = 6.3, 5.7 Hz, 6H). ^{13}C-NMR (CDCl₃, 100 MHz) δ = 170.76, 145.75, 145.02, 139.19, 139.02, 130.68 127.16, 126.11, 114.11, 107.23, 73.34, 68.89, 52.60, 38.67, 33.85, 29.64, 29.51, 29.49, 29.43, 29.34, 29.23, 29.21, 26.05, 7.58. Maldi-Tof MS: m/z calculated for [M-NC₈H₂₀]⁺: 794,51 found: 794,50.

Sodium sulfonate derivative (Na·Sulf)

Sodium hydroxide (5.3 mg, 0.133 mmol 1 equiv.) and **SulfAc** (106 mg, 0.133 mmol, 1 equiv.) were dissolved in 5 ml of MeOH and left stirring overnight. A pH paper was used to check the pH to be neutral. The solvent was evaporated and the residue was dissolved in chloroform and was filtered. The chloroform was evaporated, and the product was dried under vacuum oven at 60 ^{0}C over the weekend. ^{1}H-NMR (DMSO-d$_6$, 400 MHz,) δ = 7.50 (d, J = 8.0 Hz, 2H), 7.11 (d, J = 8.0 Hz, 2H), 6.50 (s, 2H), 5.77 (dtd, J = 17.0, 6.7, 3.4 Hz, 3H), 4.95 (dd, J = 24.0, 13.7 Hz, 6H), 3.73 (dt, J = 34.7, 6.2 Hz, 6H).

Potassium sulfonate derivative (K·Sulf)

SulfAc (100.5 mg, 0.126 mmol, 1 equiv.) and potassium hydroxide (7.1 mg, 0.127 mmol, 1 equiv.) were dissolved in water (5 ml). The solution was stirred overnight at 60°C. The solvent was evaporated. The residue was dissolved in chloroform and filtrated. The filtrate was collected, and the solvent was evaporated under vacuum. ^{1}H-NMR (CDCl₃, 400 MHz) δ = 7.79 (d, J = 8.0 Hz, 2H), 7.11 (d, J = 8.1 Hz, 2H), 6.60 (s, 2H), 5.79 (qt, J = 9.7, 4.8 Hz, 3H), 4.99-4.80 (dd, J = 24.4, 13.6 Hz, 6H), 3.90 (t, J = 6.7 Hz, 2H), 3.83 (d, J = 6.5 Hz, 4H), 3.33 (s, 3H), 2.02 (q, J = 7.3 Hz, 6H), 1.69 (h, J = 6.4 Hz, 6H), 1.55 – 0.99 (m, 41H, alkyl chain).

Magnesium sulfonate derivative (Mg·Sulf$_2$)

MgCl$_2$ (6.58 mg, 0.069 mmol 1 equiv.) and **SulfAc** (110 mg, 0.138 mmol, 2 equiv.) were dissolved in 5 ml of MeOH and left stirring at room temperature for 3 hours. A pH paper was used to check the pH to be neutral. The MeOH was evaporated, and the residue was dried in vacuum oven at 60 ^{0}C overnight. ^{1}H-NMR (CDCl$_3$, 400 MHz) δ = 7.80 (d, *J* = 8.0 Hz, 4H), 7.13 (d, *J* = 8.1 Hz, 4H), 6.55 (s, 4H), 5.79 (ddd, *J* = 16.9, 11.5, 5.4 Hz, 6H), 4.95 (dd, *J* = 24.8, 13.6 Hz, 12H), 3.85 (dt, *J* = 42.9, 6.5 Hz, 12H), 3.41 (s, 6H), 2.03 (q, *J* = 7.1 Hz, 13H), 1.69 (q, *J* = 8.6, 8.0 Hz, 13H).

N-methylpyridinium iodide (MPy)

Pyridine (2.0911 g, 26.44 mmol, 1 equiv.) and methyl iodide (3.07 g, 21.63, 0.82 equiv.) were dissolved in 136 ml of acetonitrile and refluxed overnight. After this, 300 ml of ethyl acetate was added to form a solid precipitate. After this the mixture was put in the fridge for 2 hours. N-methylpyridinium iodide was obtained by vacuum filtration. ^{1}H NMR (DMSO-*d$_6$*, 400 MHz,) δ = 8.81-8.59 (m, 4H), 7.96- 7.68 (m, 4H). ^{13}C NMR (DMSO-*d$_6$*, 100 MHz,) δ 145.53, 145.05, 127.68, 47.96.

N-methylpyridinium sulfonate derivative (MPy·Sulf)

MPy (15.5 mg, 0.132 mmol 1 equiv.) and **HNEt$_3$Sulf** (105 mg, 0.132 mmol 1 equiv.) were dissolved in 5 ml of methanol and refluxed overnight. When the reaction was finished, methanol was evaporated and the residue was dried under in a vacuum oven at 60 ^{0}C. ^{1}H-NMR (CDCl$_3$, 400 MHz) δ = 9.05 (d, *J* = 5.9 Hz, 2H), 8.39 (t, *J* = 7.9 Hz, 1H), 7.95 (t, *J* = 7.1 Hz, 2H), 7.74 (d, *J* = 8.0 Hz, 2H), 7.04 (d, *J* = 8.0 Hz, 2H), 6.53 (s, 2H), 5.81 (ddt, *J* = 13.8, 10.2, 6.9 Hz, 3H), 4.96 (dd, *J* = 25.0, 13.6 Hz, 5H), 4.49 (s, 3H), 3.82 (dt, *J* = 49.1, 6.5 Hz, 6H), 3.43 (s, 3H), 2.03 (t, *J* = 7.0 Hz, 6H). ^{13}C-NMR (DMSO-*d$_6$*, 100 MHz,) δ = 169.21, 152.05, 146.86, 149.37, 146.76, 145.19, 139.19, 139.14, 138.64, 130.85, 128.11, 127.92, 126.29, 114.98, 107.73, 72.75, 68.69, 48.24, 40.56, 40.35, 40.15, 40.04, 39.94, 39.73, 39.52, 39.31, 38.54, 33.62, 30.18, 29.52, 29.45, 29.33, 29.24, 29.18, 29.13, 29.01, 28.99, 28.73, 25.94.

N,N-dimethyl-4,4-bipyridinium diiodide (DMBP)

4,4-bipyridine (1.25 g, 8.00 mmol, 1 equiv.) and methyl iodide (11.36 g, 80 mmol, 10 equiv.) were dissolved in 75 ml of acetonitrile and the mixture was refluxed overnight. After complexion, ethyl acetate (200 ml) was added to form a solid precipitate. The mixture was put in the fridge for 2 hours to get more precipitation and more clean crystals. N,N-dimethyl-4,4-bipyridine was isolated by vacuum filtration and dried in the vacuum oven at 60 ^{0}C. ^{1}H-NMR (DMSO-*d$_6$*, 400 MHz,) δ = 9.29 (d, *J* = 6.5 Hz, 4H), 8.90 – 8.57 (m, 4H), 4.44 (s, 6H). ^{13}C-NMR (DMSO-*d$_6$*, 100 MHz,) δ = 169.21, 152.05, 146.86, 145.97, 145.46, 145.19, 139.19, 139.14, 138.64, 130.85, 128.11, 126.72, 126.29, 114.98, 107.73, 72.75, 68.69, 48.33, 40.56, 40.35, 40.15, 40.04, 39.94, 39.73,

39.52, 39.31, 38.54, 33.62, 30.18, 29.52, 29.45, 29.33, 29.24, 29.18, 29.13, 29.01, 28.99, 28.73, 25.94.

### *N,N-dimethyl-4,4-bipyridinium derivative (DMBP·Sulf₂)*

HNEt₃·Sulf (56.8 mg, 0.0715 mmol 2 equiv.) and **DMBP** (15.7 mg, 0.036 mmol, 1 equiv.) were dissolved in 15 ml of MeOH and left stirring overnight at 50 °C. The pH was tested with a pH paper, which indicated that the pH was neutral. The MeOH was evaporated and the residue was filtered with chloroform. After evaporation of the solvent the product was obtained pure after drying in the vacuum oven at 40 °C for 2 hours. ^{1}H-NMR (DMSO-*d*6, 400 MHz,) δ 9.27 (d, *J* = 6.2 Hz, 4H), 8.74 (d, *J* = 6.3 Hz, 4H), 7.48 (d, *J* = 8.3 Hz, 4H), 7.10 (d, *J* = 8.1 Hz, 4H), 6.50 (s, 4H), 5.78 (tq, *J* = 10.4, 6.9 Hz, 6H), 5.09 – 4.80 (m, 10H), 4.43 (s, 6H), 3.73 (dt, *J* = 34.4, 6.2 Hz, 12H), 2.00 (d, *J* = 7.4 Hz, 13H), 1.58 (s, 13H). ^{13}C-NMR (DMSO-*d*6, 100 MHz,) δ 169.21, 152.05, 146.86, 145.97, 145.46, 145.19, 139.19, 139.14, 138.64, 130.85, 128.11, 126.72, 126.29, 114.98, 107.73, 72.75, 68.69, 48.33, 40.56, 40.35, 40.15, 40.04, 39.94, 39.73, 39.52, 39.31, 38.54, 33.62, 30.18, 29.52, 29.45, 29.33, 29.24, 29.18, 29.13, 29.01, 28.99, 28.73, 25.94.

6.6 References

[1]   U. Beginn, L. Yan, S. N. Chvalun, M. A. Shcherbina, A. Bakirov, M. Moller, *Liq. Cryst.* **2008**, *35*, 1073.
[2]   H. Zhang, L. Li, M. Möller, X. Zhu, J. J. H. Rueda, M. Rosenthal, D. A. Ivanov, *Adv. Mater.* **2013**, *25*, 3543.
[3]   J. J. Hernandez Rueda, H. Zhang, M. Rosenthal, M. Möller, X. Zhu, D. A. Ivanov, *Eur. Polym. J.* **2016**, *81*, 674.
[4]   X. Zhu, M. A. Scherbina, A. V. Bakirov, B. Gorzolnik, S. N. Chvalun, U. Beginn, M. Möller, *Chem. Mater.* **2006**, *18*, 4667.
[5]   P. P. Patrick Oswald, *Smectic and Columnar Liquid Crystals. Concepts and physical properties illustrated by experiments* (Ed.: G.W. Gray, J. . W. G. and A. F.), CRC Press, Taylor and Francis, **2005**.
[6]   S. Laschat, A. Baro, N. Steinke, F. Giesselmann, C. Hägele, G. Scalia, R. Judele, E. Kapatsina, S. Sauer, A. Schreivogel, M. Tosoni, *Angew. Chemie - Int. Ed.* **2007**, *46*, 4832.
[7]   S. Bhattacharjee, J. A. M. Lugger, R. P. Sijbesma, *Chem. Commun.* **2018**, *54*, 9521.
[8]   X. Dong, A. Al-Jumaily, I. C. Escobar, *Membranes (Basel).* **2018**, *8*, 23.
[9]   B. M. Carter, B. R. Wiesenauer, R. D. Noble, D. L. Gin, *J. Memb. Sci.* **2014**, *455*, 143.
[10]   S. M. Dischinger, M. J. McGrath, K. R. Bourland, R. D. Noble, D. L. Gin, *J. Memb. Sci.* **2017**, *529*, 72.
[11]   G. Artuğ, I. Roosmasari, K. Richau, J. Hapke, *Sep. Sci. Technol.* **2007**, *42*, 2947.
[12]   R. Feil, J. E. Lunn, In *Plant Metabolomics. Methods in Molecular Biology*, Humana Press, New York, **2018**, pp. 87–100.

Chapter 7

Optimization of molecular design and performance of LC-based filtration membranes

H-bonding stacking

Fabrication process

Modification of membrane properties
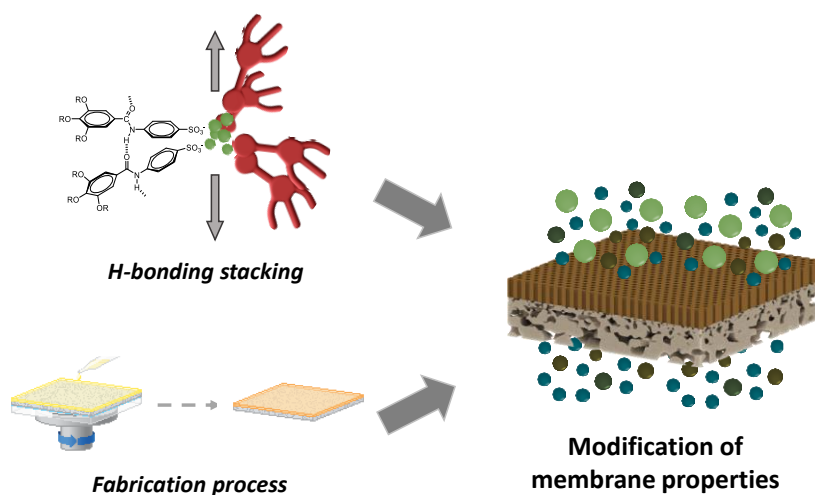
Abstract | One of the biggest challenges in improving state-of-the-art membranes for water filtration is to adapt research concepts to large-scale wastewater treatment systems. In this Chapter, a discussion of strategies to improve the properties of the membranes described in the earlier Chapters of the thesis is presented. The orientation of the pores in these nanostructured materials is an essential factor in the optimization of water flux. We demonstrate that better organization in the columnar LC phase *via* hydrogen bonding increases membrane permeabilities. General optimization of the membrane fabrication parameters such as the thickness of the active layer and the coating method is explored to improve performance of the membranes. Finally, the water flux is successfully increased by a process of thermal annealing of the columnar mesophase in the active layer. However, further work needs to be done to fully understand the origin of the improvements at the molecular level.

7.1 Introduction: Enhancement of membrane properties

Research on nanofiltration membranes for the removal and/or recovery of organic solutes focuses on reaching optimal selectivity and permeability. In the earlier Chapters of this Thesis, it was shown that membranes based on self-assembled liquid crystals (LCs) have great potential in this respect because they have uniform nanometer-sized pores that can be functionalized chemically to tune filtration characteristics. The filtration properties of the membranes can be tuned with the modification of the pore functionalities (by molecular design, ionic exchange or covalent chemistry, see Chapter 3) or by using light as external stimuli (see Chapter 5). In the current Chapter, a number of processing parameters for optimization of membrane performance are used to obtain control over the active layer thickness and orientation of pores, important factors to maximize water flux. The preliminary results presented here serve as an outlook for future improvements in membrane fabrication.

This Chapter is divided into two main sections: *i)* improvement of the columnar order *via* unidirectional H-bonding the mesophase to create better-oriented pores and *ii)* thermal annealing of the active layer before crosslinking to improve membrane permeability. Efforts to produce the thinnest active layer without creating defects is discussed in both sections. Finally, a small overview of the future possibilities for the application of these membranes in industrial systems is presented.

7.2 Membranes based on H-bonded wedge-shaped sulfonates

One of the challenges in the development of membranes based on self-assembled nanostructures is to obtain control over the orientation of the pores. The membranes presented in this thesis have been prepared from non-aligned columnar phases as the selective layer on top of a porous support. Ideally, the pores should point perpendicularly to the support (homeotropic alignment) over the whole surface area to obtain maximum permeability. Usually, discotic LCs show planar alignment with the director vector parallel to the surface, which is unfavorable for the fabrication of high flux membranes. Even though the use of external agents like magnetic or electric fields[1] or even IR excitation[2] have shown to be effective, the most common method to get homeotropic alignment is by tuning the surface energy of the substrate.[3] An easy way to apply this approach to columnar mesophases is by using an alignment sacrificial agent with the proper interfacial energy and chemistry to orient the LC phase.[4] However, spontaneous self-orientation without an external agent is preferred, for which supramolecular chemistry is a potential tool. Hydrogen bonding is one of the most useful non-covalent interactions in supramolecular chemistry due to its strength and versatility.[5],[6] A special example of the application of hydrogen bonding in porous

materials uses BTA (benzene-1,3,5-tricarboxamide) derivatives and the ability of disc-shaped molecules to form long and stable hydrogen boned stacks.[7] In earlier works from the group, the orthogonal self-assembly of BTA-based discotic molecules and ionic dendrimers into columnar LCs is used to obtain nanostructured materials with induced porosity.[8],[9]

In this section, the goal is to make use of hydrogen-bonding between amides in order to improve the stacking of the discotic molecules into columnar structures. The presence of hydrogen bonds will induce the formation of uniaxially oriented stacks. Applied to membranes, better oriented pores will result, which improve the transport properties.

To address this, new molecular building units are prepared and studied: **HNEt₃·Sulf-H** and **NEt₄·Sulf-H**, analogous compounds to the salts studied in previous Chapter 6. The hydrogen bonds formed will create a columnar stacking with enhanced orientation (**Figure 7.1a.b**) from which an improvement of the filtration membrane performance is expected (**Figure 7.1c**).

(a) H-bonded wedge shaped sulfonates

(b) Columnar stacking by H-bonding — Columnar mesophase

(c) Filtration membrane
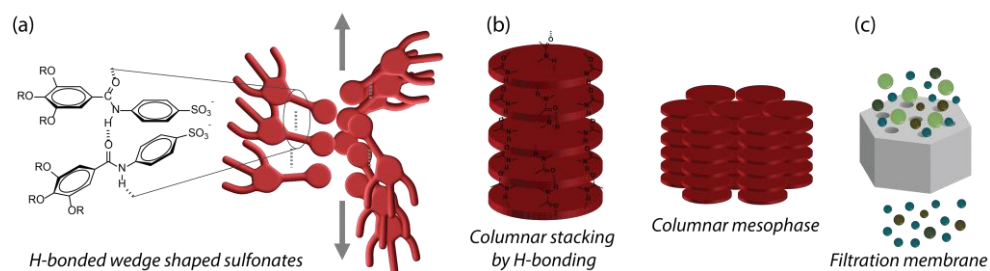
Figure 7.1 | Representation of the self-assembly process of wedge-shaped sulfonated salts and influence of the H-bond on the columnar stacking, which improves flux in the filtration process.

7.2.1 Preparation of new sulfonate salts with N-H bonding

First, the sulfonic acid derivative **HNEt₃·Sulf-H** was synthesized in four steps following a synthetic route analogous to that described in Chapter 2, now using unsubstituted sulfanilic acid:
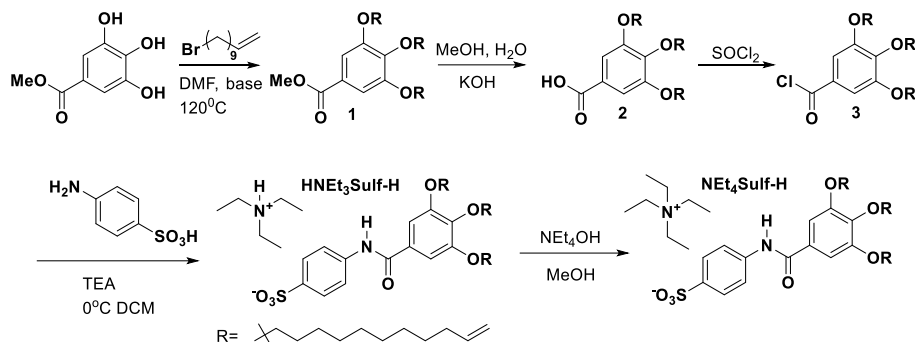
Scheme 7.1 | 4-step synthesis of **HNEt₃·Sulf-H** and **NEt₄·Sulf-H**

Compound **3,** described in Chapter 2, was reacted with sulfanilic acid in DCM with TEA at 0 °C to give **HNEt₃·Sulf-H** as a white solid. By reacting **HNEt₃·Sulf-H** with NEt₄OH in methanol, **NEt₄Sulf-H** was quantitatively obtained as a waxy white solid. FT-IR studies confirmed the formation of hydrogen bonds in compounds **HNEt₃·Sulf-H** and **NEt₄·Sulf-H** due to the presence of the free hydrogen atom on the amide group (**Figure 7.2**). The appearance of a N-H band around 3295 cm⁻¹ for **HNEt₃·Sulf-H** and **NEt₄Sulf-H** indicated the presence of hydrogen bonds in the compounds.[10,11] Shifts to lower frequencies of the vibration band of C=O (amide II) also indicate hydrogen bonding: compounds **HNEt₃·Sulf-H** and **NEt₄Sulf-H** showed peaks at 1640 cm⁻¹ and 1664 cm⁻¹, meaning that a mix of hydrogen bonded and free amides is present, creating a heterogeneous and non-continuous columnar stacking.
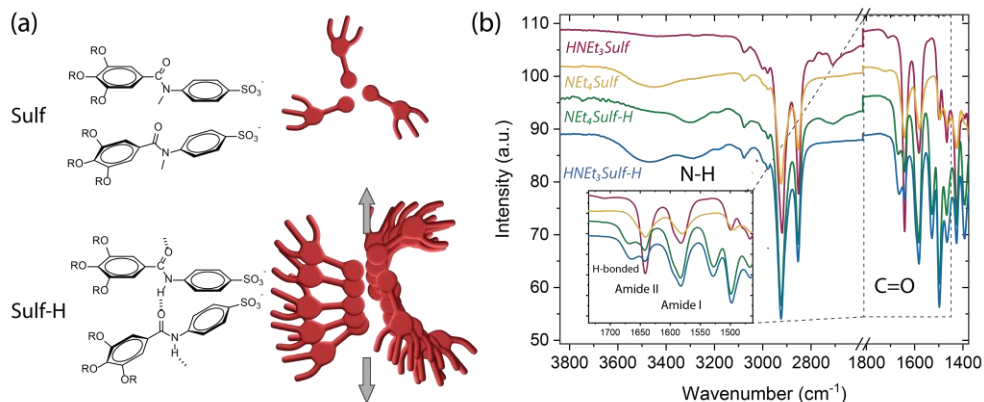

Figure 7.2 | a) Illustration of the columnar stacking promoted by H-bonding present in **HNEt₃·Sulf-H** and **NEt₄Sulf-H** salts and b) FT-IR comparison spectra of the compounds in bulk.

The thermal properties of the new compounds were investigated with Polarized Optical Microscopy (POM) and Differential Scanning Calorimetry (DSC). Samples of

both salts were observed under crossed polarizers after heating and cooling at a rate of 5 ^{0}C/min to favor the formation of larger domains. As depicted in **Figure 7.3**, birefringent textures related to columnar mesophases appeared. For **NEt₄·Sulf-H** the presence of more black areas indicated a higher fraction of homeotropically aligned domains. Additionally, DSC traces showed high isotropization temperatures of 202 ^{0}C and 230 ^{0}C for **HNEt₃·Sulf-H** and **NEt₄·Sulf-H** respectively (**Table 7.1**).
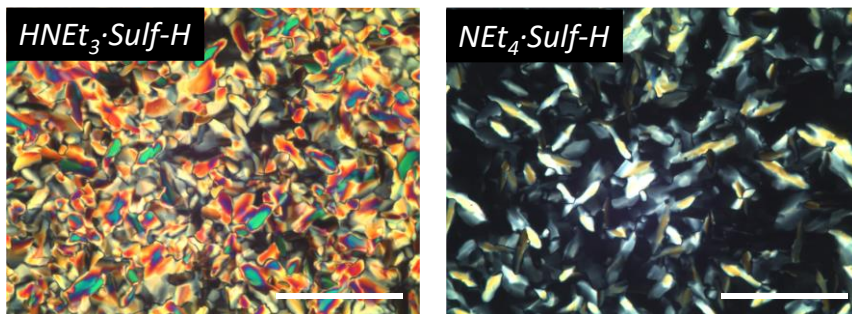

Figure 7.3 | Polarized optical micrographs of **HNEt₃·Sulf-H** and **NEt₄Sulf-H** at room temperature. Scale bar 100 μm.

Table 7.1 | Phases and transition temperatures (^{0}C) measured with DSC in the second heating run at a heating rate of at 5 ^{0}C/min:

Compound	Phase transition*	T (ºC)
HNEt₃·Sulf-H	clearing (M → I)	202.02
NEt₄·Sulf-H	glass transition	80.52
	clearing (M → I)	231.17

*M = mesophase, I = isotropic phase

The mesophases of the compounds were further investigated with X-ray scattering at room temperature after annealing by heating above the corresponding isotropization temperatures and subsequently cooling down to room temperature. The WAXS patterns showed peaks with q-ratios of 1:√3:2:√7 corresponding to a columnar hexagonal mesophase like for compound **NEt₄·Sulf** (**Figure 7.4a**). However, the narrower peaks of the new compounds suggested more defined mesophases. The lattice parameter obtained for **NEt₄·Sulf-H** (*a* = 4.39 nm) is slightly larger than **HNEt₃·Sulf-H** (*a* = 4.34 nm). Based on the lattice parameters obtained, it was concluded that **NEt₄Sulf-H** aggregates in columns with 4 wedges per disc, just like **NEt₄Sulf** (see Chapter 6). This allows a comparison of the parameters of the hydrogen bonding and the non-hydrogen wedges. The larger value of *a* = 4.71 nm for **NEt₄·Sulf**, indicates a higher aggregation of the molecules within the disc when H-bonding is

present, creating smaller columns. Additionally, a sharp peak related to the interdisc distance *c* from the π-π stacking appeared for **NEt₄·Sulf-H** at 0.345 nm, a peak that was not observed for **NEt₄·Sulf**. Due to the lack of information about the packing of the columns in **NEt₄·Sulf**, only the comparison of the lattice parameter a is possible. Since the pore size can only be estimated when both parameters a and c are known, it is not possible to draw conclusions about differences in pore size between the mesophases of **NEt₄·Sulf** and **NEt₄·Sulf-H**.

To further study the orientation of the molecules in a thin film, Grazing Incidence X-ray scattering (GISAXS)measurements were carried out. In GISAXS, the X-rays have a very small incident angle - almost parallel to the surface, and information about the arrangement and orientation of the columns at the surface of the mesophase can be obtained. The compounds studied with this experiment are **HNEt₃·Sulf, NEt₄·Sulf, HNEt₃·Sulf-H** and **NEt₄·Sulf-H**. Samples of the 4 compounds spin-coated on glass (layers of around 500 nm) were measured and compared (**Figure 7.4b**). High order in the mesophase of **HNEt₃·Sulf** resulted in narrow diffraction peaks and allowed the indexation of the peaks related to the orientation of the mesophase. The primary reflection 0 1 resulted in a strong signal which, together with the perpendicular positions of first and second-order diffraction signals 1 0 and 2 0 respectively, indicates the presence of an in-plane orientation.[12] **NEt₄·Sulf** showed a diminished intensity of 2 0 and 1 1 reflections suggesting that the in-plane orientation is less defined. Moreover, broadening of the 0 1 and 1 0 reflections in samples of compounds with H-bonding, which was most pronounced for **NEt₄·Sulf-H** with a shift from 30^0 to almost 0^0, indicates an out-of-plane orientation of the columns at the surface. It is concluded that in these phases, hydrogen bonding induces an out-of-plane orientation of the columns on a glass substrate.
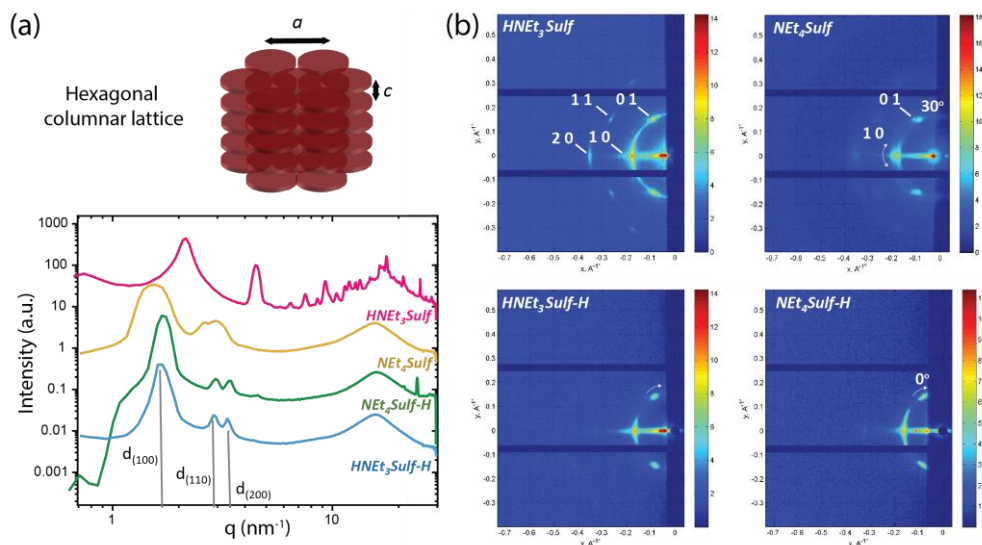
Figure 7.4 | a) Comparison of WAXS patterns for the 4 salts with and without H bonding, revealing a columnar hexagonal arrangement of the lattice; b) GIMAXS 2D patterns of the 4 compounds and indexation of the most important diffraction peaks related to in-plane or out-of-plane molecular orientations.

It was decided to use **NEt₄·Sulf-H** for the fabrication of filtration membranes to allow direct comparison with the **NEt₄Sulf** membranes presented in previous Chapter 6. Then, the filtration performance of the membranes can be compared. The membranes formed from **NEt₄Sulf** and **NEt₄Sulf-H** are labeled **NMe** and **NH** respectively.

7.2.2 Membrane fabrication and characterization

Supported membranes with **NMe** and **NH** as the active layer were produced using the direct coating procedure detailed in Chapter 6 (**section 6.3.2**): a thin layer of the material is deposited on top of a polyethersulfone (PES) support and crosslinked with UV light. High-Resolution Scanning Electron Microscopy (HR-SEM) measurements established the absence of macro and micro defects in the surface and the thickness of the active layer was determined to be 250-300 nm (**Figure 7.5**).
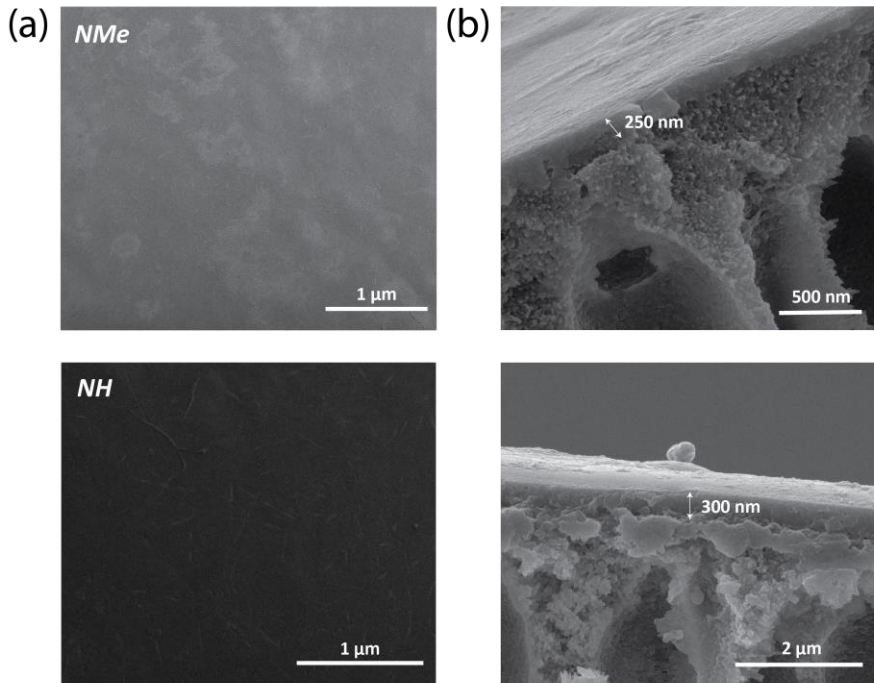
Figure 7.5 | HR-SEM top view (a) and cross-section (b) of supported membranes containing **NMe** and **NH** salts.

The permeability of pure water was measured for both membranes (**Figure 7.6**): after 1 h, a stable flux was reached with a higher permeability for **NH (**2.07 L·m^{-2}·h^{-1}·bar^{-1}) than for **NMe** (1.43 L·m^{-2}·h^{-1}·bar^{-1}). It is hypothesized that the higher permeability of the **NH** membrane is a result of the influence of the hydrogen bonding that promotes some ordering of the columnar channels. Additionally, the presence of defects in the membranes was investigated by filtration of bovine serum albumin (BSA) and green fluorescence proteins (GFP) with molecular sizes of 6 and 5 nm respectively. The high rejection values of >98% for both proteins confirmed the absence of micro-defects in the active layer of both membranes (**Table 7.2**).

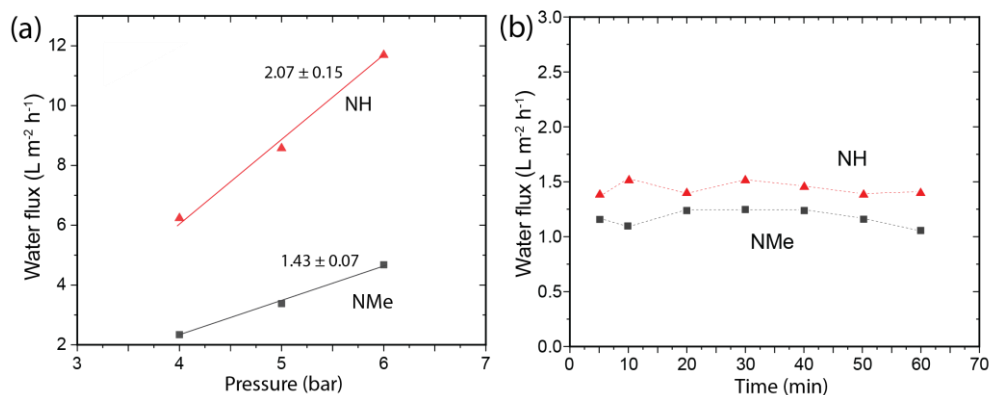**Figure 7.6 |** Plots comparing a) water flux through **NH** (red triangles) and **NMe** (grey squares) membranes vs pressure and b) water flux of both membranes vs time at 4 bars of external pressure.

Table 7.2 | Water permeability and rejection values of GFP and BSA proteins for **NMe** and **NH** membranes:

Membrane	Permeability ($L \cdot m^{-2} \cdot h^{-1} \cdot bar^{-1}$)	Rejection GFP, 5 nm (%)	Rejection BSA, 6 nm (%)
NMe	1.43 ± 0.07	98.90	99.21
NH	2.07 ± 0.15	99.74	99.84

To estimate the relative pore sizes of the **NH** the **NMe** membrane, the rejection of 4 PEGs with Mn ranging from 600 to 7000 KDa was measured. The results of the filtration experiments showed a rejection curve with a MWCO value of around 1500 g·mol^{-1} (**Figure 7.7**). Based on this value, a pore size of 1.2 nm was calculated based on the hydrodynamic radius of PEG 1500 and the estimated size of the pores of the material in Chapter 2.[13] This value is smaller than the **NMe** membrane (1.3 nm) and in line with the smaller lattice parameters previously obtained from X-ray data (**Figure 7.4a**). Therefore, combining the results from the X-ray studies and the filtration tests, it is concluded that **NH** membranes with smaller pores have higher water flux than **NMe** membranes because of the higher order in the columnar pores induced by hydrogen bonding.
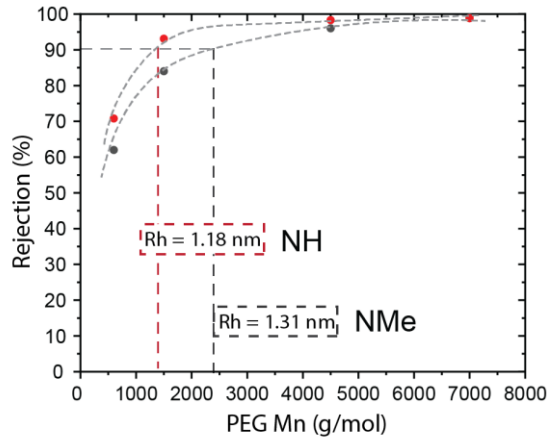
Figure 7.7 | Comparison of PEG rejection curves of **NMe** and **NH** membranes**.**

Table 7.3 | MWCO values with the corresponding pore sizes comparing **NMe**, **NH** membranes and **Sulfac₃TB** membrane of Chapter 2:

Membrane	M_n (g·mol^{-1})	R_h (nm)*
Sulfac$_3$TB	4.6×10^3	1.68
NMe	2.4×10^3	1.31
NH	1.5×10^3	1.18

**Pore size equivalent to $R_h = 0.06127 \cdot M_n^{0.3931}$*

7.2.3   Optimization of the thickness of the active LC layer

In the previous Chapters of this Thesis, molecular design was the main tool to modify membranes and improve their performance by e.g. introducing functionalities that induce the desired morphology and create specific interactions with solutes. However, the membrane fabrication process also plays a crucial role in the overall quality of the membrane, allowing further improvements by the optimization of processing parameters. The thickness of the porous active layer (µ) is an important factor in determining filtration performance and can be controlled during spin coating by tuning concentration and spinning speed.   The water flux (Q) is inversely related to the thickness following the Hagen-Poiseuille equation[14][15]:

$$Q = \frac{\pi \varepsilon (\Delta P) R^4}{8 \mu L} \quad \text{(eq. 7.1)}$$

In order to investigate the lowest layer thickness that can be fabricated without introducing excessive density of micro defects, samples of **NEt₄Sulf-H** membranes with different layer thicknesses were prepared. Spin coating speed and concentration of the monomeric solution were selected as variable parameters. Moreover, the differences between the direct and indirect coating methods used in the previous Chapters were investigated. To this end, for each coating method a batch of membranes was prepared using different concentrations (1, 2, 2.5, 5 and 10 wt. %) and 2 coating speeds (1500 or 2000 rpm). The membranes were visualized with HR-SEM and the thickness of the layer was determined from the electronic micrographs resulting in thinner layers for less concentrated samples and faster spin coating (**Figure 7.8a**).

As **eq. 1** indicates, decreasing the thickness reduces the resistance to flow, which increases the permeability of pure water. Theoretical permeability was calculated assuming the length of all cylinders to be equal to the thickness of the film, L (m), porosity (ε) = 2.2 10^{-17} and R = 0.234 (calculated using the lattice distance d obtained by X-ray diffraction in section 7.2.1), ΔP = 1 bar and μ (water) = $0.89\cdot10^{-3}$ Pa·s^{-1} (see Chapter 2).
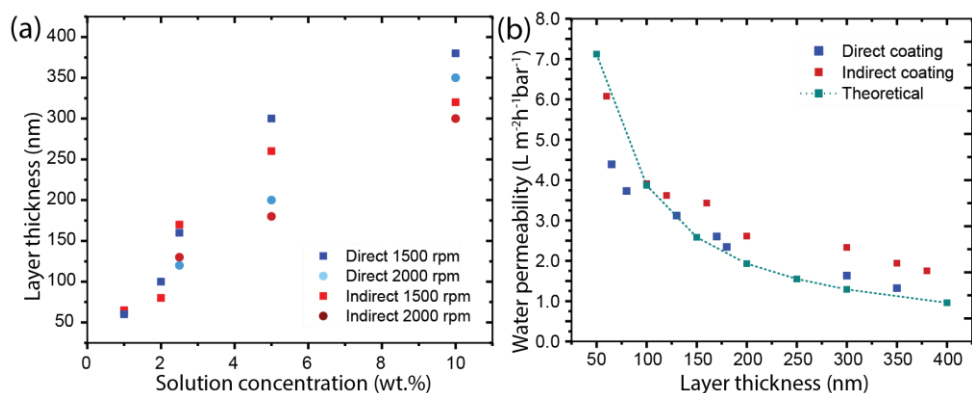
Figure 7.8 | a) Relation of the layer thickness and concentration (wt. %) of spin-coated membranes for both direct and indirect coating at speeds of 1500 and 2000 rpm; b) Water permeability values vs layer thickness plot for directly and indirectly coated membranes and theoretical values.

The plot of permeability vs layer thickness in **Figure 7.8b** shows a similar trend for both experimental methods and permeabilities close to, or even exceeding the theoretical values. In particular, the indirect coating method showed values higher than the theory. This might be ascribed to the presence of defects in the active layer at low coating thicknesses. The presence of a small fraction of defects can drastically increase the permeation of water and this is more likely to occur at low thicknesses. To evaluate the presence of defects, rejection of BSA protein (6 nm diameter size) was

measured. **Figure 7.9** shows high BSA rejection values (above 98%) for both methods, except for concentrations of 1 and 2 wt.%, which indicates that micrometer defects are rare above 150 nm but become more important below a thickness of 100-150 nm.

Noticeably, the difference between calculated and measured water permeability is larger for the thicker membranes with higher BSA rejection. This indicates that the discrepancy is not caused by defects but suggests that the parameter estimates used in the calculation of the theoretical flux are inaccurate. The estimated pore radius can be a particularly large source of error as the calculated permeability increases with r^4 for a given value of the columnar spacing.
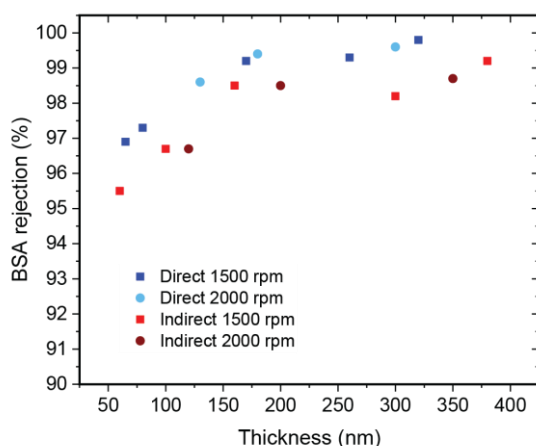
Figure 7.9 | Plot with relation of BSA rejection % values and thickness of active layer showing a thickness limit of 150 nm.

Summarizing this section, it can be concluded that firstly, the design of wedge-shaped H-bonded sulfonate salts is presented with the aim of enhancing columnar orientation for improved filtration performance in membranes. Smaller networks with an out-of-plane molecular orientation than the analogous previous system in Chapter 6 are obtained. The filtration tests of **NEt₄·Sulf-H** defect-free membranes show higher permeability and smaller pore sizes than **NEt₄·Sulf** membranes, suggesting a better orientation of the pores towards the flux.

Additionally, optimization of the fabrication parameters (deposited amount of LC material and spin coating speed) showed a thickness limit of 150 nm for the obtention of defect-free membranes with good performance. Moreover, the evaluation of water flux and defect formation suggests that the direct coating is more effective to produce better-quality membranes, also with easier scalability.

7.3 Influence of thermal annealing process on the membrane performance

To improve the transport through the columnar pores in the presented membranes, a homeotropic alignment of pores is preferred over the spontaneous planar orientation that is normally adopted. Different strategies already mentioned in **section 7.1** can be used to control the columnar alignment and particularly with thermotropic LCs, it is possible by thermal annealing.[3],[16] During this process, which consists of heating and subsequent cooling, the columns in the mesophase adopt the preferred orientation by molecular re-arrangement.[17] The control over the orientation of pores leads to an improvement in transport properties, with better filtration performance of the membranes.[18],[19]

As investigated in Chapter 6, **NEt₄·Sulf** has a low isotropization temperature (Col → I) of 72 ^{0}C, making thermal annealing a feasible approach to get homeotropic alignment. The effect of this process on the optical behavior of **NEt₄·Sulf** was studied with polarized optical microscopy (POM). After heating up to 80 ^{0}C (above isotropization) and slow cooling down to room temperature, optical textures with bigger domains and more homeotropic areas (black) appeared (**Figure 7.10**).
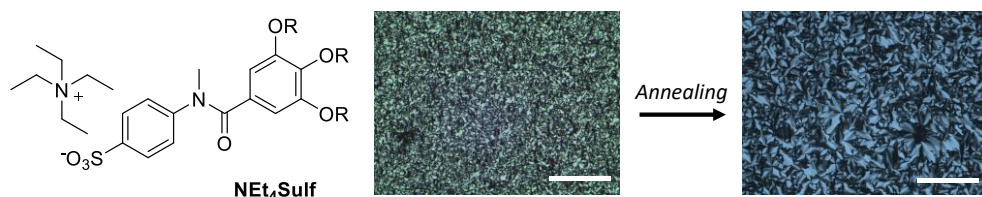
Figure 7.10 | Molecular structure of **NEt₄·Sulf** and cross-polarized micrographs at room temperature of the compound before and after thermal annealing consisting of heating up to isotropization and cooling down at 10 ^{0}C/min. Scale bar: 100 µm.

The influence of thermal annealing on the filtration performance was investigated: supported membranes were prepared as described in Chapter 6 (**section 6.3.2**). The samples were divided into 3 batches to be crosslinked with UV light at different temperatures: 1) **non-treated** membranes, directly polymerized at room temperature; 2) isotropic membranes, polymerized at 80 ^{0}C, which is above the isotropization temperature (72 ^{0}C) and 3) annealed membranes, polymerized after heating to 80 ^{0}C and cooled down to room temperature (**Figure 7.11a**). After washing with deionized water and drying the samples, the cross-section of the membranes was checked with High-Resolution Scanning Electron Microscopy (HR-SEM) to measure the thickness of the active layer (**Figure 7.11b**). Non-treated membranes showed a differentiated layer on top of the support of around 200-300 nm. Annealed membranes did not present a

clear separation between the active layer and the support due to the penetration of the material in¡ the pores of the support when it is in the isotropic phase. Lastly, in the **isotropic** membranes, the penetration is even deeper as the membrane stays longer at higher temperatures during the polymerization.
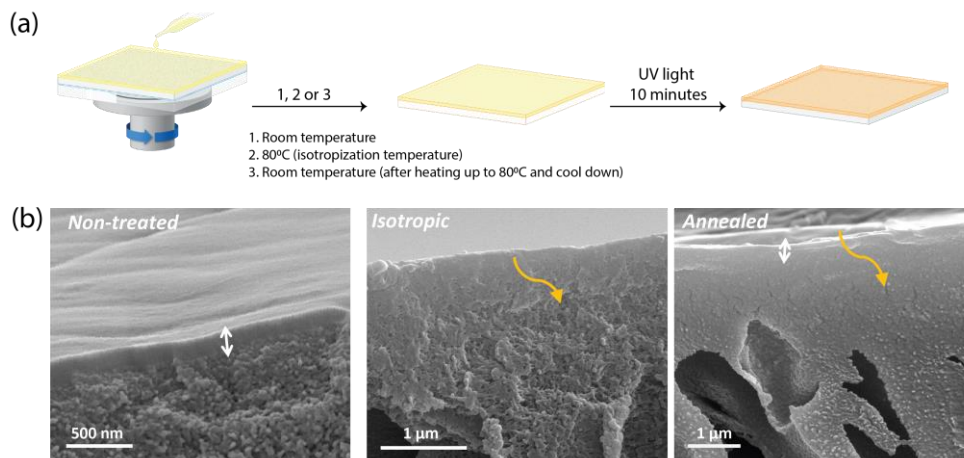
Figure 7.11 | a) Illustration of the membrane fabrication of the different samples with polymerization at room temperature (1 = non-treated), isotropic at 80 ^{0}C (2 = isotropic) and after annealing up to 80 ^{0}C and cooling to RT (3 = annealed); b) HR-SEM cross-section images of the 3 membranes. The yellow arrows show the thickness of the separated layer and the penetration effect of the layer inside the PES.

To check the quality of the samples, BSA rejection was measured to detect micro defects in the active layer. **Table 7.5** shows >95% rejection of BSA in all cases meaning that the membranes produced had few defects. The higher water permeability values for annealed and isotropic membranes suggest that the thermal treatment considerably improves the transport of water through the pores. The intrusion of the material inside the pores of the support strongly affects the transport through the membrane. Moreover, the highest permeability value is found for the annealed membrane.

Table 7.5 | Water permeability and BSA rejection values of the 3 membranes.

Membrane	Permeability (L·m^{-2}·h^{-1}·bar^{-1})	BSA rejection (%)
Non-treated	1.30 ± 0.09	99.2 ± 0.57
Isotropic	4.25 ± 0.06	97.8 ± 0.28
Annealed	6.88 ± 0.34	96.9 ± 0.31

The MWCO of the membranes was determined from the filtration of 4 PEGs with different Mn (g·mol^{-1}). Aqueous solutions (1 mg/ml) of PEGs with Mn 1500, 4600, 7000 and 10000 g·mol^{-1} were used. The results plotted in **Figure 7.12** showed similar rejection values for big PEGs but a drop for the small PEG 1500, especially for the isotropic membrane. The MWCO of the annealed and non-treated membranes is considerably lower than that of the isotropic membranes (**Table 7.6**). Together with the higher permeability, this suggests that the disorder in the membrane that is polymerized in the isotropic state, creates a broader pore size distribution.
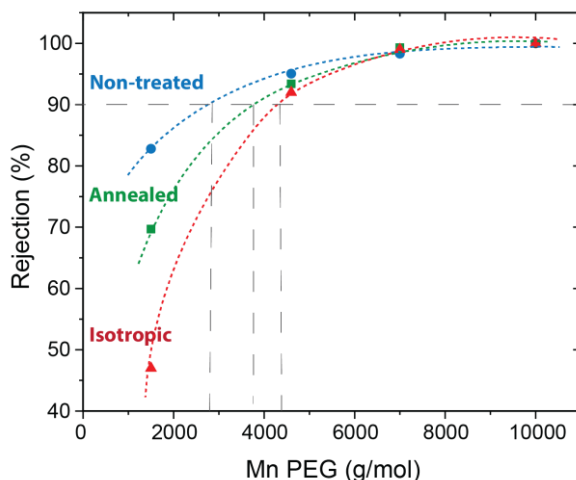
Figure 7.12 | a) Rejection curve of PEG comparing the 3 membranes showing different MWCO values.

Table 7.6 | Calculated MWCO values and corresponding R_h of non-treated, isotropic and annealed membranes of **NEt$_4$·Sulf** on PES support:

Membrane	M_n (g·mol^{-1})	R_h (nm)*
Non-treated	2.8 x 10^3	1.31
Annealed	3.8 x 10^3	1.44
Isotropic	4.4 x 10^3	1.62

*Hydrodynamic radius R_h (nm)= 0.06127·$M_n^{0.3931}$

It is known from literature that columnar LCs can align by nanoconfinement in ordered porous templates, such as anodic aluminum oxide or silica membranes, giving 1D alignment of the columns in the mesophase with the pore axis of the template.[20],[21] This alignment process requires a surface energy in the pore walls of

the template favorable for planar alignment. It is hypothesized that such alignment takes place in the pores of the PES support when annealing mesomorphic **NEt₄·Sulf**.[22] This would explain the previously observed increase in water flux.

Annealing would produce a reorganization of the columnar domains inside the pores of the PES support.[23] It is difficult to obtain experimental evidence of the alignment of the LC phase inside the support due to the irregular and heterogeneous shape and size of the pores in PES. This makes the study of the orientation of the columnar nanostructures a real challenge. Moreover, the presence of monodomains of the columnar mesophase of **NEt₄·Sulf** inside the pores of the PES support is preferable to properly study the alignment, which is also difficult to achieve.

To get insight into the effects of thermal annealing on the molecular alignment of the LC material inside the pores of the support, several annealed and non-treated membranes were prepared by spin coating solutions with different concentrations (wt.%) on the PES support and the layer thickness was determined with HR-SEM (**Figure 7.13**). The micrographs showed a decrease of the top layer thickness with lower concentrations, as already seen in **section 7.2**. Comparing both membranes, as previously observed, the active layer in non-treated membranes appeared more differentiated from the support, while after annealing, some material penetrated the pores of the support, decreasing the thickness of the active layer on top. However, due to the intrusion inside the support, it is difficult to either calculate the real thickness of the annealed system or determine the amount of material that penetrates.

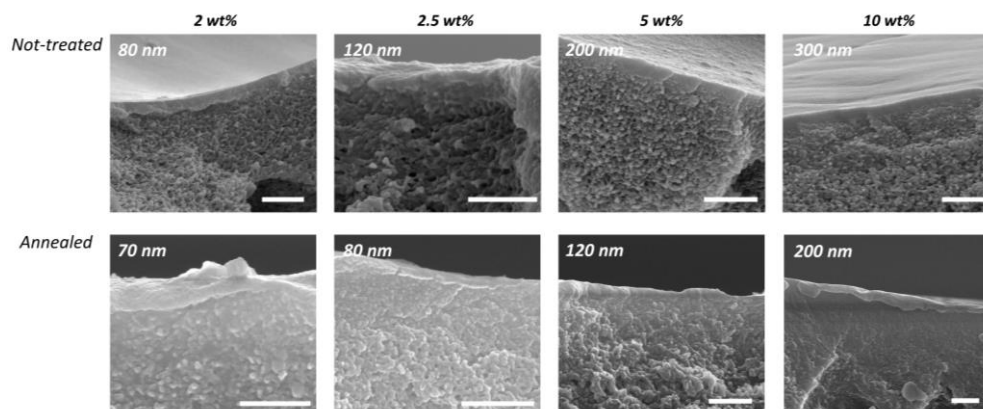**Figure 7.13 |** HR-SEM images of the supported membranes prepared from different concentration solutions with and without thermal annealing. Scale bar 100 nm.

A plot of the permeability vs the amount of material inside/on the membrane is presented in **Figure 7.14**. The values are compared with the calculated values using **eq. 7.1**. The length of all cylinders was assumed to be equal to the thickness of the

film (L [m]), which in this case is taken from the non-treated membranes. The rest of the parameters are the same ones used in Chapter 6.
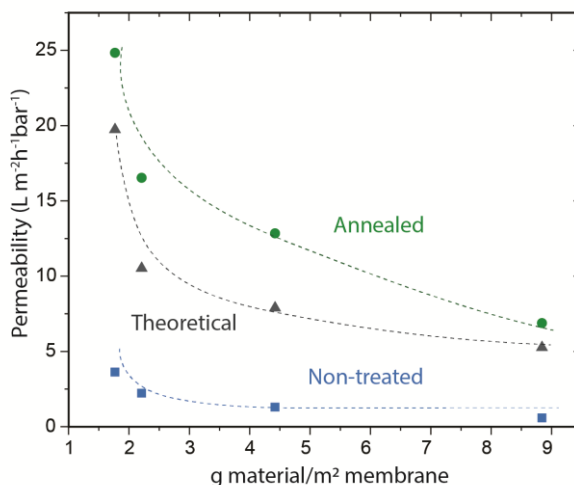

Figure 7.14 | a) Plot of water permeability vs the amount of material deposited on the support comparing annealed and non-treated membranes with values calculated for the membrane based on the thickness of the non-treated membrane.

A remarkable increase in water permeability was observed for the annealed membranes, reaching higher values than the values calculated for the thickness of the non-treated membrane, but showing a similar trend. The high permeabilities can be caused by either an improvement on the alignment of the active material inside the pores or by the presence of defects (expected with the reduction of thickness as seen in the previous **section 7.2.3**, but this would then be applied to both annealed and non-treated membranes). To further elucidate this, BSA rejection was measured and additionally, different Mn PEGs within the range of the pore size (1500-7000 g·mol⁻¹) were filtered through the membranes to determine the pore size of the membranes, given by the molecular weight cut-off (MWCO). The results are presented in **Table 7.7.**

The results showed high rejection values of BSA for all the non-treated membranes except for the thinnest which has only 91.8% rejection (red value). For the annealed membranes, the BSA rejection is lower (thinner membranes with 90-80 % rejection, red values). The obtained MWCO from the PEG rejection curves showed a difference of approx. 1000 g·mol⁻¹ over the concentration range for the non-treated membranes when less material is deposited. However, for annealed membranes, the MWCO increased reaching values more than double (orange shaded values). Considering only the membranes without remarkable defects (concentrations of 5 and 10 wt.%), MWCO values of annealed membranes are 1000-2000 g·mol⁻¹ higher, in line with the increase in water flux compared to non-treated membranes previously observed.

Table 7.7 | Rejection of BSA and a series of different Mn PEG and calculated MWCO values (g·mol⁻¹) for **non-treated** and **annealed** membranes with different amount of material deposited (different concentration solutions):

Concentration (wt. %)		2	2.5	5	10
Rejection values % for Non-treated membranes					
BSA (66 KDa, 7 nm)		91.8	95.6	96.1	99.8
	7000	90.7	93.7	95.9	98.9
PEG Mn(g·mol⁻¹)	4600	91.2	91.0	92.1	92.0
	1500	85.6	76.3	87.4	84.0
MWCO calculated (g·mol⁻¹)		4100	4300	3300	3100
Rejection values % for annealed membranes					
BSA (66 KDa, 7 nm)		80.6	90.6	95.7	99.3
	7000	76.5	90.8	92.1	98.3
PEG Mn(g·mol⁻¹)	4600	70.6	82.2	89.1	93.4
	1500	61.8	62.9	66.8	69.7
MWCO calculated (g·mol⁻¹)		>10000	6750	5200	4100

The hypothesis is that the higher flux observed for the annealed membranes is due to the intrusion of the material into the support when annealing. This material fills dead-end superficial pores of the PES and partially coats the walls of large pores. The rest forms a thinner layer on top, enough to create a dense barrier with high flux. When the amount of deposited material is decreased, thinner layers are obtained and a situation without top layer is reached. Instead, in such a case, the pores of the support that have been filled with material control the mass transport and determine the selectivity of the membrane. In this situation, the material that penetrates the support would re-organize in a more ordered structure after thermal annealing of the membranes. Nevertheless, to confirm this mechanism, further information such as the thickness of the material filling the pores or the organization of the liquid crystalline domains inside the pores is required. However, it is difficult to determine these parameters accurately for this system.

Concluding, the low isotropization temperature of **NEt₄·Sulf** allows the improvement of water permeability of membranes after thermal annealing. We propose that this is a result of the intrusion of some material in the support with the subsequent alignment of the columnar domains with the pores of the support.

7.4 Conclusions and future perspectives

In this Chapter, two strategies to optimize the filtration performance of the membranes presented in the earlier Chapters are described. The first strategy, based on the use of H-bonded molecules in the columnar structure, showed increased permeability of the membranes with smaller pore sizes due to better organization of the pores. Variation of the fabrication parameters of these membranes yields an optimum thickness of the active layer of approximately 150 nm that combines a high permeability with a low defect density. In the second approach, we demonstrate that a thermal annealing of the LC layer before polymerization increases the water flux in membranes. This is explained by the filling of the pores of the support with the material when heating, and subsequent re-orientation by molecular confinement when cooling down. However, a full understanding of the process needs further investigation.

The membrane improvements presented here have been achieved with a lab-scale process of molecular design and material characterization. The next step comprises the application and development of methodologies to fulfill industrial requirements when the fabrication of the composite membrane, is scaled-up.

The industrial market of membranes for water treatment and medical devices is irrefutably growing; it has established worldwide sales of up to USD 14 billion in 2019 from USD 2 billion in 2005, and it is expected to reach USD 24 billion in 2026.[24] The success of polymeric membranes for water treatment has been more than proven, with the application of membrane technologies on a strikingly large scale despite the skepticism in the past about the feasibility of using polymeric materials for this purpose. The development of large-scale nanofiltration plants began in the 1980s, with the introduction of low-pressure nanofiltration membranes, and it was followed by high-pressure reverse osmosis filtration.[25] Current use of nanofiltration systems in water treatment is focused on the removal of pesticides and other toxic organic substances. [26] In industrial plants, large water flows from polluted rivers can be treated with low energy cost [27] and at a smaller scale with already widely spread point-of-use drinking water units, it is possible to remove low-level contaminants from relatively clean water. In addition to waste-water treatment, drinking water production and desalination, new applications of membranes for water purification are being pursued: e.g. the treatment of industrial effluents for the recovery and re-use of components from water or the removal of specific micropollutants. This stimulates the development of the so-called "new generation" membranes. Important milestones in membrane materials have been reached with improvements in molecular design introduced at the laboratory scale, where an insight into membrane transport mechanisms is the focus. The results described in this Thesis, are an example of such an effort, with a better control over pore size and pore functionalization as the main

outcome, leading to higher filtration selectivity. Nevertheless, an extensive supply of clean water requires scaling up these filtration systems to the industrial level. The transition from fabrication and testing in the laboratory to the commercialization and industrial application at a large scale is a long and challenging process with many hurdles. To be able to compete with commercial membranes, new membrane materials must fit the established criteria of design and performance: chemical stability, longevity, good performance with high yields and low fouling.[28] These requirements have to be combined with low material costs to make LC-based membranes commercially feasible. The scale-up makes the total expenses of a membrane module in an industrial plant higher. LC materials are more expensive than polymers used for current membranes due to the difficulty of synthesis and preparation. The fabrication of supported membranes with very thin LC films will increase the throughput of water production and lower the membrane module price (less material is needed). This is needed to include these new generation materials in the membrane market.

7.5 Experimental section

7.5.1. Materials and methods

All the reagents and solvents for synthesis were purchased from Sigma-Aldrich or TCI America. The ultrafiltration support, PES UF (30 kDa MWCO) was purchased from Sartorius Stedim Biotech, monodispersed PEG with a polydispersity of ~ 1.05 was purchased from Agilent. Ultrapure water was used for all filtration experiments.

NMR spectra were recorded at room temperature on a Bruker FT-NMR spectrometer AVANCE III HD-NanoBay (400 MHz, Bruker UltraShield magnet, BBFO Probehead, BOSS1 shim assembly) in $CDCl_3$. Chemical shifts are given in ppm for tetramethylsilane (TMS, 0 ppm). MALDI-TOF-MS analysis was performed on a Bruker speed autoflex operated in reflectron mode with a positive voltage polarity, 500 shots. ATR FT-IR spectra were recorded at room temperature on a PerkinElmer Spectrum Two spectrometer equipped with a universal attenuated total reflectance (ATR) sampling accessory. Polarized Optical Microscopy (POM) was performed with a Jeneval microscope equipped with crossed polarizers and a Linkam THMS 600 heating stage. Differential Scanning Calorimetry (DSC) measurements were performed in hermetic T-zero aluminum sample pans using a TA Instruments Q2000−1037 DSC instrument equipped with a RCS90 cooling accessory. Transition temperatures and enthalpies were typically determined from the first cooling and second heating run using Universal Analysis 2000 software (TA Instruments). X-ray scattering measurements were performed on a Ganesha lab instrument equipped with a Genix-Cu ultralow divergence source producing X-ray photons with a wavelength of 0.154 nm and a flux

of $1 \cdot 10^8$ photons s^{-1}. Diffraction patterns were collected using a Pilatus 300 K silicon pixel detector with 487 × 619 pixels of 172 µm^2 in size, placed at a sample to detector distance of 91 mm (wide-angle, WAXS), or 500 mm (medium angle, MAXS). On the obtained diffraction patterns an azimuthal integration was performed using SAXSGUI software, to calculate the intensity against the scattering vector q, where q = $(4\pi/\lambda)$sin σ (σ is the angle of incidence and λ is the wavelength). The beam center and the q-range were calibrated using silver behenate ($d_{(100)}$ = 1.076 nm; 5.839 nm) as a reference. The $d_{(300)}$ was used for calibration. The temperature was controlled with a Linkam HFSX350 heating stage and cooling unit. Measurements were performed on bulk samples sealed in 1.0 mm diameter glass capillaries, 0.01 mm wall thickness (Hilgenberg). UV-Vis experiments were performed on a Jasco V-750 spectrophotometer. All experiments were performed in 10 × 10 mm quartz cuvettes at 20 ^{0}C. Fluorescence experiments were measured using a Spark® Tecan 10M. Spectra were recorded using 100 of gain and 50 % mirror at 20 ^{0}C. The photopolymerization was performed for 15 min with a mercury lamp (Omnicure s2000, emitting at 320−500 nm). The intensity was approximately 22 mW·cm^{-2} at the sample surface. HR-SEM was measured with Quanta 3D FEG (FEI/TFS) with EDT secondary detector. Samples were sputter-coated with a thin layer of gold using a Balzer Union SCD 040 sputter device.

7.5.2 Detailed experimental conditions

Sample preparation and GISAXS measurements

Samples of **section 7.2.1** were prepared by spin-coating a solution in MeOH of the 4 compounds separately (**HNEt₃Sulf, NEt₄Sulf, HNEt₃Sulf-H, NEt₄Sulf-H**) All samples were coated on PVA coated glass substrates.

Membrane fabrication

Composite membranes we prepared using polyethersulfone as support. Glass plates were cleaned with acetone and isopropanol under sonication for 10 minutes in a bath. Solutions for spin coating were prepared by mixing the wedge-shaped monomer (**NEt₄Sulf** or **NEt₄Sulf-H**) (3.2 equivalents) with 1,10-decanedithiol (4.6 equivalents) in EtOH in concentrations from 1 to 10 wt. % (1, 2, 2.5, 5, 10). Finally, Bis(2,4,6-trimethylbenzoyl)-phenylphosphineoxide (Irgacure 819, 3 wt.%) was added as the initiator. A sacrificial layer of polyvinyl alcohol (PVA) was spin-coated from a 10 wt.% aqueous solution onto clean glass at 1500 rpm for 60 s. Then the polyethersulfone (PES) support was pasted on top, and the monomer mixtures were spin-coated on top for 30 s at 1500 rpm (in section 7.2.3 also 2000 rpm). The polymerization was performed with UV light for 15 min with 8 mW·cm^{-2} of intensity giving thin film-supported membranes after dissolving the PVA in water and drying in the oven at 40 ^{0}C.

Filtration tests

Filtration tests were performed using a 20 ml custom-made, stainless steel, stirred "Amicon type" dead-end filtration cell of 1.5 cm diameter. Samples of the membrane were cut to the desired size and pre-cleaned with deionized water. For each filtration test, a membrane was placed in the cell that was filled with ultrapure water (total volume of 20 ml). The cell was closed and subsequently pressurized with nitrogen at the desired pressure.

The permeability of the membranes was determined by measuring the flux of pure water at different pressures (3–6 bar) *in triplo* for 3 samples. Pure water was filtered for 2 h at 5 bar to stabilize the flux.

Protein rejection was determined with the filtration of aqueous solutions (50 µM) of BSA and GFP in PBS. With the cell previously cleaned with water, the filtration was carried out at a pressure of 4 bar where 4 samples of 1 ml of permeate were collected from which the first one was discarded to avoid mixtures with residual water below the membrane in the cell.

The MWCO of the membranes was determined by measuring the rejection of polyethylene glycol (PEG). Membranes were subjected to PEG filtrations at 4 bar in the Amicon cell. Aqueous solutions in ultrapure water were made containing PEGs with number average molecular weights (Mn) ranging from 600 to 8000 $g \cdot mol^{-1}$ with a concentration of 0.5 $g \cdot L^{-1}$ for each polymer. The filtration procedure and the rejection analysis of all these experiments was done as described in previous Chapters (e.g. **section 2.6.2**).

Synthetic procedures

HNEt₃·Sulf-H

Acid chloride (**3**) (1.75 g, 2.71 mmol, 1 equiv.), which was obtained as detailed in chapter 2, was dissolved in 3 ml of THF at 0 °C. Then 4-amino-benzenesulfonic acid (1 g, 5.77 mmol, 1.2 equiv.) and triethylamine (0.55 g, 5.43 mmol, 2 equiv.) were dissolved in another round bottom flask in THF (10 ml). The amine solution was slowly added to the solution with the acid chloride. The solution was left stirring overnight at room temperature. After completion of the reaction, the solvent was evaporated. The residue was dissolved in water and CH_3Cl, extracted with CH_3Cl, dried with $MgSO_4$ and filtered. The solvent was evaporated to yield a white solid. ^{1}H-NMR ($CDCl_3$, 400 MHz) δ = 7.72 (d, *J* = 8.1 Hz, 1H), 7.60 (d, *J* = 8.3 Hz, 1H), 7.16 (s, 1H), 5.79 (ddtd, *J* = 16.9, 10.3, 6.7, 3.7 Hz, 1H), 5.03 – 4.87 (m, 2H), 3.95 (d, *J* = 7.2 Hz, 2H), 3.05 – 2.94 (m, 2H), 2.08 – 1.96 (m, 3H), 1.75 (d, *J* = 6.6 Hz, 1H), 1.51 – 1.40 (m, 2H), 1.36 (q, *J* = 6.6 Hz, 1H), 1.32 (s, 4H), 1.31 – 1.17 (m, 10H, alkyl chains). ^{13}C-NMR ($CDCl_3$, 100 MHz) δ = 166.16, 153.11, 141.29, 140.22, 139.23, 129.21, 126.75, 120.88, 114.23, 106.08, 73.52, 69.23,

46.34, 33.94, 30.51, 29.82, 29.3, 29.07, 26.29, 8.65. Maldi-Tof MS: m/z calculated for [M-Na]$^+$: 780,46 found: 780,46

NEt$_4$·Sulf-H

HNEt$_3$·Sulf-H (500 mg, 0.56 mmol, 1 equiv.) and 323.73 µL of tetraethylammonium hydroxide (solution of 20 wt. % in water (0.56 mmol, 1 equiv.) were dissolved in methanol (8 ml). The solution was stirred overnight at room temperature with the system closed. The solvent was evaporated with rotavap. The residue was dissolved in chloroform and filtrated. Chloroform was evaporated and the product was dried under vacuum at 60 ^{0}C yielding quantitatively a waxy white solid. ^{1}H-NMR (CDCl$_3$, 400 MHz) δ = 7.82 (d, J = 8.0 Hz, 2H), 7.65 (d, J = 8.3 Hz, 2H), 7.18 (s, 2H), 5.89 – 5.74 (m, 2H), 4.95 (dd, J = 25.4, 13.6 Hz, 6H), 4.16 – 3.59 (m, 8H), 3.20 (q, J = 7.1 Hz, 8H), 2.09 (t, J = 39.3 Hz, 6H), 1.73 (d, J = 14.5 Hz, 6H), 1.55-1.20 (m, 10 H, alkyl chains). ^{13}C-NMR (CDCl$_3$, 100 MHz) δ = 166.36, 153.47, 141.49, 140.28, 139.62, 129.63, 127.03, 121.19, 114.57, 106.53, 73.87, 69.67, 52.82, 34.27, 30.83, 30.02, 29.63, 29.41, 26.55, 7.82.

7.6 References

[1]   X. Feng, M. E. Tousley, M. G. Cowan, B. R. Wiesenauer, S. Nejati, Y. Choo, R. D. Noble, M. Elimelech, D. L. Gin, C. O. Osuji, *ACS Nano* **2014**, *8*, 11977.
[2]   H. Monobe, H. Hori, Y. Shimizu, K. Awazu, *Mol. Cryst. Liq. Cryst.* **2007**, *475*, 13.
[3]   K. Kwon, K. Park, H. T. Jung, *Nanoscale* **2018**, *10*, 8459.
[4]   E. Pouzet, V. De Cupere, C. Heintz, J. W. Andreasen, D. W. Breiby, M. M. Nielsen, P. Viville, R. Lazzaroni, G. Gbabode, Y. H. Geerts, *J. Phys. Chem. C* **2009**, *113*, 14398.
[5]   D. González-Rodríguez, A. P. H. J. Schenning, *Chem. Mater.* **2011**, *23*, 310.
[6]   Z. Li, L.-Z. Wu, *Lecture Notes in Chemistry 88 Hydrogen Bonded Supramolecular Materials*, **2015**.
[7]   S. Cantekin, T. F. A. de Greef, A. R. A. Palmans, *Chem. Soc. Rev.* **2012**, *41*, 6125.
[8]   C. F. C. Fitié, I. Tomatsu, D. Byelov, W. H. De Jeu, R. P. Sijbesma, *Chem. Mater.* **2008**, *20*, 2394.
[9]   C. F. C. Fitié, E. Mendes, M. A. Hempenius, R. P. Sijbesma, *Macromolecules* **2011**, *44*, 757.
[10]   K. Venkata Ramiah and P. G. Puranik, *HYDROGEN BONDING IN AMIDES (Electrostatic Interaction and Resonance)*, **1962**.
[11]   G. Giubertoni, O. O. Sofronov, H. J. Bakker, *Commun. Chem.* **2020**, *3*, 1.
[12]   K. Nickmans, G. M. Bögels, C. Sánchez-Somolinos, J. N. Murphy, P. Leclère, I. K. Voets, A. P. H. J. Schenning, *Small* **2017**, *13*, 1.
[13]   P. Marín San Román, K. Nijmeijer, R. P. Sijbesma, *J. Memb. Sci.* **2021**, *644*, 120097.
[14]   R. E. Kesting, *Synthetic polymeric membranes, Chapter 4*, Mc-Graw Hill, **1971**.
[15]   M. Zhou, T. J. Kidd, R. D. Noble, D. L. Gin, *Adv. Mater.* **2005**, *17*, 1850.
[16]   W. Pisula, Ž. Tomović, B. El Hamaoui, M. D. Watson, T. Pakula, K. Müllen, *Adv. Funct. Mater.* **2005**, *15*, 893.
[17]   E. Grelet, H. Bock, *Europhys. Lett.* **2006**, *73*, 712.
[18]   X. Feng, K. Kawabata, G. Kaufman, M. Elimelech, C. O. Osuji, *ACS Nano* **2017**, *11*, 3911.
[19]   X. Feng, S. Nejati, M. G. Cowan, M. E. Tousley, B. R. Wiesenauer, R. D. Noble, M. Elimelech, D. L. Gin, C. O. Osuji, *ACS Nano* **2016**, *10*, 150.
[20]   M. Steinhart, S. Zimmermann, P. Göring, A. K. Schaper, U. Gösele, C. Weder, J. H. Wendorff, *Nano Lett.* **2005**, *5*, 995.
[21]   C. V. Cerclier, M. Ndao, R. Busselez, R. Lefort, E. Grelet, P. Huber, A. V. Kityk, L. Noirez, A. Schönhals, D. Morineau, *J. Phys. Chem. C* **2012**, *116*, 18990.
[22]   A. V. Kityk, M. Busch, D. Rau, S. Calus, C. V. Cerclier, R. Lefort, D. Morineau, E. Grelet, C. Krause, A. Schönhals, B. Frick, P. Huber, *Soft Matter* **2014**, *10*, 4522.
[23]   R. Zhang, X. Zeng, B. Kim, R. J. Bushby, K. Shin, P. J. Baker, V. Percec, P. Leowanawat, G. Ungar, *ACS Nano* **2015**, *9*, 1759.
[24]   P. M. Research, *Membrane Filtration Market Share, Size, Trends, Industry Analysis Report, By Application (Water & Waste Water, Food & Beverages); By Module Design (Spiral Wound, Tubular Systems, Plate & Frame and Hollow Fiber); By Membrane Material (Polymeric, Ceramic);* , **2020**.
[25]   R. J. Petersen, *J. Memb. Sci.* **1993**, *83*, 81.
[26]   B. Van Der Bruggen, C. Vandecasteele, *Environ. Pollut.* **2003**, *122*, 435.
[27]   C. Ventresque, G. Turner, G. Bablon, *J. / Am. Water Work. Assoc.* **1997**, *89*, 65.
[28]   M. Ulbricht, *Polymer (Guildf).* **2006**, *47*, 2217.

Summary

The ongoing growth of the global population results in water shortage, industrial pollution, and overuse of natural resources. To address these issues, a transition from the current "linear" to "circular" economy is required, with a strong focus on the removal, recovery, and reuse of 'waste' compounds from industrial processes. In this new concept of resource management, water purification plays an important role, and it requires the use of effective and sustainable separation methods to ensure clean water. This involves not only the production of clean water but also the retention of emerging contaminants (micropollutants) that have many negative effects on aquatic species and human health such as pesticides, hormones, plasticizers, pharmaceuticals, etc. and the recovery of valuable components from water streams for reuse. Membrane filtration is an efficient method with low energy consumption, that uses few chemicals, and it is easily processable and scalable. This makes it one of the most applied techniques that already plays an important role in separation technology. Current commercial membranes present a trade-off between permeability and selectivity which makes it difficult to achieve molecular selectivity at sub-nanometer sizes combined with high fluxes in the filtration process. To have more efficient molecular separation processes, better control over pore size, morphology and membrane chemistry is desired.

In this thesis, the self-assembly of liquid crystals is used to achieve control over the molecular organization and pore formation with defined sizes and chemical functionalities. The followed strategy relies on the use of columnar liquid crystals as the selective layer that is spin-coated on a porous support. The columnar nanostructure is formed by the self-assembly of sulfonate monomers and is easily fixated with light. Ideally, the homeotropic alignment of the columns is desired to get higher flux but selectivity is based on the particular pore size created in the structure, which has a size around 1 nm. Two main strategies are followed to get our pores in the columnar nanostructure: 1) the use of a templated discotic complex in which the central molecule is removed after the crosslinking leaving a fixated pore size and 2) the nano-segregation of sulfonate salts leaving the polar regions in the center creating channels as pores. Using different counterions the channel can vary in size and also the arrangement of the molecules within the nanostructure. Beside this, the modification of the pores to tailor the filtration performance *in situ* without the necessity of new molecular design and fabrication is shown as a way to get versatile membranes. Different approaches for membrane modification were explored. The exchange of ions is an easy way to have a reversible modification of the filtration properties, especially on rejection due to associated pore size variation. Chemical modification by covalent bonds is a way to create new functionalities within the pores and therefore, to change their sizes and charges permanently. Furthermore, the use of light can be also applied to get dynamic reversible systems in which uptake kinetics vary after irradiation, or water fluxes and mass transport through the membrane are controlled using light with different wavelengths. Optimization of these membranes includes playing with the

molecular design and the membrane processing to achieve a better orientation of the pores, permitting the adaptation in industrial processes, where high fluxes are required.

The use of membranes for water purification purposes is presented in **Chapter 1** which follows with a discussion of the state-of-the-art membranes and their limitations. To overcome the weak points, new materials and strategies that reach control over the pore size (distribution) and molecular environment or functionalities are shortly discussed. The use of self-assembled liquid crystals is explored more in detail as this approach offers versatility in the morphologies and the molecular designs and the potential to prepare functional small pores with narrow distributions.

In **Chapter 2** a templated supramolecular complex *Sulfac₃TB* is designed and it arranges in a columnar nanostructure, that becomes porous after removing the template molecule in the center once the network is crosslinked. Membranes are obtained from the deposition of a defect-free thin layer of the crosslinked material on top of a porous support. The filtration performance shows water permeability values similar to current nanofiltration membranes and control over the molecular separation is demonstrated with both size and charge selectivity for neutral and charged solutes.

The possibility of having different functionalities in the pores brings versatility to self-assembled membranes. The influence of these functionalities on filtration performance is investigated in **Chapter 3** following two different approaches. First, membranes based on an analogous *Benzac₃TB* complex are produced, and filtration studies confirm the improvement of transport properties when sulfonate functionalities are used compared to carboxylic acids due to ionic dissociation-association effects. Second, the modification of the membranes of Chapter 2 is accomplished *via* covalent functionalization of the sulfonate groups inside the pores into 3 different sulfonamides. The pore size and charge selectivity of the new membranes are modified compared to the starting one, which influences the water permeability and rejection properties.

The photo-switchability properties of templated porous systems are studied in **Chapter 4**. The supramolecular discotic complex *Azoac₃TB* is prepared and characterized, showing a columnar mesophase at room temperature in bulk. Polymer films are obtained by photo-polymerization and the columnar pores are created with the removal of TB as well. The *trans-cis-trans* photo-switching of the system is confirmed in both the monomer in solution and the porous films in solid-state. The uptake kinetics of rhodamine 6g are studied showing an 8-fold difference between isomer trans and cis of the porous film. This establishes the basis for the application of this material as a dynamic system for membranes.

Making use of the fundamentals showed in the previous Chapter, the modification of the pore size is studied in **Chapter 5** with photo-switchable membranes based on a new discotic supramolecular complex *SulfAzo₃TB*. Sulfonic acids are used instead of carboxylic as water transport was proven to be enhanced for membranes with the first ones (Chapter

3). The azo moieties of the nanostructure close to the pores permit the isomerization *trans-cis-trans* with irradiation. This results in a pore size change (and thus change in molecular weight cut-off value) that allows variation of the water flux and the rejection for small molecules in a reversible way, providing a promising *on-off* dynamic transport system.

In **Chapter 6**, the formation of columnar nanostructures from the aggregation of wedge-shaped sulfonated salts with different counterions is explored. The crystallinity and thermal properties of the compounds obtained depend on the counterion used; charge and size influence the arrangement of the molecules within the columnar lattice. The better stability and order of the mesophase of the *NEt₄Sulf* salt is used for the formation and characterization of filtration membranes. Lower water permeability and MWCO values than for the *Sulfac₃TB* membrane (templated system) are obtained, suggesting a smaller pore size. The rejection for organic charged and neutral molecules is higher because of the smaller pore size and this allows even the retention of smaller organic solutes like saccharides.

Finally, in **Chapter 7** a preliminary outlook of an optimization process is explored including the molecular design of the active material of the membrane and variation of the fabrication parameters. To obtain a better orientation of the pores in the structure, the development of molecular units *NEt₄Sulf-H*, analogous to wedge-shaped sulfonated salts used in Chapter 6, but with hydrogen bonding that promotes stacking, is explored. These new membranes shows higher water permeability and smaller pores than the analogous membranes. Additionally, optimization of the layer thickness and coating method is done to reach the limit for a good performance of the membrane. Finally, preliminary results of the application of a thermal annealing process to the membranes of Chapter 6 is presented. The performance of the membranes is investigated with and without annealing showing improvement of the water permeability upon annealing. However, further studies need to be done to give consistent conclusions regarding the influence of the annealing process on the composite membrane system. As a closure of the chapter, a small technological assessment is given for the application of the developed membranes at the industrial level.

The overall work presents an important step in filtration membranes based on self-assembled liquid crystals. Indeed, the research is done at a laboratory scale and the improvements shown here are mostly focused on the molecular design of the selective material. An improved and tunable molecular selectivity is achieved due to the control over the structure, chemistry, pore size and charge of the active material of the composite membrane. Also, the optimization of the membrane fabrication is an important point to pay attention to study the filtration performance properly. A basic analysis was carried out, filtrating standard solutes (inorganic and organic) of different sizes with and without charges to show the fundamentals of the performance and understand the separation mechanism.

Comparing the different systems presented in the chapters, the following features can be highlighted:

1. Wedge-shaped molecules that present thermotropic columnar mesophases are used to produce nanoporous materials. Pore size can be fixed in a controlled manner using templated molecular systems and these can be easily modified by changing counterions.
2. Functionalities of the pores play an important role regarding ionic interactions with the solutes which directly affects the rejection properties. For instance, it was proven that carboxylic acids interact more and transport decreases. The variation of functionalities can be done by simply using different molecular units in the nanostructure or *in-situ* in the membrane. To address the last one, ion exchange or covalent modification chemistry are presented as useful tools.
3. The presence of responsive moieties in the membranes provides a way to tailor the filtration properties due to pore size and chemical changes in the porous structure. Azo benzenes are the best candidates because of their easiness to reversibly isomerize with light.
4. Supramolecular chemistry and, more specifically, self-assembly, allows, as an advantage, to play with molecular structures to improve the organization in the network, for instance using hydrogen bonds that orient the molecules towards the water flux in the case of membranes.
5. Finally, the use of thermotropic liquid crystals provides the system with versatility regarding processability and the possibility of molecular rearrangement to orient the pores for instance by just thermally annealing the material.

In conclusion, this thesis proves the capability of the presented membranes to perform water-based separations at a molecular level with competing permeabilities. It shows the potential of new materials to be used in the future as membrane materials with tunable properties that can be easily adapted to the separation requirements of specific applications, especially in water purification and the recovery and reuse of components from wastewater and industrial streams.